UNITED STATES AIR FORCE

SUMMER RESEARCH PROGRAM -- 1996

SUMMER RESEARCH EXTENSION PROGRAM FINAL REPORTS

VOLUME 4A
WRIGHT LABORATORY

RESEARCH & DEVELOPMENT LABORATORIES

5800 Uplander Way

Culver City, CA 90230-6608

Program Director, RDL
Gary Moore

Program Manager, AFOSR
Major Linda Steel-Goodwin

Program Manager, RDL
Scott Licoscos

Program Administrator, RDL
Johnetta Thompson

Program Administrator
Rebecca Kelly-Clemmons

Submitted to:

AIR FORCE OFFICE OF SCIENTIFIC RESEARCH

Bolling Air Force Base

Washington, D.C.

December 1996

20010316 066

AQM01-06-1066

REPORT DOCUMENTATION PAGE

AFRL-SR-BL-TR-00-

0705

1. AGENCY USE ONLY *(Leave blank)*	2. REPORT DATE December, 1996	3. REPORT TYPE AND DATES COVERED

4. TITLE AND SUBTITLE 1996 Summer Research Program (SRP), Summer Research Extension Program (SREP), Final Report, Volume 4A, Wright Laboratory	5. FUNDING NUMBERS F49620-93-C-0063

6. AUTHOR(S)

Gary Moore

7. PERFORMING ORGANIZATION NAME(S) AND ADDRESS(ES) Research & Development Laboratories (RDL) 5800 Uplander Way Culver City, CA 90230-6608	8. PERFORMING ORGANIZATION REPORT NUMBER

9. SPONSORING/MONITORING AGENCY NAME(S) AND ADDRESS(ES) Air Force Office of Scientific Research (AFOSR) 801 N. Randolph St. Arlington, VA 22203-1977	10. SPONSORING/MONITORING AGENCY REPORT NUMBER

11. SUPPLEMENTARY NOTES

12a. DISTRIBUTION AVAILABILITY STATEMENT Approved for Public Release	12b. DISTRIBUTION CODE

13. ABSTRACT *(Maximum 200 words)*

The United States Air Force Summer Research Program (SRP) is designed to introduce university, college, and technical institute faculty members to Air Force research. This is accomplished by the faculty members, graduate students, and high school students being selected on a nationally advertised competitive basis during the summer intersession period to perform research at Air Force Research Laboratory (AFRL) Technical Directorates and Air Force Air Logistics Centers (ALC). AFOSR also offers its research associates (faculty only) an opportunity, under the Summer Research Extension Program (SREP), to continue their AFOSR-sponsored research at their home institutions through the award of research grants. This volume consists of a listing of the participants for the SREP and the technical report from each participant working at the AF Wright Laboratory.

14. SUBJECT TERMS Air Force Research, Air Force, Engineering, Laboratories, Reports, Summer, Universities, Faculty, Graduate Student, High School Student	15. NUMBER OF PAGES
	16. PRICE CODE

17. SECURITY CLASSIFICATION OF REPORT Unclassified	18. SECURITY CLASSIFICATION OF THIS PAGE Unclassified	19. SECURITY CLASSIFICATION OF ABSTRACT Unclassified	20. LIMITATION OF ABSTRACT UL

Standard Form 298 (Rev. 2-89) (EG)
Prescribed by ANSI Std. 239.18
Designed using Perform Pro, WHS/DIOR, Oct 94

GENERAL INSTRUCTIONS FOR COMPLETING SF 298

The Report Documentation Page (RDP) is used in announcing and cataloging reports. It is important that this information be consistent with the rest of the report, particularly the cover and title page. Instructions for filling in each block of the form follow. It is important to *stay within the lines* to meet *optical scanning requirements.*

Block 1. Agency Use Only *(Leave blank)*.

Block 2. Report Date. Full publication date including day, month, and year, if available
(e.g. 1 Jan 88). Must cite at least the year.

Block 3. Type of Report and Dates Covered. State whether report is interim, final, etc. If applicable, enter inclusive report dates (e.g. 10 Jun 87 - 30 Jun 88).

Block 4. Title and Subtitle. A title is taken from the part of the report that provides the most meaningful and complete information. When a report is prepared in more than one volume, repeat the primary title, add volume number, and include subtitle for the specific volume. On classified documents enter the title classification in parentheses.

Block 5. Funding Numbers. To include contract and grant numbers; may include program element number(s), project number(s), task number(s), and work unit number(s). Use the following labels:

C -	Contract	**PR** -	Project
G -	Grant	**TA** -	Task
PE -	Program	**WU** -	Work Unit
	Element		Accession No.

Block 6. Author(s). Name(s) of person(s) responsible for writing the report, performing the research, or credited with the content of the report. If editor or compiler, this should follow the name(s).

Block 7. Performing Organization Name(s) and Address(es). Self-explanatory.

Block 8. Performing Organization Report Number. Enter the unique alphanumeric report number(s) assigned by the organization performing the report.

Block 9. Sponsoring/Monitoring Agency Name(s) and Address(es). Self-explanatory.

Block 10. Sponsoring/Monitoring Agency Report Number. *(If known)*

Block 11. Supplementary Notes. Enter information not included elsewhere such as: Prepared in cooperation with....; Trans. of....; To be published in.... When a report is revised, include a statement whether the new report supersedes or supplements the older report.

Block 12a. Distribution/Availability Statement. Denotes public availability or limitations. Cite any availability to the public. Enter additional limitations or special markings in all capitals (e.g. NOFORN, REL, ITAR).

DOD -	See DoDD 5230.24, "Distribution Statements on Technical Documents."
DOE -	See authorities.
NASA -	See Handbook NHB 2200.2.
NTIS -	Leave blank.

Block 12b. Distribution Code.

DOD -	Leave blank.
DOE -	Enter DOE distribution categories from the Standard Distribution for Unclassified Scientific and Technical Reports. Leave blank.
NASA -	Leave blank.
NTIS -	

Block 13. Abstract. Include a brief *(Maximum 200 words)* factual summary of the most significant information contained in the report.

Block 14. Subject Terms. Keywords or phrases identifying major subjects in the report.

Block 15. Number of Pages. Enter the total number of pages.

Block 16. Price Code. Enter appropriate price code *(NTIS only)*.

Blocks 17. - 19. Security Classifications. Self- explanatory. Enter U.S. Security Classification in accordance with U.S. Security Regulations (i.e., UNCLASSIFIED). If form contains classified information, stamp classification on the top and bottom of the page.

Block 20. Limitation of Abstract. This block must be completed to assign a limitation to the abstract. Enter either UL (unlimited) or SAR (same as report). An entry in this block is necessary if the abstract is to be limited. If blank, the abstract is assumed to be unlimited.

PREFACE

This volume is part of a five-volume set that summarizes the research of participants in the 1996 AFOSR Summer Research Extension Program (SREP.) The current volume, Volume 1 of 5, presents the final reports of SREP participants at Armstrong Laboratory. Volume 1 also includes the Management Report.

Reports presented in this volume are arranged alphabetically by author and are numbered consecutively — e.g., 1-1, 1-2, 1-3; 2-1, 2-2, 2-3, with each series of reports preceded by a 35 page management summary. Reports in the five-volume set are organized as follows:

VOLUME	TITLE
1	Armstrong Laboratory
2	Phillips Laboratory
3	Rome Laboratory
4A	Wright Laboratory
4B	Wright Laboratory
5	Arnold Engineering Development Center Air Logistics Centers

Report #	Report Title Author's University	Report Author
1	Chlorinated Ethene Transformation, Sorption & Product Distr in Metallic Iron/Water Systems: Effect of Iron Properties Washington State University, Pullman, WA	Dr. Richelle M Allen-King Dept. of Geology AL/EQ
2	Dynamically Adaptive Interfaces: A Preliminary Investigation Wright State University, Dayton, OH	Dr. Kevin B Bennett Dept. of Psychology AL/CF
3	Geographically Distributed Collaborative Work Environment California State University, Hayward, CA	Dr. Alexander B Bordetsky Dept. Decesion Sciences AL/HR
4	Development of Fluorescence Post Labeling Assay for DNA Adducts: Chloroacetaldeh New York Univ Dental/Medical School, New York, NY	Dr. Joseph B Guttenplan Dept. of Chemistry AL/OE
5	The Checkmark Pattern & Regression to the Mean in Dioxin Half Life Studies University of South Alabama, Mobile, AL	Dr. Pandurang M Kulkarni Dept. of Statistics AL/AO
6	Determination of the Enzymatic Constraints Limiting the Growth of Pseudomonas University of Dayton, Dayton, OH	Dr. Michael P Labare Dept. of Marine Sciences AL/HR
7	Tuned Selectivity Solid Phase Microextraction Clarkson University, Potsdam, NY	Dr. Barry K Lavine Dept. of Chemistry AL/EQ
8	A Cognitive Engineering Approach to Distributed Team Decision Making During University of Georgia, Athens, GA	Dr. Robert P Mahan Dept. of Psychology AL/CF
9	Repetative Sequence Based PCR: An Epidemiological Study of a Streptococcus Stonehill College, North Easton, MA	Dr. Sandra McAlister Dept. of Biology AL/CF
10	An Investigation into the Efficacy of Headphone Listening for Localization of Middle Tennessee State University, Murfreesboro, TN	Dr. Alan D. Musicant Dept. of Psychology AL/CF
11	The Neck Models to Predict Human Tolerance in a G-Y CUNY-City College, New York, NY	Dr. Ali M. Sadegh Dept. of Mech Engineering AL/CF

1996 SREP FINAL REPORTS

Phillips Laboratory

VOLUME 2

Report #	Report Title Author's University	Report Author
1	Experimental Study of the Tilt Angular Anisopalantaic Correlation & the Effect Georgia Tech Research Institute, Atlanta, GA	Dr. Mikhail Belen'kii Dept. of Electro Optics PL/LI
2	Performance Evaluations & Computer Simulations of Synchronous & Asynchronous California State University, Fresno, CA	Dr. Daniel C. Bukofzer Dept. of Elec Engineering PL/VT
3	MM4 Model Experiments on the Effects of Cloud Shading Texas Tech University, Lubbock, TX	Dr. Chia-Bo Chang Dept. of Geosciences PL/GP
4	Miniature Laser Gyro consisting in a Pair of Unidirectional Ring Lasers University of New Mexico, Albuquerque, NM	Dr. Jean-Claude M. Diels Dept. of Physics PL/LI
5	Simulations & Theoretical Studies of Ultrafast Silicon Avalanche Old Dominion University, Norfolk, VA	Dr. Ravindra P. Joshi Dept. of Elec Engineering PL/WS
6	Theory of Wave Propagation in a Time-Varying Magnetoplasma Medium & Applications to Geophysical Phenomena University of Massachusetts Lowell, Lowell, MA	Dr. Dikshitulu K. Kalluri Dept. of Elec Engineering PL/GP
7	Thermal Analysis for the Applications of High Power Lasers in Large-Area Materials Processing University of Central Florida, Orlando, FL	Dr. Arvinda Kar Dept. of Engineering PL/LI
8	Analytical Noise Modeling and Optimization of a Phasor-Based Phase Texas Tech University, Lubbock, TX	Dr. Thomas F. Krile Dept. of Elec Engineering PL/LI
9	Mathematical Modeling of Thermionic-AMTEC Cascade System for Space Power Texas Tech University, Lubbock, TX	Dr. M. Arfin K. Lodhi Dept. of Physics PL/VT
10	Preparation & characterization of Polymer Blends Ohio State University, Columbus, OH	Dr. Charles J. Noel Dept. of Chemistry PL/RK
11	Evaluation of Particle & Energy Transport to Anode, Cathode University of Texas-Denton, Denton, TX	Dr. Carlos A. Ordonez Dept. of Physics PL/WS
12	Analysis of the Structure & Motion of Equatorial Emission Depletion Bands Using Optical All-Sky Images University of Massachusetts Lowell, Lowell, MA	Dr. Ronald M. Pickett Dept. of Psychology PL/GP

1996 SREP FINAL REPORTS

Rome Laboratory

VOLUME 3

1996 SREP FINAL REPORTS

Wright Laboratory

VOLUME 4A

Report #	Author's University	Report Author
13	A Time Slotted Approach to Real-Time Message Scheduling on SCI University of Nebraska-Lincoln, Lincoln, NE	Dr. Sarit Mukherjee Dept. of Comp Engineering WL/AA
14	Dielectric Resonator Measurements on High Temperature Superconductor (HTS) Wright State University, Dayton, OH	Dr. Krishna Naishadham Dept. Elec Engineering WL/ML
15	Modeling of Initiation & Propagation of Detonation Energetic Solids University of Notre Dame, Notre Dame, IN	Dr. Joseph M. Powers Dept. of Aerospace WL/MN
16	Robust control Design for Nonlinear Uncertain Systems by Merging University of Central Florida, Orlando, FL	Dr. Zhihua Qu Dept. of Elec Engineering WL/MN

1996 SREP FINAL REPORTS

Wright Laboratory

VOLUME 4B

Report #	Author's University	Report Author
29	Eigenstructure Assignment in Missile Autopilot Design Using a Unified Spectral Louisiana State University, Baton Rouge, LA	Dr. Jianchao Zhu Dept. of Elec Engineering WL/FI
30	Design & Implementation of a GNSS Software Radio Receiver Ohio University, Athens, OH	Dr. Dennis M. Akos Dept. of Elec Engineering
31	Experimental & Numerical Study of Localized Shear as an Initiation Mechanism University of Notre Dame, Notre Dame, IN	Mr. Richard J. Caspar Dept. of Aero Engineering WL/MN
32	A Molecular-Level view of Solvation in Supercritical Fluid Systems State University of New York – Buffalo, Buffalo, NY	Ms. Emily D. Niemeyer Dept. of Chemistry WL/PO
33	Initiation of Explosives by High Shear Strain Rate Impact University of Notre Dame, Notre Dame, IN	Mr. Keith M. Roessig Dept. of Aero Engineering WL/MN

1996 SREP FINAL REPORTS

VOLUME 5

Ronald Barrett
Report not available at time of publication.

Modeling and Design of New Cold Cathode Emitters Using Wide Bandgap Semiconductors

M.Cahay

Associate Professor

Department of Electrical Engineering

University of Cincinnati, 832 Rhodes Hall

Cincinnati, Ohio 45221

email: mcahay@planck.ececs.uc.edu

Tel: (513) 556-4754, Fax: (513) 556-7326

Final Report for:

Summer Research Extension Program

Modeling and Design of New Cold Cathode Emitters
Using Wide Bandgap Semiconductors

M.Cahay

Associate Professor

Department of Electrical Engineeering

University of Cincinnati

ABSTRACT

We analyze the importance of current crowding in a new cold cathode emitter which consists of a thin wide bandgap semiconductor material sandwiched between a metallic or heavily doped semiconductor and a low work function semimetallic thin film. Potential material candidates are suggested to achieve low-voltage (< 10 V), room-temperature cold cathode operation with emission currents of several tens of A/ cm^2. We calculate the lateral potential drop which occurs across the emission window of cold cathodes with circular geometry and describe its effects on the emitted current density profile. The power dissipation in the cold cathode is calculated as a function of a dimensionless parameter characterizing the importance of current crowding. We determine the range of dc bias over which cold cathodes of different radii must be operated to minimize current crowding and self-heating effects.

I. INTRODUCTION

Recently, there has been renewed interest into cold cathode emitters for applications to a variety of electronic devices, including microwave vacuum transistors and tubes, pressure sensors, thin panel displays, high temperature and radiation tolerant sensors, among others [1, 2]. Introduction of such emitters would permit an unprecedented compactness and weight reduction in device and equipment design. Low temperature operation in nonthermionic electron emitters is very desirable for keeping the statistical energy distribution of emitted electrons as narrow as possible, to minimize thermal drift of solid state device characteristics, and to avoid accelerated thermal aging or destruction by internal mechanical stress and fatigue. To keep the emitter temperature rise small appears easy if the emitters are built as thin epitaxial films using vertical layering technology due to the extremely short heatpaths and excellent heatsinking possibilities offered with this architecture. For an electron emitter to be useful in microwave tube applications it should be capable of delivering current densities in excess of 10 A/ cm^2 and to sustain emission during operational lifetimes over periods of 10^5 hrs. To satisfy this requirement, the structural and chemical composition must be stable. This rules out the historically practiced use of alkali metal films on emitter surfaces for the lowering of electronic work functions. These films sublimate, evaporate or surface migrate over time and end up on various surfaces inside the vacuum envelop.

Several cold cathode emitters have been proposed since their first successful demonstration by Williams and Simon [3] using a cesiated p-type GaP structure. A review and criticism of the different cold cathode approaches was given recently by Akinwande et al. [4]. In this work, we propose a new cold cathode emitter concept and use a simple model to show that the new emitter is capable of achieving low voltage (< 10 V) room temperature operation with emission current approaching 100 A/cm^2 and large efficiencies. A preliminary report of this work has been published earlier [5]. The architecture of the structure is shown in Fig. 1. The main elements in the design and functioning of such an emitter are : (1) a wide bandgap semiconductor slab equipped on one side with a metallic contact [6] or a heavily doped semiconductor ($n^{++} - InP$) on one side of an undoped CdS region that supplies electrons at a sufficient rate into the conduction band and (2) on the opposite side, a thin semimetallic film that facilitates the coherent transport (tunneling) of electrons from the semiconductor conduction band into vacuum. Of importance is the mutual alignment of the crystalline energy levels at the semiconductor-semimetal film junction. This requires the use of new materials and development of their epitaxial growth technologies. For that

reason, the choice of InP as a substrate is particularly attractive since the lattice constant of InP (5.86 Å) closely matches the lattice constant of the zincblende cubic CdS (5.83 Å). Furthermore, there have been recent reports on the deposition of crystalline layers of CdS on InP by molecular beam epitaxy [7], chemical bath deposition [8], and pulsed laser deposition [9]. The proposed cold cathode should therefore be realizable with present day technology.

As shown in Fig. 1(a), a thick metal grid is defined on the surface of the LaS thin film to bias the structure. There are openings in the grid structure to expose the thin LaS film which forms the active emission area of the cold cathode. Cathodes with rectangular (Fig.1(b)) emission windows were studied previously [5]. Current crowding and self-heating effects in cathodes with circular geometry (Fig.1(c)) emission windows will be considered hereafter. The bias is applied between the back metallic contact and the metal grid with emission occuring from the exposed LaS surface. If the applied voltage is equal or larger than the semiconductor bandgap energy and the quotient of the applied voltage divided by the semiconductor thickness approaches $0.1 eV/Å$, then electrons are tunnel injected into the conduction band and ascend during their travel across the semiconductor film to levels of increasing energy. Referring to Fig. 2, the conduction band of the wide bandgap semiconductor provides the launching site for electrons where they are - through a thin film - injected into vacuum. This injection of electrons into vacuum becomes possible and is effective as long as the semimetallic film is very thin and has a work function small enough so that its vacuum edge is located energetically below the conduction band edge of the semiconductor. This situation is referred to as negative electron affinity (NEA) for the semiconductor material [10]. Depending on the particular materials choices, this implies that the semimetal work function ϕ_M in relation to the semiconductor energy bandgap E_G must obey one of the inequalities $\phi_M < 0.5E_G$ or $\phi_M < E_G$ if an intrinsic or p-type doped wide bandgap semiconductor is used, respectively. A negative ϕ_M implies according to Fig.2 that the vacuum level would be located below the lower conduction band edge. In that case, electrons in the conduction band with momenta pointing toward the surface have a good chance to get emitted unless deflected by collision or trapped by impurities or defects.

This paper is organized as follows. In section II, we derive the basic equations describing the forward bias operation of the cold cathode emitter described above. We then calculate the current density-voltage characteristics of the newly proposed cold cathode for specific sets of materials and device parameters. In section III, we investigate the importance of current crowding effects in various cold cathodes with circular geometry. Our analysis includes a

self-consistent modeling of current crowding effects and an analysis of power dissipation in the cold cathode active area. The influence of power dissipation on self-heating effects in the active area of the cathode is also described. Finally, Sec. IV contains our conclusions.

II. THE MODEL

Hereafter, we analyze the cold cathode whose energy band diagram is shown in **Fig. 2** [5]. Under the influence of a large electric field in the wide bandgap semiconductor, electrons will eventually tunnel from the left contact through the barrier at the metal-semiconductor interface. A portion of the current emitted at the metal or heavily doped semiconductor -CdS contact (which we model assuming Fowler-Nordheim injection) is transmitted at the boundary of the LaS as well as the vacuum boundary. However, a fraction of the current is lost in the thin LaS quantum well gives rise to the dynamic shift of the effective material work function (Fig. 2). For a cathode operated at room temperature, we model this internal field emission at the injection junction using a Fowler-Nordheim (FN) type expression for the injected current (in A/cm^2) [11]

$$J_{FN} = C_1(E^2/\Delta)e^{C_2\Delta^{3/2}/E},\tag{1}$$

where C_1 and C_2 are constants which depend on the wide bandgap semiconductor. In our numerical simulations, we chose $C_1 = 1.5X10^6$ A/V and $C_2 = 6.9X10^7(V^{1/2}cm)^{-1}$ which are of the same order of magnitude as the constants appearing in the FN expression [11]. In Eq.(1), Δ is the barrier height (in eV) at the metal-semiconductor junction and E is the electric field (in V/cm) in the wide bandgap semiconductor [12]. We assume that the semiconductor layer thickness is such that the transport of injected electrons is close to being ballistic up to the interface between the semiconductor and the thin semimetallic film. In so doing, we also neglect carrier ionization processes in the semiconductor slab which could be the main antagonist to ballistic transport in that region.

Because of the finite probabilities for the injected current to be transmitted at the semiconductor-semimetal (probability T_1) and semimetal-vacuum interfaces (probability T_2), the contributions to the total emitted current can be calculated as the sum of the contributions resulting from the mutiple reflections of electrons in the semimetallic layer (See Fig. 2). The magnitudes of the emitted current components decreases with the number of multiple reflections in the semimetallic layer. Rather than trying to calculate these contributions exactly, we assume that the current amplitude is decreased by a factor $\epsilon = exp(-L_2/\lambda_{LaS})$

for each traversal of the semimetallic layer, where λ_{LaS} is the collisional mean free path in the semimetallic layer and L_2 is the length of the semimetallic layer. Adding the contributions resulting from multiple crossings of the semimetallic layers, the total emitted current is found to be

$$J_{em} = \epsilon T_1 T_2 J_0 (1 + x + x^2 + ...),\tag{2}$$

where $x = \epsilon^2 (1 - T_1)(1 - T_2)$. In calculating J_{em} we limited the number of traversals of the semimetallic slab to five to include the fact that electrons loose energy in each crossing and eventually do not have enough energy to surmount the barrier at the semimetal-vacuum interface. According to Eq.(2), the contributions from the multiple reflections decrease rapidly since, in general, the quantity x will be much smaller than unity [13]. Once the emitted current is found, the total current contributing to the increase in the sheet carrier concentration in the thin semimetallic film can easily be written as $J_{capt} = J_{FN} - J_{em}$. The total trapped current is then given by

$$i_T = A J_{capt} = A R J_{FN} \tag{3}$$

where A is the area of each LaS emission window which in practice can be either rectangular or circular (See Fig. 1b and 1c). In Eq.(3), R is the trapping coefficient of the well

$$R = 1 - \epsilon T_1 T_2 \left(1 + x + x^2\right).\tag{4}$$

The semimetallic thin film can be modeled as a quantum well (Q.W) which will loose the trapped electrons essentially at its lateral boundaries. In reality, Fig. 1(a) indicates that not all electrons will move to the three-dimensional contact regions surrounding the thin semimetallic layer but many of them will get reflected at the lateral thin film layer with an average probability r (calculated for electrons with the Fermi velocity in the thin film). The exiting number of electrons will depend on the thickness of the semimetallic layer and could be adjusted by intentional passivation so that reflection at the boundaries of the thin semimetallic film could be tuned from almost zero to nearly unity. Taking into account the finite reflection amplitude at the thin film boundaries, the leakage current of the Q.W can be rewritten

$$\frac{dQ_T}{dt} = 2eL N_{2D} v_F (1 - r),\tag{5}$$

for the case of a rectangular emission window and

$$\frac{dQ_T}{dt} = 2\pi e a N_{2D} v_F (1 - r),\tag{6}$$

for the case of a circular emission window.

In Eqns.(5) and (6), Q_T is the total charge captured by the well, e is the magnitude of the electronic charge, N_{2D} is the excess sheet carrier concentration in the thin film due to the captured electrons, and v_F is the Fermi electron velocity in the semimetallic thin film. Under steady state operation of the cold cathode, the excess charge in the two-dimensional semimetallic film is found using Eq.(3) and imposing the current balance requirement $\frac{dQ_T}{dt} = i_T = AJ_{capt}$. This leads to

$$N_{2D} = WJ_{capt}/2e(1-r)v_F, \tag{7}$$

for the case of a rectangular geometry and

$$N_{2D} = aJ_{capt}/2e(1-r)v_F, \tag{8}$$

for the case of a circular geometry.

Simultaneously, the change N_{2D} in the excess sheet carrier concentration in the Q.W due to trapped electrons leads to the occupation of the boundstate energy levels according to the energy density of states up to an energy level which will establish the dynamic Fermi level $E_F{}^1$. The Fermi velocity v_F entering Eqns.(5) and (6) must be calculated self-consistently because of the dynamic work function shift $|\Delta\chi|$ illustrated in Fig. 2. This dynamical shift $|\Delta\chi|$ is equal to $|E_F{}^1 - E_F{}^0|$, where $E_F{}^0$ is the Fermi level in the thin semimetallic layer under zero bias. For simplicity, we assume that the electrons in the conduction band of the semimetallic films can be described using the Sommerfeld theory of metals while assuming s-band conduction in the semimetallic thin film and while modeling the thin film using the particle in a box model for the quantum well [14]. The set of equations (1-8) is then solved self-consistently to calculate the work function shift $|\Delta\chi|$ as a junction of the externally applied bias. Once the dynamic shift has been determined self-consistently, Eq.(2) can then be used to determine the emitted current.

RESULTS

We consider a specific structure with the material and structural parameters listed in Table I and II, respectively. Both Au and Ag are known to form contacts to thin films of semiconducting (n-type) CdS. In that case, the barrier height Δ shown in Fig. 2 is quite small and is equal to 0.78 eV and 0.56 eV for the case of Au and Ag contacts, respectively [11]. The lattice constant of CdS (5.83Å) is very close to the lattice constant of the thin semimetallic surface layer LaS (5.85 Å) which in its cubic crystalline structure will therefore

be lattice matched to the semiconducting material. Additionally, LaS is expected to have quite a low room temperature work function (1.14 eV) [15], a feature when combined with the large energy gap (2.5 eV) of CdS leads to NEA of the semiconductor material. In the following numerical simulations. the thicknesses of the CdS (L_1) and LaS (L_2) layers are set equal to 500 $\mathring{A}$ and 24.6 $\mathring{A}$ (4 monolayers), respectively. We model a cathode with a square (W = L) emission window with a 1 cm^2 area.

Figure 3 is a plot of the dynamic work function shift as a function of applied bias for the cold cathode emitter with both Au and Ag injecting contacts. The following parameters were used: $\lambda_{LaS} = 300\mathring{A}$, $T_1 = T_2 = 0.5$, and $v_F = 1.36 X 10^8 cm/s$. Figure 3 indicates that the dynamic shift of the LaS work function is sensitive to the quality of the interface between the two-dimensional semimetallic layer and the three-dimensional contacts which we model by varying the reflection coefficient r between the two-dimensional semimetallic thin film and the three-dimensional contact regions (See Fig. 1(a)). It should be noticed that the LaS work function shift can approach the LaS workfunction even for the case of a *leaky* interface between the thin semimetallic layer and the 3D contact regions. The dynamic shift $|\Delta\chi|$ is comparable to the work function of LaS for a smaller value of the applied bias in the case of Ag contact because of the lower barrier at the Ag/CdS interface.

Figure 4 compares the emitted current densities J_{em} for the structure with Au and Ag contacts calculated while including or neglecting the effects of the dynamic shift of the LaS work function. The current density versus bias plots are stopped at the values of V_{bias} at which $|\Delta\chi| = \phi_M(LaS) = 1.14eV$. Beyond that point, the theory exposed here is no longer valid since we would need to include the spill over of the excess trapped carriers into vacuum. As can be seen in Fig. 4, the emitted current densities can be more than a factor two larger when the effects of the dynamic shift of the work function of the semimetal are included. The effects could be made more drastic if a set of materials and device parameters could be found for which the dynamic shift of the work function could be made comparable to the work function itself at fairly low value of the applied bias ($< 5V$).

Sensitivity of Dynamic Work Function Shift on Design Parameters

The previous numerical examples have shown that, under forward bias operation, the electrons captured in the low work function material are responsible for an effective reduction of the semimetallic film work function together with a substantial increase of the cathode emitted current. This dynamic work function shift was shown to increase with the amount of

injected current. Hereafter, we perform a more extensive study of the dynamic work function shift which includes variations of the length of the CdS region (L_1), the electron mean free path in the LaS region (λ_{LaS}), the emission window size (W), the transmission coefficients at the CdS/LaS (T_1) and LaS/Vacuum interfaces (T_2), and the reflection at the 2D/3D interface region in the LaS quantum well (r).

Figure 3 indicates that the dynamic work function shift $|\Delta\chi|$ rises exponentially above a threshold voltage of several volts and reaches rapidly (within a few volts range) a value comparable to the LaS work function. For a structure with the parameters listed in Table I and with the structural and physical parameters ($L_1 = 500$ Å, $L_2 = 24.6$Å, W = 1cm, $\lambda_{LaS} = 300$Å, $T_1 = T_2 = 0.5$, $\Delta(A_g) = 0.56 eV$), Fig. 5(a) shows that the dynamic work function shift rises exponentially at a lower bias as the reflection coefficient at the 2D/3D interface in the LaS region approaches unity. Figure 5(b) also shows that the difference between the current densities calculated with and without including the dynamic work function shift are more pronounced for smaller values of the applied bias when the reflection coefficient between the 2D and 3D LaS regions is approaching unity. This results from the fact that any mechanism (like r being closer to unity) which increases the amount of charge being trapped in the LaS quantum well leads to an enhancement of the dynamic work function shift at a given bias. For instance, all other cathode parameters being equal, the dynamic work function rises much faster as a function of applied bias in structures with thinner CdS regions (Fig. 6), with smaller values of the transmission coefficients T_1 and T_2 (Fig. 7), or with smaller mean free path (λ_{LaS}) in the semimetallic thin film (Fig. 8). As shown in Fig. 8(a), the dynamic work function shift occurs at a lower bias as λ_{LaS} is decreased. On the other hand, the emitted current density is lesser at a given bias in a cathode whose LaS thin film has a lower electron mean free path (Fig. 8(b)). We have found this trend to be valid for all values of the reflection coefficient at the LaS 2D/3D interface. However, there is a larger spread in the family of curves representing the bias dependence of the dynamic work function and emitted current densities as a function of the mean free path in the LaS thin film for smaller values of the reflection coefficient r. Finally, even though not shown here, the exponential rise of the dynamic work function shift and emitted current density has been shown to occur at lower value of the bias by either reducing the thickness of the CdS layer or by lowering the barrier height Δ at the metal/CdS interface.

Before leaving this section, we make two additional remarks on the bias dependence of the emitted current density and the dynamic work function shift which we have checked

numerically on all the cold cathodes modelled in this work. First, since the emission of electrons at the metal(or heavily semiconductor)/CdS interface is assumed to be of the Fowler-Nordheim type, the emission current is expected to have a bias dependence of the form

$$J_{FN} = AV_{bias}^2 exp(-B/V_{bias}). \tag{9}$$

This was checked numerically for all the cold cathodes modelled here. A typical example is given in Fig.9(a), with the values of the parameters A and B listed in the inset. Most of the quantities of interest to be determined hereafter (power dissipation, lateral variation of emitted current and lateral potential drop,...) can be calculated exactly analytically if the following approximation is used

$$J_{FN} = J_0 e^{\alpha V_{bias}}. \tag{10}$$

For all the cold cathodes simulated here, we have shown that Eq.(10) gives a fairly accurate fit to the plot of the emitted current density versus applied bias if the range of the fit is restricted to current densities between 1 and 1000 A/cm^2 . A typical fit for the one of the cold cathode studied here is shown in Fig.9(b) with the values of the parameters J_0 and α in Eq.(8) shown in the inset. Table III gives a summary of the parameters J_0 and α for cold cathodes of different width and with the physical parameters listed in the caption of Fig.5. We have found that the bias dependence of the dynamic work function shift is also of the Fowler-Nordheim type, i.e,

$$\Delta\chi = \Delta_0 V_{bias}^2 exp(-V_0/V_{bias}). \tag{11}$$

This is illustrated in Fig.10 for the cold cathode with the same parameters as in Fig.9. The values of Δ_0 and V_0 are indicated in the inset of Fig.10. We point out that the values of the parameters B and V_0 in Eqns.(9) and (10) are nearly identical.

Temperature Rise in the Cold Cathode

Hereafter, we derive an upper estimate of the temperature rise in the LaS thin film as a result of the power dissipation mechanisms discussed above. We focuss on a cold cathode where the CdS thin film is deposited on a InP substrate as shown in Fig.1(a). The successful growth of cubic CdS thin films with good crystalline quality on InP substrates has been reported recently by Shen and Kwok [9]. For the case of a InP/CdS interface, there has not been any report of the conduction band discontinuity ΔE_c at the interface between the two

materials, to the best of our knowledge. For that reason, ΔE_c was assumed to be given by Anderson's rule, i.e, Δ in Fig. 2 is assumed to be given by $|\chi(InP) - \chi(CdS)| = 0.2$ eV [16]. This estimate was based on the measured electron affinities of InP (4.4 eV) and CdS (4.2 eV) reported in refs. [17] and [18], respectively. The back contact to the substrate is assumed to be perfectly ohmic and to act as a perfect heat sink (300K). Since the device area (heat source formed of the LaS thin fim) is much thinner than the substrate, it is necessary to consider the effect of heat spreading laterally in the substrate. Furthermore, we assume that the temperature of the CdS layer will be the same as the LaS top layer. The active area of the cathode (CdS and LaS layers) is therefore assumed to be acting as a heat source with the power density calculated in the previous section. Because of the finite thermal conductivity of the substrate, we expect self-heating effects to affect the operation of the cold cathode if the power level dissipated in the active area of the cathode becomes too important. Hereafter, we model the thermal conductivity of the InP substrate as follows

$$\kappa(T) = \kappa_0(T/T_0)^{-b}, \tag{12}$$

where κ_0 is the thermal conductivity at T_0 (300K), $\kappa_0 = 0.74$ W/Kcm is the room temperature thermal conductivity of InP and b=1.45. Starting with Fick's law and making use of a Kirchoff transformation to take into account the temperature dependence of the thermal conductivity of the InP substrate given by Eq.(12), it can be shown that the active area of the cold cathode will be operated at a temperature given by

$$T = \left[\frac{1}{T_0^{b-1}} - (b-1)\frac{R_{th,0}P_{diss}}{T_0^b} \right]^{\frac{-1}{(b-1)}}, \tag{13}$$

where T_0 is the ambient room temperature (assumed to be 300 K hereafter), P_{diss} is the total power dissipated per finger as calculated in the previous section, and

$$R_{th,0} = \frac{1}{\kappa_0} \int_0^{z_S} \frac{dz}{A(z)}, \tag{14}$$

where Z_S is the thickness of the InP substrate. Our estimate of the temperature rise in the active cold cathode area will give an upper estimate of the temperature of operation since we neglected heat conduction to the top Au contacts in the thick portion of the LaS thin film.

III. Current Crowding Effects in Proposed Cold Cathode with a Circular Geometry

In this section, we study the effects of current crowding in the case of an emission window with circular geometry (see Fig.1(c)). The lateral potential drop in the circular LaS window satisfies the following differential equation [19]

$$\frac{dV}{dr} = \frac{\rho_s}{t} i(r), \tag{15}$$

where i(r) is the total lateral current per unit length flowing outward across a circle of radius r, whose center coincide with the center of the emission window. The lateral current satisfies the following equation

$$2\pi r i(r) = 2\pi R \int_0^r dr' r' j(r'). \tag{16}$$

If we further assume that the Fowler-Nordheim emitted current j(r) can be approximated by Eq.(10) over the range of dc bias considered here, the following second-order differential equation must be satisfied by the lateral potential drop:

$$\frac{d^2V}{dr^2} + \frac{1}{r}\frac{dV}{dr} = \frac{\rho_S R J_0}{t} e^{V(r)/V_T}. \tag{17}$$

This differential equation must be solved subject to the following boundary conditions valid for the circular geometry

$$\frac{dV}{dr} = 0, \tag{18}$$

at r = 0, and

$$V(r = a) = V_{bias}, \tag{19}$$

at the edge of the circular window. Introducing the reduced variable $r' = r/a$ and the quantity

$$Y = \frac{V - V_{bias}}{V_T}, \tag{20}$$

Eq.(17) can be recast as follows

$$\frac{d^2Y}{dr'^2} + \frac{1}{r'}\frac{dY}{dr'} = 2\gamma^2 e^Y, \tag{21}$$

where $\gamma^2 = \frac{\beta^2 a^2}{2}$ and the parameter β is identical to the one defined for the planar problem [20].

The general solution of Eq.(21) can be found analytically and is given by

$$e^Y = (c\delta^2/\gamma^2)[r'^{\delta-2}/(1 - cr'^{\delta})^2], \tag{22}$$

where δ and c are constants to be determined so the boundary conditions (18) and (19) are satisfied. Using the new system of variables, Eq.(18) becomes

$$\frac{dY}{dr'}|_0 = 0, \tag{23}$$

while Eq.(19) now reads

$$Y(1) = 0. \tag{24}$$

Equation (23) leads to

$$\delta = 2. \tag{25}$$

and Equation (24) becomes

$$\delta^2 = (1 - c)^2\gamma^2/c. \tag{26}$$

Combining these last two equations, we obtain the following result

$$\gamma^2 = \frac{4c}{[1 - c]^2}, \tag{27}$$

Equation (27) can be solved exactly for the parameter c

$$c = [\gamma^2 + 2 - 2\sqrt{\gamma^2 + 1}]/\gamma^2 \tag{28}$$

in terms of which we can write various quantities of interest, including the ratio

$$J(0)/J(a) = [1 - c]^2, \tag{29}$$

characterizing the importance of current crowding in the circular geometry. Using Eqn.(22), the radial dependence of the lateral potential drop if found to be

$$V(r) = V_{bias} - 2V_T ln[\frac{a^2 - cr^2}{a^2(1 - c)}], \tag{30}$$

from which the maximum value of the in plane electric field is found to be

$$E_r(r = a) = \frac{4c}{c - 1}\frac{V_T}{a}. \tag{31}$$

As in the case of the rectangular geometry, the total power dissipated in the *LaS* thin film is given by the sum of the following four contributions [20]. The power dissipated by the electrons being trapped in the *LaS* circular thin film is given by

$$P_1 = 2\pi R \int_0^a dr j(r)V(r). \tag{32}$$

The power dissipated by Joule heating as trapped electrons move to the edge of the *LaS* window is given by

$$P_2 = \frac{2\pi\rho_s R^2}{t}\int_0^a \frac{dr}{r}[\int_0^r r'j(r')dr']^2. \tag{33}$$

The third contribution to power dissipation comes from from Joule heating linked to the current making it from the *LaS* thin film to the *Au* contacts on top of the thick *LaS* regions.

$$P_3 = R_c(2\pi ai(a))^2. \tag{34}$$

where R_c is the resistance of the *LaS* region between the edge of the *LaS* thin film and the top *Au* layer. This resistance can be estimated as follows [21]

$$R_c = \frac{\rho_S H}{t2\pi a}\frac{lnk}{k-1}, \tag{35}$$

where $k = b/t$, a is the radius of the circular window, and H is the height of the thick *LaS* region.

Finally, there is also a contribution to power dissipation due to the blocking effect on the Folwer-Nordheim emission current emitted under the wide *LaS* contacts:

$$P_4 = \pi b(b + 2a)J_0 e^{aV_{bias}}. \tag{36}$$

Starting with Eqns.(10) and (30), the different contributions to the power dissipation can be calculated exactly and are found to be

$$P_1 = \pi a^2 J_0 Re^{aV_{bias}}V_{bias}(1-c) - \pi a^2 J_0 Re^{aV_{bias}}V_T[2(1-c) + \frac{(1-c)^2}{c}ln(1-c)^2], \tag{37}$$

$$P_2 = R(\pi a^2 J_0 e^{aV_{bias}})V_T[2(1-c) + \frac{(1-c)^2}{c}ln(1-c)^2], \tag{38}$$

P_3 is given by Eq.(34) and P_4 is found to be

$$P_4 = \frac{R_c R^2}{2(1-R)^2}I_{em}^2, \tag{39}$$

where I_{em} is the total emitted current through the circular window

$$I_{em} = 2\pi(1-R)\int_0^a rj(r)dr. \tag{40}$$

The latter can be calculated explicitely and is found to be

$$I_{em} = (1-R)[\pi a^2 J_0 e^{aV_{bias}}](1-c). \tag{41}$$

2-14

The input power (per emission window) delivered by the power supply biasing the cold cathode is given by

$$P_{input} = \int_0^{a+b} 2\pi r j(r) V(r) dr, \tag{42}$$

which can readily be shown to be given by

$$P_{input} = P_1/R + P_4. \tag{43}$$

The power efficiency of the cold cathode can be calcualted as follows

$$\eta_P = \frac{P_{input} - P_{diss}}{P_{input}}. \tag{44}$$

and the temperature rise in the cathode is given by Eq.(13). where the thermal resistance $R_{th,0}$ must be calculated for the case of power dissipation through the substrate from a heat source with circular geometry. In this case, we find

$$R_{th,0} = \frac{1}{\kappa_0} \frac{z_s}{a} \frac{1}{[a + z_s tan\theta]}, \tag{45}$$

in which the heat spreading angle θ is set equal to 45° in the numerical examples below, for simplicity.

Numerical Examples

Figure 11 shows the variation of the parameter c in Eq.(28) as a function of applied bias for cold cathodes with circular emission window of different radii. For all cathodes, the physical parameters are the same as listed in the caption of Fig.5. As in the case of a rectangular window, we use the criterion that current crowding is negligible if the lateral potential drop between the center and the edge of the LaS circular window, $V(r = 0) - V_{bias}$, is kept less than $0.1V_T$. Using Eqns.(28) and (30), we find that this criterion requires the parameter c to be less than 0.05. This limit is indicated as a vertical line in Fig. 11. The family of curves in Fig.11 is parametrized with the radius of the emission window. Figure 11 shows that the range of dc bias over which current crowding can be neglected in a circular window is comparable to the range of dc bias over which current crowding is negligible in a rectangular window whose width is equal to the radius of the circular emission window [20].

Figure 12 illustrates the importance of current crowding on the lateral potential drop in emitter windows of different radii. The left frames show the radial dependence of the electrostatic potential for four different values (1,10,100,1000 A/cm^2) of the current density at

the rim of the circular *LaS* window. The right frames in Fig.12 show the corresponding radial dependence of the emitted current density. From Fig.12, it can be seen that current crowding is negligible in emitter windows with radius less than 50 μm if the emitted current density is kept under 10 A/cm^2. As in the case of *LaS* windows with rectangular geometry, Figure 12 shows that the current density profiles are much more sensitive to the finite resistivity of the *LaS* thin film than the lateral potential drop.

Figure 13 is a plot of the four contributions to the total power dissipated in cold cathodes with different radii plotted as a function of the parameter c. For all cathodes, the power dissipation due to Joule heating in the LaS thin film and the thick *LaS* regions is negligible compare to the power released by electrons being trapped in the *LaS* thin film and by electrons blocked in the thick *LaS* regions. The latter is always about one of magnitude higher than the former. Figure 13 shows that substantial power dissipation occurs in the cathode with radius under $50\mu m$ while the cathode is still operating without any substantial current crowding effects (i.e, c < 0.05). The power efficiency η_P of cathodes of different width is plotted as a function of V_{bias} and the emitted current density J_{em} in Figs. 14(a) and 14(b), respectively. For all window size, the efficiency decreases with V_{bias} and J_{em} as a result of current crowding. The efficiency is more or less constant over a wider range of V_{bias} for window with smaller radius because current crowding is less important in that case, as illustrated in Fig. 12. The overall lower efficiency for window with smaller radius illustrated in Fig. 14 comes from the fact that the width of the thick *LaS* regions was set equal to $100\mu m$ for all cathodes. The efficiency of cathodes could be increased by making the ratio b/a in Fig.1(b) closer to unity.

Figure 15 shows the temperature of the active area of a cold cathode with the parameters listed in Table I as a function of V_{bias} for emitter window with different radii. The thickness of the *LaS* contacts and *InP* substrate was set equal to $100Å$ and $100\mu m$, respectively. As in case of cold cathodes whose emission window as a rectangular geometry [20], Fig. 15 indicates that to limit the temperature rise in any cathode to less than 200 K, the dc bias must be limited to a smaller range for emitters with smaller window radius. For instance, according to Figures 11 and 15, a cathode with a $20\mu m$ diameter can be operated up to 8.3 V with negligible self-heating effects (ΔT around 100 K). For that bias, Figure 12 indicates that current crowding would be negligible in the cathode and the emitted current density would be around 100 A/cm^2 (See Fig. 16). On the other hand, Figure 11 indicates that a $100\mu m$ diameter window can be operated up to 6.8 V before current crowding becomes

non negligible. At this bias, the emitted current density would be around 15 A/cm^2 (Fig. 16) while the temperature rise in the device would be only about 15 K as shown in Fig. 15.

IV. CONCLUSIONS

We have proposed a new cold cathode emitter which consists of a thin wide bandgap semiconductor material sandwiched between a metallic material or heavily doped semiconductor, and a low work function semimetallic thin film. We have shown that the capture of electrons by thin semimetallic layers grown on the escape surface of wide bandgap semiconductors can lead to a dynamical shift of the work function of the semimetallic layers together with an increase of the cathode emission current. While varying the device and physical parameters of the structure, our studies suggest that any mechanism which promotes additional charge deposit in the well enhances the dynamic work function shift phenomenon thereby increasing the emitted current. Potential material candidates were proposed for cold cathode operation with applied bias under 10 V, with current densities approaching several tens of A/cm^2, and with large power efficiencies (η_P approaching 15 %).

The results of our analysis show that a cold cathode with either a rectangular or circular emission window and with the parameters listed in Tables I and II would emit a uniform current density of about 15A/cm^2 at a dc biasing voltage of about 8V. For that bias, the effects of current crowding would be negligible and the temperature rise in the active area of the cathode (CdS/LaS layers) as a result of self-heating effects would be negligible.

Further improvements to the theory should include a more realistic model for the emission current and transport through the wide bandgap material. Also, the semimetallic film energy density of states (to account for the d-band character of the conduction band in the chosen rare-earth semimetallic samples [14]), the finite probability for electron wavefunctions in the thin semimetallic films to extend in the semiconductor material [22], a more accurate description of the energy loss mechanisms [23] and screening effects (including the lateral ohmic voltage drop) in thin semimetallic layers [24]. Finally, our study of self-heating effects should include partial cooling of the cathode due to heat conduction through the thick LaS layers which was neglected in this study. The latter would allow to extend slightly the dc biasing operating range of the cathode beyond the estimate reported here. Furthermore, the thermal and electrical models of the cathode described here should be solved self-consistently. Once all these effects are taken into account, we believe the quantitative operation of the cold cathode exposed here will stay essentially correct predicting a dynamical shift of the

2-17

work function of the thin semimetallic film of the same order of magnitude than the one reported here.

Our analysis provides the basic design rules to fabricate a new cold cathode with emission windows with a rectanguler or circular geometry. The growth of the structure would require the epitaxial growth of the structure shown in Fig.1. As discussed above, the epitaxial growth of InP/CdS heterostructures has been reported in the literature in the past [9]. The deposition of epitaxial LaS thin films has not been reported, to the best of our knowledge. We believe, however, that the figures of merits of the various cold cathodes analyzed in this work are a strong incentive towards the experimental investigation of these devices. If successful, such an experimental effort would lead to big pay-offs with the design of highly efficient cold cathodes for large panel displays, IR image convertors and sensors, and active power devices in mobile and airborne electronic equipment for military, commercial, and private use.

ACKNOWLEDGMENT

References

[1] S. Iannazzo, Solid State Electronics, Vol. 36(3), 301 (1993).

[2] I. Brodie and C. A. Spindt, Advances in Electronics and Electron Physics, Vol. 83, p.2 (1992).

[3] B. K. Williams and R. E. Simon, Physical Review Letters, Vol. 18(13), 485 (1967).

[4] A. I. Akinwande, P. P. Ruden, B. L. Goldenberg, D. K. Arch, and John King, Proceedings of 1994 Tri-Service (NASA) Cathode Workshop, Cleveland, Ohio, March 1994, p. 105.

[5] A preliminary account of this work has been published in: P. D. Mumford and M. Cahay, Journal of Applied Physics, Vol. 79(5), 2176 (1996). This work follows suggestions which are documented in two in-house reports by W. Friz, Final Technical Report, Task ELM-

9, June 1992, and Technical Note, Task ELM-6, January 1995 (Wright-Patterson Air Force Base).

[6] The most desirable form of electron injection is accomplished by an ohmic contact because it puts minimal electrical stress on the material and, at the same time, provides the highest current densities.

[7] Deposition of crystalline layers of CdS on InP by MBE are presented by W. G. Wilke, R. Seedorf, and K. Horn, J. Vac. Sci. Technology. B, Vol.7, p.807 (1989).

[8] Chemical bath deposition (CBD) of crystalline layers of CdS on InP are discussed by D. Lincot, R. Ortega-Borges, and M. Froment, Appl. Phys. Letters, Vol. 64, p.569 (1994).

[9] W. P. Shen and H. S. Kwok, Appl. Phys. Letters, Vol. 65(17), p.2162 (1994). In this article, the authors report the epitaxial growth of various II-VI compound semiconductors ($ZnS, ZnSe, CdS, CdSe$, and $CdTe$) on (111) and (1000) InP and $GaAs$ substrates by excimer laser ablation. All the films have good crystalline quality (fully in-plane) and mirror-like surface morphology. They found that, on (111)-oriented substrates, CdS and $CdSe$ films were in the hexagonal phase with the c axis perpendicular to the surface, while ZnS and $ZnSe$ flms were in the cubic phase. The films grwon on (100)-oriented substrates were all cubic. See also W. P. Shen and H. S. Kwok in *Compound Semiconductor Epitaxy*, edited by C. W. Tu, L. A. Kolodziejski, and V. R. McCrary, [Mater. Res. Soc. Symp. Proc. **340**, 1994].

[10] P. R. Bell, Negative Electron Affinity Devices, Oxford: Claredon Press, 1973

[11] Sze, Physics of Semiconductor Devices, 2nd Edition, Wiley, p. 291 (1981).

[12] Assuming that the most part of the wide bandgap semiconductor is an intrinsic material (See Fig. 1), accumulation and depletion effects can be ignored. Referring to Fig. 1, the resulting uniform electric field across the wide bandgap semiconductor is then given by

$$E = \frac{1}{L_1}[V_{bias} + \Delta - (\frac{E_G}{2} - |\Delta\chi|)]. \tag{46}$$

[13] Both T_1 and T_2 should actually be function of the number of reflections in the semimetallic slab since the electrons loose energy during each traversal. This is however just a refinement to the general theory exposed in this paper.

[14] N. W. Aschcroft and N. D. Mermin, Solid State Physics, Saunders College, Philadelphia, 1976.

[15] The room temperature work function for LaS was calculated by extrapolating measured work function values at high temperature as reported by S. Fomenko in *Handbook of Thermionic properties* (Plenum, New York, 1966). Within the range of temperature investigated by Fomenko, the LaS work function increases with temperature at a rate of $2meV/K$.

[16] There are other reports for the electron affinity of CdS, including $\Delta\Xi_{CdS} = 4.5$ eV in [11]. In this case, Anderson's rule would allow electrons to spill over from the InP to the CdS region, an injection mechanism hard to control. The problem of the InP/CdS interface deserves more attention [9].

[17] Shyh Wang, Fundamental of Semiconductor Theory and Device Physics, Prentice Hall Series in Electrical and Computer Engineering, Leon O. Chua, Series Editor (1989).

[18] There are conflicting reports for the measured electron affinity of CdS. The affinity is known to vary with the surface orientation and the phase of the semiconductor material. Here, we use the electron affinity $\chi_{CdS} = 4.2$ eV reported in O. Madelung, "Semiconductors other than Group IV elements and III-V compounds ", Springer (1992).

[19] E. S. Kohn, Journal of Applied Physics, Vol. 42(6), 2493 (1971).

[20] M. Cahay, Final report, Summer Faculty Research Program, AFOSR, September 1996.

[21] J. A. Edminister, Electromagnetics, Schaum's Outline Series, McGraw-Hill Book Company (1979).

[22] M. L. Huberman and J. Maserjian, Physical Review B, Vol. 37(15), 9065 (1988).

[23] R. C. Jaklevic and J. Lambe, Phys. Rev. B, Vol. 12, 4146 (1975).

[24] Y. Silberberg and T. Sands, IEEE Journal of Quantum Electronics, Vol. 28 (7), 1663 (1992).

Table I: Material Parameters of the Cold Cathode

Material	Au (Ag)	n^{++}-InP	i-CdS	LaS
Lattice Thickness (Å)	optional	optional	300.0	24.6
Lattice Constant (Å)	4.04 (4.09)	5.86	5.83	5.85
Workfunction (eV)	4.3 (4.3)	4.4	4.2	1.14
Bandgap (eV)		1.42	2.5	
# of free electrons ($10^{22}cm^{-3}$)	n^{++}	5.9 (5.86)	—	1.99
Electron Mass (m_0)	1.0	0.0765	0.14	1.0
Electron Mobility ($cm^2 V^{-1} s^{-1}$)		5370.	400.0	
Thermal conductivity @ 300K (W/cmK)	3.1 (4.18)	0.74	0.05..1	0.17
Electrical resistivity (273K) ($\mu\Omega cm$)	1.51 (2.04)			92.0
Melting temperature (K)		1335.		2500

Table II: Physical Parameters of the Cold Cathode

Thickness of InP substrate	50 - 200 μm
Thickness of CdS thin film	300 - 500 Å
Emission window length	1 cm
Thickness of LaS thin film	24.6 Å
Thickness of LaS thick regions	100 - 500 Å
Electron mean free path in LaS thin film	50 - 300 Å

Table III: Parameters for numerical fit (Eq.(10)) to the Fowler-Nordheim current expression (Eq.(9)). The fit is made over a current density range from 1 to 1000 A/cm^2.

Width of Rectangular Window (μm)	J_0 (A/cm^2)	α (V^{-1})
10,000	7.2186×10^{-7}	2.3651
1,000	3.6483×10^{-6}	2.1302
500	3.8505×10^{-6}	2.1224
200	4.7337×10^{-6}	2.0933
100	4.7902×10^{-6}	2.0916
50	4.8207×10^{-6}	2.0907
20	4.8424×10^{-6}	2.0901
10	4.8424×10^{-6}	2.0901
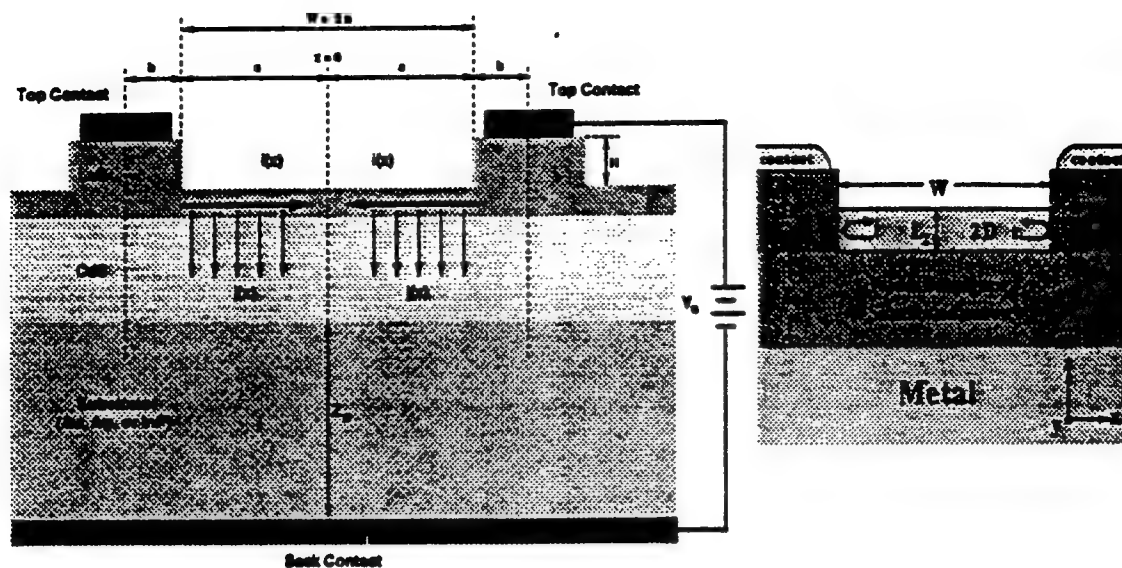
(a)
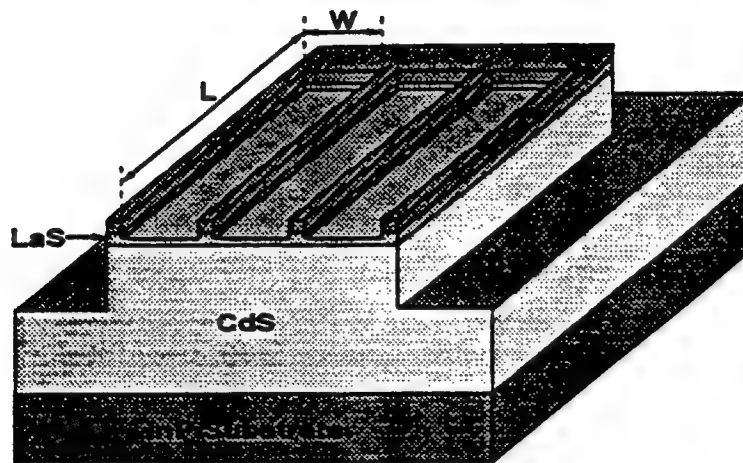
(b)

Figure 1: (a) Left: cross-section of the newly proposed cold cathode between two emitter fingers. Trapping of electrons by the *LaS* semimetallic thin film leads to a lateral current flow and current crowding in the structure. Right: illustration of the partial reflection of the two-dimensional electron gas in the *LaS* thin film upon entering the three-dimensional contact regions where the external bias is applied to *Au* contacts made to the thick *LaS* regions. (b) Illustration of the multiple finger metallic structure used to bias appropriately a cold cathode with rectangular emission window.
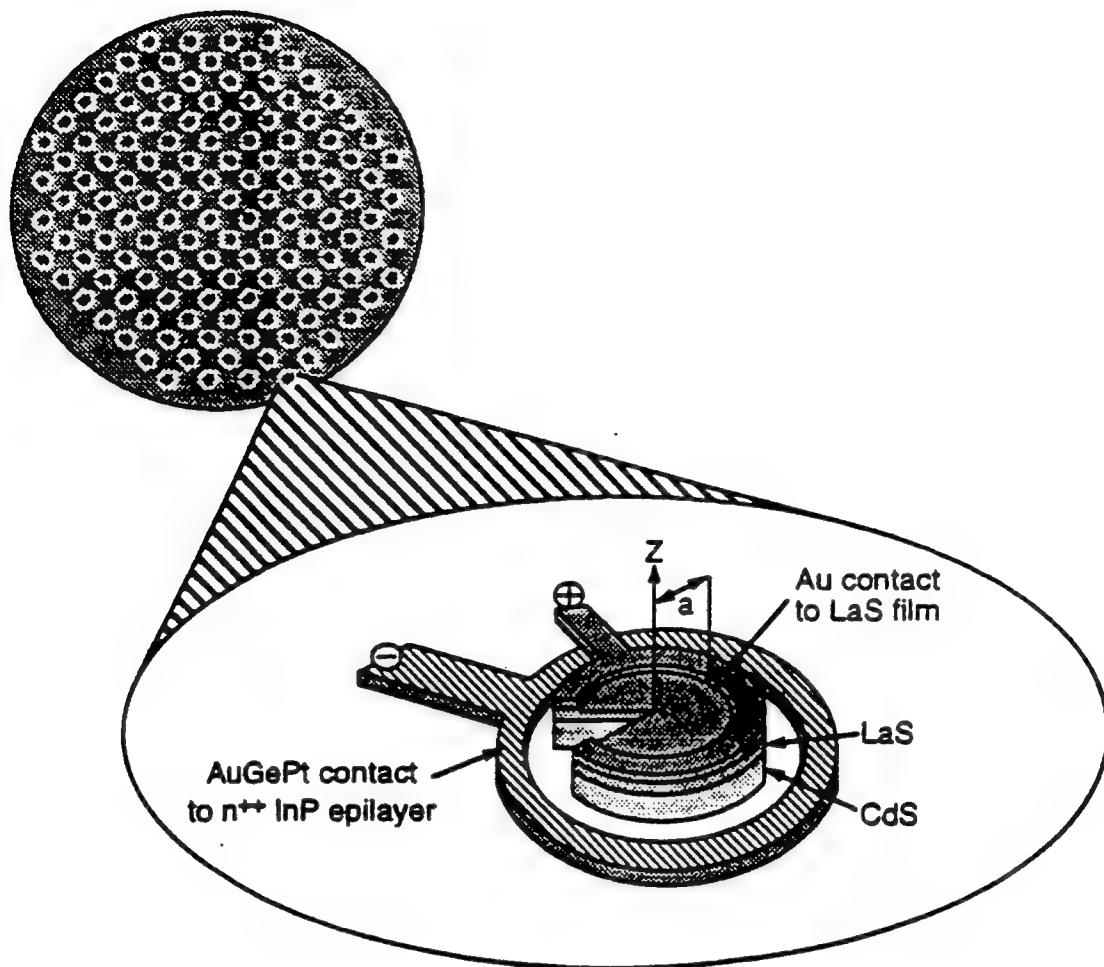
(c)

Figure 1 (cont'd): (c) Array of circular cold cathode emitters arranged in a honeycomb configuration and close-up view of one of the emitters showing the various layers in the epitaxially grown structure and the contacts made to the LaS metallic grid and the $n^{++} - InP$ heavily doped injection layer. [After W. Friz, Task ELM-2, "Dissipative Processes in Veiled Work Function Emitters", Contract F 33615-C-95-1755, WPAFB, Dayton, May 1996].
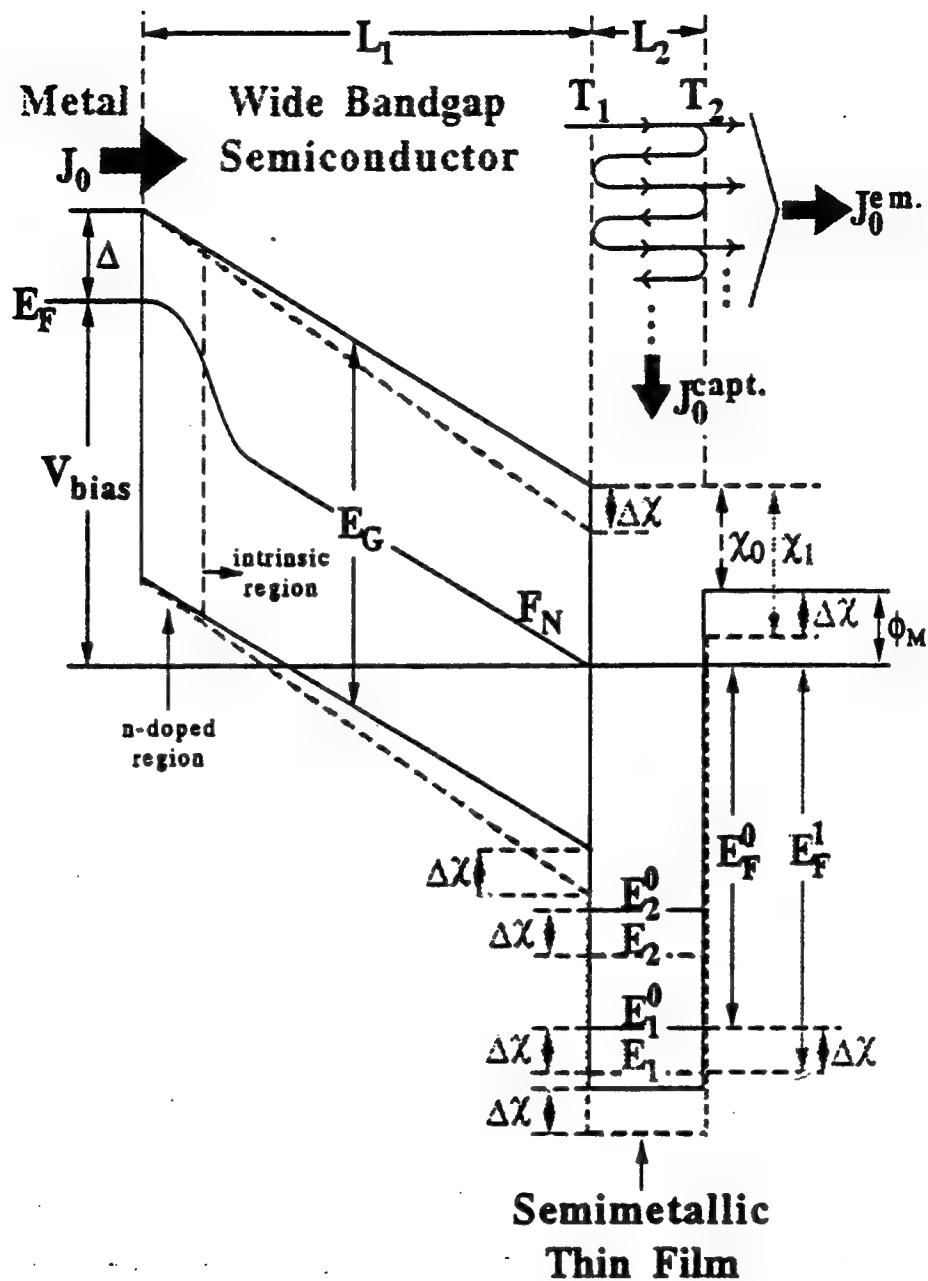
Figure 2: Schematic representation of the conduction band profile throughout the cold cathode emitter described in the text. Under forward bias, a fraction of the emitted current is captured in the semimetallic slab. The subsequent excess sheet carrier concentration in the quantum well formed by the semimetallic slab leads to a shift of the fermi level in the thin film which is similar to a lowering of the work function of the thin film. For a given forward bias, this leads to an increase in the electric field in the wide bandgap semiconductor (dashed line versus full line) and in an increase in the injection and emitted currents. Also shown in the quasi Fermi level spatial dependence across the wide bandgap semiconductor.
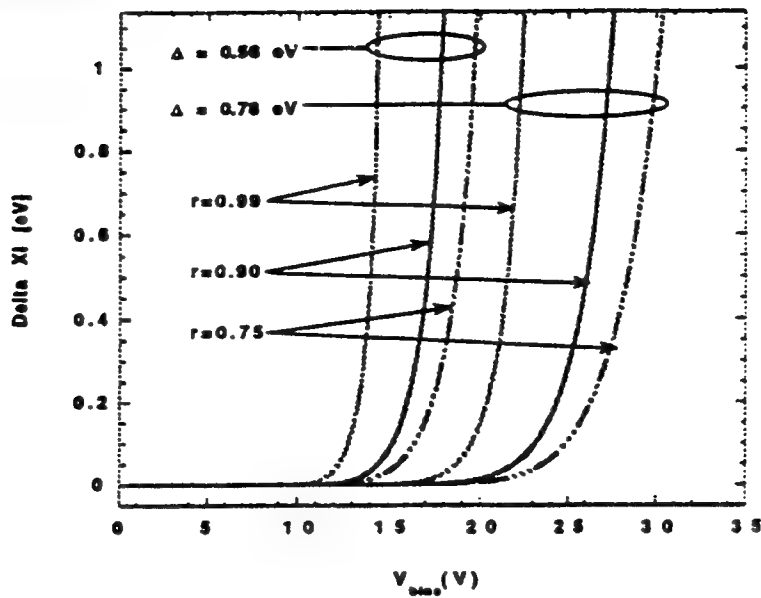
Figure 3: Dynamical shift of the work function as a function of the external applied bias for a cold cathode emitter with the parameters listed in Table I. For each group of curves, r = 0.99, 0.9, and 0.75, from left to right. The following physical parameters were used: $\lambda_{LaS} = 300$ Å, $T_1 = T_2 = 0.5$, and $v_F = 1.36 \times 10^8 cm/s$.
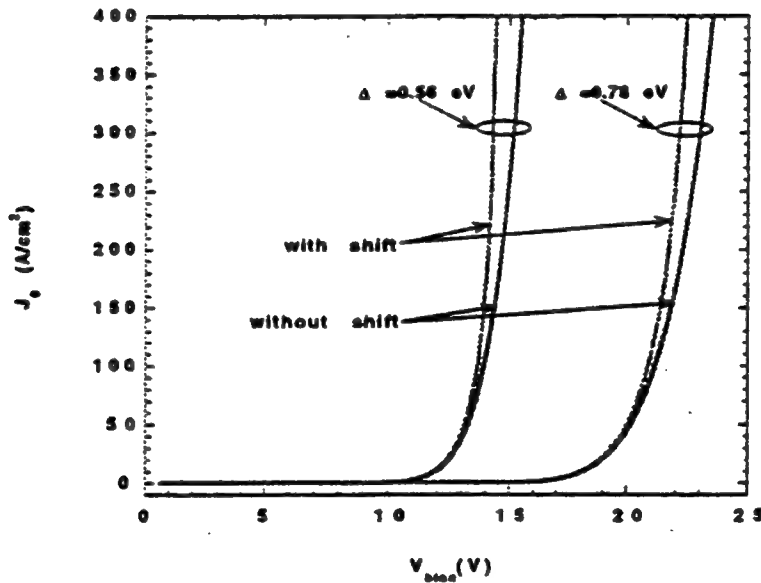
Figure 4: Comparison between the emitted current as a function of the applied bias while including (dashed line) and neglecting (full line) the dynamical shift of the work function of the semimetallic slab described in the text. The parameters of the device are listed in Table I. The coefficient C_1 and C_2 in Eq.(1) were chosen equal to 1.5×10^6 A/V and 6.9×10^7 $(V^{1/2}cm)^{-1}$, respectively. Other choices for the parameters C_1 and C_2 with similar magnitudes lead to similar dynamical shift of the work function. The reflection coefficient r shown in Fig. 1(a) was set equal to 0.99. The following parameters were used: $\lambda_{LaS} = 300$ Å, $T_1 = T_2 = 0.5$, and $v_F = 1.36 \times 10^8 cm/s$.
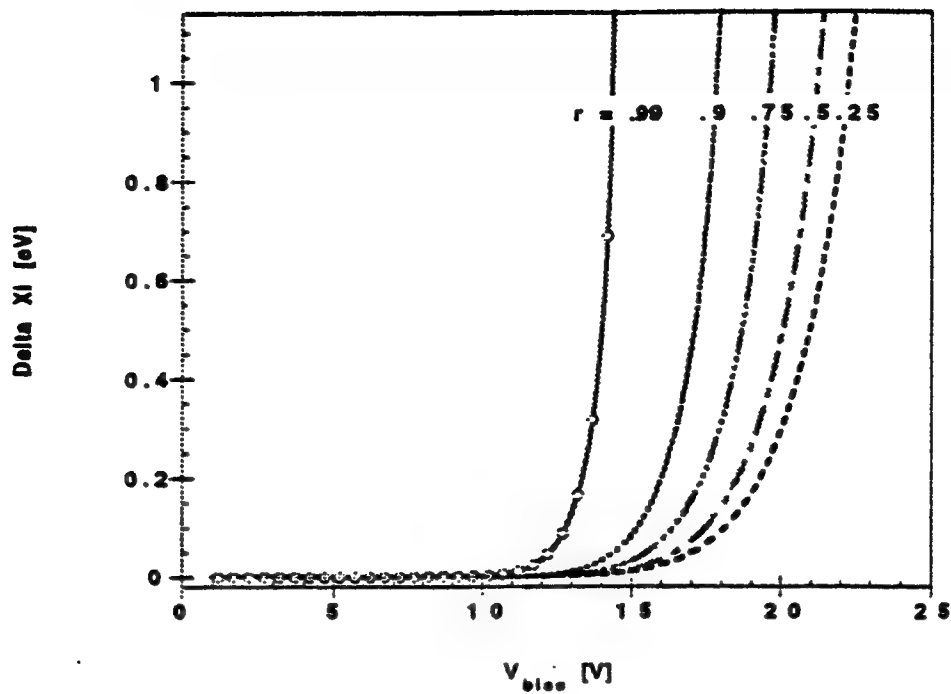
(a)
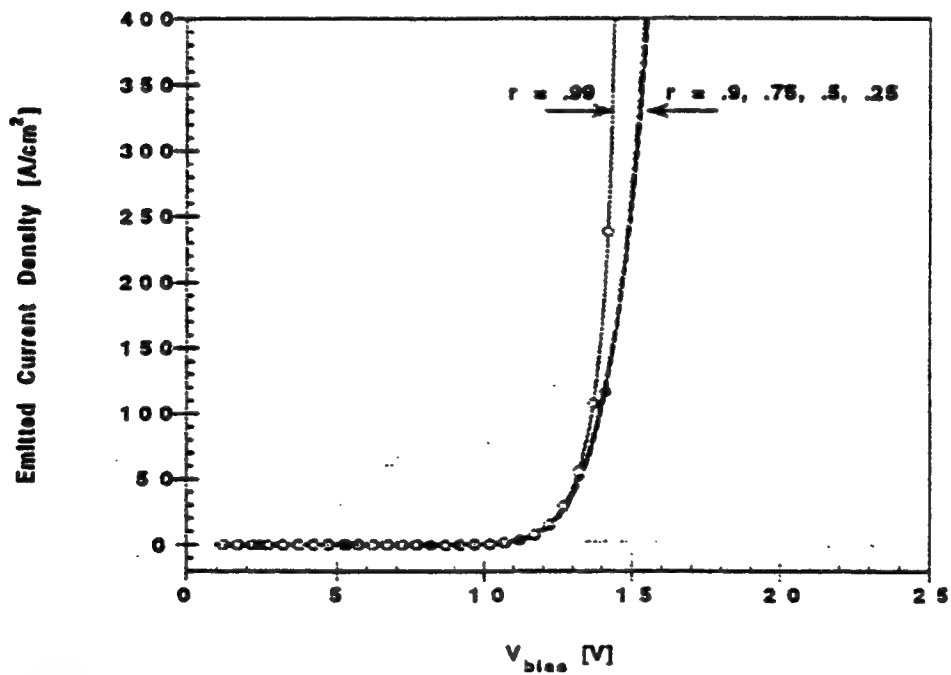
(b)

Figure 5: (a) Bias dependence of the dynamic work function shift in a typical cold cathode while varying the reflection coefficient of electrons between the 2D thin film and LaS contact regions. (b) Corresponding bias dependence of emitted current density. The following parameters were used ($L_1 = 500$ Å, $L_2 = 24.6$ Å, W = 1 cm, $T_1 = T_2 = 0.5$, $\lambda_{LaS} = 300$ Å, $\Delta(A_g) = 0.56eV$).
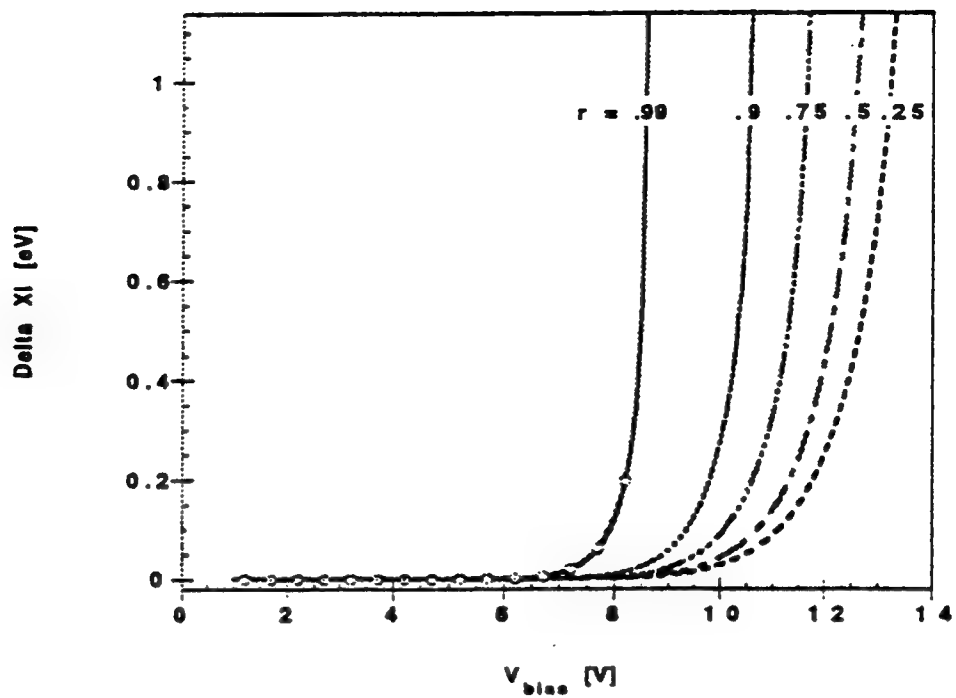
(a)
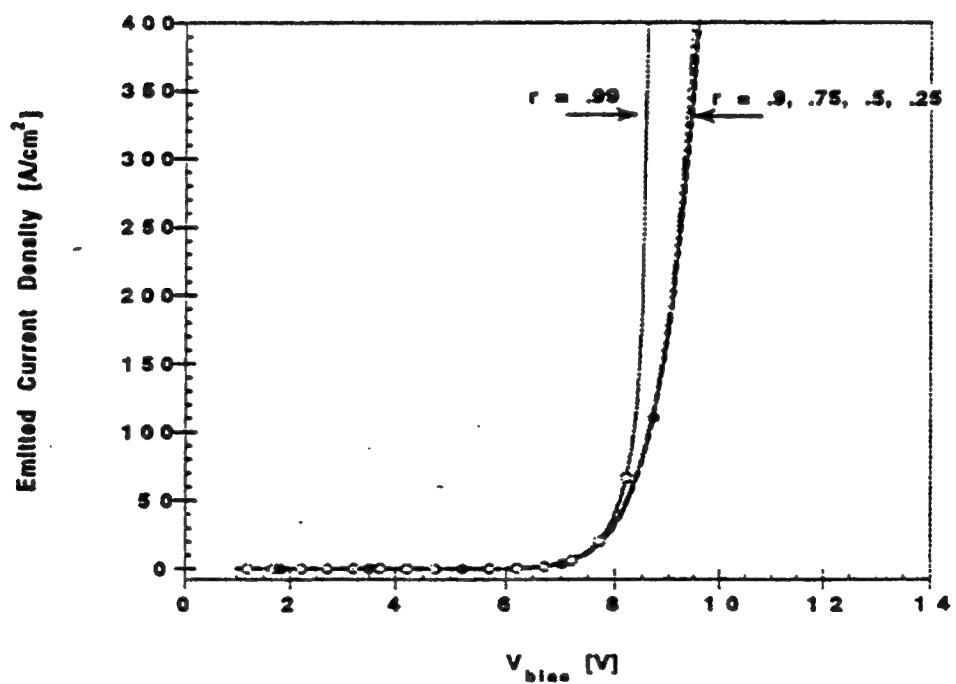
(b)

Figure 6: Same as Figure 5 for a cathode with a 300 Å thick CdS region, all other parameters being kept the same. Comparison with Figure 5 shows that the exponential rise of the dynamic work function shift and the emitted current density occurs at smaller values of the applied bias.
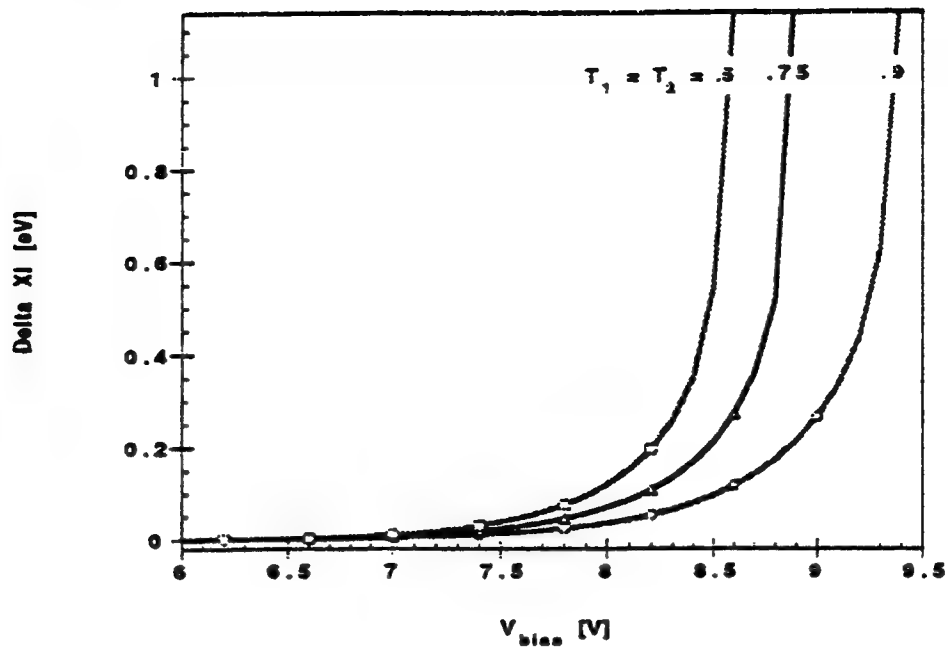
(a)
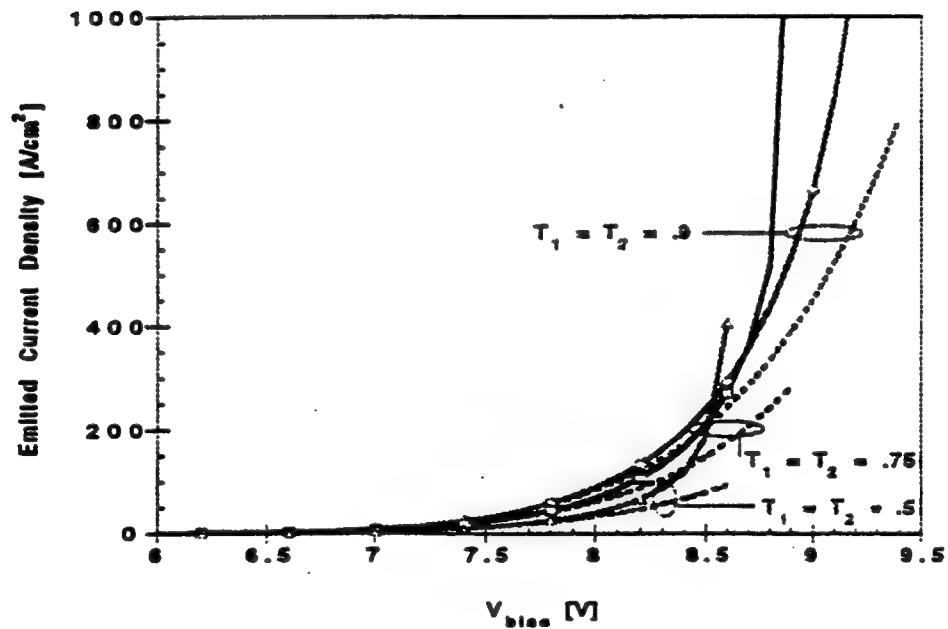
(b)

Figure 7: (a) Bias dependence of the dynamic work function shift in a typical cold cathode while varying the transmission coefficients T_1 and T_2 at the CdS/LaS and LaS/vacuum interfaces. (b) Corresponding bias dependence of emitted current density. The full and dashed lines are the current density plots calculated with and without the effect of the dynamic work function shift. The following parameters were used ($L_1 = 300$ Å, $L_2 = 24.6$ Å, $W = 1$ cm, $\lambda_{LaS} = 300$ Å, and $\Delta(A_g) = 0.56eV$). The curves are labelled with the values of the transmission probabilities T_1 and T_2 which were assumed to be identical.
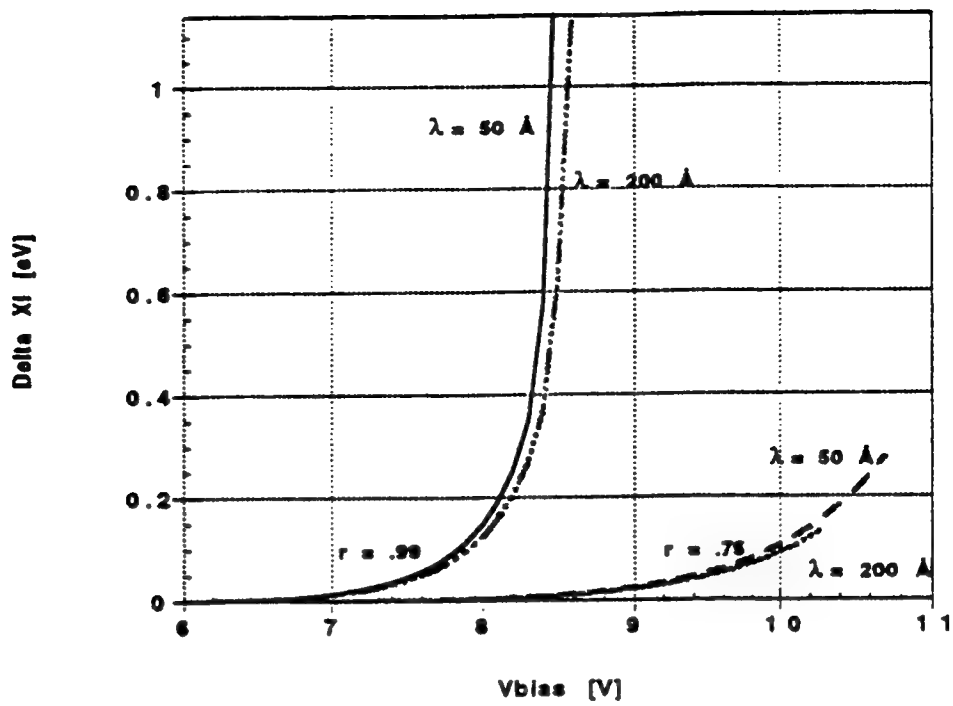
(a)
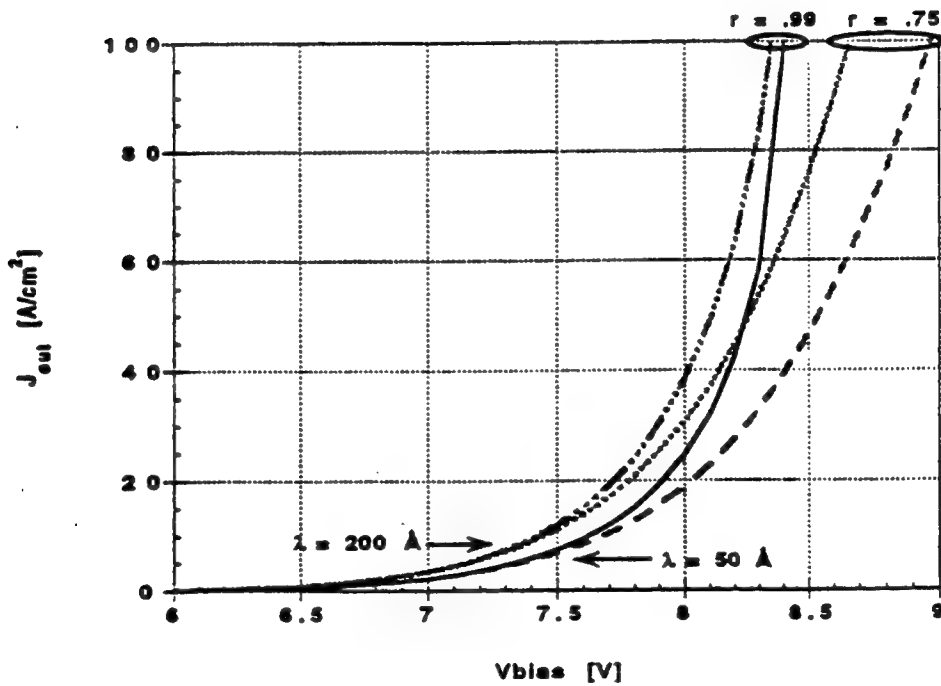
(b)

Figure 8: (a) Bias dependence of the dynamic work function shift in a typical while varying the electron mean free path λ_{LaS}. (b) Corresponding bias dependence of emitted current density. The following parameters were used ($L_1 = 300$ Å, $L_2 = 24.6$ Å, W = 1 cm, $\lambda_{LaS} = 300$ Å, $\Delta(A_g) = 0.56eV$, $T_1 = T_2 = 0.5$, and r = 0.99).
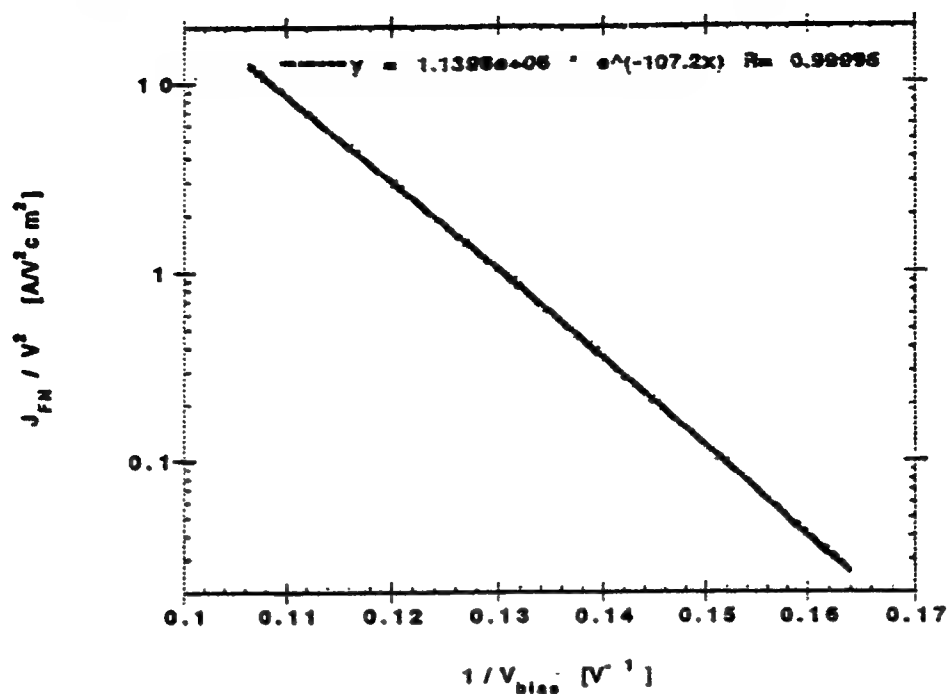
(a)
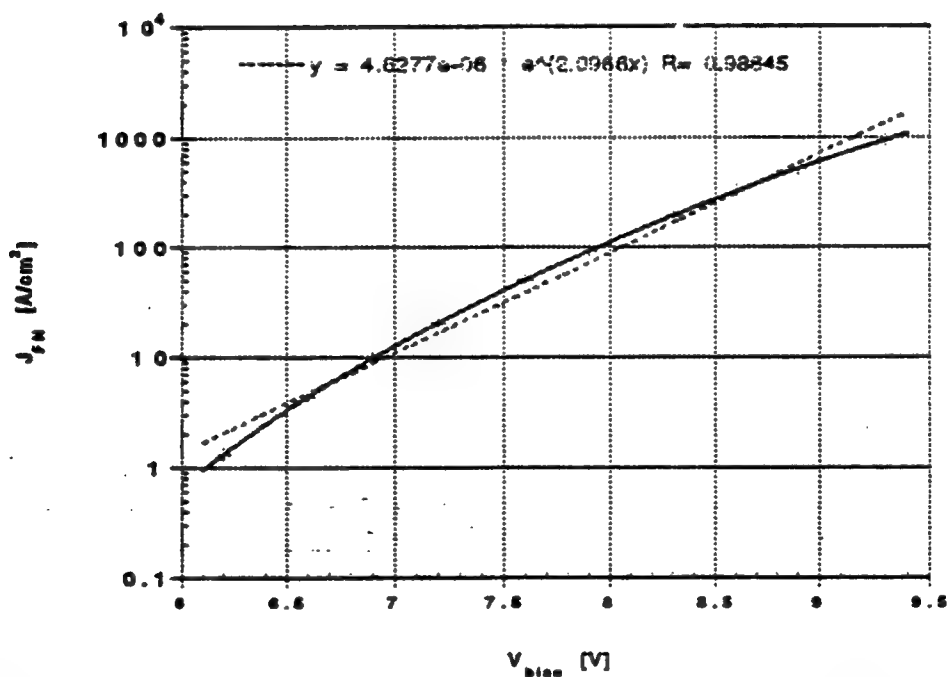
(b)

Figure 9: (a) Fowler-Nordheim fit to the bias dependence of the emission current of a cold cathode with the physical parameters listed in the caption of Figure 5. (b) Fit of the same J_{FN} versus V_{bias} calculation by an expression of the type $J_{FN} = J_0 e^{\alpha V_{bias}}$ for a range of V_{bias} for which the emitted current density varies between 1 and 1000 A/cm^2.
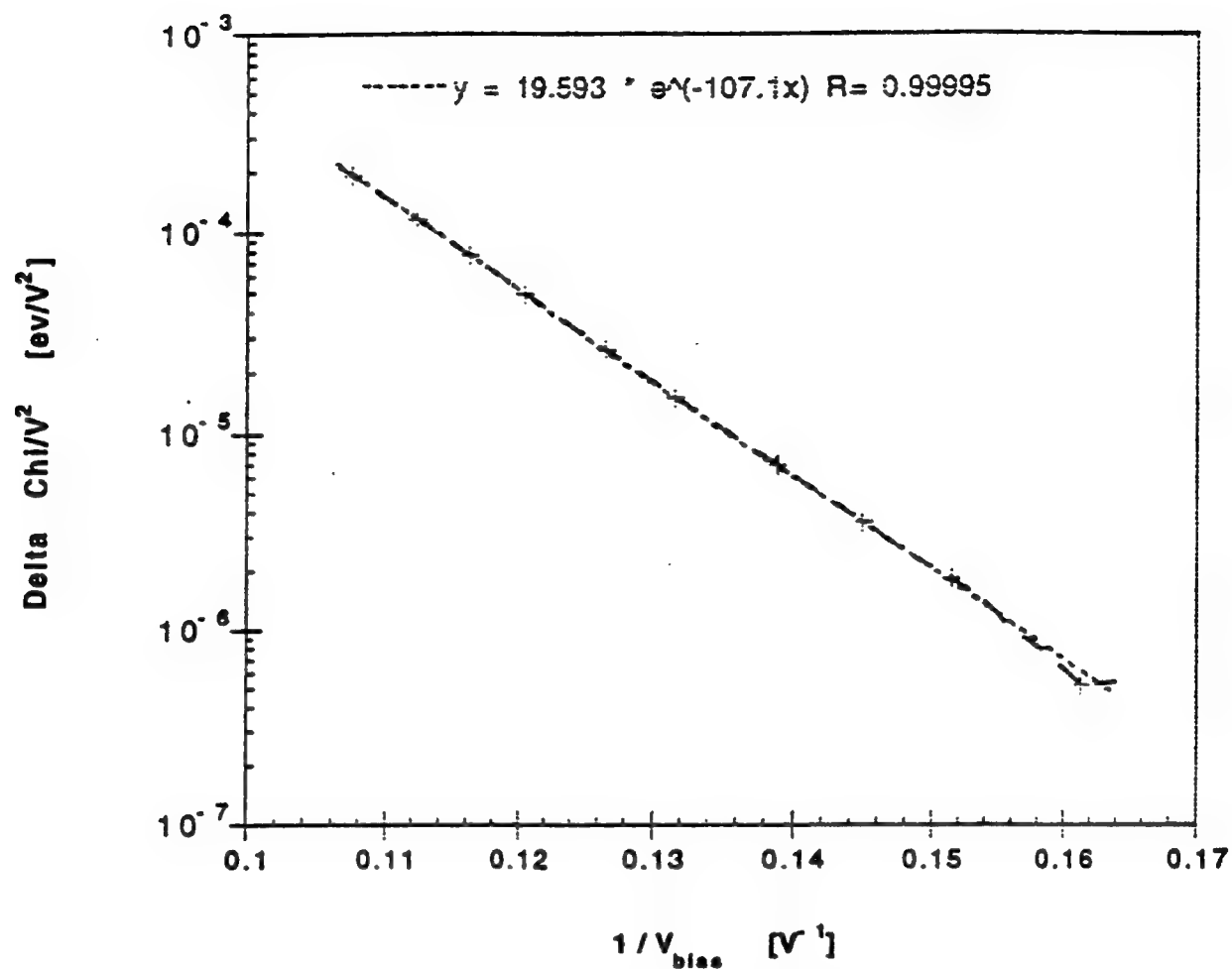
Figure 10: Fowler-Nordheim fit to the bias dependence of the dynamic work function shift for a cold cathode with the physical parameters listed in the caption of Figure 5. The following parameters were used ($L_1 = 300$ Å, $L_2 = 24.6$ Å, W = 1 cm, $\lambda_{LaS} = 300$ Å, and $\Delta(A_g) = 0.56 eV$).
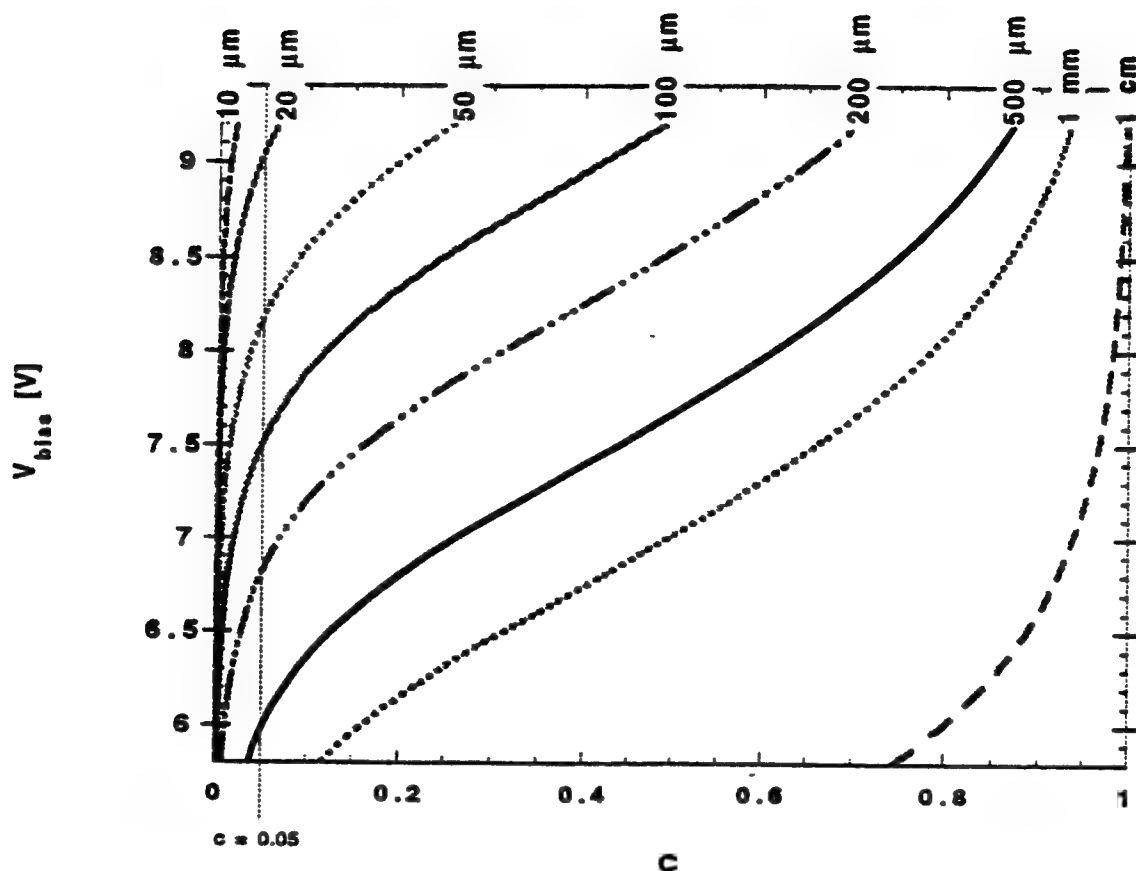
Figure 1.1: Bias dependence of the parameter c as a function of applied bias for different radii of a cold cathode emitter with a circular geometry. Cold cathodes with narrower emitter window must be operated over a smaller dc bias range to avoid current crowding. The following parameters were used ($L_1 = 300$ Å, $L_2 = 24.6$ Å, $W = 1cm$, $\lambda_{LaS} = 300$ Å, $\Delta(A_g) = 0.56eV$, and $r = 0.99$). Current crowding effects are negligible as long as the parameter c is kept under 0.05.
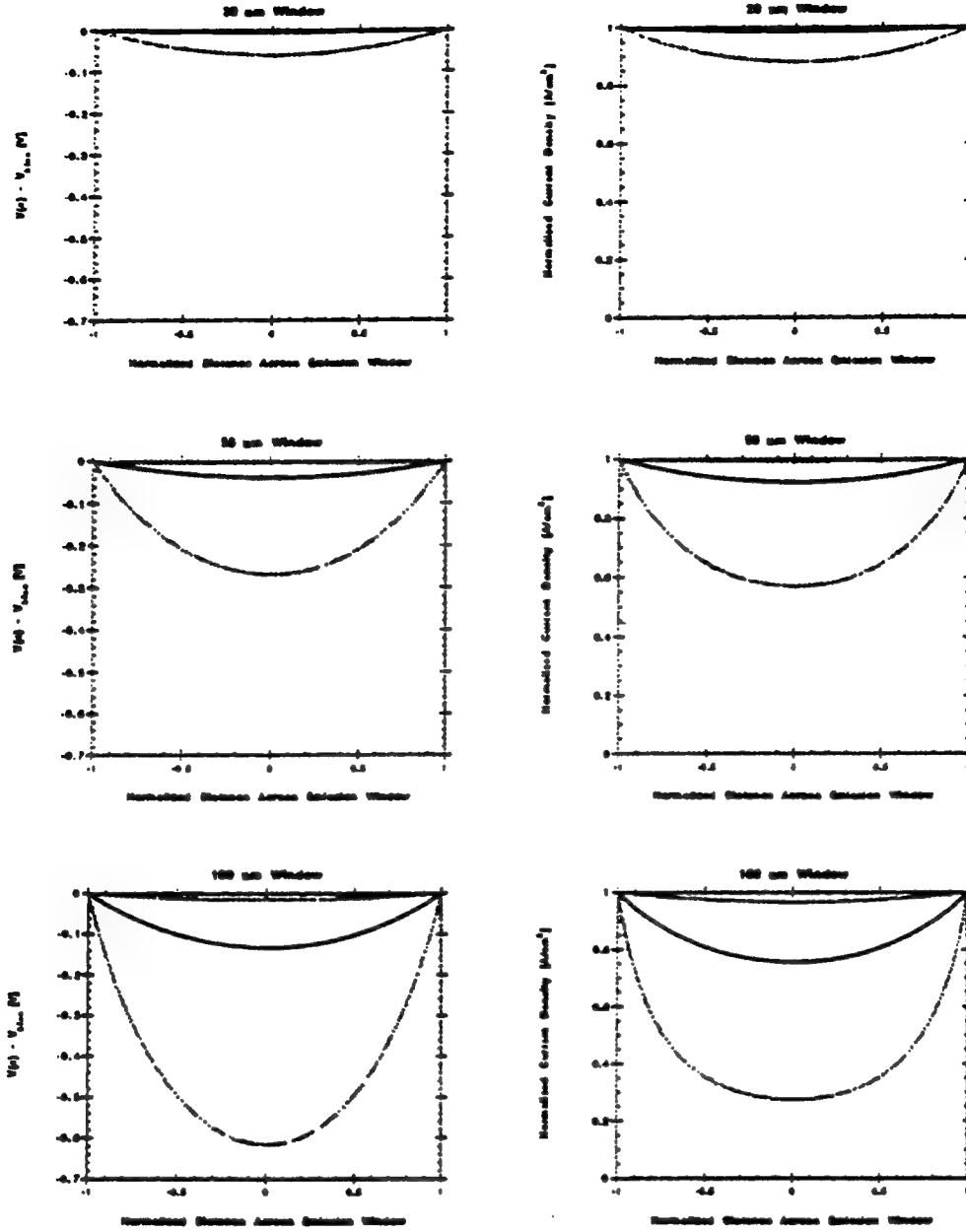
Figure 12 : Radial variation of the potential drop across the LaS windows of various radii. The cathode is assumed to operate at room temperature and the electrical resistivity of LaS is set equal to 92 $\mu\Omega cm$. The potential is measured relative to the potential at the rim of the LaS circular window where the electrostatic potential is assumed to be equal to the applied bias. For each figure, the values of the normalizing current density are from top to bottom 1, 10, 100, 1000 A/cm^2. The LaS window radius is indicated on top of each figure. The following parameters were used ($L_1 = 300$ Å, $L_2 = 24.6$ Å, W = 1cm, $\lambda_{LaS} = 300$ Å and $\Delta(A_g) = 0.56eV$). Right frames : corresponding radial dependence of the emitted current densities. Current densities are normalized to the values of the emitted current at the window rim.
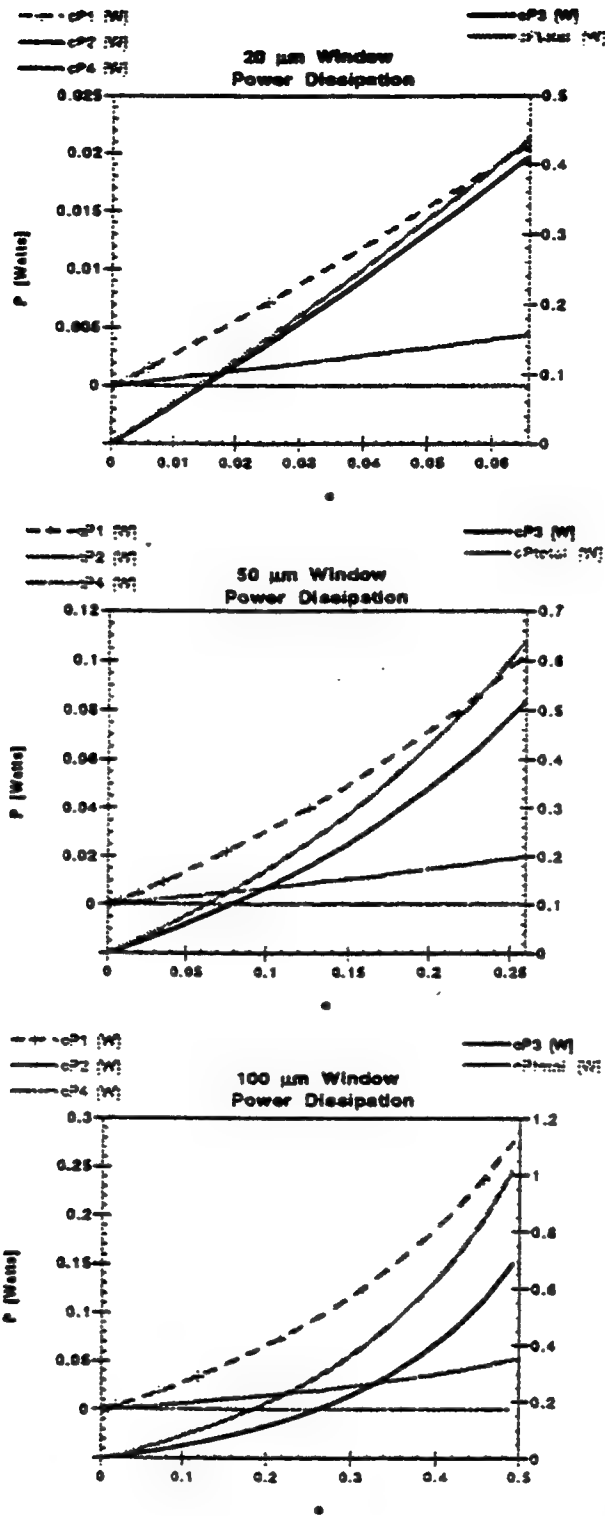
Figure 13 : Variation with the parameter c of the different contributions to the total power dissipated in circular cold cathodes with different radii (see Eqns.(32-39)). The physical parameters of the cathodes are listed in Table I and in the caption of Fig.5. The CdS layer is assumed to be grown on a heavily doped InP substrate $100\mu m$ thick. The thermal conductivity of the InP substrate was taken equal to 0.74 W/Kcm and the parameter b in Eq.(13') was set equal to 1.45. The thickness of the LaS contact regions was set equal to 100 Å.
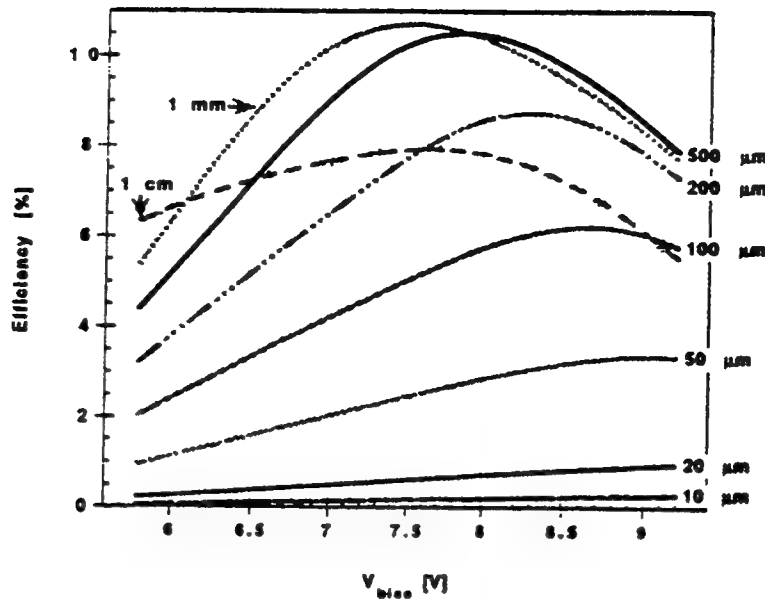
(a)
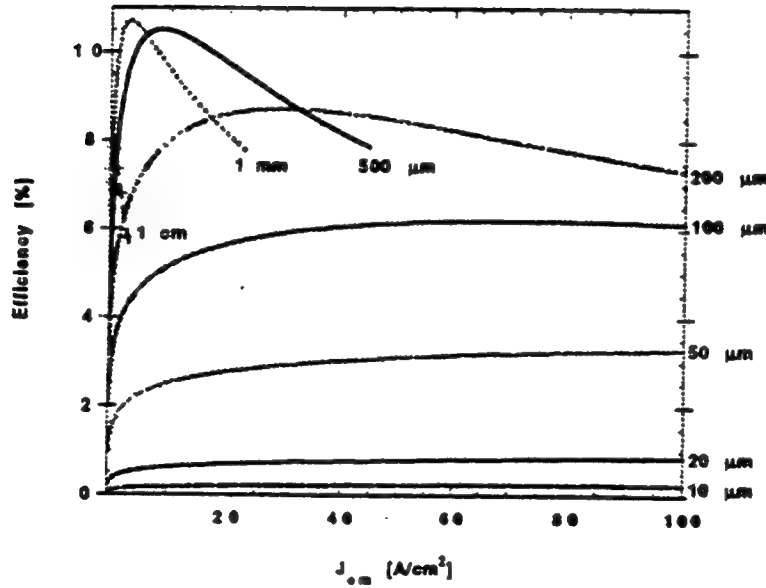
(b)

Figure [14] : Power efficiency η_P of cathodes of different radii is plotted as a function of (a) V_{bias} and (b) the emitted current density J_{em}. For all window sizes, the efficiency decreases with V_{bias} and J_{em} as a result of current crowding. The efficiency is more or less constant over a wider range of V_{bias} for window with smaller radius because current crowding is less important in that case, as illustrated in Fig.12 . The overall lower efficiency for smaller size window comes from the fact that the width b of the thick LaS regions was set equal to $100\mu m$ for all cathodes. The efficiency of cathodes can be increased by making the ratio b/a in Fig.1 closer to unity. The following parameters were used ($L_1 = 300$ Å, $L_2 = 24.6$ Å, W = 1cm, $\lambda_{LaS} = 300$ Å, $\Delta(A_g) = 0.56eV$, $T_1 = T_2 = 0.5$, and r = 0.99).
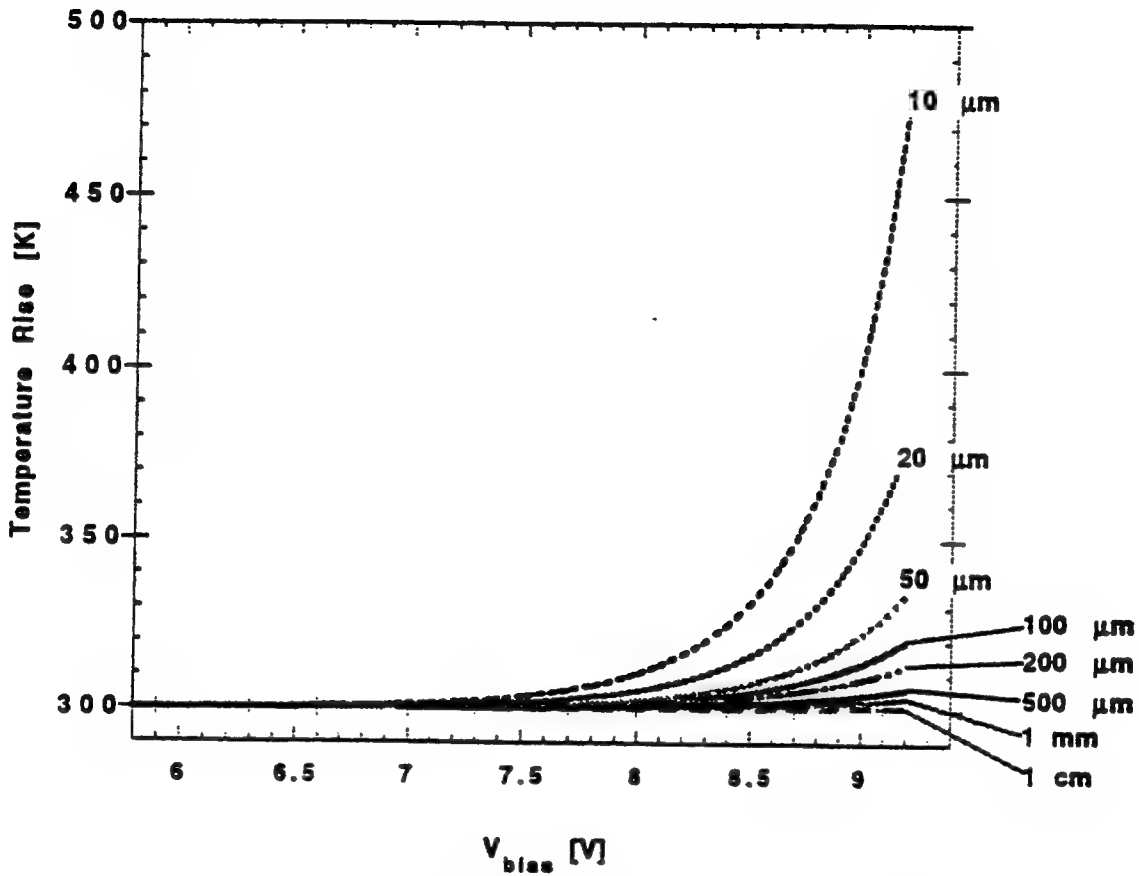
Figure 15.: Temperature rise in the *LaS* thin film as a function of the applied bias for the various cold cathode structures studied in Figure 13. The active area of the cathode (CdS/LaS layers) is assumed to be grown on a 100μm thick InP substrate with the back of the substrate acting as a perfect heat sink (300K).
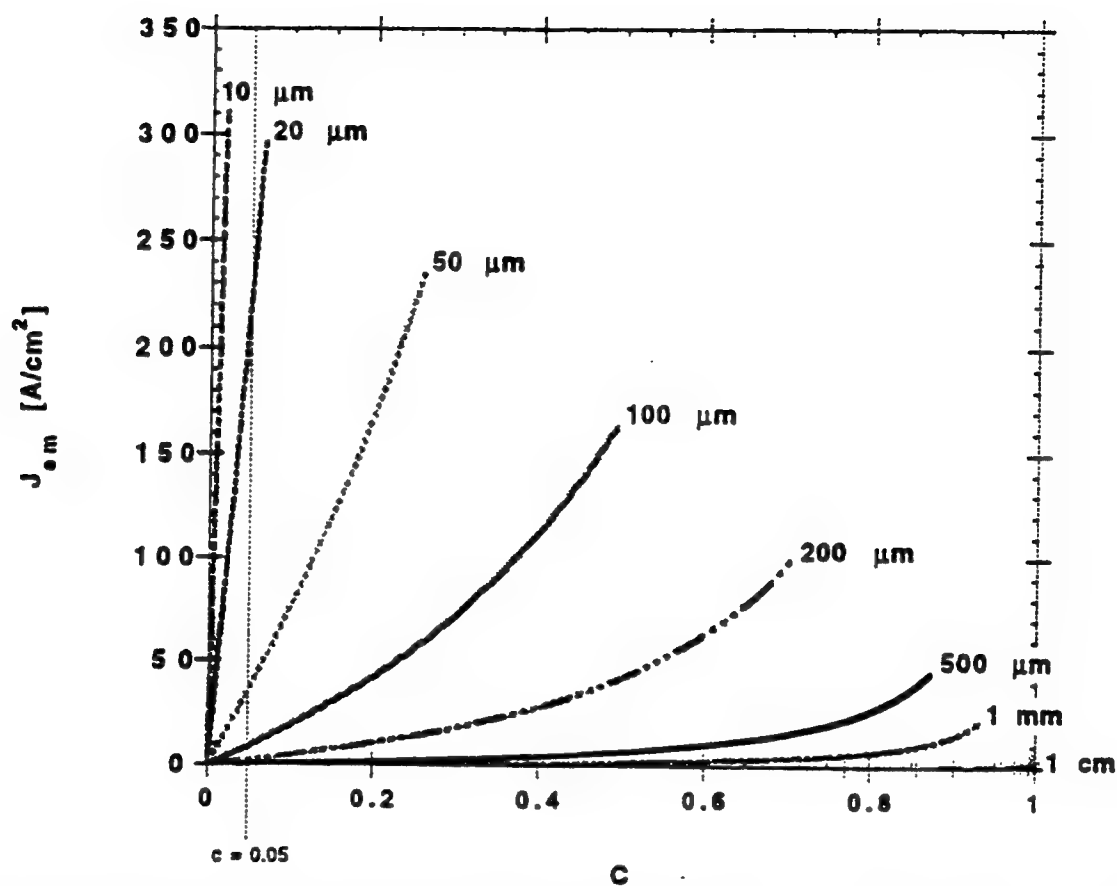
Figure16 : Emitted current densities for emitter window of different radii as a function of the parameter c. The vertical line at c=0.05 is the line to the right of which the effects of current crowding can not be neglected. Appreciable emitter current densities can be obtained for cathodes with emitter window width under $50\mu m$. The following parameters were used ($L_1 = 300$ Å, $L_2 = 24.6$ Å, $W = 1cm$, $\lambda_{LeS} = 300$ Å, $\Delta(A_g) = 0.56eV$, $T_1 = T_2 = 0.5$, and r = 0.99).

Gary Chapman
Report not available at time of publication.

CHARACTERISTICS OF THE TEXTURE
FORMED DURING THE ANNEALING OF COPPER PLATE

Robert J. De Angelis
Professor
Department of Mechanical Engineering

University of Nebraska-Lincoln
Lincoln, NE 68588-0656

4-1

CHARACTERISTICS OF THE TEXTURE
FORMED DURING THE ANNEALING OF COPPER PLATE

Robert J. De Angelis
Professor
Department of Mechanical Engineering
University of Nebraska-Lincoln

Abstract

The production of copper plate with controlled degrees of anisotropy is important because a regulated texture provides significant assurance that subsequent plastic deformation can be performed to successfully produce a reliable product. To proceed to this condition, the degree of anisotropy in a material must be quantified in the cold worked state and at a number of intervals during the recrystallization process.

In this investigation the recrystallization kinetics of copper plate was monitored by determination of the microhardness, the energy released and the microstructure during annealing. The texture was determined, by x-ray pole figure methods. The degree of anisotropy was inferred by calculating the orientation distribution functions (ODF) from the pole figure data.

One of the main objectives of this research was to quantify the changes in texture occurring during the annealing of a cold worked copper plate.

A finite element model of a 30 caliber cylindrical copper shell shot at a rigid wall at 541.6 ft/sec has been developed. The post mortem radial profiles of copper specimens fired at 570.9 ft/s show excellent correlation with the shape of the projectile predicted by the finite element model after impact. Contour plots of Von-Mises stress and effective plastic strain after impact have also been created. These results indicate finite element modeling is an effective way to predict final deformed shape of these types of ballistic impacts.

CHARACTERISTICS OF THE TEXTURE
FORMED DURING THE ANNEALING OF COPPER PLATE

Robert J. De Angelis

Introduction:

Annealing phenomena have both a scientific and engineering importance because these phenomena play important roles in the formation of the microstructure and in determining the engineering properties of the processed metallic materials. Annealing or softening of the cold worked or hardened metals has been described by two mechanisms recovery and recrystallization. These may occur separately or sequentially depending on the initial grain size, the degree of cold work, and the annealing thermal cycle. Recovery is associated with the annihilation of crystalline defects and the migration of dislocations into arrays which form small angle boundaries. Recrystallization takes place by the nucleation and growth of new strain free grains at the expense of the deformed matrix.

The recrystallization of copper was investigated in the late 1940's (1,2) through the observation of changes in mechanical properties and the integrated intensity of the (200) Bragg diffraction peak during isothermal annealing. In addition to the usual variables of amount of cold work and annealing times and temperatures, Cook and Richards (1) investigated the role of the initial grain size on the recrystallization behavior of copper. They reported that copper (containing 0.04 oxygen, 0.003 silver and 0.001% iron) with grain sizes of 0.015 mm, 0.025 mm and 0.06 mm cold rolled to 97.5% reduction demonstrated times for 50% recrystallization at 125°C of 0.3 hrs., 0.7 hrs. and greater than 8000 hrs respectively. This result clearly indicates the necessity to characterize the initial grain size prior to cold working.

Unquestionably, recrystallization produces a change in the texture of a polycrystalline material. This change from the cold worked to the annealed texture is accompanied by a corresponding change in engineering properties and is the prime cause of anisotropy in polycrystalline metallic materials. Texture or preferred orientation imparts the anisotropic properties of the single crystal to the polycrystalline aggregate.

Despite the general recognition that detailed texture description is needed to control macroscopic properties very few investigations of materials processing have included the quantification of texture. Since the 1980's the description of material textures or crystal orientations in polycrystalline wires and sheets started to move beyond the crystallographic pole figure representation of texture (3). In recent years the orientation distribution function (ODF) has become the method of choice for presenting the description of material textures (3,4). A great advantage of the ODF method of texture representation is that the coefficients of the harmonic equations employed to describe the function provide weighing factors for the determination of the anisotropic elastic and plastic properties of the material.

Also included in this report are the results of a dynamic nonlinear finite element analysis of the firing of a 30 caliber cylindrical copper shell at a rigid wall. The finite element code utilized for the analysis was LS-Dyna3d as it provides excellent nonlinear material behavior. The objective of this analysis is to compare the shape following

impact predicted from the finite element method with experimentally observed shapes of projectiles that impacted a stationary wall.

Materials Processing:

<u>Nebraska Plate</u>: A 0.375 inch thick copper plate was produced from a one inch thick pancake by cold rolling, employing a clockwise rotation of 135° between passes. The copper pancake was made by upset forging a three inch diameter, three inch long bar cut from a hot rolled three inch thick slab. One half of the "as cold rolled" plate was provided by Mr. Joel W. House of Wright Laboratory (AWEF) at Eglin Air Force Base. This one-half section of material shown in Fig. 1 will be referred to as the Nebraska plate.

<u>**ATK Plate:**</u> A second plate provided by Mr. Joel House was processes by Allianttech Systems and was from Lot A2365. The alloy is C10100 copper supplied by the mill as 3.5 inch diameter bar. The bar was annealed at 343°C (650°F) for one hour. Billets of 2.6 inch length were cold upset forged to 0.39 to 0.35 inch thick plate (strains of -1.9 to -2.0) in five hammer blows. After annealing at 343°C (650°F) for one hour the copper plate had a grain size of 10 to 15 microns with a few isolated 20 micron grains. An approximately six inch diameter one inch high dome was cold formed into the center of the plate leaving a one and a half inch diameter rim around the dome. This plate will be referred to as the ATK plate. Testing on this plate was performed at Eglin AFB AWEF facilities during the summer of 1996.

Experimental Procedures:

The experimental and analytical techniques employed in this investigation can be partitioned into five task areas: Materials processing; X-ray pole figure determinations; Thermal analysis; Microstructural characterization; Mechanical Property Determination and Finite Element Modeling of impact behavior of copper. These tasks were executed at the University of Nebraska-Lincoln (UN-L) and at Wright Laboratories, Eglin Air Force Base, AWEF (WL/MNMW). This division of the experimental efforts effectively took advantage of the expertise and equipment existing at both locations. The hardness measurements, the thermal analysis experiments, the metallography observations and the finite element modeling of the impact behavior of copper were performed at the UN-L. The x-ray pole figure determinations, the mechanical property determinations and the 30 caliber gun impact tests were performed at WL/MNMW.

<u>Nebraska Plate</u>: Metallographic, x-ray, and mechanical test specimens were machined from the Nebraska plate at 1/4, 3/4 and 4/4 radial positions. These specimens were located in the plate half section such that their radial center lines coincided with zero, forty five and ninety degrees to the cut surface. These nine specimens, plus the specimen from the center, were the ten locations in the plate where structural determinations were made. The specimen layout in the Nebraska plate is shown in Fig. 2.

<u>**ATK Plate:**</u> The rim of the ATK plate was basically not effected by the cold deformation during the formation of the dome in the ATK plate. The rim material provided specimens for metallography, x-ray diffraction, quasi-static,

high strain rate mechanical testing and Taylor impact tests from the positions shown in Fig. 3.

Heat Treatment:

<u>Nebraska Plate:</u> Samples from several positions in the Nebraska plate were heat treated in flowing argon at temperatures between 260°C and 300°C for various times. These samples were employed for optical microstructure investigation. The specimens employed for pole figure determinations were wrapped in tantalum foil and vacuum annealed at 300°C for one hour.

Microstructural Characterization:

<u>Nebraska Plate:</u> Optical and scanning electron microscopy (SEM) were employed to characterize the microstructure of the copper plate prior to cold rolling, in the cold rolled condition and at each of the annealing intervals at each temperature. Employing the Köhlhoff etching technique, which reveals (111) planes and shear bands, permits, by SEM examination, the qualitative identification of grain orientation relationships (5).

X-Ray Pole Figures:

<u>Nebraska Plate:</u> X-ray pole figures were determined using the Siemens diffractometer at WL/MNMW. The specimens were prepared and the data was collected by the author and Mr. Todd Snyder, a UN-L graduate research assistant. Pole figures were determined at the ten locations on the Nebraska plate as shown in Fig. 4. These ten samples were split near to mid-plane and milled flat. The midplane surface was prepared for x-ray investigation by metallographically polishing and etching. The (111), (200) and (220) pole figures were collected from the midplane surface of the ten specimens. The pole figure data was transformed to ODFs employing both POPLA and Siemens software. The specimens were vacuum annealed at 300°C for one hour. The identical surfaces were prepared as described above and the (111), (200) and (220) pole figures were determined on the ten annealed specimens. The ODFs of the annealed specimens were calculated from the pole figure data.

<u>ATK Plate:</u> Pole figures of the (111), (200) and (220) planes were determined for the ATK plate. These data were employed to calculate the ODF of this plate and the inverse pole figures.

Thermal Analysis:

<u>Nebraska Plate:</u> The rate and amount of energy release was investigated using differential thermal analysis (DTA) and differential scanning calorimetry (DSC). Isothermal and scanning modes were utilized to monitor the fraction of stored energy released. This information was used to provide insights into the kinetics of the recrystallization process.

Finite Element Model:

The solid finite element model of the 30 caliber copper projectile was created using Altair's Hypermesh mesh

generator version 2.0e. The projectile was 0.9 inches long with a diameter of 0.289 inches. The average element size has a length of 0.02 inches. Located 0.01 inches from the end of the projectile was a rigid wall that is fixed in space. The friction existing between the wall and the projectile was assumed to be zero in the simulation. The full model consisted of 6360 elements and 8150 nodes. The initial geometry and setup of the simulation is shown in Figs. 5 and 6. The projectile was given an initial velocity of 541.6 in/sec in a direction toward the wall. The simulation ran for 10 milliseconds of impact time which took 21.661 minutes of CPU time on a Cray J 916 computer using fully integrated solids on the model.

The material behavior of the copper projectile was determined using a piecewise linear plasticity constitutive model. This model permitted for the input of the mass density of copper and the values of it's Poisson's ratio, elastic modulus, and yield strength. Table I contains the bulk material property values that were employed in the simulation. The strain rate sensitivity of the material was introduced into the model by the creation of a family of stress versus effective plastic strain curves for various strain rates. Here, two experimentally determined stress-strain curves for copper were employed at strain rates of: 0.0222 per second and 1777.58 per second. Values between these two strain rates were linearly interpolated. The experimentally determined relationships between stress and effective plastic strain for the copper material at the two strain rates is shown in Fig. 7.

Table I - Bulk Material Properties of Copper.

Material	Density $(lb_f\text{-}s^2)/in^4$	Poisson's Ratio	Elastic Modulus (psi)	Yield Strength (psi)
Copper	8.336E-04	0.30	16.0E+06	1.00E+04

Results and Discussion:

Heat Treatment:

Optical metallography of the isothermally annealed as-rolled copper (CU-HR7-AR) specimens indicated approximately 90% recrystallization after annealing at 260 °C for 20 hr. Increasing the temperature 10°C to 270°C and annealing for 20 hr. resulted in full recrystallization. These observations are confirmed by microhardness measurements which indicate a softening transition in the temperature range between 230°C and 270°C.

Microstructural Characterization:

Nebraska Plate: As-rolled and heat-treated specimens were examined at representative positions along the three sampling directions. The as-rolled microstructure was typical of heavily cold-worked material, with no obvious distinction among samples taken form the three plate directions. For local texture measurement a crystallographic etching technique (5) (concentrated nitric acid attacks {111} planes most slowly) indicates differences in the directions parallel and perpendicular to the rolling direction.

The microstructure of the heat treated samples were partially recrystallized at all annealing temperatures between 260° and 300°C. Large (50 μm) elongated grains were observed after annealing at all temperatures. The microstructure of specimens heat treated under various conditions were investigated to aid understanding of the recrystallization process and kinetic behavior and to help evaluate the texture development. An optical micrograph of a typical recrystallized microstructure is shown in Fig. 8. Table II contains a summary description of the microstructure observations of specimens annealed to various conditions.

Table II - Summary of Microstructural Observations.

Temperature (°C)/ Time (h)	Avg. Recrystallized Grain Size (μm)	Approximate Percent Recrystallized	Comments
260 / 1	3	<10	sparsely located grains
260 / 20	12	58	large regions of unrecrystallized metal
270 / 1	8	15	unrecrystallized region elongated in radial direction
270 / 20	14	78	-
280 / 1	12	22	-
280 / 20	18	83	large unrecrystallized regions remain
290 / 1	22	90	-
290 / 20	-	-	-
300 / 1	30	100	-

SEM micrographs of an as-rolled specimen and a specimen vacuum annealed for one hour at 300°C which were etched in concentrated nitric acid is shown in Fig. 9. Etching the radial direction of the as-rolled specimen revealed an organization of lamellar volumes of similar orientation. In addition, deformation banding was observed to be extensive as shown in Fig. 10. These deformation bands produce regions of high lattice curvature, which in turn strongly influence the nucleation and growth of recrystallized grains.

X-Ray Pole Figures:

<u>Nebraska Plate:</u> The pole figures from all positions except for the center position of the Nebraska plate showed the cold worked textures to be mainly a combination of (200) and (220) wire textures. This texture combination reduced the (111) component at the center of the cold worked plate to almost zero. The specimen taken from the center position had a much weaker (220) wire texture in the cold worked condition, and a generally weaker texture in the annealed condition. The pole figures on the annealed center specimen were statistically less reliable due to the large grain size that developed during annealing. Presumably this was because the material in the center of the plate was subjected to much less deformation during the upset forging and subsequent rolling procedure.

Differences between predominately wire textures that occurred during annealing can be demonstrated by plotting the integrated intensity of the annealed condition at any chi tilt angle minus the integrated intensity of the cold

worked condition at the same chi angle. This difference in pole figures is shown for the specimen taken from the center of the plate in Fig. 11.

The changes in crystallographic orientation during annealing were averaged for the 0°, 45°, and 90° specimens at each radial position of 1/4R, 3/4R and 4/4R. The average change in the (111), (200), and (220) pole densities at the three radial positions as a function of chi tilt angle are shown in Figs. 12, 13 and 14. It is apparent from these results that the annealing protocol combined with the rolling procedure to produce the as-deformed microstructure, though very distinct at various positions in the plate, formed similar recrystallization textures during annealing.

The pole figures of the cold worked materials showed significant variations in texture as the radial position increased. The as-deformed textures had (220) pole density maximums ranging from 2.67 to 15.88. Vacuum annealing the specimens for one hour at 300°C resulted in very similar texture for all the specimens. These results were very unexpected and lead to the very important possibility that the annealing thermal treatment determines the final recrystallization texture of the cold worked copper plate.

ATK Plate: The x-ray specimen taken from the plate position shown in Fig. 3 was prepared for x-ray diffraction by polishing and etching as described in the previous section for the Nebraska plate. The resulting pole figures indicated the texture to be (220) pure wire with a maximum strength of 2.53 times random. The (111) pole figure had a strength of 1.73 time random distributed uniformly on a circle centered 35° from the center of the pole figure. An attribute of the texture to be emphasized is the remarkable uniformity of the wire texture distribution. This, along with the uniform nature of the texture, is due to the processing history, the cold upsetting a rolled bar into plate.

Thermal Analysis:

Nebraska Plate: Attempts made to determine the amounts and rates of energy released during annealing of the plate processed copper specimens were not completely successful. These measurements were to allow, in addition to other materials parameters, the determination of the activation energy for recrystallization. The rates and amounts of energy released were investigated by employing a differential thermal analysis system (Perkin-Elmer DTA-7) and differential scanning calorimetry unit (Perkin-Elmer Delta Series DSC-7). Recrystallization information obtained from the annealing, microstructure and hardness investigation was employed to select the temperature and time parameters for the isothermal and scanning experimental modes of thermal analysis.

Initial isothermal investigations were performed on the DTA-7 which measures a differential temperature between a reference cup and a sample cup. Isothermal temperatures between 260°C and 290°C were investigated with time periods of 30 hours. No indication of stored-energy release was observed in these experiments. However, post microstructural observations indicated recrystallization had taken place. Similar results were observed in the scanning mode thermal studies conducted at scan rates of 5, 10, and 20°C /min. To increase the sensitivity of the measurements, a differential scanning calorimeter (DSC) was used for scanning mode studies with a temperature span starting at room temperature and ending at 700°C. These experiments produced incomplete energy release data. The energy release would go through a maximum, but the rate of energy release would not return to the baseline value.

These results were of little quantitative or qualitative value. A significant amount of effort was invested into the thermal analysis experimentation; however, no definite conclusions can be extracted from the data.

Hardness Measurements:

Nebraska Plate: Rockwell B hardness traverses were taken along OA, OB, OC, and OD. The individual hardness determinations made one half inch apart along the traverses are plotted in Fig. 15. There is some scatter in the data; however it is apparent that the plate is slightly harder (RHB 62) at the edge and slightly softer (RHB 55) in the center of the plate. Table III shows the statistics for each traverse.

Table III - Average Rockwell B Hardness of Traverses A, B, C, and D.

Traverse	Mean Hardness	Std. Dev.
A	56.4	2.6
B	55.7	4.4
C	55.8	3.3
D	57.4	3.0

Microhardness, measurements on a Wilson Tukon Series 200 machine, of specimens annealed for one hour at temperatures between 230°C and 330°C indicated that significant softening occurs at temperatures above 230°C. Annealing at 260°C for 1 hour produced the largest decrease in hardness. Increasing the annealing temperatures produced material with hardnesses slightly higher than the values observed after annealing at 260°C.

ATK Plate: Rockwell F hardness data were taken on the "as received " ATK plate at the positions shown in Fig. 16. The hardness measured in the rim of the plate were about R_F 55, same as the hardness of the annealed Nebraska plate contained in Table III. The hardness increases rapidly at the start of the dome were the bending is extensive. In the dome section of the ATK plate the increase in hardness is gradual from R_F 56 at the base of the dome to R_F 83 at the apex of the dome. These results allow the specimens from the rim section to be considered to be annealed.

Mechanical Properties:

The mechanical properties determined on the plate materials were performed at low strain rate (Instron Machine), high strain rate (Hopkinson Bar) and 30 caliber ballistic tests (Taylor Impact). These tests were performed on the ATK plate, however only the Taylor impact tests were performed on the Nebraska plate. The results of the other two types of mechanical tests, reported here, were obtained from a copper plate processed on exactly the same schedule as the Nebraska plate referred to as the MSC plate.

Nebraska Plate: Three Taylor impact test specimens were machined from the Nebraska plate at zero degrees, 45° and 90° to the minor axis of the plate (see Fig. 2). These specimens were tested at Eglin AFB, AWEF resulting in the data shown in Table IV.

Table IV - Data from Taylor Impact Specimens.

SHOT #	MATERIAL	L / D RATIO	IMPACT VELOCITY	FINAL LENGTH	L-NOT DEFORM	ECCENTRICITY
SC-5	MSC-16	3.0	738 ft/s	0.536 in	0.000 in	0.314
SC-6	MSC-16	3.0	656	0.591	0.000	0.283
SC-78	MSC-16	3.0	561	0.638	0.000	0.267
SC-79	MSC-16	3.0	571	0.657	0.000	0.293
SC-82	ATK-T-90	3.0	600	0.635	0.000	0.201
SC-83	ATK-T-45	3.0	571	0.646	0.000	0.206
SC-84	NEB-T-0	3.0	581	0.626	0.000	0.130
SC-85	NEB-T-90	3.0	571	0.635	0.000	0.191
SC-86	NEB-T-45	3.0	581	0.629	0.000	0.289

In addition to the data included in the table above Mr. Joel House, Eglin Air Force Base, AWEF measured the radii of the specimens, after impact, as a function of position along its length. Data from two of the specimens SC-79 and SC-82 were employed to determine the validity of the finite element model.

ATK Plate: The specimen locations for the Instron, Hopkinson bar and Taylor test mechanical test was shown in Fig. 3. All sixteen of the 0° and 90° static and high strain rate specimens were tested at AWEF. The data obtained from the Instrion and Hopkinson bar tests are shown in Figs. 17a to 17f and 18a to 18h.

Finite Element Model:

Analysis of the data obtained from the finite element model of a copper cylindrical projectile impacting a rigid wall at 541.6 ft/sec shows good correlation with actual testing data obtained for shots fired at 570.9 ft/sec. Two views of the geometry of the copper projectile after impact are shown in Figs. 19 and 20. A comparison of profiles of the radii along the length of the projectile after impact for two experimental tests and for the computer simulation are shown in Fig. 21. The two experimental tests are designated SC79 and SC83 were copper specimens machined from MSC-Plate 16 and ATK-T-90 respectively. Both specimens had a anvil striking velocity of 570.9 ft/sec. While the difference in striking velocities for the finite element model and the actual tests are somewhat different they are close enough to draw qualitative comparisons. The data contained in Fig. 21 indicated the computer simulation profile compares very favorably with the data from the specimens undergoing the actual impact. The Von-Mises stress contour plot and a effective plastic strain contour plot through the middle of the projectile after impact are shown in Figs. 22 and 23. These data indicate how the material flowed during plastic deformation following impact by tracking the material regions subjected to either high or low values of stress. Figures 9 and 10 also show a The

4-10

Von-Mises stress contour plot and effective plastic strain plot at the impact end of the cylinder, the end that struck the wall, are shown in Figs. 24 and 25. These plots are also useful in understanding how the material flowed under impact.

Conclusions

An initial study has been performed to understand the correlation between the forming processes (die upsetting and rolling) and the recrystallization texture of copper plate. An experimental plan consisting of materials processing; microstructural characterization; mechanical properties; x-ray pole figure determinations; finite element simulations of the impacting of copper and thermal analysis was used to characterize the copper plate. Annealing and microstructural studies indicate complete recrystallization after 1 hour at 300°C. Additional data accumulated in thermal analysis experiments concerning the amount of stored energy and activation energies for recrystallization are inconclusive at this point.

X-ray pole figures of the as-rolled specimens showed significant variations in texture as the radial position increased (i.e., nearer the edge of the plate). Annealing the specimens resulted in recrystallization textures similar for each specimen. These unexpected results indicate that the annealing procedure determines the final recrystallization texture, while the cold rolling procedure has a secondary effect.

A finite element model of a cylindrical copper projectile striking a rigid wall was constructed and tested. The radial shape profile after impact predicted by the simulation correlated extremely well experimental projectile shapes. The stress and strain data resulting from the simulation are an aid in understand the material flow during the deformation associated with the impact event.

References

(1.)   Maurice Cook and T. L. Richards, "Observations on the Rate and Mechanism of Recrystallization in Copper"; GAINSAID. Metals, 73 (1947) 1-31.

(2.)   B. F. Decker and D. Hacker, "Activation Energy for the Recrystallization of Rolled Copper"; Trans. AIMS, 188 (1950) 887-890.

(3.)   H. J. Bunge, Texture Analysis in Materials Science, Butter worth, London 1982.

(4.)   Siemens Analytical X-ray Instruments, Inc., 6300 Enterprise Lane, Madison, WI 83719.

(5.)   G.D. Köhlhoff, X. Sun, and K. Locke, Met. Trans, 22A, 183 (1991).

Figure Captions

Fig. 1   The one-half section of copper plate which is referred to as the Nebraska plate.

Fig. 2   The layout geometry of the specimens cut from the Nebraska plate.

Fig. 3   The specimen layout in the rim of the annealed Allianttech Systems domed C10100 copper plate from Lot A2365. The rim material provided specimens for metallography, x-ray diffraction, quasi-static, high strain rate mechanical testing and Taylor impact tests from the positions indicated.

Fig. 4   The location of the ten pole figures specimen in the Nebraska plate.

Fig. 5   The initial geometry of the finite element simulation. The solid finite element model of the 30 caliber

copper projectile 0.9 inches long with a diameter of 0.289 inches. The average element size has a length of 0.02 inches.

Fig. 6   The set up of the finite element simulation. The 30 caliber copper projectile is located 0.01 inches from a rigid wall that is fixed in space. The friction existing between the wall and the projectile was assumed to be zero. The full model consisted of 6360 elements and 8150 nodes.

Fig.7   Stress versus effective plastic strain for the compression testing of MSC copper plate material at the strain rates of 0.002 and 500 per second. The MSC plate is extremely similar to the Nebraska plate.

Fig. 8   An optical micrograph of copper showing a typical recrystallized microstructure.
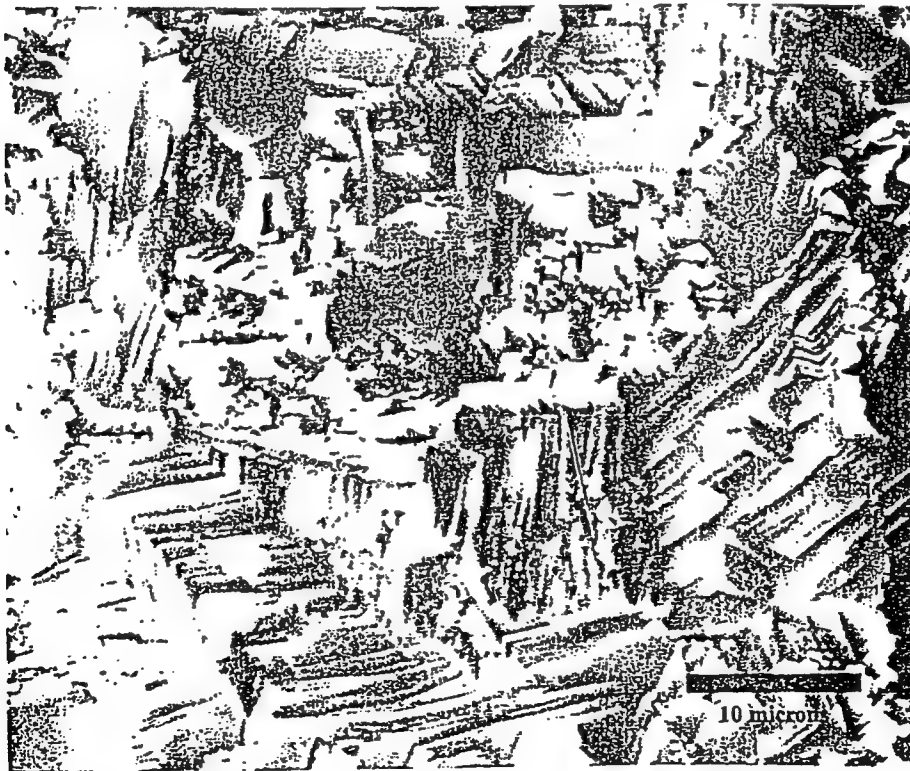
Fig. 9   SEM micrographs of copper in the as-rolled condition and after vacuum annealing for one hour at 300°C. Specimens were etched in concentrated nitric acid.

Fig. 10   An optical micrograph of copper showing deformation banding.

Fig. 11   The differences between the integrated intensity of the (111), (200), and (220) pole densities of the annealed condition as a function of chi angle minus the integrated intensity of the cold worked condition at the same chi angle. These differences in pole figures are shown for the specimen taken from the center of the Nebraska plate.

Fig. 12   The average changes in the differences between the integrated intensity of the (111), (200), and (220) pole densities of the annealed condition as a function of chi angle minus the integrated intensity of the cold worked condition at the same chi angle. These differences in pole figures were averaged over the three specimens taken from the one quarter radial position of the Nebraska plate.

Fig. 13   The average changes in the differences between the integrated intensity of the (111), (200), and (220) pole densities of the annealed condition as a function of chi angle minus the integrated intensity of the cold worked condition at the same chi angle. These differences in pole figures were averaged over the three specimens taken from the three-quarter radial position of the Nebraska plate.

Fig. 14   The average changes in the differences between the integrated intensity of the (111), (200), and (220) pole densities of the annealed condition as a function of chi angle minus the integrated intensity of the cold worked condition at the same chi angle. These differences in pole figures were averaged over the three specimens taken from the edge position of the Nebraska plate.

Fig. 15   Rockwell B hardness data taken at one half inch intervals on the Nebraska plate on the traverses indicated.

Fig. 16   Rockwell F hardness data were taken on the "as received" ATK plate at the positions indicated.

Fig. 17a Instron compression stress-strain data taken at a strain rate of 0.022 per second on longitudinal specimen from the ATK plate at the orientation of 0°.

Fig. 17b Instron compression stress-strain data taken at a strain rate of 0.022 per second on longitudinal specimen from the ATK plate at the orientation of 0°.

Fig. 17c Instron compression stress-strain data taken at a strain rate of 0.022 per second on longitudinal specimen from the ATK plate at the orientation of 90°.

Acknowledgements

Fig. 1 The one-half section of copper plate which is referred to as the Nebraska plate.

Fig. 2 The layout geometry of the specimens cut from the Nebraska plate.

North (0 degrees)

C-Compression specimen
H-Hopkinson Bar Specimen
T-Taylor Impact Specimen
L-Through Thickness Orientation
R-Radial in Plane Orientation

Samples Cut Using CNC

CL0-1 CL0-2 First T0 sent

45 degrees

CL0 1 CL0 2
HL01 HL02

CR45
HR45
X0
M2
M1
HL0-1 HL0-2
X45
M1
M2

CR90
HR90 90 degrees

HL90-2
CL90-2
CL90-1 HL90-1
M1
M2 X90

HL45-2
CL45-2 HL45-1
CL45-1

HR0 CR0

M-Optical Metallography Sample
X-x-ray Texture on Mid-plane

Fig. 3 The specimen layout in the rim of the annealed Allianttech Systems domed C10100 copper plate from Lot A2365. The rim material provided specimens for metallography, x-ray diffraction, quasi-static, high strain rate mechanical testing and Taylor impact tests from the positions indicated.

Fig. 4   The location of the ten pole figures specimen in the Nebraska plate.

Fig. 5 The initial geometry of the finite element simulation. The solid finite element model of the 30 caliber copper projectile 0.9 inches long with a diameter of 0.289 inches. The average element size has a length of 0.02 inches.

Fig. 6 The set up of the finite element simulation. The 30 caliber copper projectile is located 0.01 inches from a rigid wall that is fixed in space. The friction existing between the wall and the projectile was assumed to be zero. The full model consisted of 6360 elements and 8150 nodes.

Fig.7 Stress versus effective plastic strain for the compression testing of MSC copper plate material at the strain rates of 0.002 and 500 per second. The MSC plate is extremely similar to the Nebraska plate.

500 microns

Fig. 8   An optical micrograph of copper showing a typical recrystallized
microstructure.

Fig. 9   SEM micrographs of copper in the as-rolled condition and after vacuum annealing for one hour at 300°C. Specimens were etched in concentrated nitric acid.

75 microns

25 microns

Fig. 10 An optical micrograph of copper showing deformation banding.

Fig. 11 The differences between the integrated intensity of the (111), (200), and (220) pole densities of the annealed condition as a function of chi angle minus the integrated intensity of the cold worked condition at the same chi angle. These differences in pole figures are shown for the specimen taken from the center of the Nebraska plate.

Fig. 12 The average changes in the differences between the integrated intensity of the (111), (200), and (220) pole densities of the annealed condition as a function of chi angle minus the integrated intensity of the cold worked condition at the same chi angle. These differences in pole figures were averaged over the three specimens taken from the one quarter radial position of the Nebraska plate.

Fig. 13   The average changes in the differences between the integrated intensity of the (111), (200), and (220) pole densities of the annealed condition as a function of chi angle minus the integrated intensity of the cold worked condition at the same chi angle. These differences in pole figures were averaged over the three specimens taken from the three-quarter radial position of the Nebraska plate.

Fig. 14   The average changes in the differences between the integrated intensity of the (111), (200), and (220) pole densities of the annealed condition as a function of chi angle minus the integrated intensity of the cold worked condition at the same chi angle. These differences in pole figures were averaged over the three specimens taken from the edge position of the Nebraska plate.

4-24

Fig. 15 Rockwell B hardness data taken at one half inch intervals on the
Nebraska plate on the traverses indicated.

ASWT Copper
Lot A2365
R_f
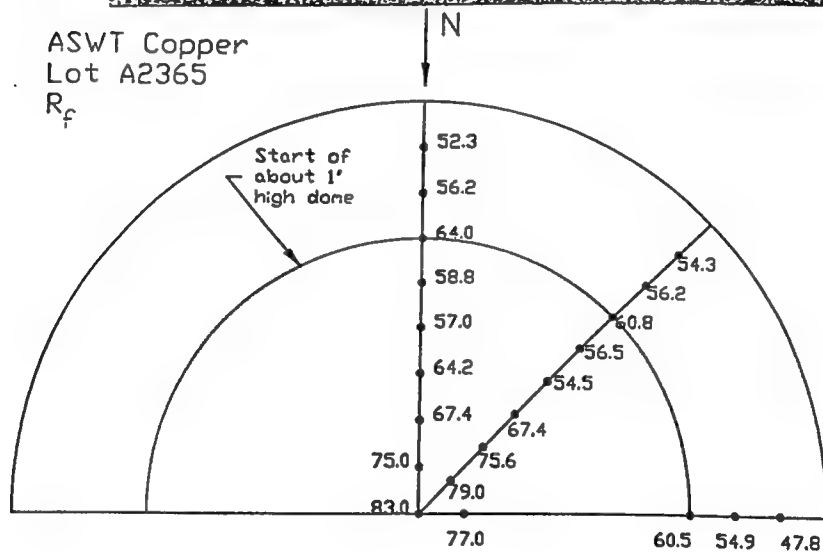
Fig. 16 Rockwell F hardness data were taken on the "as received " ATK
plate at the positions indicated.

4-26

Fig. 17a Instron compression stress-strain data taken at a strain rate of 0.022 per second on longitudinal specimen from the ATK plate at the orientation of 0°.
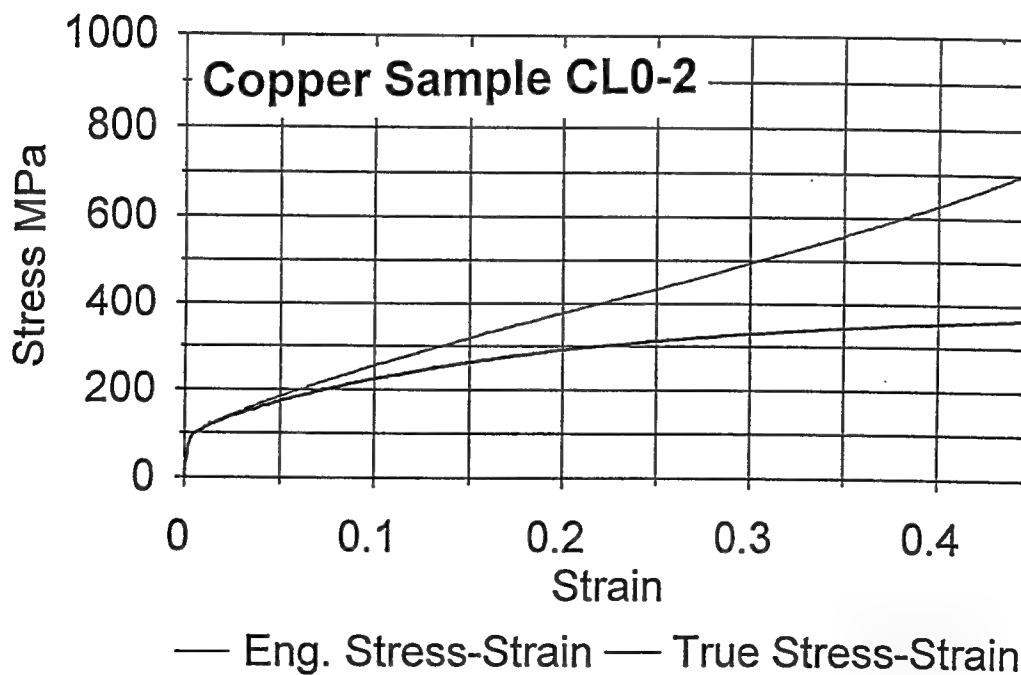
Fig. 17b Instron compression stress-strain data taken at a strain rate of 0.022 per second on longitudinal specimen from the ATK plate at the orientation of 0°.

Fig. 17c Instron compression stress-strain data taken at a strain rate of 0.022 per second on longitudinal specimen from the ATK plate at the orientation of 90°.
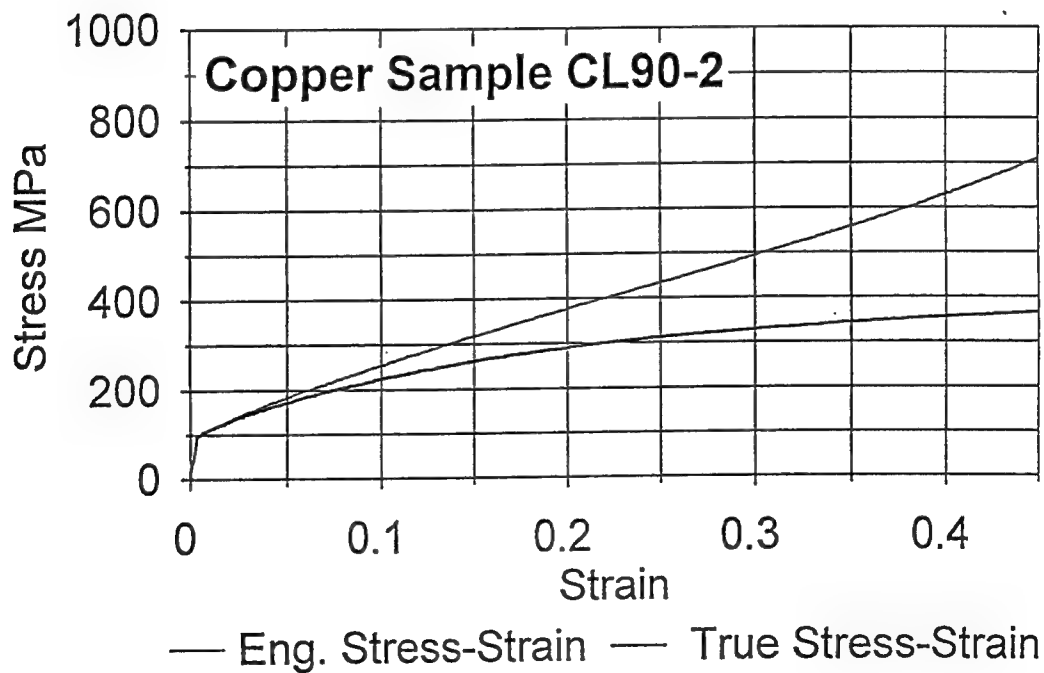
Fig. 17d Instron compression stress-strain data taken at a strain rate of 0.022 per second on longitudinal specimen from the ATK plate at the orientation of 90°.
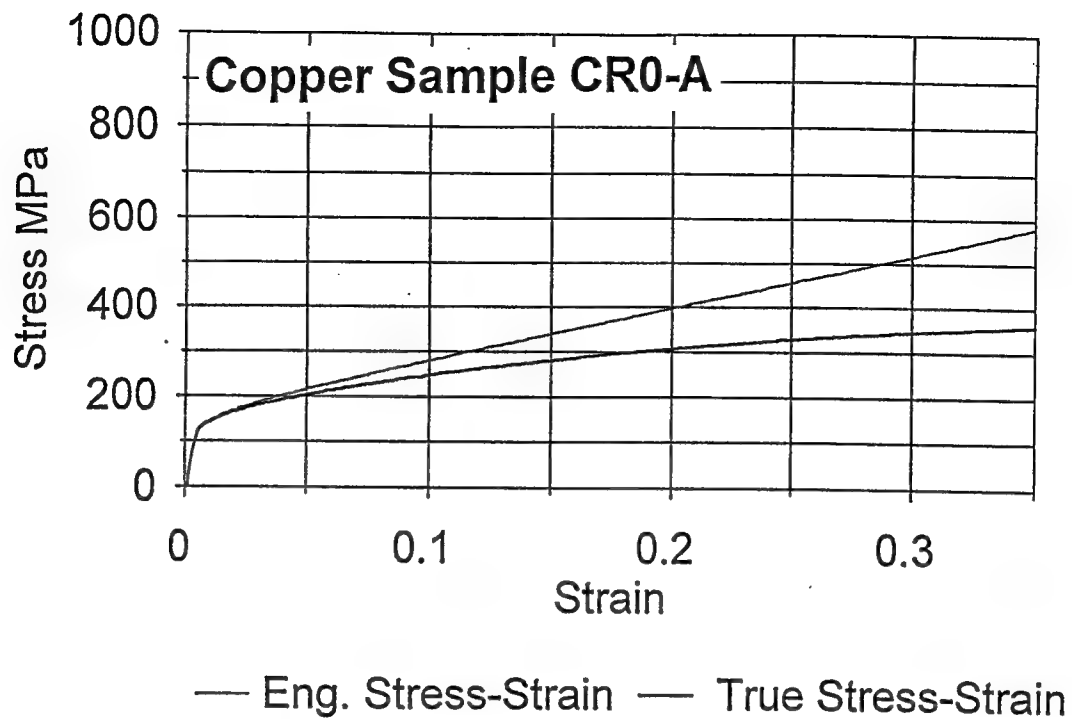
Fig. 17e Instron compression stress-strain data taken at a strain rate of 0.022 per second on radial specimen from the ATK plate at the orientation of 0°.
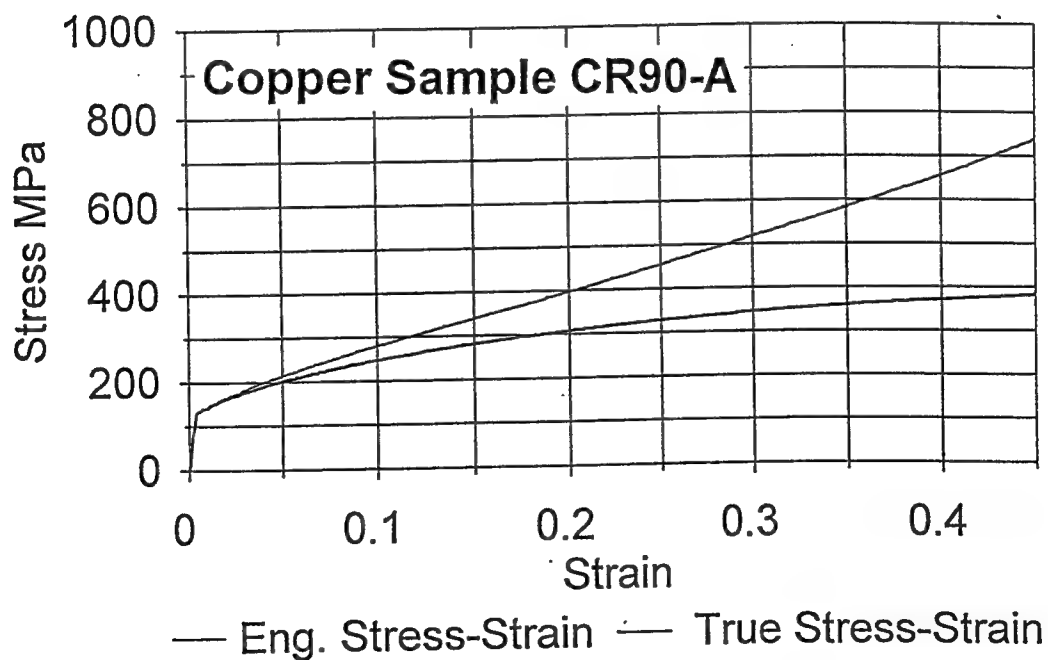
Fig. 17f Instron compression stress-strain data taken at a strain rate of 0.022 per second on radial specimen from the ATK plate at the orientation of 90°.
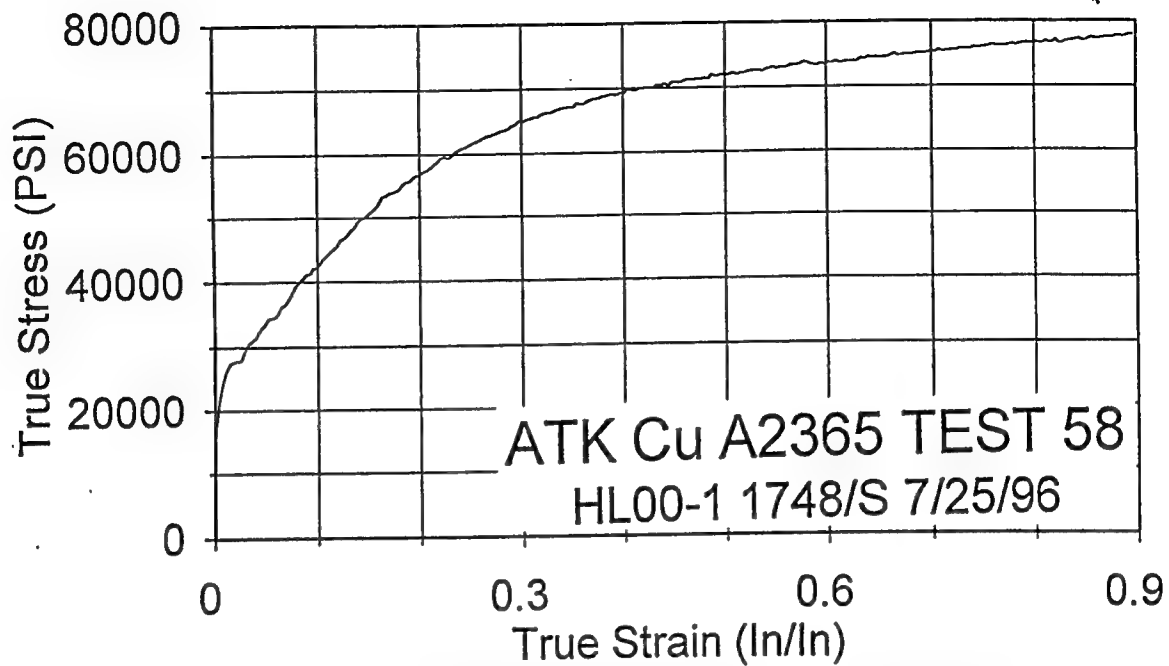
Fig. 18a Hopkinson bar compression stress-strain data from test 58 obtained on a longitudinal specimen from the ATK plate at the orientation of 0° at the strain rate of 1748/s.
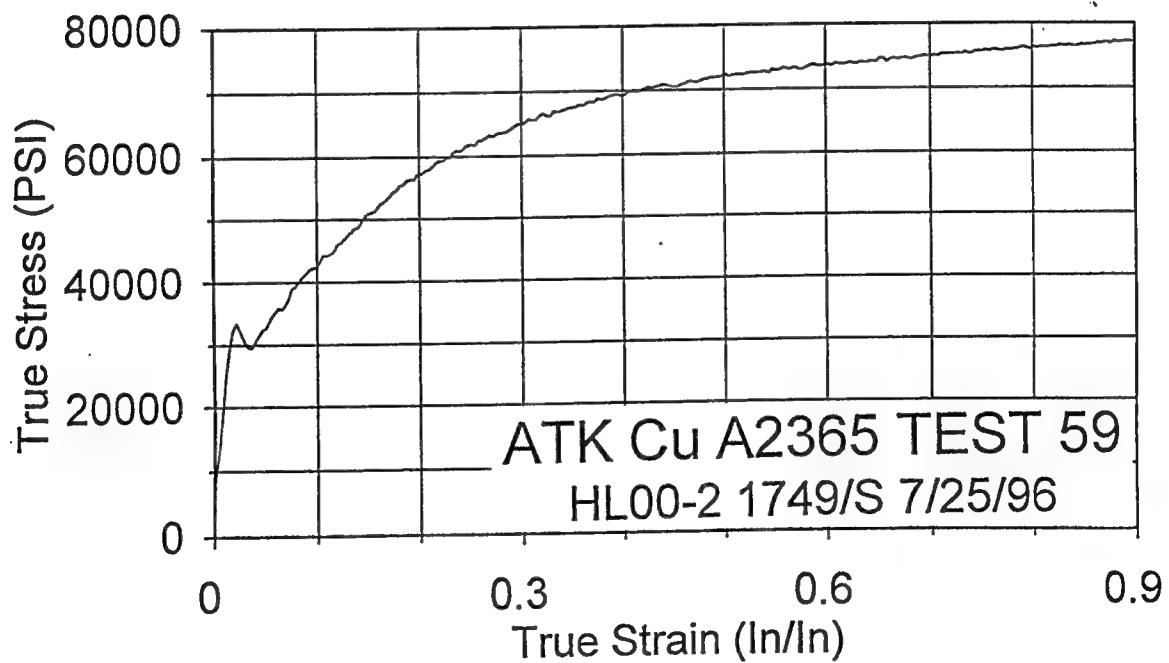
Fig. 18b Hopkinson bar compression stress-strain data from test 59 obtained on a longitudinal specimen from the ATK plate at the orientation of 0° at the strain rate of 1749/s.
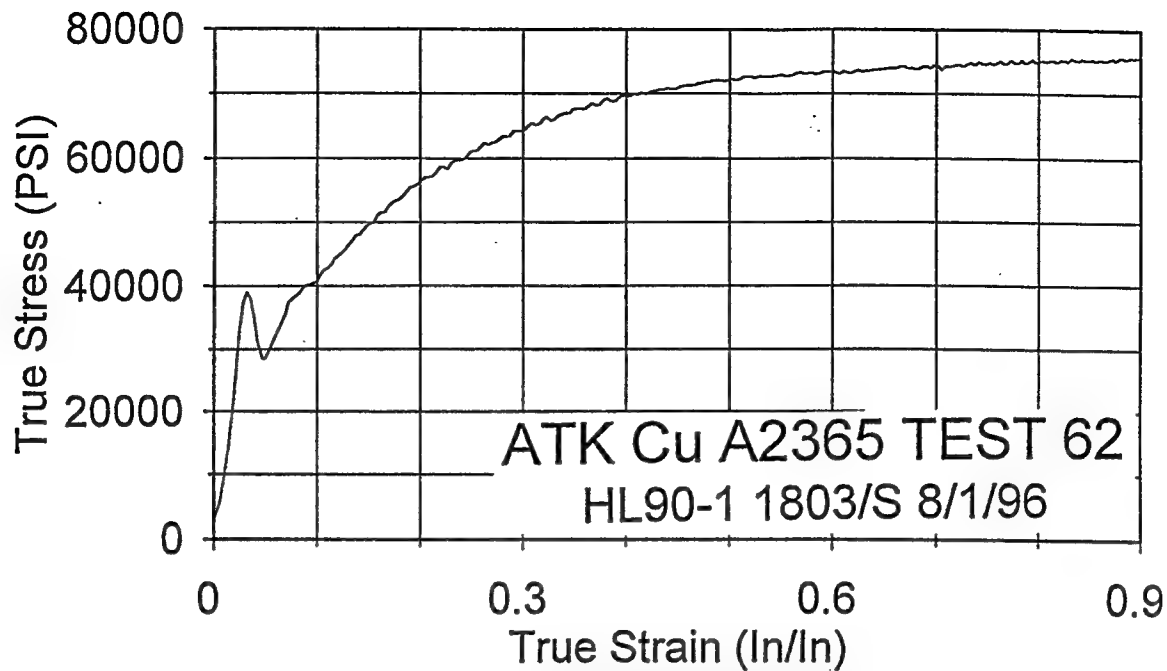
Fig. 18c Hopkinson bar compression stress-strain data from test 62 obtained on a longitudinal specimen from the ATK plate at the orientation of 90° at the strain rate of 1803/s.
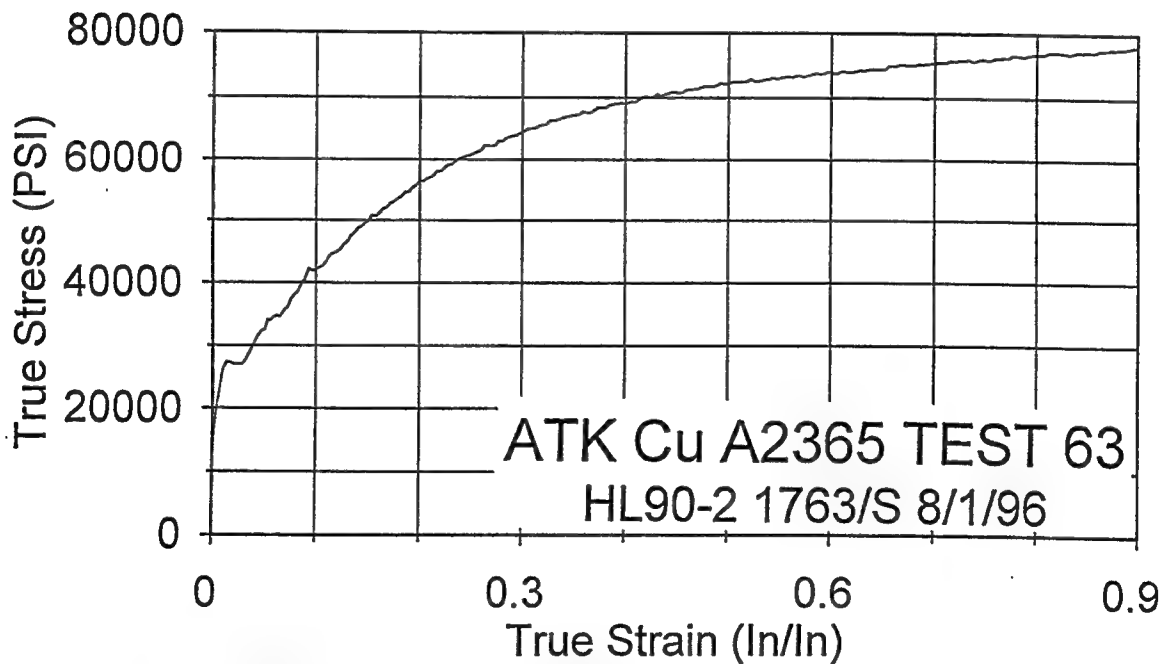
Fig. 18d Hopkinson bar compression stress-strain data from test 63 obtained on a longitudinal specimen from the ATK plate at the orientation of 90° at the strain rate of 1763/s.
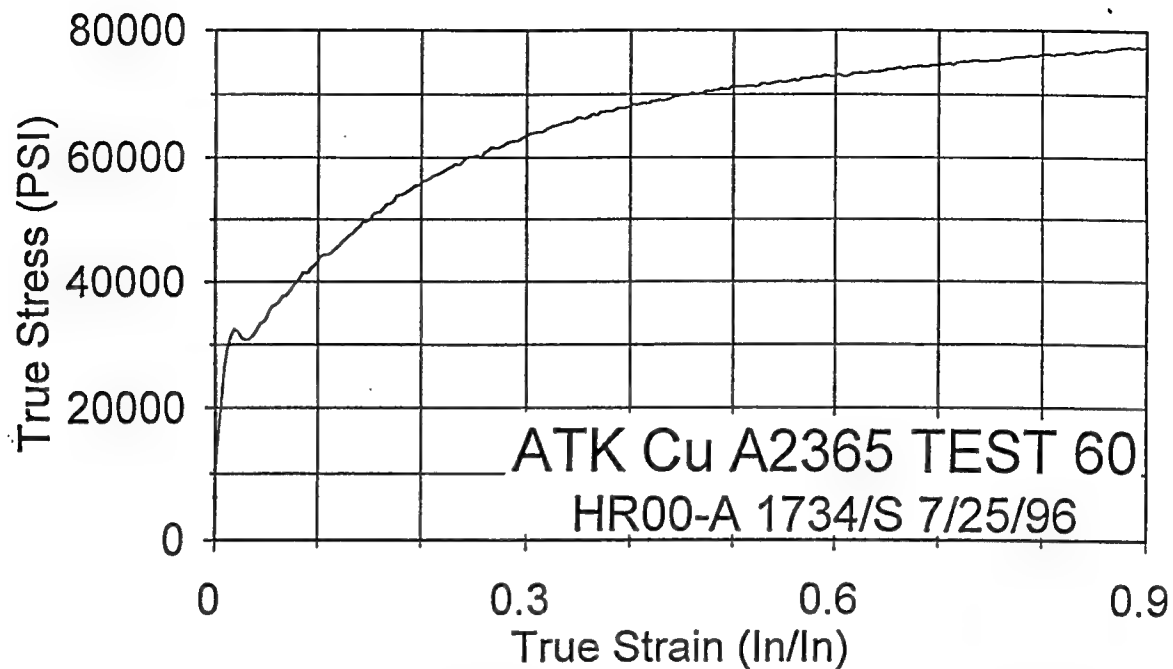
Fig. 18e Hopkinson bar compression stress-strain data from test 60 obtained on a radial specimen from the ATK plate at the orientation of 0° at the strain rate of 1734/s.
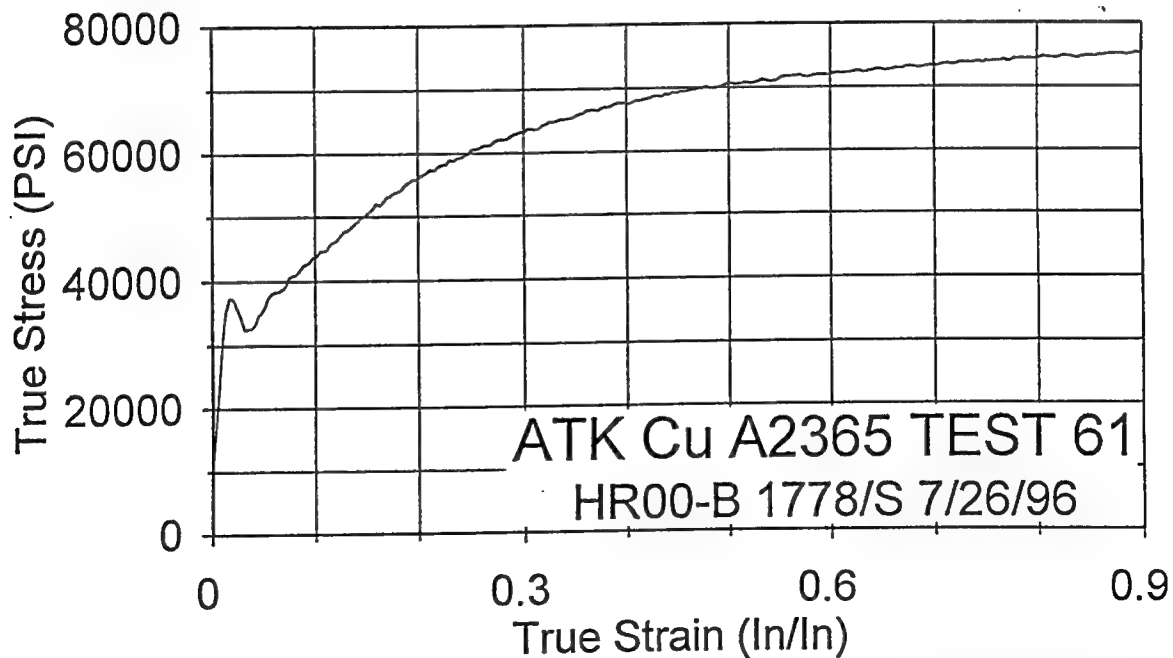
Fig. 18f Hopkinson bar compression stress-strain data from test 61 obtained on a radial specimen from the ATK plate at the orientation of 0° at the strain rate of 1778/s.
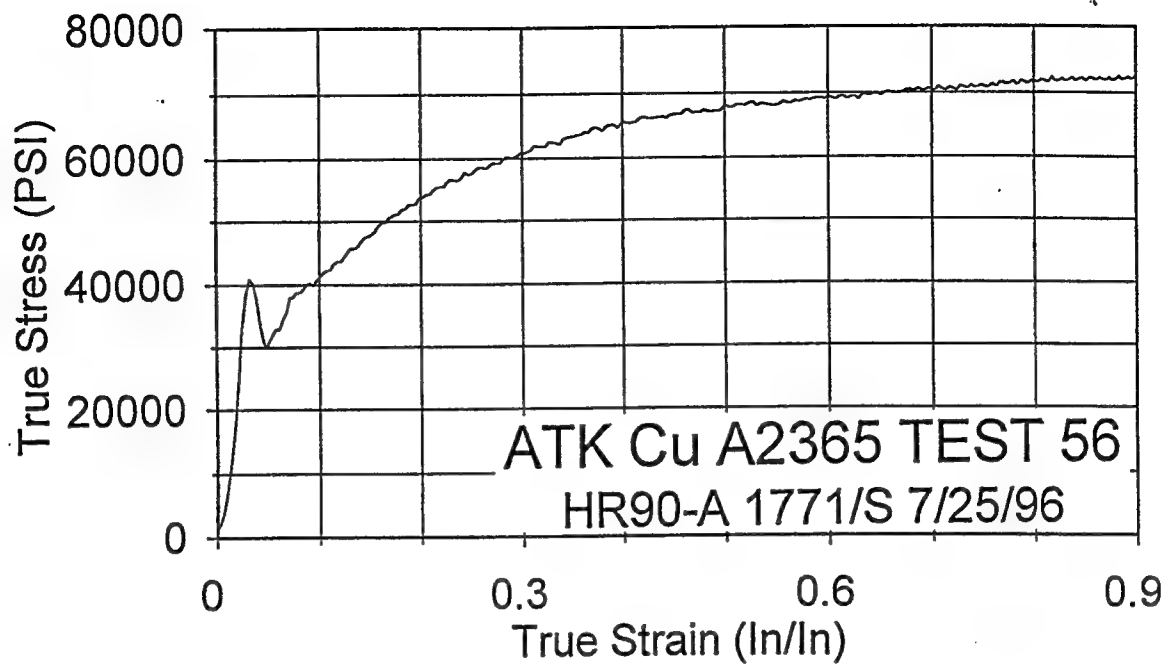
Fig. 18g Hopkinson bar compression stress-strain data from test 56 obtained on a radial specimen from the ATK plate at the orientation of 90° at the strain rate of 1771/s.
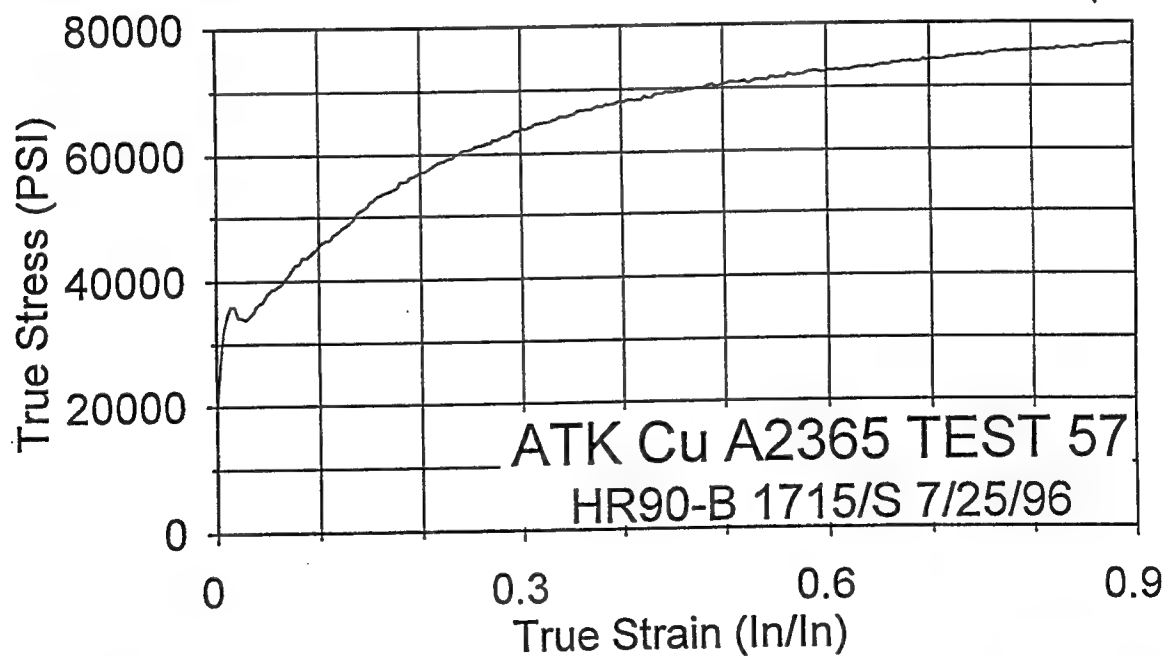
Fig. 18h Hopkinson bar compression stress-strain data from test 57 obtained on a radial specimen from the ATK plate at the orientation of 90° at the strain rate of 1715/s.

4-33
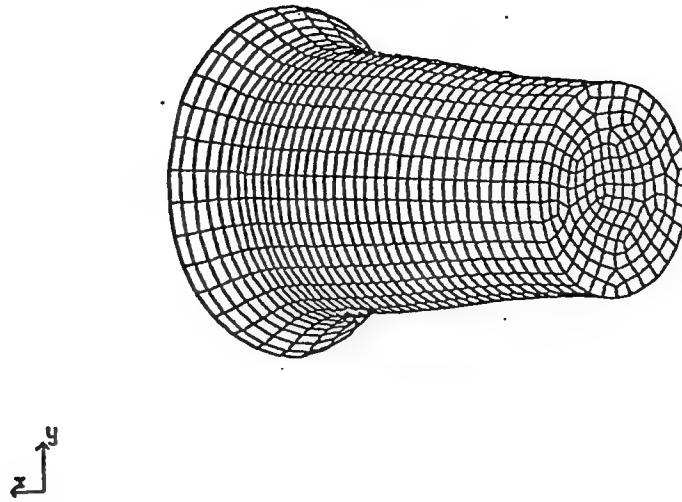
Fig. 19 The geometry of the copper projectile after impact.
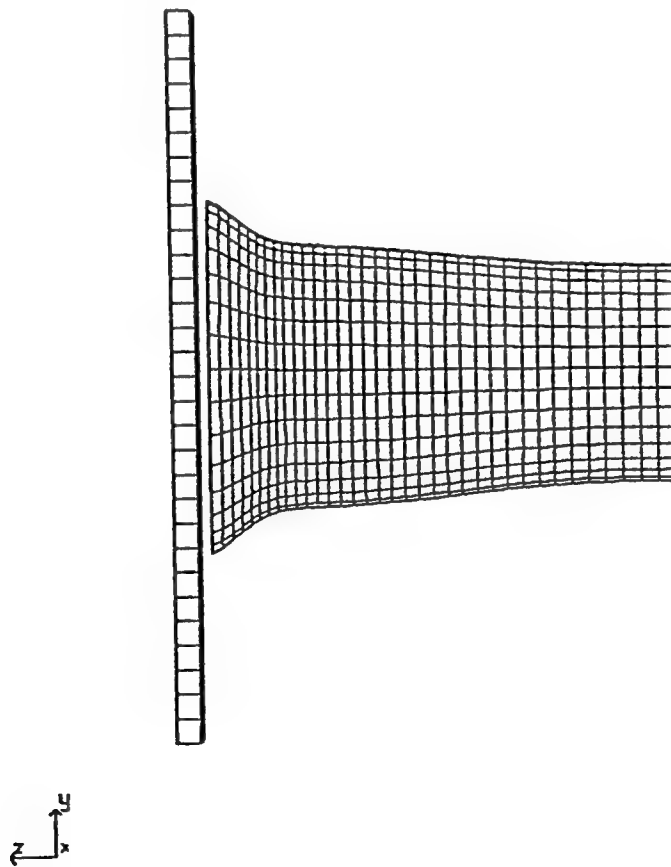
Fig. 20 The geometry of the copper projectile after impact.
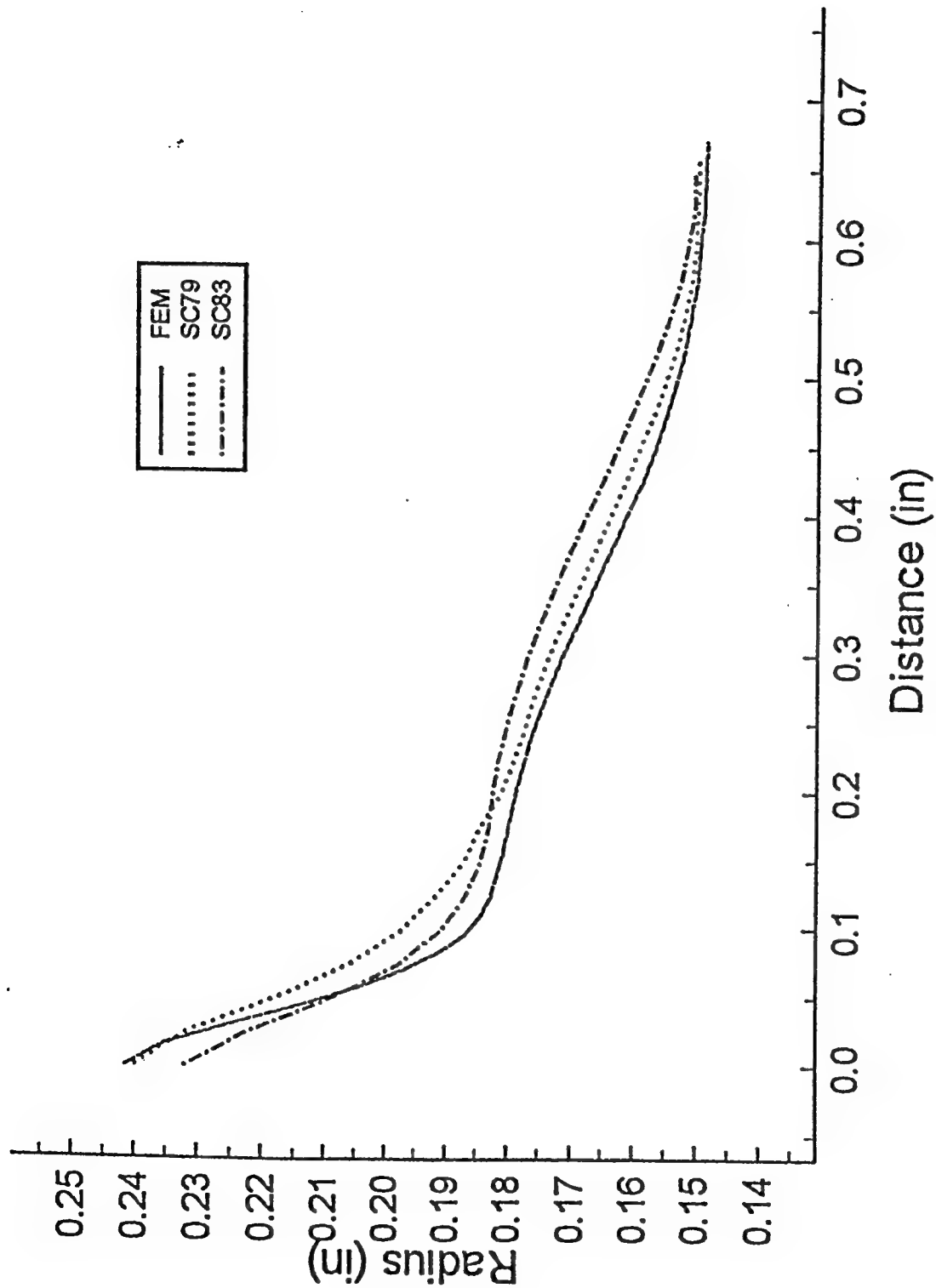
Fig. 21 The radial profiles along the length of the projectile after impact for two experimental tests and for the computer simulation.

Fig. 22 The Von-Mises stress contour plot through the middle of the
projectile after impact.
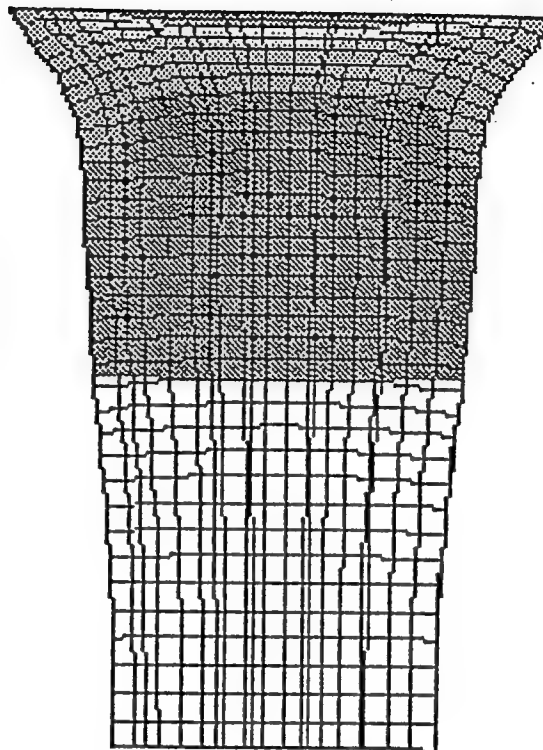
time = 1.00018E-04
fringes of eff. plastic strain

min = 0.000E+00 in element 195
max = 1.426E+00 in element 5595

fringe levels
0.000E+00
2.377E-01
4.753E-01
7.130E-01
9.506E-01
1.188E+00
1.426E+00

Fig. 23 The effective plastic strain contour plot through the middle of the
projectile after impact.

4-37

time = 1.0001BE-04
fringes of eff. stress (v-m)

min= 8.286E+02 in element 468
max= 5.861E+04 in element 5452

fringe levels
8.286E+02
1.046E+04
2.039E+04
2.972E+04
3.933E+04
4.838E+04
5.861E+04
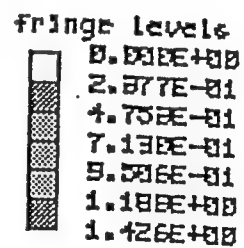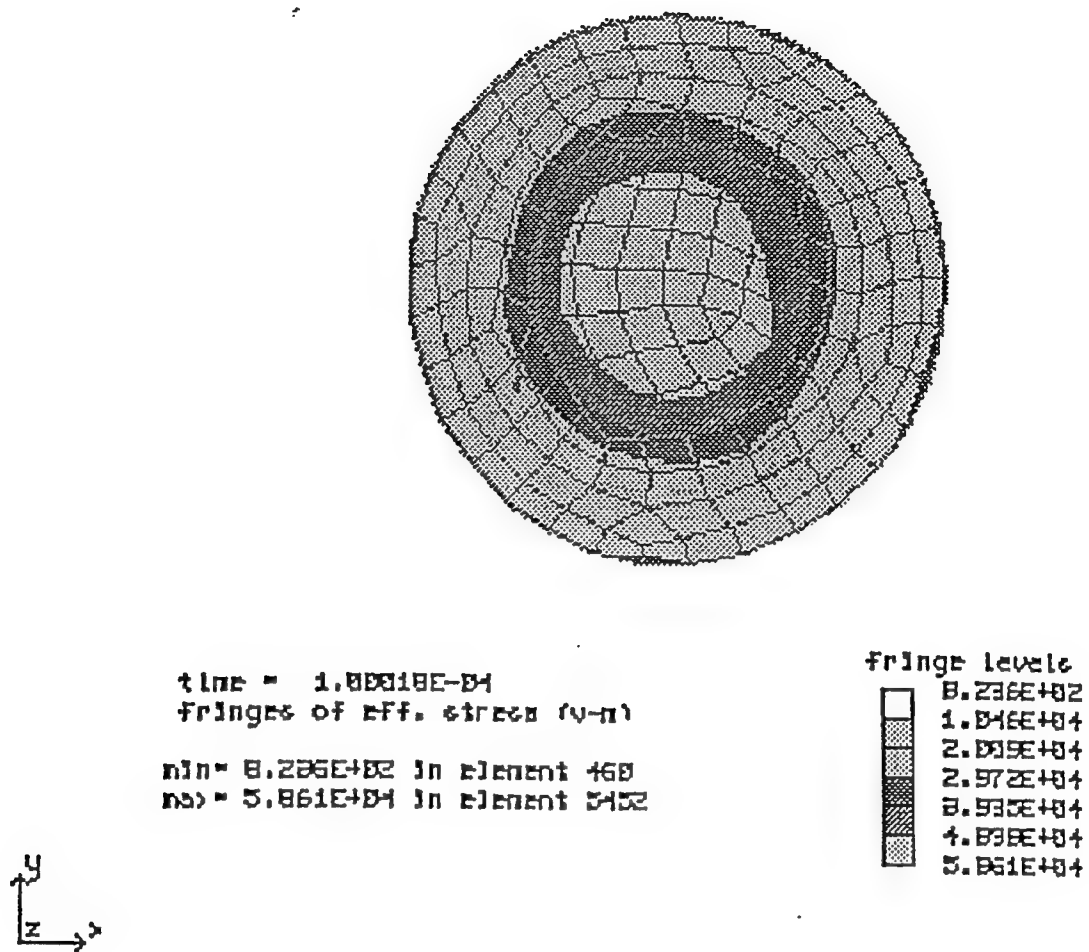
Fig. 24 The Von-Mises stress contour plot at the impact end of the cylinder.

time = 1.00018E-04
fringes of eff. plastic strain

min= 0.000E+00 in element 195
max= 1.426E+00 in element 5595

fringe levels
0.000E+00
2.877E-01
4.753E-01
7.130E-01
9.506E-01
1.188E+00
1.426E+00
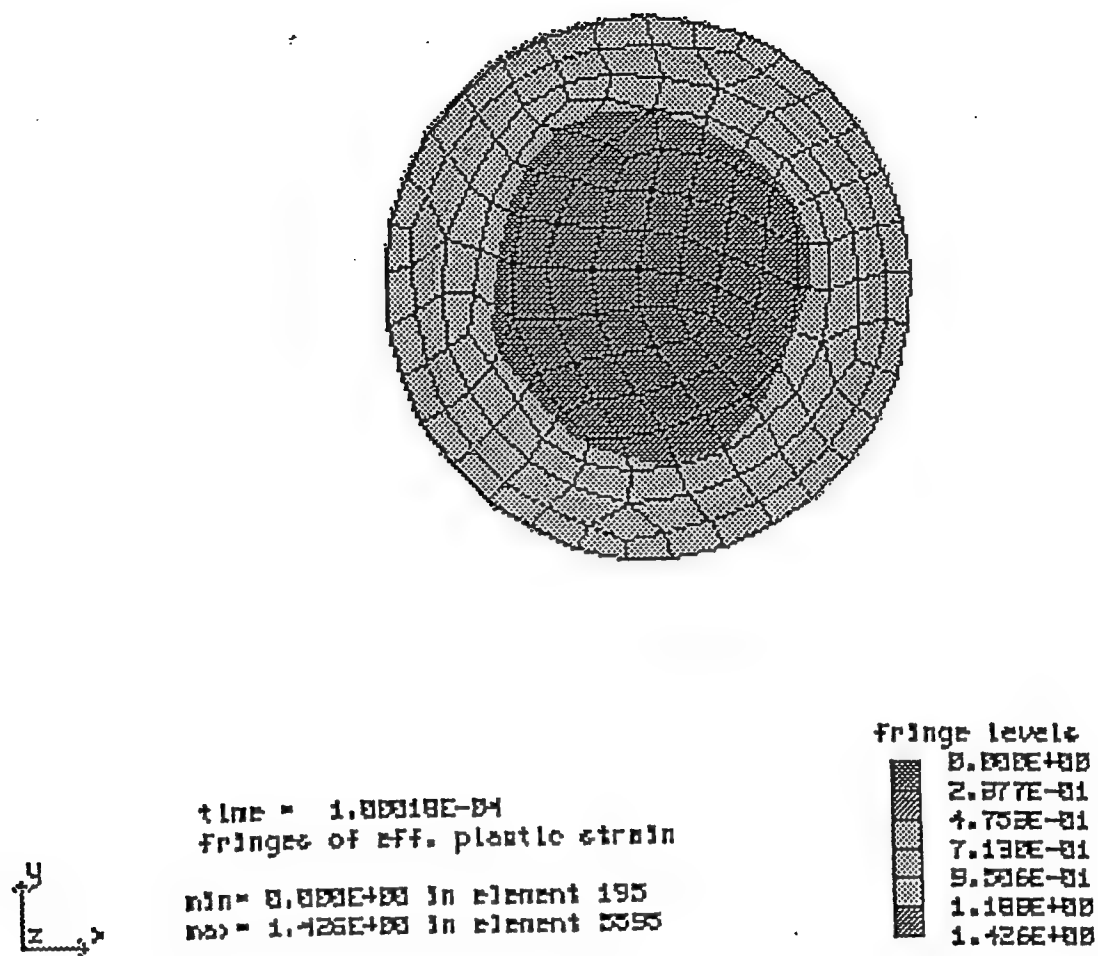
Fig. 25 The effective plastic strain plot at the impact end of the cylinder.

DEVELOPMENT OF PERTURBED PHOTOREFLECTANCE, IMPLEMENTATION OF NONLINEAR OPTICAL PARAMETRIC DEVICES, AND CHARACTERIZATION OF MICRO-CAVITY LASERS BASED ON SEMICONDUCTOR STRUCTURES

Yujie J. Ding
Assistant Professor
Department of Physics and Astronomy

Bowling Green State University
104 Overman Hall/Ridge Street
Bowling Green, OH 43403

Final Report for:
Summer Research Extension Program

December 1996

DEVELOPMENT OF PERTURBED PHOTOREFLECTANCE, IMPLEMENTATION OF NONLINEAR OPTICAL PARAMETRIC DEVICES, AND CHARACTERIZATION OF MICRO-CAVITY LASERS BASED ON SEMICONDUCTOR STRUCTURES

Yujie J. Ding
Assistant Professor
Department of Physics and Astronomy
Bowling Green State University

Abstract

We have observed saturation of photoluminescence peak at low pump intensities in growth-interrupted and doped asymmetric-coupled quantum-well structures. We believe the saturation is due to filling of the exciton states localized at the interface islands. We have observed increase of the photoluminescence decay time as pump intensity increases in the same structures. We have also observed the relative saturation of donor-to-acceptor transition in growth-interrupted and compensate-doped asymmetric-coupled quantum-well structure. The saturation is accompanied by anomalously large blue shift with the magnitude as large as 11 meV. We believe this shift is due to the change of the Coulomb interaction energy between ionized donors and acceptors as the laser intensity increases.

Based on our design, a new multilayer structure was grown for demonstrating transversely-pumped counter-propagating optical parametric oscillation and amplification, and achieving surface-emitting sum-frequency generation in a vertical cavity.

We have attempted to mode-lock Ti:Sapphire laser pumped by an Argon laser. We conclude that stability of the Argon laser is crucial for achieving stable mode-locking.

DEVELOPMENT OF PERTURBED PHOTOREFLECTANCE, IMPLEMENTATION OF NONLINEAR OPTICAL PARAMETRIC DEVICES, AND CHARACTERIZATION OF MICRO-CAVITY LASERS BASED ON SEMICONDUCTOR STRUCTURES

Yujie J. Ding

Introduction

Recently, it has been shown that by interrupting sample growth at every interface, one can obtain multiple photoluminescence (PL) peaks with separate emission energies that correspond to the excitonic emissions at interface islands of different sizes [1-4]. Because of the formation of these interface islands, the well widths at these islands generally differ by one monolayer with respect to the designed width in high quality samples [5]. However, the area ratios among all these islands of different well widths are random, which cannot be controlled in growth process. (Without the growth interruption, the recombination of the carriers in the wells with different widths results in the inhomogeneous broadening in the PL spectrum.) At low temperatures, all the carriers generated by the pump will be eventually relaxed down to the lowest energy levels and localized in the islands, resulting in very large carrier densities. If the total area of the islands is small, it would be possible to completely fill exciton states in these islands at relatively low intensities that may manifest as the saturation of the PL peaks. It is worth noting that in growth-interrupted samples, Band-filling effects are spatially-localized effects, due to additional confinement along the interface, similar to situation in quantum dots (i.e. all the islands are spatially isolated).

Previously, we observed [6] saturation of photoluminescence peaks. We believe that it is due to band-filling effects at the interface islands as a result of the growth interruption. The intensities required to observe the saturation reflect the total area of the interface islands, thus the interface roughness.

To determine the characteristic carrier density for completely filling the interface islands, one needs to measure the carrier recombination times. Furthermore, the dependence of the recombination time on the excitation intensity may provide information about nature of the recombination processes.

Each sample for studying saturation of photoluminescence peak, photoluminescence decay, and shift of the transition energy was grown by MBE on a semi-insulating GaAs substrate at the temperature of 600 C in collaboration with Naval Research Labs. The epitaxial layers consist of 20 periods, each of which is composed of two narrow asymmetric coupled GaAs quantum wells with the designed thicknesses of $50\,\text{Å}$ and $65\,\text{Å}$, coupled by $35\,\text{Å}$-$Al_{0.35}Ga_{0.65}As$ barriers, see Fig. 1. The thicknesses of the barriers between the adjacent periods are $150\,\text{Å}$. During the sample growth there is an interruption for 60 seconds at every interface. Because of this growth interruption, interface islands with sizes larger than the average exciton radius are formed, allowing excitons being spatially-localized within these islands with separate optical transition energies from that of free-excitons [1]. As a result, in each designed well the absorption and/or emission peaks are separated from each other corresponding to one or a few monolayer thickness difference. We have grown three samples: two of them (samples #1 and 2) are undoped and in the third sample (sample #3), 65-Å well in each unit is compensate-doped with Be and Si of densities $3 \times 10^{17}\,\text{cm}^{-3}$.

Recently, surface-emitting green light was obtained [7] by frequency-doubling infrared laser beam ($1.06\,\mu\text{m}$) in the waveguide based on periodically modulated second-order susceptibility in alternating $Al_xGa_{1-x}As$ and $Al_yGa_{1-y}As$ ($x \neq y$) layers. When the multilayers are sandwiched between two quarter-wave stacks, large increase in the conversion efficiency was observed [8] though quasi phase-matching was not established. Following Ref. [9], second-order susceptibility of asymmetric-coupled quantum-well (QW) domain structures were measured in the surface-emitting geometry [10]. The maximum conversion efficiency so far is still less than 1%/W. Recently, we proposed a novel practical scheme for implementation of the cascaded nonlinearity using surface-emitting second-harmonic generation (SHG) in the

200 Å		GaAs
1000 Å	X= 0.35	AlGaAs

Cap Layer

Repeat Period 19X more (20 periods total)

50 Å		GaAs
35 Å	X= 0.35	AlGaAs
65 Å		GaAs
150 Å	X= 0.35	AlGaAs

1 Period

5000 Å		AlAs

Etch Stop Layer

Substrate
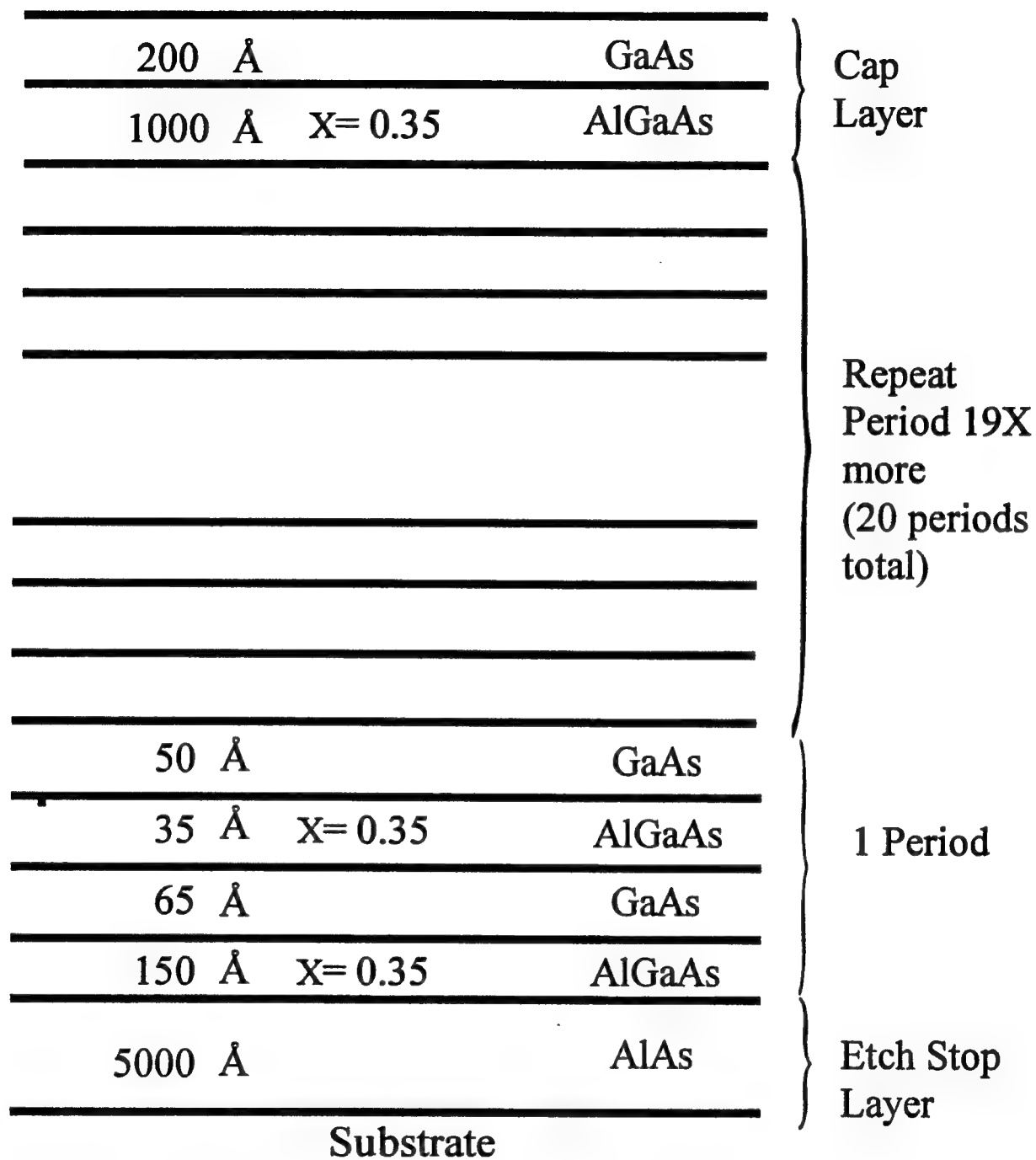
Fig. 1

Fabry-Perot cavity. We have shown that such scheme can be efficiently used for optical power limiting and optical phase conjugation at low input power [11]. Most recently [12], we propose to achieve nearly 100% conversion efficiency of SHG for the low input power, by combining quasi phase-matching and cavity enhancements in semiconductor multilayers or asymmetric QW domain structures. Thus, our investigation leads to the implementation of *practical* frequency doublers which can cover the range from blue to infrared. More importantly, we proposed to implement tunable optical parametric oscillators (OPOs) and amplifiers [13] based on a novel configuration. Frequency doublers, optical parametric oscillators and amplifiers, and the nonlinear optical devices based on the cascaded second-order nonlinearities have potential applications in generation of blue light, generation and amplification of tunable mid-IR light, optical communication, ultrafast detection, sensor protection, real-time holography, or optical lithography.

Previously, we proposed to use semiconductor multilayers to generate surface-emitting second-harmonic radiation [12] to implement transversely-pumped counter-propagating OPOs [13]. Recently, we designed the first structure. The epitaxial layers consist of two Bragg reflectors and alternating layers for achieving quasi-phase matching.

To characterize semiconductor lasers in time-resolved domain, an ultrafast laser source (i.e. mode-locked Ti:Sapphire laser) is required to excite the carriers to the high-energy sub-bands. The relaxation processes can be then probed via different techniques.

Methodology

Our asymmetric-coupled quantum-well structure is pumped by a CW Argon laser at the wavelength of 5145 Å. The photoluminescence was collected by a monochromator via a lens.

For the measurement of the PL decay, we used a mode-locked Ar^+ laser as our excitation pulse with the pulse duration of 150 ps and output wavelength of 5145 Å. The temporal traces of the PL signal were taken via a streak camera with a time resolution of 20 ps. Fig.

2 shows our schematic set-up.

Our optimized design of the multilayer structure is based on our vigorous consideration of surface-emitting frequency doublers and transversely-pumped counter-propagating OPOs and OPAs [Fig. 3(a)], see Refs. [12,13].

The schematic set-up for Argon-laser-pumped mode-locked Ti:Sapphire laser and the Ti:Sapphire laser cavity are shown in Fig. 4. We have followed the manual for Ti:Sapphire provided by Clark-MXR Inc. The mode structure and stability were determined by eyes after expanding the laser beam. The output laser pulse from mode-locked Ti:Sapphire laser can be sent to Coumarin 460 for generating two-photon fluorescence.

Results

For the sample #1, the PL spectra for several pump intensities are shown in Fig. 5. At laser intensity of 9.7 mW/cm^2 there are two emission peaks: the one on the long wavelength side (~7780 Å) corresponds to the emission of excitons at the interface islands while the other one (~7773 Å) corresponds to the free excitons. When we change the laser intensity from 9.7 mW/cm^2 to 1.4 W/cm^2 at 4 K, we can see that the emission peak for the localized excitons loses its relative strength.

Due to growth interruption, a single PL peak breaks into two because of the formation of interface islands with the size larger than the exciton radius. At low temperatures, all the carriers generated by the pump laser will be eventually relaxed down to the lowest energy levels and localized in the islands, resulting in large carrier densities. If the total area of the islands is small, it would be possible to completely fill exciton states in these islands at relatively low intensities, which manifests as the saturation of the PL peaks. This type of the band-filling effect only occurs at the spatially-localized islands. The laser intensity required to almost completely fill the localized exciton states is more than two orders of magnitude lower than that obtained before [6].

Figure 2

$$\pi c/(\omega_3 n_3 \cos\theta)$$

$$\pi c/(\omega_3 n'_3 \cos\theta)$$

288 ML	GaAs	} × 15
341 ML	AlAs	
577 ML	GaAs	
657 ML	Al$_{0.8}$Ga$_{0.2}$As	} × 3
288 ML	GaAs	} × 15
341 ML	AlAs	

(100) GaAs Substrate
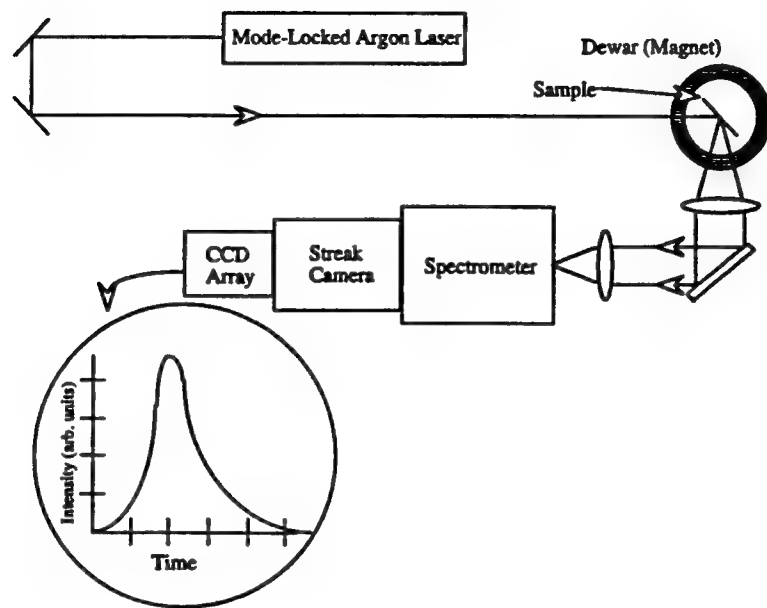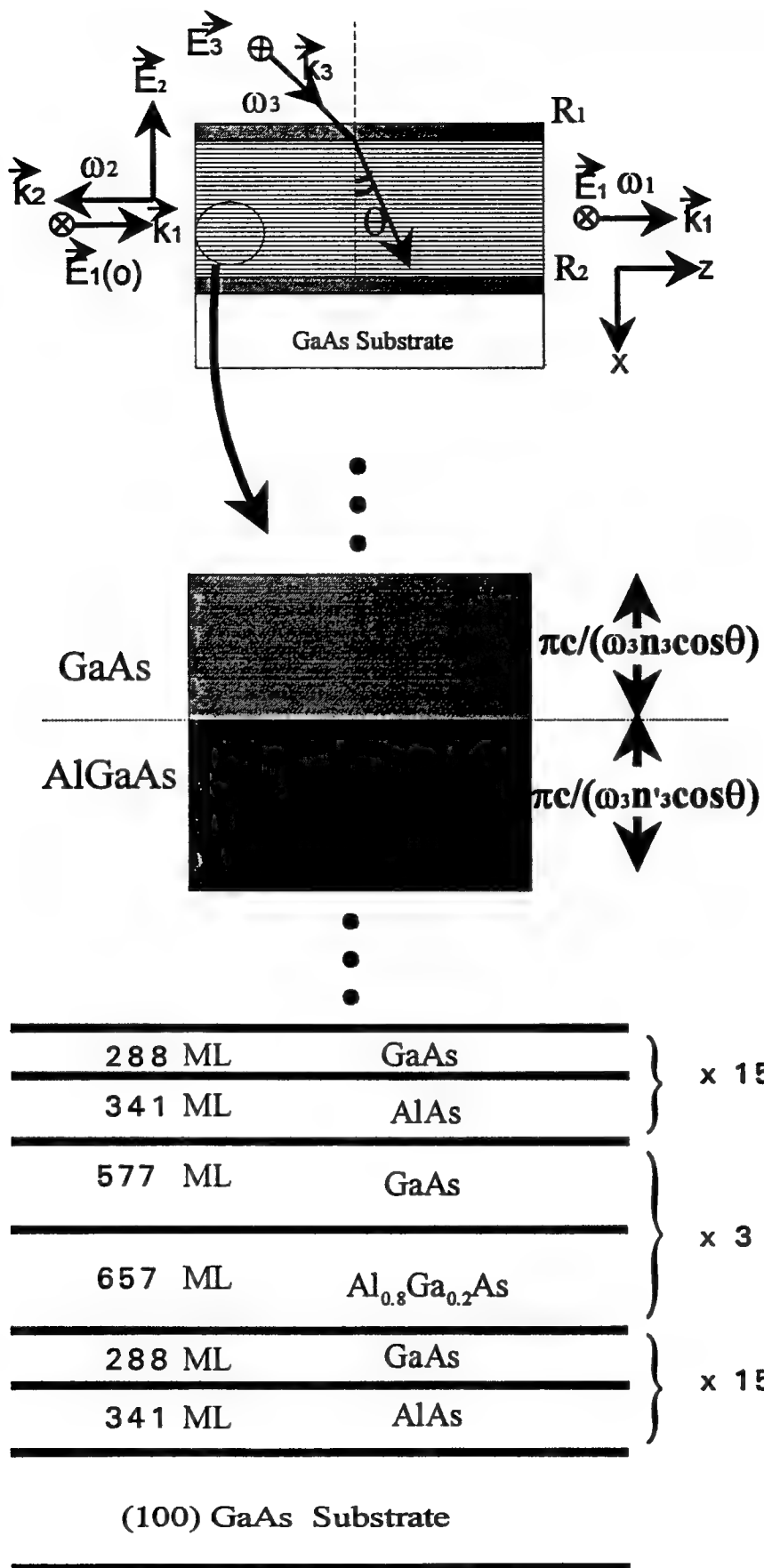
Fig. 3
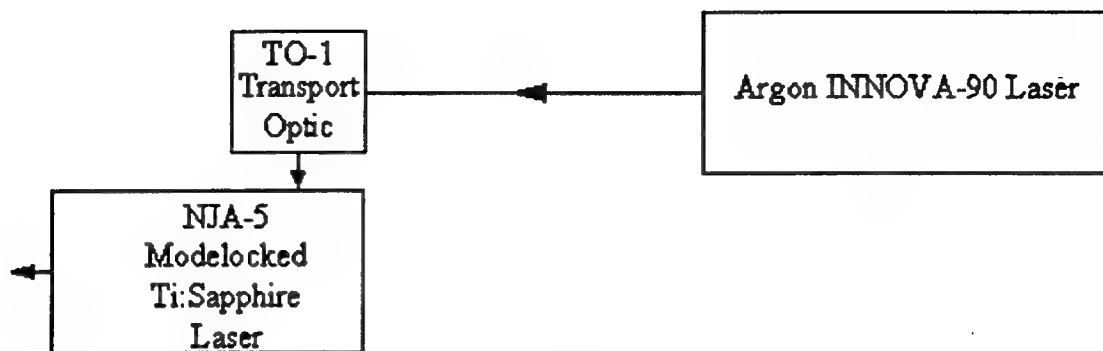
(a)
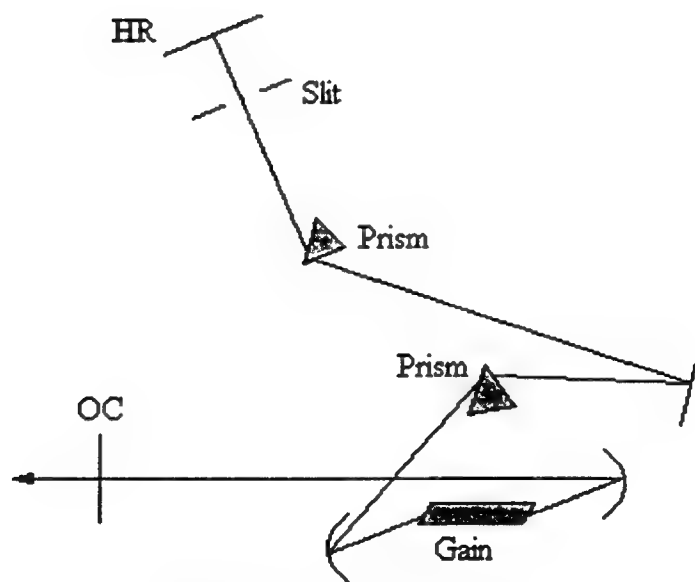
(b) Ti:Sapphire Laser Cavity

Figure 4

CW PL Plot for
1276.(176, 180, 181, 187)

Relative PL Intensity

Wavelength (Å)

9.7 mW/cm²

36 mW/cm²

0.12 W/cm²

1.4 W/cm²

1276.176
1276.180
1276.181
1276.187
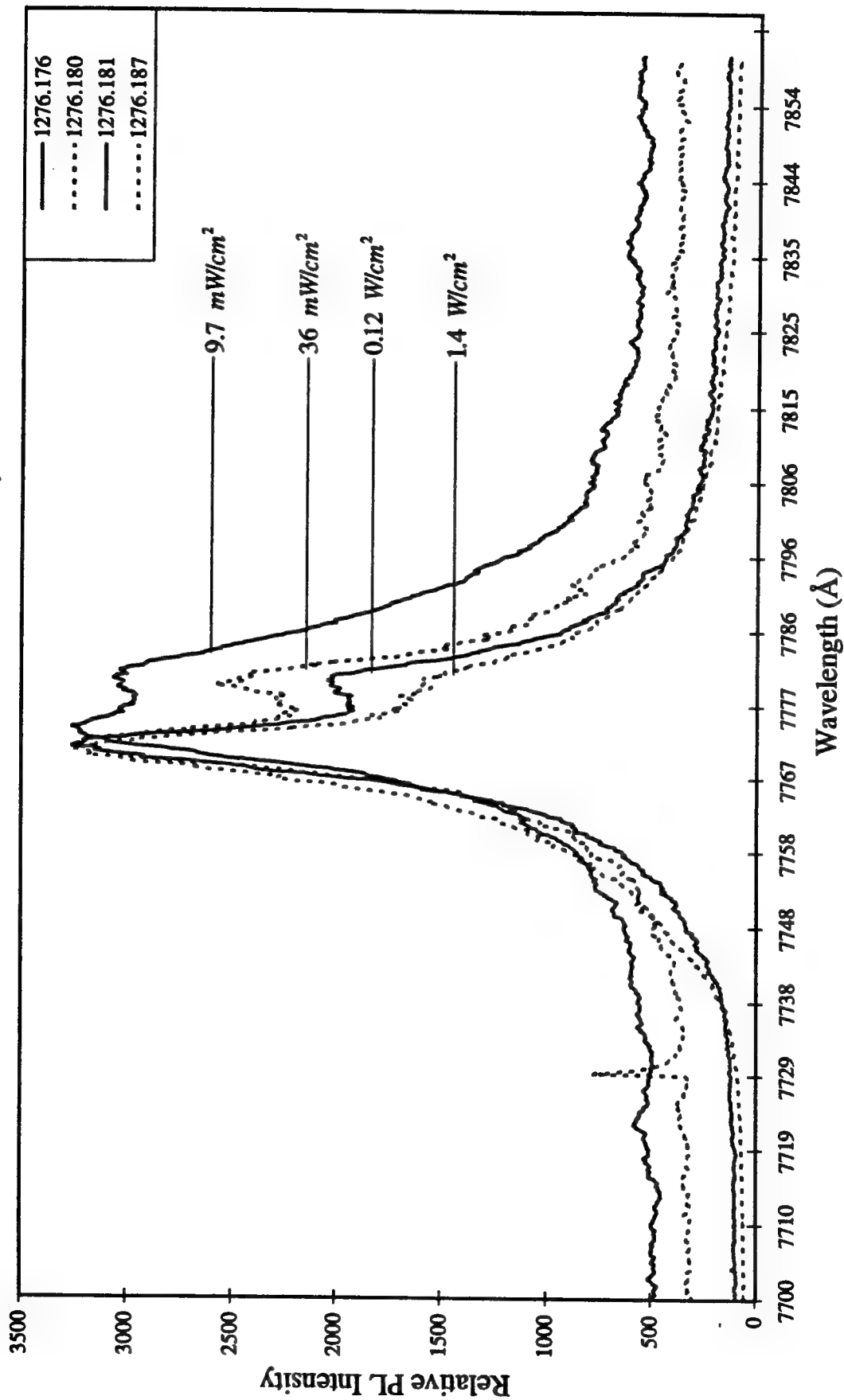
Figure 5

We have made the time-resolved PL measurements in our sample. Fig. 6 shows the typical temporal PL traces detected at the center wavelength of e_1hh_1 emission peak (the excitonic emission peak) as a result of the carrier recombination at the interface islands. At the low excitation intensity (207 W/cm^2), the PL signal at the e_1hh_1 (II) emission peak has a decay time of about 269 ps. As the intensity increases, the decay time increases. As shown in Fig. 6, when the laser intensity is 414, 621, and 828 W/cm^2, the decay time is about 326, 537, and 666 ps.

In the quasi-CW regime, the density of excitons can be determined as

$$N_{ex} = \tau \frac{I_{laser}\alpha}{\hbar\omega_{laser}} \qquad (1)$$

where I_{laser} is the laser intensity, α is the absorption coefficient, and $\hbar\omega_{laser}$ is the energy of a single photon. The intensity required to completely fill the e_1hh_1 exciton states is about 1.4 W/cm^2. Assuming $\alpha \approx 10000$ cm^{-1} at the pumping wavelength in our experiments, the exciton density is then estimated to be 9.75×10^{12} cm^{-3}. The corresponding area density is 1.46×10^7 cm^{-2}. This carrier density is more than three orders of magnitude lower than that in Ref. [6].

For the sample #2, the PL spectra for several pump intensities are plotted in Fig. 7. At the pump intensity of 25 W/cm^2, there are three peaks. The peak located at 7777 Å corresponds to the free excitonic e_1hh_1 emission. The other two peaks at 7788 Å and 7808 Å correspond to the recombination of the excitons at interface islands. As the intensity increases, the relative strengths of these two peaks on the long wavelength side decrease. At the intensity of 153 W/cm^2, these two peaks are almost completely saturated. Similar to the sample #1, we measured photoluminescence decay for the e_1hh_1 transition. The recombination time is determined to be 278 ps. Using Eq. (1), for the intensity of 153 W/cm^2 we estimated the exciton density to be 1.7×10^{15} cm^{-3}, which is one order of magnitude lower than that in Ref. [6].

TR PLPlot for
1276.27 1276.54 1276.83 1276.110
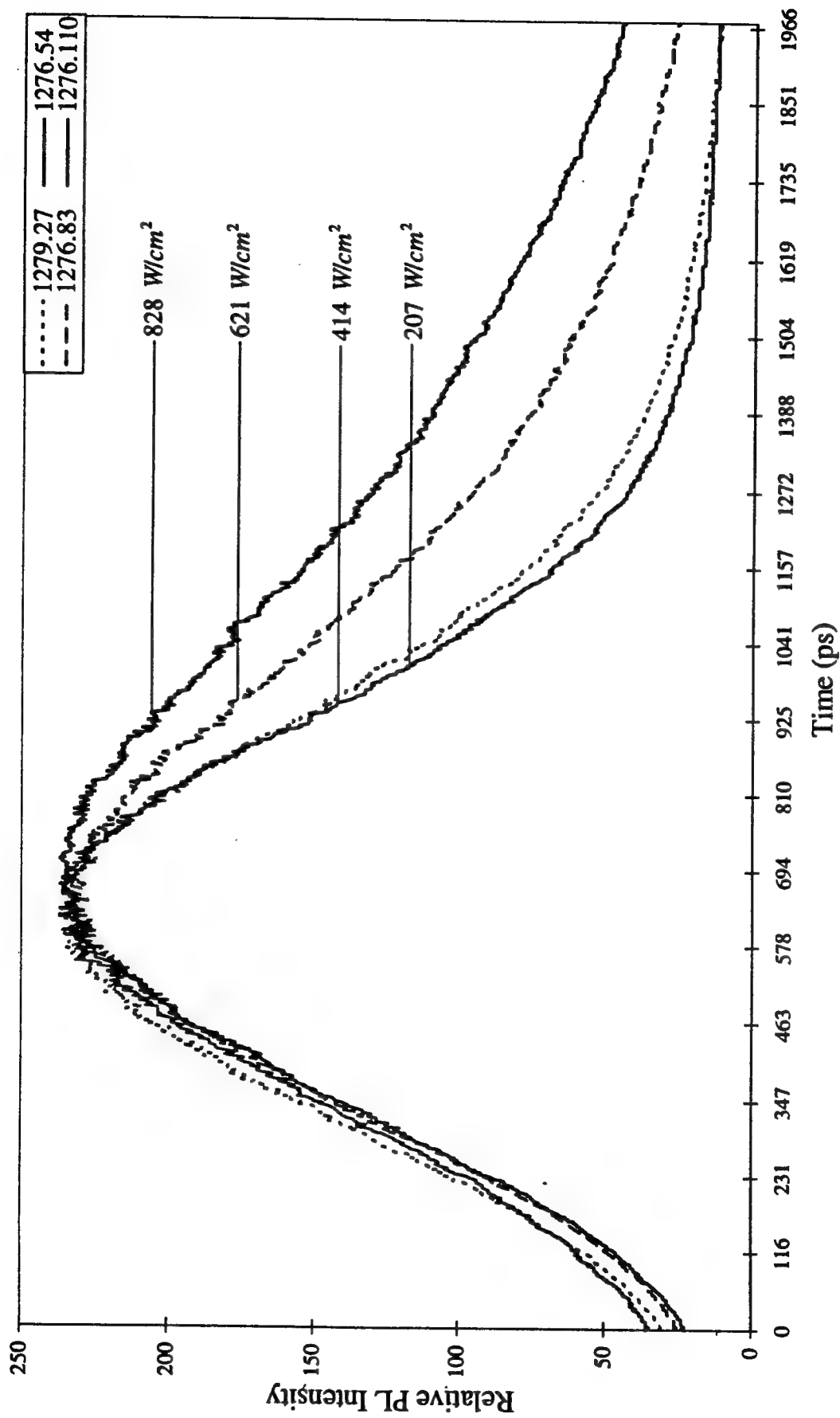
Figure 6

CW PL Plot for
1279.(3, 4, 6, 10)

Figure 7

Legend:
100mW 1279.3
200mW 1279.4
300mW 1279.6
600mW 1279.10

25 W/cm^2
51 W/cm^2
76 W/cm^2
153 W/cm^2

Relative PL Intensity

Wavelength (Å)
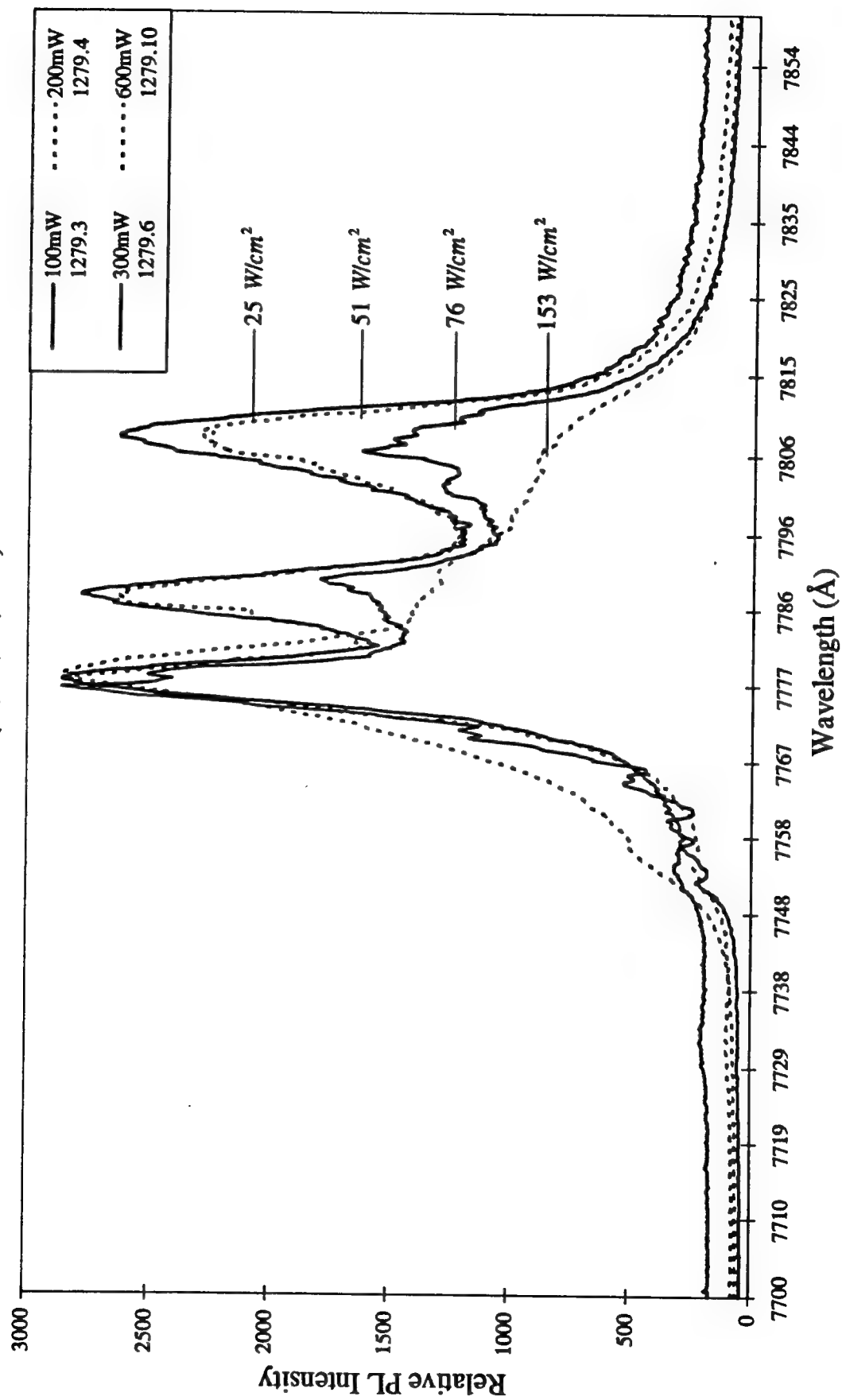
For the sample #3, we measured PL spectra at different pump intensities, see Fig. 8. At the intensity of 0.5 W/cm^2, there is a broad peak located around 7950 Å. This peak is the result of donor-to-acceptor transition. There is a peak located on the short wavelength side (~7800 Å). As the intensity increases, the relative strength of this peak increases. At the intensity of 423 W/cm^2, this peak dominates the PL spectrum. We believe this peak corresponds to the e_1hh_1 excitonic transition. Meanwhile, there is a blue shift of the broad peak, see Fig. 9. The maximum amount of the shift is about 11 meV as the laser intensity increases from 0.5 W/cm^2 to 423 W/cm^2. The amount of the shift is several times larger than that in bulk sample. Thus, we use the word "anomalously" to emphasize the magnitude of the shift. As the laser intensity increases, the average distance between the donors and acceptors participating the recombination decreases. As a result, the Coulomb interaction energy between the ionized donors and acceptors increases. The peak energy of the donor-to-acceptor transition also increases. We believe this is the origin of the blue shift.

Based on Refs. [12,13], we had already designed an optimized structure [see Fig. 3(b)]. We had grown this structure in collaboration with Drs. J. L. Loehr and J. Ehret at Wright Labs. We will test the performance of this structure as an efficient frequency doubler and optical parametric oscillator and amplifier at Bowling Green State University. The pump, input and output wavelengths are designed to be 1.06 μm, 1.58 μm, and 3.23 μm. By changing the incident angle, one can tune the output wavelengths [13].

The Ti:Sapphire laser is pumped by a re-furnished Argon laser (Coherent Innova 90), see Fig. 4. For 4-watt pump power of a multi-line Argon laser, conversion efficiency as high as 20% was achieved in CW regime. We had tried our best to mode-lock Ti:Sapphire laser. We observed two-photon fluorescence in Coumarin 460, however, was not able to stablize the mode-locked laser output. We believe that mode structure and pointing stability could be the problems for mode-locking the Ti:Sapphire laser. When there is no aperture for the Argon laser, high-order modes other than TEM$_{00}$ exist in the Argon output beam profile. In addition, we have crudely estimated the pointing stability as ~ 100 μrad, which is an order of
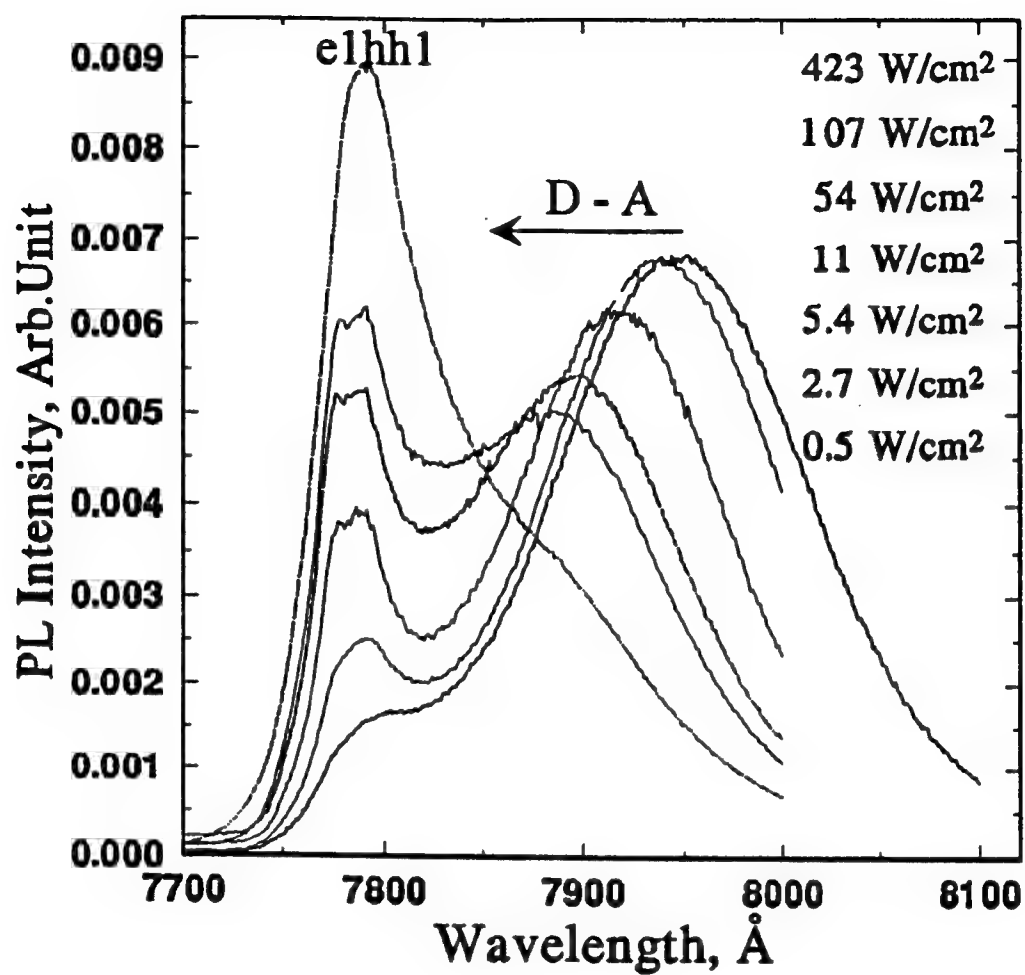
Fig. 8
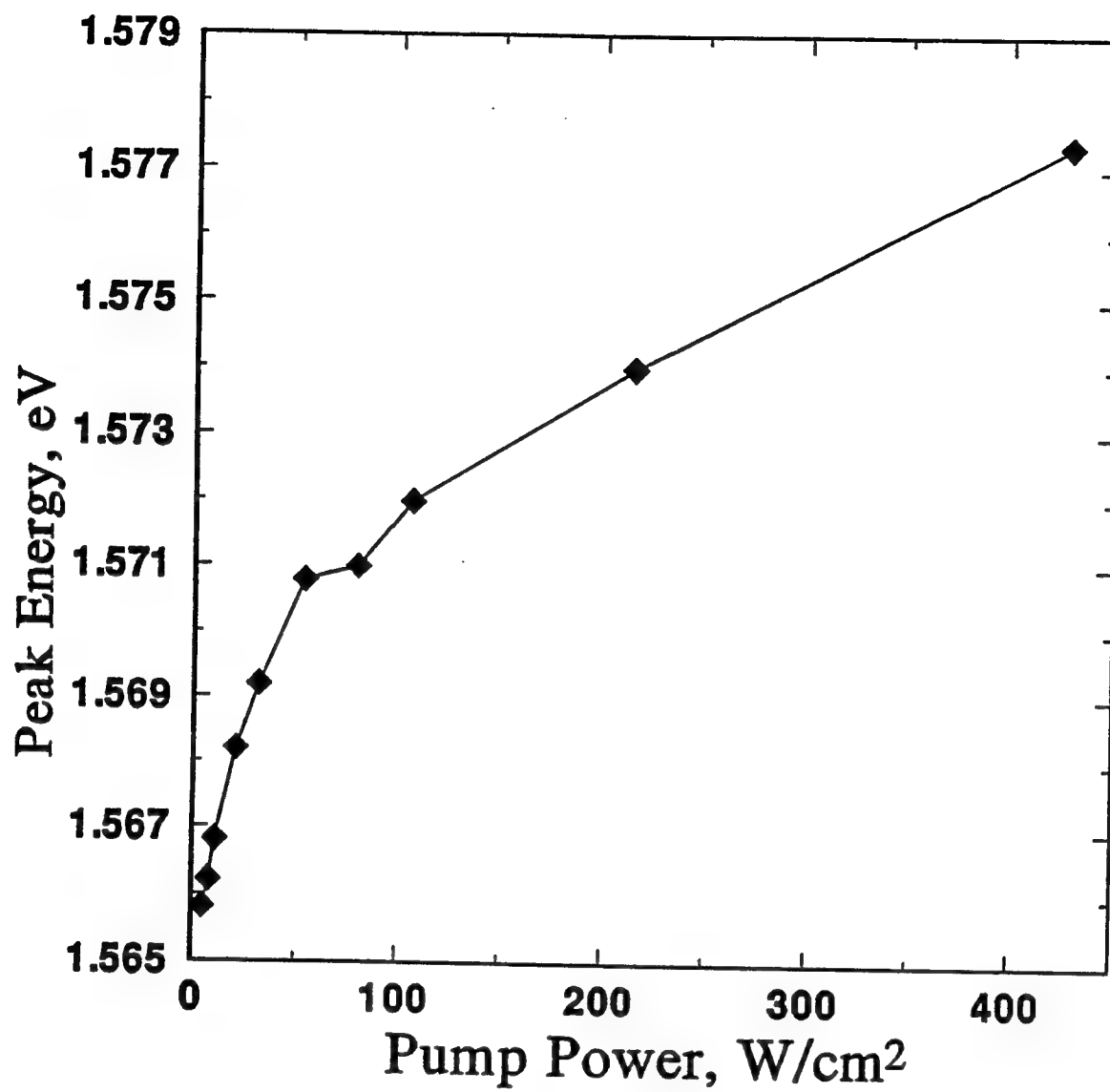
Fig. 9

magnitude larger than that required for stable mode-locking.

Conclusion

We have observed saturation of photoluminescence peak at low pump intensities. We have measured time-resolved photoluminescence decay in growth-interrupted and undoped asymmetric-coupled quantum wells. We have subsequently determined decay times and characteristic carrier densities for the observed photoluminescence intensity saturation. We have observed anomalously large blue shift of the donor-to-acceptor transition peak in a compensate-doped asymmetric-coupled quantum-well structure. We have proposed a mechanism for such a large shift. We have grown a multilayer structure that can be used to implement an optical parametric oscillator and amplifier and frequency doubler in a novel configuration. Finally, we have tried to mode-lock Ti:Sapphire laser and summarized potential problems causing unstable mode-locked output.

As a result of our research supported by this grant, we have four conference presentations [a,b,c,d] and submitted two journal papers for publication [e,f]. Three more journal papers based on our results will be submitted for publication [g,h,i].

Acknowledgement

We are indebted to Drs. R. E. Sherriff, J. P. Loehr, J. Ehret, J. Hoelscher, and D. C. Reynolds for their expertise in the areas above, that had made it possible for us to carry out the projects mentioned above.

References

[1] D. Bimberg, D. Mars, J. N. Miller, R. Bauer, O. Oertel, and J. Christen, Supperlatt. Microstruc. 3, 79 (1987).

[2] M. Kohl, D. Heitmann, S. Tarucha, K. Leo, and K. Ploog, Phys. Rev. B39, 7736 (1989).

[3] D. C. Reynolds, K. K. Bajaj, C. W. Litton, P. W. Yu, J. Singh, W. T. Masselink, R. Fischer, and H. Morkoc, Appl. Phys. Lett. 46, 51 (1985).

[4] K. Fujiwara, K. Kanamoto, and N. Tsukada, Phys. Rev. B40, 9698 (1989).

[5] B. Devcaud, A. Chomctte, N. Roy, B. Scrmagc, and D. S. Katzer, Sur. Sci. 267, 199 (1992); D. Gammon, B. V. Shanabrook, and D. S. Katzer, Appl. Phys. Lett. 57, 2710 (1990).

[6] A. G. Cui, Y. J. Ding, S. J. Lee, J. V. D. Veliadis, J. B. Khurgin, S. Li, D. C. Reynolds, and J. Grata, J. Opt. Soc. Am. B 13, 536 (1996).

[7] R. Normandin, R. L. Williams, and F. Chatenoud, Electr. Lett. 26, 2088 (1990); R. Normandin, H. Dai, S. Janz, A. Delage, J. Brown, and F. Chatenoud, Appl. Phys. Lett. 62, 118 (1993); D. Vakhshoori, R. J. Fischer, M. Hong, D. L. Sivco, G. J. Zydzik, G. N. S. Chu, and A. Y. Cho, Appl. Phys. Lett. 59, 896 (1991).

[8] R. Lodenkamper, M. L. Bortz, M. M. Fejer, K. Bacher, and J. S. Harris, Jr., Opt. lett. 18, 1798 (1993).

[9] J. Khurgin, Appl. Phys. Lett. 21, 2100 (1987); Phys. Rev. B38, 4056 (1988); J. Appl. Phys. 64, 5026 (1988); J. Opt. Soc. Amer. B 6, 1673 (1989).

[10] S. Janz, F. Chatenoud, and R. Normandin, Opt. Lett. 19, 622 (1994).

[11] J. B. Khurgin and Y. J. Ding, Opt. Lett. 19, 1066 (1994).

[12] Y. J. Ding, S. J. Lee, and J. B. Khurgin, J. Opt. Soc. Am. B 12, 1586 (1995).

[13] Y. J. Ding, S. J. Lee, and J. B. Khurgin, Phys. Rev. Lett. 75, 429 (1995); Y. J. Ding, S. J. Lee, and J. B. Khurgin, IEEE J. Quant. Electr. 31, 1648 (1995).

PI's Presentations and Publications Supported by This Grant

[a]   Y. J. Ding and J. B. Khurgin, "Spatially-localized band-filling effects and band-gap renormalization in growth-interrupted quantum wells," Invited, to be presented at Novel optical materials and applications, Jun. 8-13, 1997, Cetraro, Italy.

[b]   Y. J. Ding, D. C. Reynolds, S. J. Lee, J. B. Khurgin, W. S. Rabinovich, and D. S. Katzer, "Evidence for strong spatially-localized band-filling effects in interface islands for extremely low laser intensities," submitted to QELS'96.

[c]   Y. J. Ding and D. C. Reynolds, "Evidence of spatially-localized band-filling effects in interface islands at low laser intensities," 1996 Advisory Meeting of the Center for Photochemical Sciences.

[d]   R. Korotkov, O. Gorbounova, Y. J. Ding, and J. B. Khurgin, "Saturation of donor-to-acceptor transition," 1996 Advisory Meeting of the Center for Photochemical Sciences.

[e]   Y. J. Ding and J. B. Khurgin, "Transversely-pumped counter-propagating optical parametric amplification and difference-frequency generation," submitted to J. Opt. Soc. Am. B.

[f]   A. G. Cui, O. Gorbounova, Y. J. Ding, J. V. D. Veliadis, S. J. Lee, J. B. Khurgin, and K. L. Wang, "Evidence of strong sequential band filling at interface islands in asymmetric coupled quantum wells," submitted to Superlattices and Microstructures.

[g]   R. Korotkov, O. Gorbounova, Y. J. Ding, S. J. Lee, J. B. Khurgin, W. S. Rabinovich, and D. S. Katzer, "Observation of anomalously large blue shift of donor-to-acceptor transition," in preparation.

[h]   Y. J. Ding, D. C. Reynolds, S. J. Lee, J. B. Khurgin, W. S. Rabinovich, and D. S. Katzer, "Saturation of photoluminescence peaks in growth-interrupted asymmetric-coupled quantum wells," in preparation.

[i]   R. Korotkov, Y. J. Ding, and J. B. Khurgin, "Optimizing transversely-pumped counter-propagating optical parametric oscillators," in preparation.

COMPUTATIONS OF DRAG REDUCTION AND BOUNDARY LAYER STRUCTURE ON A TURBINE BLADE WITH AN OSCILLATING BLEED FLOW

Dr. Elizabeth A. Ervin
Assistant Professor
Department of Mechanical and Aerospace Engineering

University of Dayton
300 College Park
Dayton, Ohio 45469-0210

COMPUTATIONS OF DRAG REDUCTION AND BOUNDARY LAYER STRUCTURE ON A TURBINE BLADE WITH AN OSCILLATING BLEED FLOW

Elizabeth A. Ervin

Abstract

Current studies suggest that an oscillating bleed flow passed through a turbine rotor blade can reduce the friction drag on the blade. Furthermore, the resulting boundary layer structure and possible separation from the blade will decrease the effective available area for the high speed flow between adjacent blades, improving off-design performance. A fundamental study of the flow dynamics around a blade with oscillating cooling flow is being investigated. A transient solution of the Reynolds-averaged Navier-Stokes, continuity, and energy equations is being developed to analyze the effects of a pulsing jet on vortex development and interaction with the blade surface. The computational investigation is the first to study the effects of an oscillating bleed flow on drag reduction and boundary layer structure about a turbine blade. This is a potential application for MEMS to control turbine off-design performance.

Existing software will be verified and revised as part of the proposed effort for the addition of cooling. Furthermore, a more sophisticated turbulence model will be implemented to describe the convection and diffusion of turbulent kinetic energy that would be expected with the ejection of cooling.

COMPUTATIONS OF DRAG REDUCTION AND BOUNDARY LAYER STRUCTURE ON A TURBINE BLADE WITH AN OSCILLATING BLEED FLOW

Elizabeth A. Ervin

INTRODUCTION

A variable area turbine typically consists of a standard rotor and a variable area turbine nozzle, which uses pivoting vanes or moveable sidewalls. Potential operating and performance benefits of a variable area turbine include high engine efficiency, modulation of work split between the high and low pressure turbines, flow capacity control, and very low blade vibration, when operated at optimum rotational speed and pressure ratio over a range of engine power. A large effort to develop gas turbine engines with a variable area turbine took place in the late 1970's and early 1980's (Chapple, et al., 1980). However, the cost of implementing pivoting vanes or moveable sidewalls in high temperature environments, typical of turbines, was considered prohibitive.

Recent developments suggest that an oscillating cooling flow through a turbine rotor blade may reduce the friction drag on the blade. The resulting boundary layer structure and possible separation from the blade would decrease the effective available area for the high speed flow between adjacent blades. This would improve off-design performance, similar to that of a variable area turbine. Oscillating blade flow can be produced by acoustic perturbation and could make strategic use of emerging micro-electro-mechanical systems. Allen and Glezer (1995), for example, are using a micro-electro-mechanical jet actuator to produce an oscillating jet to control a primary jet.

The oscillating flow would be used to control the vortex development on the blade surface. Vortex development and interaction with a surface are complex processes, and measurements in operating engines are difficult and expensive. As a consequence, a computational model of a blade with oscillating cooling flow is proposed. A transient solution of the Reynolds-averaged Navier-Stokes, continuity, and energy equations will permit analysis of the effects of the oscillating jet on vortex development and interaction with

the blade surface. The results of this study will be used to develop an experiment to be conducted at Wright Laboratory.

BACKGROUND

A wall jet consists of an outer shear layer and an inner layer that behaves like a viscous boundary layer. Cohen, et al. (1992) calculated two unstable modes: an inviscid mode that depicts the large-scale disturbances in the free shear layer, and a viscous mode that concerns the small-scale disturbances near the wall. They showed that the relative importance of each mode can be controlled by small amounts of blowing and suction.

Studies of an oscillating plane wall jet, in an external flow, have shown 10 to 40 percent reductions in shear drag, with minimal effect on maximum velocity decay and jet spreading rate (Fasel, et al., 1995). Detailed particle image velocimetry (PIV) measurements of an acoustically perturbed laminar plane wall jet showed that the perturbation enhances growth of a vortex in the outer shear layer. This, in turn, interacts with the inner layer, resulting in a counter-rotating vortex pair. (Shih and Gogineni, 1995). The vortex pair remains attached to the wall under the influence of the downstream vortex pair until it is further diffused downstream. When the vortex pair is dislodged from the surface, jet spreading and transition to turbulence follow. The forcing frequency determines the distance between adjacent vortex pairs, which in turn controls the flow field.

Little has been done to numerically simulate the interaction of turbine blade bleed jets with the primary flow. Vogel (1994) developed a steady solution of the Reynolds-averaged Navier-Stokes, continuity, and energy equations to model flow over a turbine blade section with film cooling. Internal coolant geometry was modeled as well as the outer flow region. The model demonstrated vortex development, typical of jets in crossflow, and compared favorably with flow visualization experiments that were conducted. The effect of the steady-state coolant jets on the shear drag, if any, was not reported.

Clearly, more study is needed to see if a periodic jet can reduce the shear drag on a turbine blade and simultaneously control the flow dynamics. No data concerning vortex development and control with oscillating cooling flow on an airfoil appears to have yet been published. Hence, it is believed that the current study will is the first examination of drag reduction and boundary layer structure on a turbine blade with an oscillating coolant flow.

The original two-dimensional model uses the Baldwin and Lomax (1978) model to account for turbulence. Algebraic turbulence models, such as this, are not able to model the convection and diffusion of turbulent kinetic energy that are expected with the ejection of cooling. The new two-equation algorithm is based on the recently developed k-ℓ model (Goldberg, 1994). This model is similar to the well known k-ε model of Launder and Spalding (1974), where k is the turbulent velocity fluctuation kinetic energy and ε is the viscous dissipation. ℓ is the undamped eddy viscosity and is equal to k^2/ε. It offers two advantage over previous models:

1. ℓ is zero at the wall, unlike ε.

2. The model is not based on wall functions, which makes it adaptable for external flows.

The addition of a two-equation turbulence model required two new transport equations, which has resulted in a massive software revision, impacting dozens of subroutines.

COMPUTATIONAL METHOD

The software used for the simulation of the governing equations was developed by Allison Engine Company, under U. S. Air Force Contract F33615-90-C-2028 for Wright Laboratory, to study vane-blade interaction, as described by Rao, et al. (1994a, 1994b). This software was verified and revised as part of the proposed effort for the addition of cooling as described above.

CODE DESCRIPTION

The conservative forms of the transient Reynolds-averaged Navier-Stokes, continuity, and energy equations are solved on a blade-to-blade stream surface of revolution. A numerical finite difference technique is used, with central differencing for second order accuracy in space, and a five-stage Runge-Kutta algorithm for second order accurate integration in time. An artificial dissipation model that blends second and fourth order differences is added to damp out non-physical oscillations produced by central differencing. It utilizes pressure as a sensor to capture physical discontinuities such as shock waves and stagnation points.

The code uses a body fitted hyperbolic O-grid embedded in a rectangular H-grid as shown in Figure 1. The outer grid resolves the free stream flow and the O-grid is used in the boundary layer region, with fine grid resolution near the surface.

Non-reflective inflow and outflow boundary conditions are calculated based on the methodology developed by Cline (1977). No-slip conditions are used on the airfoil surface(s) and periodic boundary conditions are used in the polar direction. The interface between the stator exit and the rotor inlet can be modeled with overlapping H-grids and a time-space phase-lag procedure, originally developed by Erdos (1977).

In the numerical simulation, body-fitted curvilinear coordinates are utilized and the flow is mapped to uniformly spaced rectangular coordinate region with the Jacobian matrix of the transformation. Also, the variables are non-dimensionalized. The second viscosity coefficient, λ, is set equal to -2/3 μ, where μ is the dynamic viscosity, and the Prandtl number is constant.

TURBULENCE MODEL

The prior-existing two-dimensional code uses the Baldwin and Lomax (1978) model to account for turbulence. Algebraic turbulence models, such as this, are not able to model the convection and diffusion of turbulent kinetic energy that are expected with the ejection of cooling. The new two-equation algorithm is based on the recently developed k-ℓ model (Goldberg, 1994). This model is similar to the well known k-ε model of Launder and Spalding (1974), where k is the turbulent velocity fluctuation kinetic energy and ε is the viscous dissipation. ℓ is the undamped eddy viscosity and is equal to k^2/ε. It offers two advantage over previous models:

1. ℓ is zero at the wall, unlike ε.
2. The model is not based on wall functions, which makes it adaptable for the H-grid, which has no wall.

The transport equations for the turbulent kinetic energy, k, and the undamped eddy viscosity, ℓ, are:

$$\frac{\partial Q}{\partial t} + \frac{\partial F_j}{\partial x_j} = \frac{\partial F_{v_j}}{\partial x_j} + \vec{S}_{source}, j = 1,2 \tag{1}$$

where:

$$Q = \begin{bmatrix} \rho k \\ \mathcal{R} \end{bmatrix}, \quad F_j = \begin{bmatrix} \rho u_j k \\ u_j \mathcal{R} \end{bmatrix}, \quad F_{v_j} = \begin{bmatrix} (\mu + \dfrac{\mu_t}{\sigma_k}) \dfrac{\partial k}{\partial x_j} \\ (\nu + \dfrac{\nu_t}{\sigma_\varepsilon}) \dfrac{\partial \mathcal{R}}{\partial x_j} \end{bmatrix},$$

$$\vec{S}_{source} = \begin{bmatrix} P - \dfrac{(\rho k)^2}{\rho \mathcal{R}} \\ -\dfrac{1}{\sigma_\varepsilon} (\nabla \nu_t \cdot \nabla \mathcal{R}) + (2 - C_{\varepsilon 1}) \dfrac{\mathcal{R} P}{\rho k} - (2 - C_{\varepsilon 2}) k \end{bmatrix}$$

(2)

Equation 2 uses the conservative form of the transport equations for k and $\mathcal{R}$ as described by (Goldberg, 1994). The source term, P, is defined as the production of turbulent energy by the work of the main flow against the Reynolds stresses:

$$P = \left[\mu_t \left(\frac{\partial u_i}{\partial x_j} + \frac{\partial u_j}{\partial x_i} - \frac{2}{3} k \delta_{ij} \right) \right] \frac{\partial u_i}{\partial x_j}$$

(3)

The latter form of P is based on the Boussinesq approximation (1877) and is the form used by Launder and Spalding (1974). The u_i terms represent the mean velocity components and u_i' is the fluctuating velocity component in the i-direction. The eddy viscosity, μ_t, is defined as:

$$\mu_t = C_\mu f_\mu \rho \mathcal{R}$$

(4)

The two equation k-$\mathcal{R}$ model affects the transport equations for momentum and energy and these effects are summarized here due to lack of completeness in the literature. The eddy viscosity, μ_t, is added to the dynamic viscosity, μ, including the expression for second viscosity coefficient. The μ/Pr terms are replaced with $\left(\dfrac{\mu}{Pr} + \dfrac{\mu_t}{Pr_t} \right)$, as in the Baldwin and Lomax (1978) model. Pr_t is typically set to 0.9 for air flows and is the value used in the prior-existing software.

The constants σ_k, σ_ε, $C_{\varepsilon 1}$, $C_{\varepsilon 2}$, and C_μ are chosen to be 1.0, 1.3, 1.44, 1.92 and 0.09, respectively, and are the standard coefficients as recommended by Launder and Spalding (1974) for plane jets, mixing

layers and flows near walls. The function f_μ is unity in the Launder and Spalding model, and was modified by Launder and Sharma (1974) and later by Lam and Bremhorst (1981) to extend the model to near-wall regions. Goldberg (1994) used a similar formulation:

$$f_\mu = \frac{1 - e^{-A_\mu R_T}}{1 - e^{-A_\epsilon R_T}}$$

(5)

where R_T is a form of a turbulence Reynolds number:

$$R_T = \frac{k^2}{\nu\epsilon} = \frac{\ell}{\nu}$$

(6)

The constants, A_μ, and A_ϵ were chosen to be 2.5×10^{-6} and $C_\mu^{3/4}/2\kappa$ ($\kappa = 0.41$), respectively, and n = 2, by prior experimentation (Goldberg, 1994).

The boundary conditions are as follows:

- Set $\ell = k = 0$ at solid walls.

- Set $\ell = O(10^{-5})$ at the freestream and initial conditions.

- Prescribe the freestream k based on a given turbulence intensity, Tu, using: $k = \frac{3}{2}(TuV_\infty)^2$.

- Extrapolate k and ℓ from interior points to outflow boundaries.

Using the k-ℓ model in the prior-existing software, required the transformation of Equations (1) and (2) to the 2-D meridonial coordinate system used by Rao, et al. (1994a, 1994b). This coordinate system was developed by Vavra (1974) and is depicted in Figure 2. Details of the development of the full Navier Stokes equations in this coordinate system is not published; therefore, this was not a trivial task. Furthermore, the meridonial coordinate system equations were mapped to a body fitted coordinate system with the Jacobian matrix of the transformation. The addition of a two-equation turbulence model required two new transport equations, which resulted in a massive software revision, impacting dozens of subroutines. The convective terms in the transport equations used first order upwind differencing (for stability), while the diffusive and source terms used the standard central-type discretizations.

6-8

BOUNDARY CONDITIONS

The boundary conditions must also be supplemented to allow for a cooling flow. The film cooling will be modeled in a manner similar to that of Vogel (1994). The ejection region will require a separate H-mesh to represent the flow channel. At the inlet to the flow channel, non-reflecting characteristic variable boundary conditions will be used. These conditions will assume subsonic normal inflow. The inlet pressure and velocity will vary periodically to create an oscillating flow at the blade surface. At the coolant exit, the H-mesh will interface with the outer O-grid. Two layers of dummy cells will be used to specify boundary conditions and ensure that the block interface nodes behave like interior nodes.

RESULTS AND DISCUSSION

COMPARISON OF TURBULENCE MODELS

The following plots show results for different turbulence models. The calculations were performed at an axial chord Reynolds numbers of 3230 and at a pitch to axial chord ratio, $p/c_x = 0.944$. The low Reynolds number was selected to compare the separation calculations. The computations were down with both a laminar model and a Baldwin-Lomax turbulence model ($Tu = 0\%$) and finally, a k-ℓ model with $Tu = 0\%$.

Figures 3 through 5 are airfoil surface plots using s/s_{max} as the distance along the airfoil. The variable, s_{max}, is defined separately for the pressure ($s/s_{max} < 0$) and suction ($s/smax > 0$) surfaces so that s/s_{max} varies from zero at the leading edge to +/- 1 at the trailing edge.

Figure 3 depicts the calculated pressure ratio, p/p_o, around the airfoil surface, where p_o is the total pressure. Skin friction and heat transfer are of primary interest and these are described in the following two figures.

In Figure 4, the skin friction coefficient, C_f, around the airfoil is described. C_f is actually the shear stress at the wall, calculated with dimensionless velocity, distance and laminar viscosity. On the pressure surface ($s/s_{max} < 0$), the negative C_f values correspond to the region between the two stagnation points, both located on this side of the airfoil. On the suction surface ($s/s_{max} > 0$), the region of negative C_f corresponds

to a region of separation. This was confirmed by an examination of velocity profiles in this region (not shown).

The heat transfer is characterized in Figure 5 using the Stanton number, St, defined here as:

$$St = \frac{\left(\frac{\partial T}{\partial n} * \mu_l * k\right)_{wall}}{T_o - T_w}$$

where T is the temperature, n is the direction normal to the surface, μ_l is the laminar viscosity, k is the thermal conductivity of the gas, T_w is the wall temperature and T_o is the total temperature. The temperatures are non-dimensionalized with T_o and the other variables are non-dimensionalized as well. The heat transfer is a maximum at the leading edge stagnation point and just before the trailing edge on the suction side. The minimum values occur at the trailing edge stagnation point and at the transition to turbulence on the suction side. A second minimum occurs at the onset of separation. The transition to turbulence is further described below. In all of these figures, the B-L data is obscured by the k-ℓ data, showing good agreement between the two models.

The maximum $y+ = yu*/v$ in the O-grid, where y is the normal distance from the airfoil surface and v is the kinematic viscosity, occurred near the leading edge. The friction velocity, u+, is the square root of the dimensionless shear stress at the wall, C_f, divided by the dimensionless density ratio, shown at the leading edge for the three models in Figure 6. The three models exhibited similar behavior.

Conclusions

A comparison of turbulence models was used to examine a low Reynolds number flows typical of a low pressure turbine stage. The calculations confirmed the phenomena of separation at low Re, low Tu and $p/c_x = 0.94$. The turbulence models exhibit similar behavior, showing that the new turbulence model is working properly. This report concerns the first phase of a study of the effects of the oscillating jet on vortex development and interaction with the blade surface.

BIBLIOGRAPHY

Allen, M. G. and Glezer, A., 1995, "Jet Vectoring Using Zero Mass Flux Control Jets," presented at AFOSR Contractor and Grantee Meeting on Turbulence and Internal Flows, Wright Patterson AFB, Dayton, OH, May, 1995, pp. 95-100.

Arpaci, V. S., 1984, *Convection Heat Transfer*, pp. 390-431, Prentice-Hall, Inc., Englewood Cliffs, NJ.

Baldwin, B. S. and Lomax, H., 1978, "Thin Layer Approximation and Algebraic Model for Separated Turbulent Flows," AIAA Paper 78-0257.

Boussinesq, Q., 1877, Theorie de l'Ecoulement Tourbillonant, Vol. 23, pp.46-50, Paris: Comptes-Rendus de l'Academie des Sciences.

Chapple, P. M., Flynn, P. F. and Mulloy, J. M., 1980, "Aerodynamic Design of Fixed and Variable Geometry Nozzleless Turbine Casings," *Journal of Engineering and Power*, Vol. 102, pp. 141-147.

Cline, M. C., 1977, "NAP: A Computer Program for the Computation of Two-Dimensional, Time-Dependent, Inviscid Nozzle Flow," Los Alamos National Laboratory Report LA-5984.

Cohen, J., Amitay, M. and Bayly, B. J., 1992, "Laminar-Turbulent Transition of Wall Jet Flows Subjected to Blowing and Sucking," *Physics of Fluids A*, Vol. 4, pp. 283-289.

Erdos, J. I., Alzner, E. and McNally, W., 1977, "Numerical Solution of Periodic Transonic Flow through a Fan Stage," *AIAA Journal*, Vol. 15, pp. 1559-1568.

Fasel, H., Ortega, A. and Wygnanski, I., 1995, "Convective Flow and Heat Transfer Due to a Forced Wall Jet," presented at AFOSR Contractor and Grantee Meeting on Turbulence and Internal Flows, Wright Patterson AFB, Dayton, OH, May, 1995, pp. 29-33.

Goldberg, U. C., 1994, "Toward a Pointwise Turbulence Model for Wall-Bounded and Free Shear Flows," *Journal of Fluids Engineering*, Vol. 116, pp. 72-76.

Lam, C. K. G., and Bremhorst, K., 1981, "A Modified Form of the k-ε Model for Predicting Wall Turbulence," *Journal of Fluids Engineering*, Vol. 103, pp. 456-460.

Launder, B. E., and Spalding, D. B., 1974, "The Numerical Computation of Turbulent Flows," *Computer Methods in Applied Mechanics and Engineering*, Vol. 3, pp. 269-289. Reprinted in Vol. 81, pp. 269-289 (1990).

Rao, K. V., Delaney, R. A., and Topp, D. A., 1994a, "Turbine Vane-Blade Interaction, Vol. 1, 2-D Euler/Navier-Stokes Aerodynamic and Grid Generation Developments," Wright Laboratory Report WL-TR-94-2073.

Rao, K. V., Delaney, R. A., and Dunn, M. G., 1994b, "Vane-Blade Interaction in a Transonic Turbine, Part 1 Aerodynamics," *Journal of Propulsion and Power*, Vol. 10, pp. 305-311.

Shih, C. and Gogineni, S., 1995, "Experimental Study of Perturbed Laminar Wall Jet," *AIAA Journal*, Vol. 33, pp. 559-561.

Vogel, D. T., 1994, "Navier-Stokes Calculation of Turbine Flows with Film Cooling," ICAS-94-2.5.3.
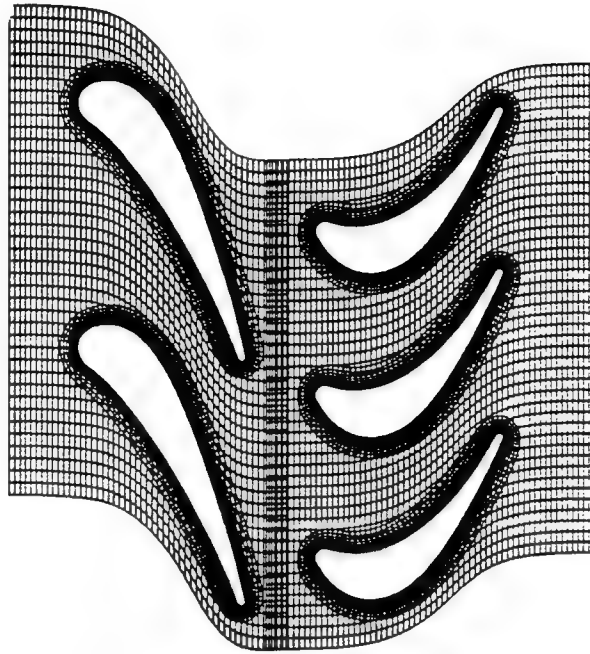
Figure 1 . Overlapped O-H grid system.
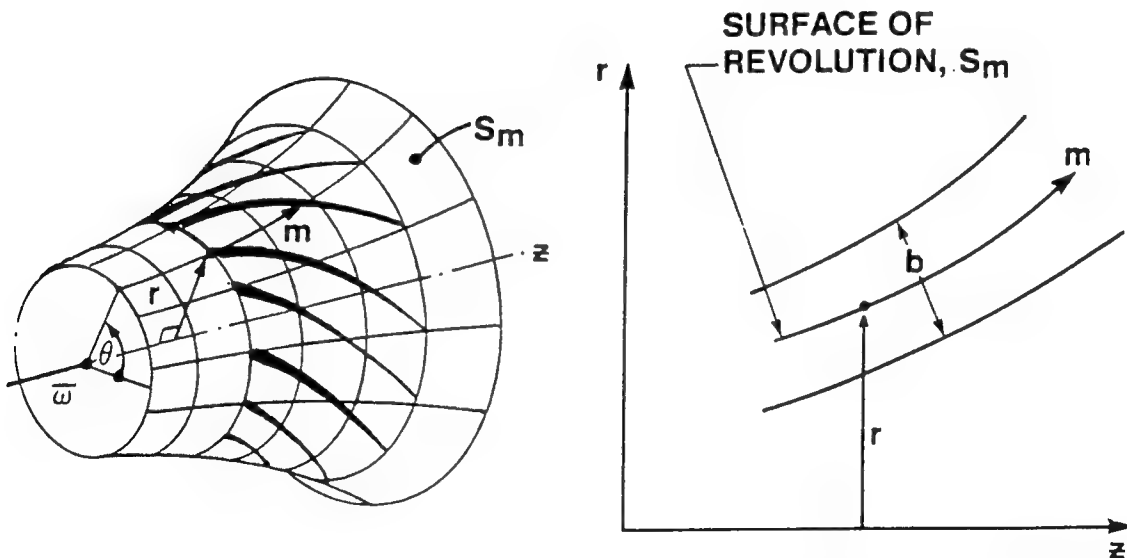
Figure 2 . Quasi-three-dimensional stream surface coordinate system.

Figure 3. Dimensionless Pressure
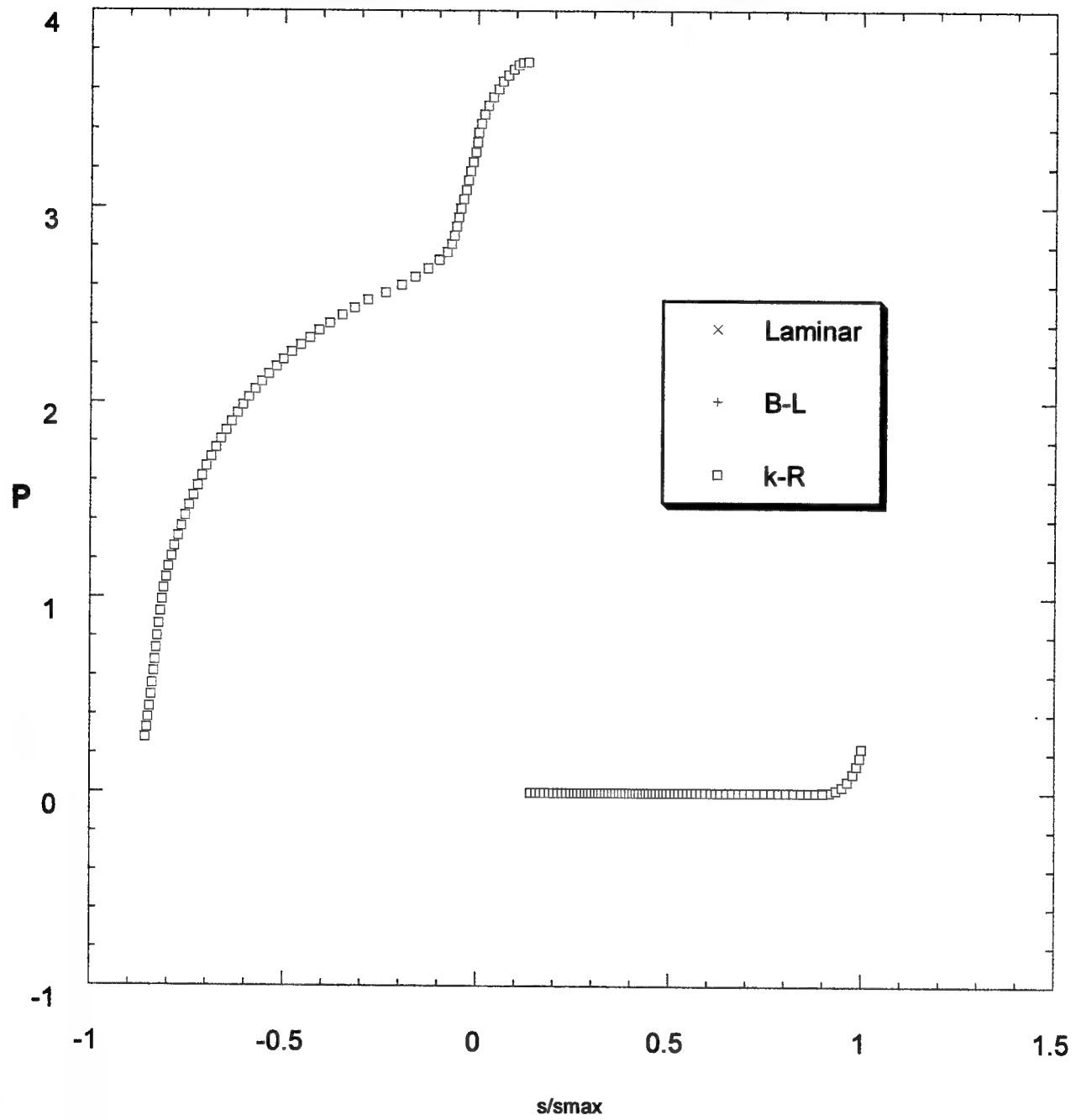
Figure 4. Skin Friction
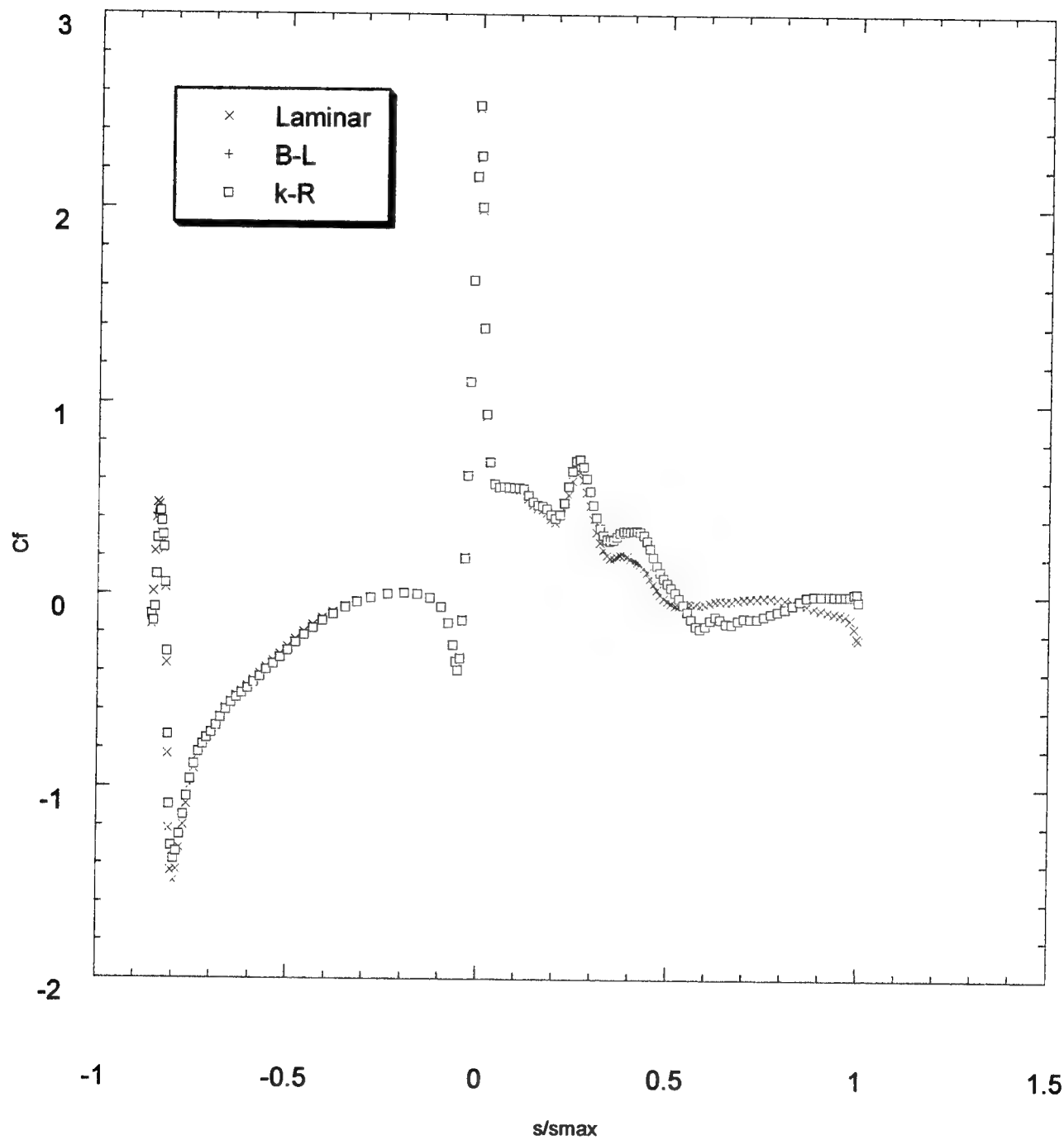
Figure 5. Heat Transfer Coefficient
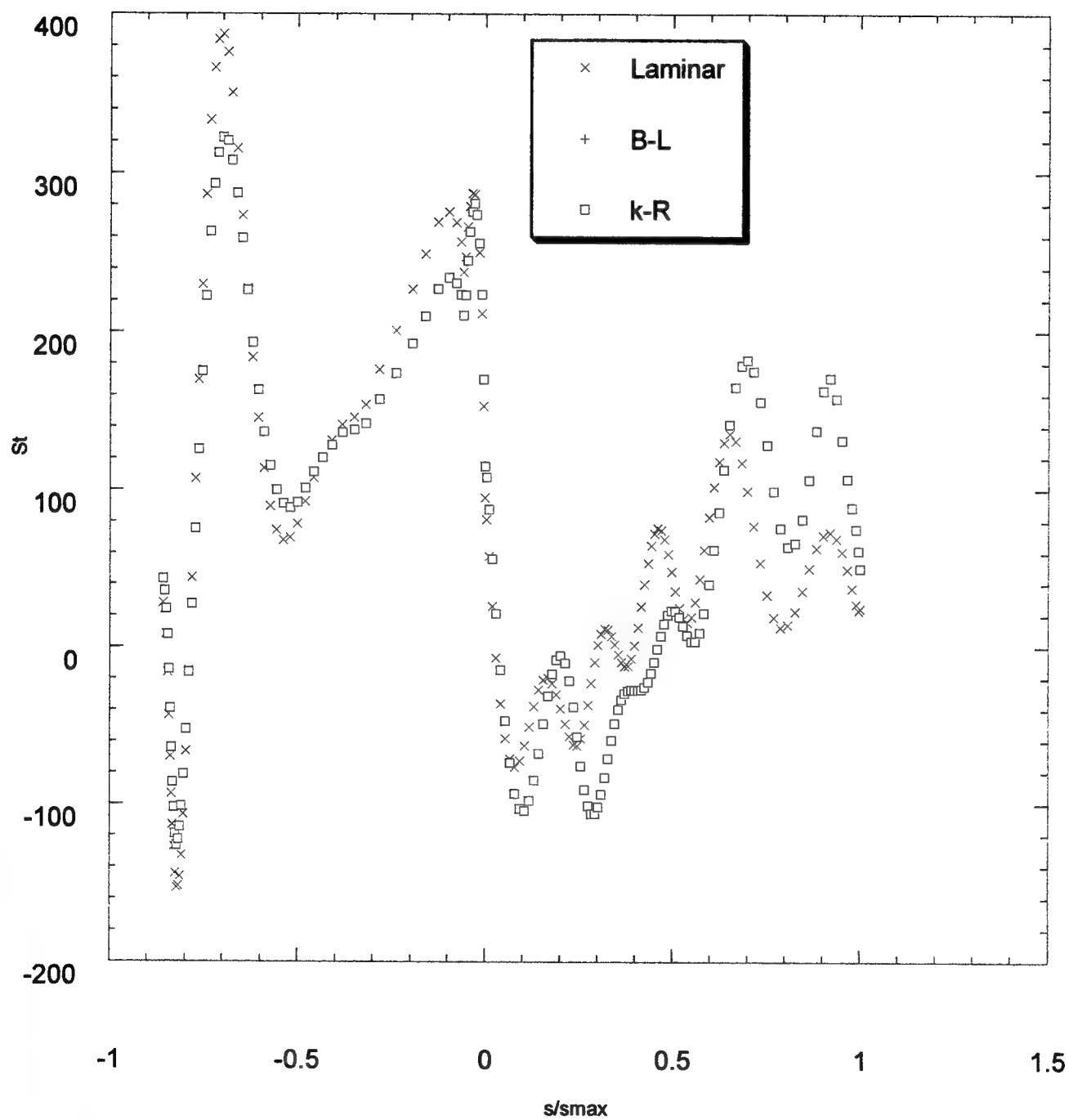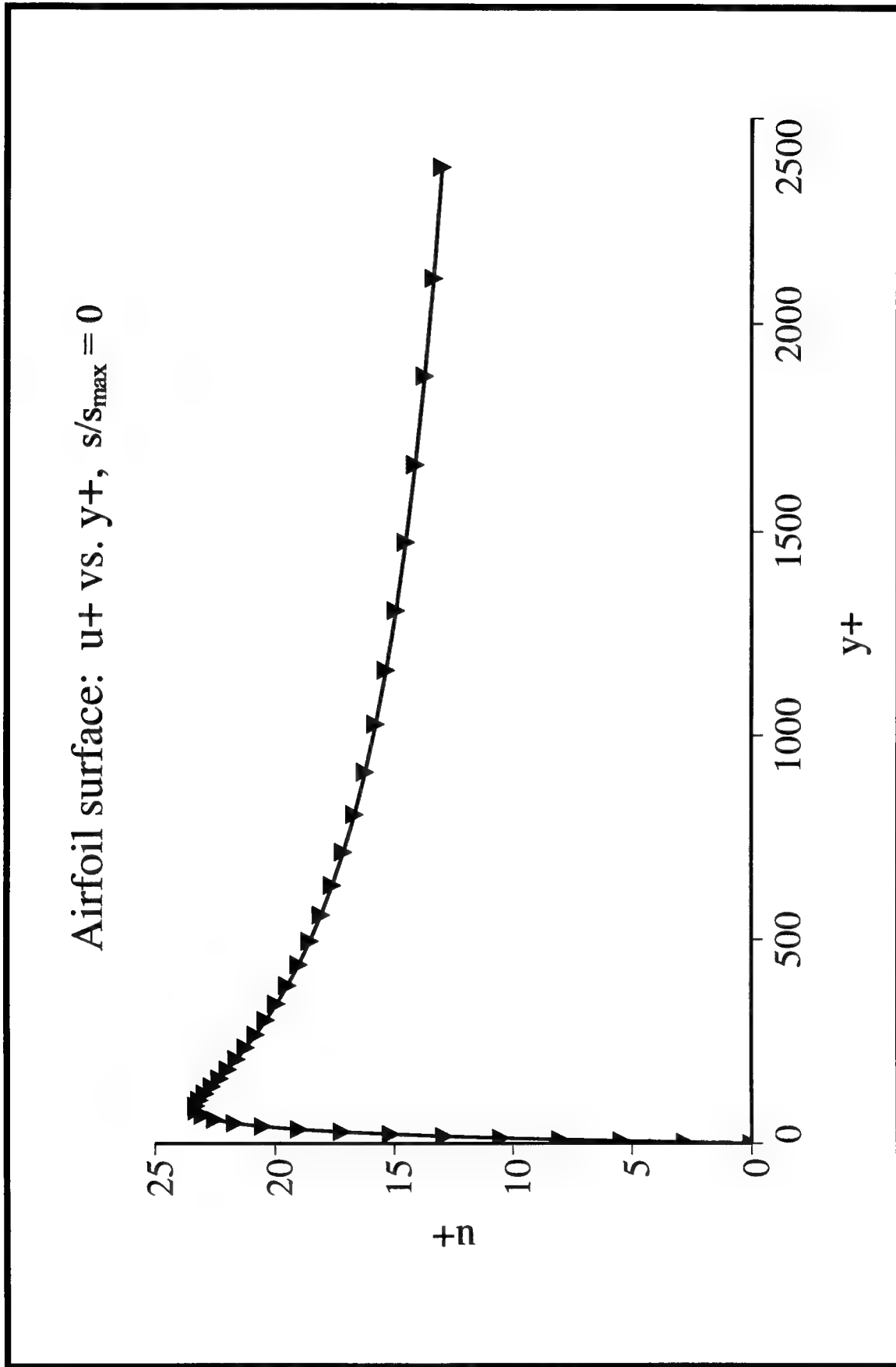
Figure 6a. Velocity profile at the leading edge using the laminar model.
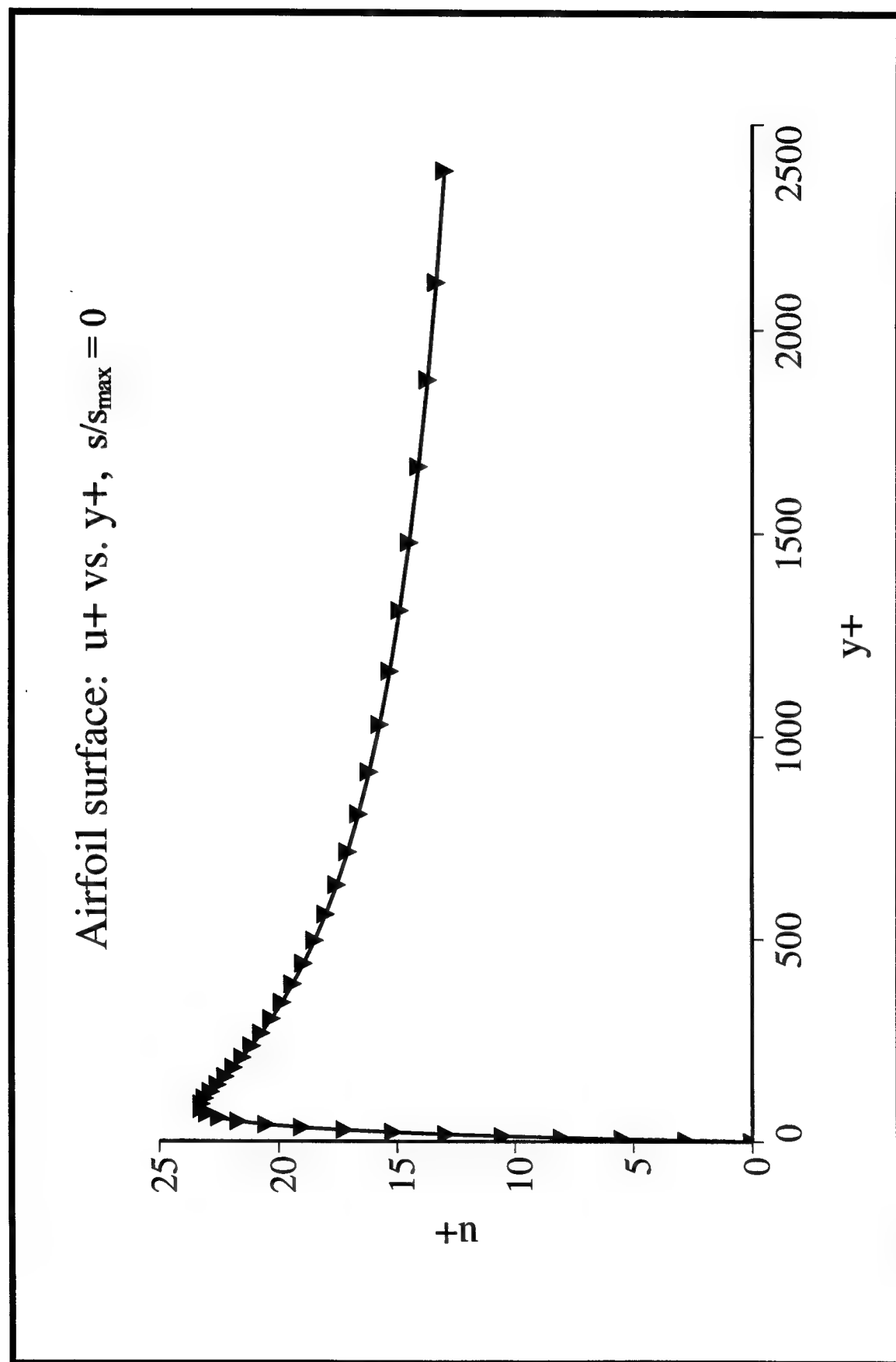
Figure 6b. Velocity profile at the leading edge using the Baldwin-Lomax turbulence model.
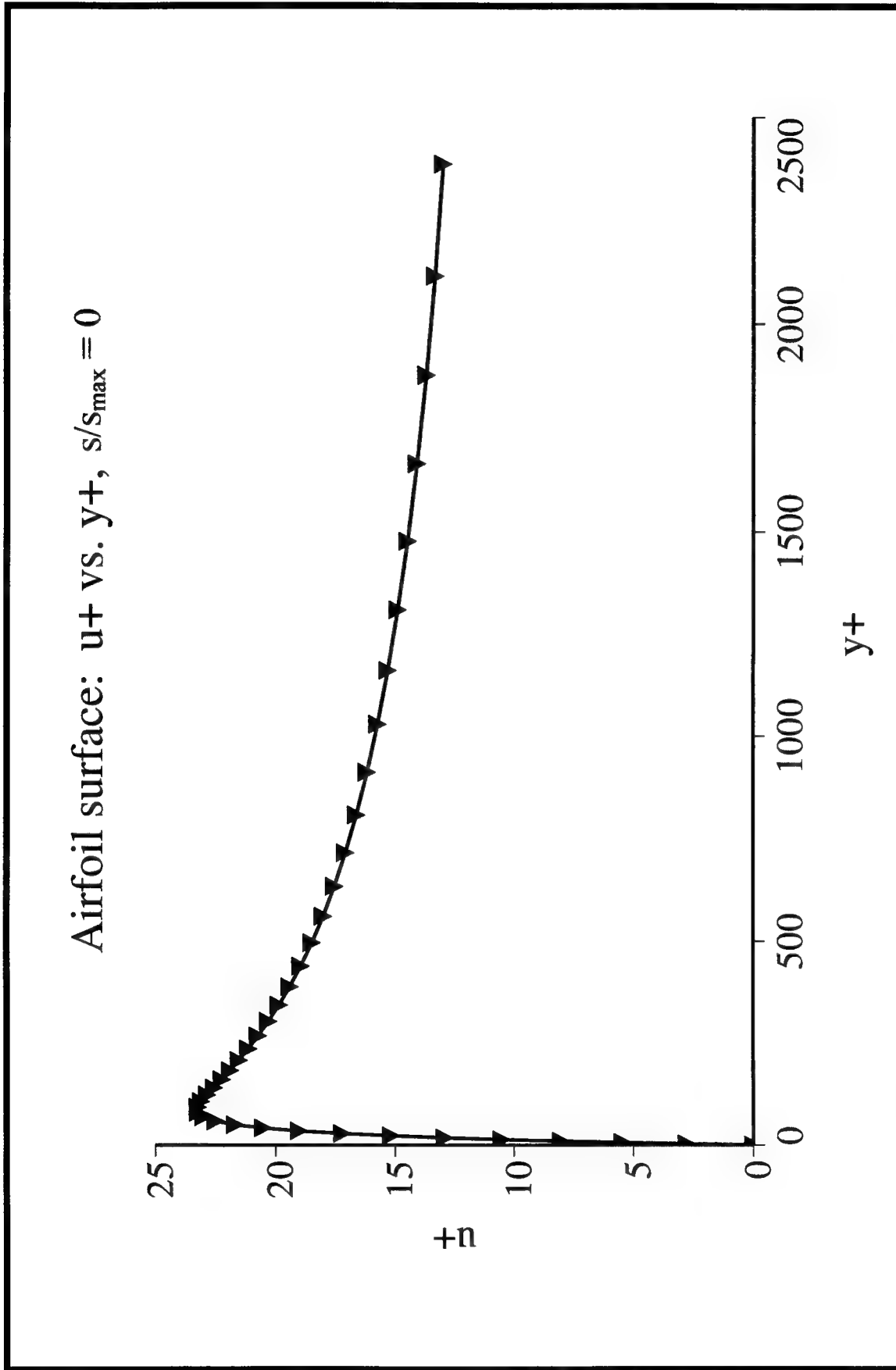
Figure 6c. Velocity profile at the leading edge using the *k-ℓ* turbulence model.

LOW SIGNAL TO NOISE SIGNAL PROCESSOR
FOR LASER DOPPLER VELOCIMETRY

Dr. Richard D. Gould
Associate Professor
Mechanical and Aerospace Engineering Dept.

Mechanical and Aerospace Engineering Dept.
North Carolina State University
Raleigh, NC   27695

LOW SIGNAL TO NOISE SIGNAL PROCESSOR
FOR LASER DOPPLER VELOCIMETRY

Richard D. Gould
Associate Professor
Mechanical and Aerospace Engineering Dept.
North Carolina State University

ABSTRACT

The primary purpose of this research project was to purchase a two-channel low signal to noise laser Doppler velocimeter (LDV) signal processor so that Dr. Gould and North Carolina State University (NCSU) will have the capability to make non-intrusive velocity measurements in the Rolls Royce/Wright Laboratory swirl combustor at NCSU. The experimental activity in test cell 18 at the Aeropropulsion and Power Directorate at Wright Laboratory has increased to the point where all test stands are currently occupied. In fact, the Rolls Royce/Wright Laboratory (WL/POPT) high swirl combustor is now in storage due to the lack of test space. In light of this, a collaborative arrangement with Dr. A. S. Nejad and his team of scientists at WL/POPT is being forged so that the swirl combustor experimental program, initiated at WL/PORT, can continue at NCSU.

This equipment, a TSI model IFA 750 LDV signal processor, is currently being used with an existing two component LDV system at NCSU and has been fully tested. This signal processor uses a correlation based analysis technique to obtain the Doppler frequency and thus can be used to make LDV measurements in flows where the signal to noise ratio is low. Combusting flows and flow where spatially resolved measurements are needed are examples of where low signal quality would occur.

LOW SIGNAL TO NOISE SIGNAL PROCESSOR
FOR LASER DOPPLER VELOCIMETRY

Dr. Richard D. Gould

1. INTRODUCTION

Dr. Gould has developed a unique technical relationship with the researchers at Wright Laboratory in the Advanced Propulsion and Power Directorate (WL/POPT) over the past six years through collaborative work supported by AFOSR through the Summer Research Program (SRP), the Summer Research Extension Program (SREP) and the University Resident Research Program (URRP). He has helped setup 4 different experiments while at Wright Laboratory and also has setup a low speed wind tunnel at North Carolina State University (NCSU). These research projects have resulted in 15 technical publications, nine of which have been co-authored by Wright Laboratory researchers. These include: (1) a unique experiment where two-point velocity correlation measurements and single point autocorrelation measurements were made in the flow behind an axisymmetric sudden expansion, (2) two-component velocity measurements in the Rolls-Royce/Wright Laboratory high swirl combustor, (3) simultaneous three-component velocity measurements in the isothermal flow behind a bluff body flame holder, and (4) planar laser induced fluorescence (PLIF) measurements of acetone and OH concentration downstream of a bluff body flame holder with normal fuel jet injection.

The purpose this research program was to purchase equipment to give North Carolina State University a long term capability to conduct experiments of interest to researchers at WL/POPT at North Carolina State University. These can include velocity and temperature measurements in the subsonic Rolls-Royce/Wright Laboratory high swirl combustor. The majority of funds were used to purchase a two-channel correlation based LDV signal processor so that LDV measurements in combusting flows (where low signal to noise signals are present) can be made at NCSU. Substantial cost sharing (37% of equipment cost) of this equipment was provided by the College of Engineering at NCSU and by the Applied Energy Research Laboratory (AERL) at NCSU. All the other equipment necessary for conducting these proposed tests are available at NCSU and thus the purchase of this signal processor completes the LDV system. The group at WL/POPT has agreed to loan the subsonic Rolls-Royce/Wright Laboratory high swirl combustor test section to Dr. Gould so that the test program initiated at Wright Laboratory can be continued at NCSU. The motivation for conducting the tests at NCSU as opposed to at Wright Laboratory is because all the test facilities in Building 18 of the Aeropropulsion and Power Directorate will

be occupied with other tests for the next two to three years. Additional funds will be sought from AFOSR or Wright Laboratory to support graduate students at NCSU to run these tests.

2. EQUIPMENT DESCRIPTION

The purchased equipment, a TSI Model IFA 750, two-channel laser Doppler velocimeter (LDV) correlation based signal processor (one master and one slave), computer interface, and data analysis software, is presently being used together with the optical portion of an existing and fully operational three-color, three-component LDV system. In an effort to save the AFOSR and North Carolina State University money, a sales department demonstration unit (with full warranty) was purchased. This decision allowed for the purchase of the IFA 750 series rather than the originally proposed IFA 650 signal processor series from TSI, Inc. The maximum Doppler frequency capability of the IFA 750 is 100 MHz, while the maximum Doppler frequency capability of the IFA 650 is only 35 MHz. LDV signal processors analyze the Doppler bursts created when small seed particles pass through crossed laser beams (*i.e.*, probe volume) giving the instantaneous velocity component perpendicular to the fringes in the probe volume. This scattered light is sensed by photodetectors which convert optical energy into an electrical signal. One signal processor is required for each velocity component. The strength of this signal is a function of laser power, seed particle material and size, collection optics and photodetector efficiency. This two-channel signal processor can be connected to any combination of two of the three channels (i.e. velocity components) in sequence (*i.e.*, 1-2, 1-3, 2-3) to obtain three component velocity information at each measurement point.

The addition of this Doppler burst signal processing hardware and software to the existing optical portion of the LDV system completes the three-component LDV system (two channels simultaneously) at NCSU thus forming the basis for a laboratory specializing in novel non-intrusive experimental measurements in turbulent isothermal and reacting flows. In particular, the turbulence characteristics of flow fields at elevated temperatures, where hot wire anemometry can not be used, can be investigated with this non-invasive instrument.

3. EQUIPMENT TESTING

The IFA 750 LDV signal processor, interface hardware, and software has been fully tested using two different flows. The hardware and software were found to operate as advertised by the manufacturer. The first flow used to test the signal processor was an aluminum oxide particle laden pulsatile jet flow having maximum axial velocities in excess of 200 m/s. The second flow

used was a counter-flow diffusion flame flow which had maximum velocities on the order of 0.2 m/s. This flow was seeded with 0.5 micron diameter aluminum oxide particles. Velocity measurements where made with and without combustion in this flow. The signal processor and included acquisition and analysis software (both TSI FIND version 4.0 for DOS and TSI FIND version 1.0 for Windows) operated flawlessly with both these flows. In addition, comparisons between the measurements made with this new signal processor and those made using counter-based LDV signal processors were also conducted. These comparisons showed excellent agreement, with the new processor giving higher data rates then the counter processors, as expected. In conclusion, the requested signal processor was purchased, installed and tested under this research program. A collaborative arrangement with Dr. A. S. Nejad and his team of scientists at WL/POPT is being discussed so that the swirl combustor experimental program, initiated at WL/PORT, can continue at NCSU.

Modeling and Control of Rotating Stall and Surge for Compressor Systems in Turbojet Engines

Guoxiang Gu
Associate Professor
Department of Electrical and Computer Engineering

Louisiana State University
Baton Rouge, LA 70803-5901

Modeling and Control of Rotating Stall and Surge for Compressor Systems in Turbojet Engines

Guoxiang Gu

Department of Electrical and Computer Engineering

Louisiana State University, Baton Rouge, LA 70803-5901

December 19, 1996

Abstract

Axial flow compressors are the vital part of turbine-based aeroengines. However, the engine performance is effectively reduced by rotating stall and surge in axial flow compressors, which are instabilities that arise in the unsteady fluid dynamics. The difficulty in suppressing rotating stall and surge via active control lies in the fact that these two instabilities are associated with nonlinear bifurcations. This motivated our bifurcation approach to rotating stall and surge control that is pursued in the past year. Specifically, bifurcation control with output feedback is studied, and stabilizability is characterized for both stationary and nonstationary bifurcations. These results complement those developed by Abed and Fu, and are applicable to compressor control. Both linear and nonlinear control laws are developed for rotating stall control based on Moore-Greitzer model. A surprising result is that the hysteresis loop associated with rotating stall can be eliminated through the use of lumped actuator and sensor that is contrast to the existing control method where distributed actuators or sensors are used. Design method for surge control is also studied that effectively reduces the impact of both deep surge (pure surge) and classic surge (coupled with rotating stall). In addition, the PI offered a special topics course on bifurcation analysis and compressor control that trained graduate students for undertaking research work in this active research area. MATLAB programs are worked out to simulate distributed nonlinear model of axial flow compressors. Hence with the effort of the PI and his students, a strong research program is established in LSU on active control of axial flow compressors that will enhance the operability of the compression system and improve the future aeroengines.

Modeling and Control of Rotating Stall and Surge for Compressor Systems in Turbojet Engines

Guoxiang Gu

1 Introduction

Axial flow compressors are subject to two distinct aerodynamic instabilities, rotating stall and surge, which effectively limit the compressor operability. Both these instabilities are disruption of the normal operating condition designed for steady and axisymmetric flow. Rotating stall is a severely non-axisymmetric distribution of axial flow velocity which manifests itself as a region of severely reduced flow that rotates at a fraction of the rotor speed. Prolonged operation under this condition may break rotor blades, and burn the turbine [28]. Surge, on the other hand, is an axisymmetric pumping oscillation which can cause flameout and thus engine damage as well. Both lead to large penalties in performance of aeroengines.

Because rotating stall and surge are difficult to predict accurately during design, problems are often identified at a later stage that incur great expense in engine development program. This fact motivated the use of feedback control to enhance compressor operability by actively suppressing rotating stall and surge. Two key developments are noticable in control of compression systems. The first is the low order state-space model developed by Moore and Greitzer [28] that can be extended into high order ones as well as "distributed" models in [2, 26]. It captures the nonlinear dynamics of the compression system through its bifurcation characteristic [27]. The second is bifurcation-based rotating stall control law developed by Abed and his coworkers [25, 37], and was shown to be effective for the implementation in industrial turbomachinery by Nett and his group [11, 12]. Other important research work along this direction is the linear control method which extends the stable operating range of the compressor up to 20% [29, 30], and the back-stepping mthod reported in [23] leading to a global stabilization feedback control law.

Our research program is the continuation of the existing work on compressor control that is characterized by a bifurcation approach. Indeed the only mathematical tool used in our research is the classic bifurcation theory. The use of bifurcation theory in control of rotating stall and surge is crucial to the extension of the operating range of the compression system, and to the improvement of the aeroengine ultimately. Specifically, bifurcation control with output feedback was studied in this research program with the objective of applications to rotating stall and surge control. This approach yields several interesting results, which are validated with computer simulations. In the next several sections, our methodology and research results will be reported in more details

together with our future research plan.

2   Research Problems and Methodology

This section addresses the research problems of rotating stall and surge control, and the methodology employed in our research program.

Rotating Stall and Surge in Axial Flow Compressors

Axial flow compressors are subject to two distinct aerodynamic instabilities, rotating stall and surge, which can severely limit the compressor performance. Both these instabilities are disruption of the normal operating condition which is designed for steady and axisymmetric flow. The transition from normal compressor operation into rotating stall is depicted in Figure 1 where Φ is the circumferential mean of the flow coefficient ϕ, and Ψ is the nondimensionalized pressure rise. As the flow coefficient through the compressor is decreased (i.e., as the downstream throttle closes in an experiment), the pressure rise increases. This trend continues until the system goes into either rotating stall, surge (deep surge), or both (classic surge).
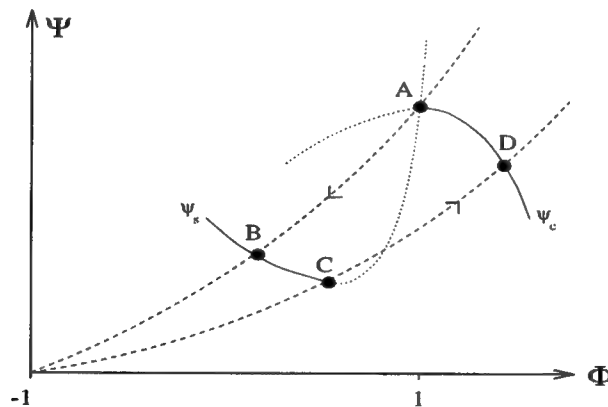
Figure 1   Schematic compressor characteristic, showing rotating stall

For the case of rotating stall, the lowest flow coefficient at which the compressor can operate with axisymmetric flow is point A, the peak of the characteristic. At lower flows, an abrupt transition occurs into rotating stall (point B). There is a substantial drop in pressure rise and a decrease in flow coefficient (segment A-B). This condition will persist until the flow is increased to point C. Thus there exists a severe 'hysteresis', or range of flow coefficients at which two stable operating conditions exist – steady axisymmetric flow and rotating stall. Once a compressor enters fully developed rotating stall, both rotor and stator blades pass in and out of the stalled flow causing tremendous stress. Any substantial length of time in this mode can result in excessive

internal temperatures due to low efficiency associated with the presence of rotating stall. In addition, an even more serious consequence that can occur in an engine is that the low flow rates obtained during rotating stall can lead to substantial overtemperatures in the burner and turbine [14]. At present, the only remedy to get out of rotating stall is to shut down the engine and restart it again [28].

Rotating stall is a severely non-axisymmetric distribution of axial flow velocity, though steady in an appropriate (moving) reference frame, around the annulus of the compressor, taking the form of a wave or 'stall cell', that propagates in the circumferential direction at a fraction of the rotor speed. Surge, on the other hand, is an axisymmetric oscillation of the mass flow along the axial length of the compressor. Deep surge is a mostly axisymmetric oscillation with such a large variation of mass flow that during part of the cycle the compressor operates in reversed flow. The frequency of the surge oscillation is typically an order (or more) of magnitude less than that associated with the passage of rotating stall cells. If surge occurs, the transient consequences such as large inlet overpressures can also be severe. However the circumstances may well be more favorable for returning to unstalled operation by opening either the throttle or internal bleed valves, since the compressor can operate in an unstalled condition over part of each surge cycle. Often surge and rotating stall are coupled (classic surge) although each can occur without the other. For the case of classic surge, the compressor may pass in and out of rotating stall during a surge cycle, with rotating stall characteristics appearing to be quite similar to those obtained during steady-state operation. Thus rotating stall and surge, though coupled, are well defined enough that each can be studied alone for low speed axial flow compressors [29].

Rotating stall and surge are mostly caused by disturbances. Those having largest and most destabilizing effects are: circumferential distortion, planar turbulence, and combustion [22]. All of these types of disturbances present in full-scale aeroengines and are major sources of rotating stall and surge.

- *Circumferential distortion* refers to non-axisymmetric flow patterns that are generated by upstream structures such as bends in inlet duct or boundary layer separation caused by high angle of attack at the engine inlet. The inlet distortion can also be correlated with aircraft angle of attack and yaw angle.

- *Planar turbulence* refers to axisymmetric oscillations in the flow field that are generated, for example, by inlet buzz or ingestion of wakes from nose gear or other aircraft. Planar turbulence is an inherently unsteady flow and has been recognized as an important source of loss in stall margin.

- *Combustion* process introduces large unsteady back-pressure disturbances to the compression system causing steady state operating conditions to exhibit fluctuations in pressure and mass flow large enough to cause the system to diverge.

Thus substantial rotating stall and surge margins are required in the selection of a compressor operating point in order to maintain steady axisymmetric flow. Consequently, compression systems are forced to operate with far less performance operating point than point A, the peak of the compressor characteristic (Figure 1). Even then, with all the above mentioned disturbances present in the worst case, it does not seem possible for the compressor to escape rotating stall and surge unless some control action is taken.

Our Methodology to Approach Compressor Control Problems

Since rotating stall and surge significantly limit the performance of turbine-based aeroengines, and have catastrophic consequences if occur in jet planes, compressor control becomes the priority in the list of research problems for AFOSR. Our research program, though small, shows the effort of AFOSR to resolve this important research problem in the near future. It is recognized in both the research community and AFOSR that employing feedback control to suppress rotating stall and surge is essential for extending compressor operating range and to improving performance of the future aeroengines. Hence the research group in MIT, led by Greitzer and in University of Maryland, led by Abed have been strongly supported in the past by AFOSR. The Moore-Greitzer model laid solid foundation for the use of feedback control for suppressing rotating stall and surge. The analytical low order state-space model derived in [28] captures the characteristics of rotating stall and surge, and used in both MIT [29, 30] and University of Maryland [25, 37] to tackle rotating stall control. This work is further pursued by the research group in Georgia Institute of technology, led by Nett [6, 12]. It is interesting to note that classic bifurcation theory provided a powerful tool for both analysis and synthesis of rotating stall control. The papers of [2, 5] were the first to describe rotating stall with subcritical pitchfork bifurcation, and surge as Hopf bifurcation. The work of McCaughan in [27] gave a through analysis of rotating stall and surge, in connection with the various parameters of the Moore-Greitzer model. The bifurcation analysis yields a nonlinear feedback controller proposed in [25, 37] that stabilizes the critical operating point, and later it is experimentally validated in [6, 12].

Our research program has focused on bifurcation approach to rotating stall and surge control using the low order Moore-Greitzer model. This is a continuation of the existing work in compressor control, and has potential to make contributions to nonlinear robust control. It should be clear that the difficulty associated with compressor control is due to the lack of corresponding

theory and practice for bifurcation control, by the fact that rotating stall and surge are both phenomena of nonlinear bifurcations. Very few results are available for bifurcation control except those in [3, 4, 19, 20] where state feedback is employed for bifurcation stabilization. Moreover the success in nonlinear control of rotating stall as reported in [25, 37, 6, 12] is based on bifurcation theory. These considerations motivated us to adopt a bifurcation control methodology to compressor control. A more profound reason for using bifurcation approach is due to nonlinear robust control. In the past, nonlinear control has focused on extension of linear control theory and design to nonlinear systems. The current trend in nonlinear robust control follows the same path. However nonlinear systems have their unique features that do not exist for linear systems. Simple generalization of linear control theory to nonlinear systems may not work. This is especially true for bifurcated systems which involve uncertain parameters. At critical values of the uncertain parameters, more than one equilibria are born at which stability changes. Often the critical modes of the linearized control systems are uncontrollable, or unobservable, or both. This is where linear control theory fails, and is exactly the same as the rotating stall control problem. The development of bifurcation control theory is clearly an important part of nonlinear robust control, and has no parallel in linear robust control. Thus the bifurcation approach to compressor control problems will advance our knowledge to bifurcation stabilization and nonlinear robust control as well.

3 Research Results

The schematic compression system is shown in Figure 2 below:
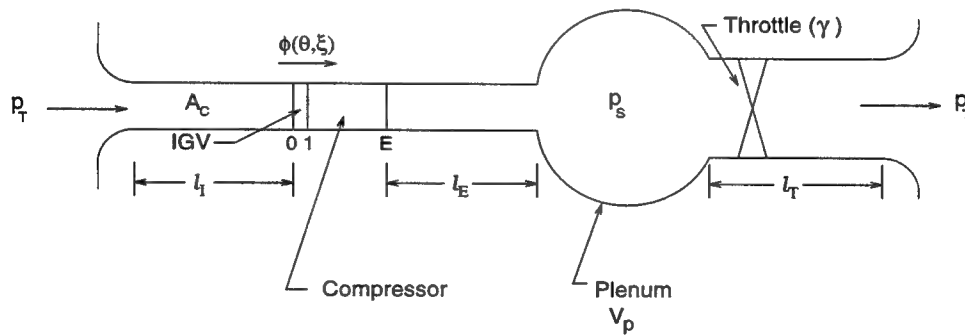
Figure 2 Schematic of compressor showing nondimensionalized lengths.

The total pressure at the upper stream of the compressor is denoted by p_T. The air flows through inlet guide vanes that straighten the flow. The compressor acts like an actuator that raises the pressure of the flow at the back of the compression system. The purpose of the compression

system is to generate the required pressure rise which is the pressure difference between p_S and p_T. The established pressure rise is then used to provide the thrust for the jet airplane. Hence the compression system is the heart of the aeroengine. The ultimate objective of our research program is the improvement of the aeroengine performance.

In the past year, our research program has focused on rotating stall and surge control that are essential to compressor performance. Classic bifurcation theory is employed to analyze the problems of rotating stall and surge, and to obtain the feedback controllers that stabilize the critical operating points and enlarge the operating range of the compression system. Our research results are reported in a series of papers ([16],[17],[9],[35],[21]), and are summarized as follows.

- Bifurcation stabilization with output feedback [16].

  As mentioned earlier, rotating stall and surge controls are closely connected with bifurcation stabilization, because rotating stall corresponds to subcritical pitchfork bifurcation and surge corresponds to Hopf bifurcation. Stabilization of nonlinear control systems with smooth state feedback control has been studied by a number of people [1, 3, 4, 7, 36]. An interesting situation for nonlinear stabilization is when the linearized system has uncontrollable modes on imaginary axis with the rest of modes stable. This is so called *critical cases* for which the linear theory is inadequate. It becomes more intricate if the underlying nonlinear system involves a real-valued parameter. At critical values of the parameter, linearized system has unstable modes corresponding eigenvalues on imaginary axis, and additional equilibrium solutions will be born. The bifurcated solutions may, or may not be stable. The instability of the bifurcated solution may cause "hysteresis loop" in bifurcation diagram for both subcritical pitchfork bifurcation and Hopf bifurcation [18], and induce undesirable physical phenomina. This is exactly the case of rotating stall in axial flow compressors. Hence bifurcation stabilization is an important topic in nonlinear control.

  While most of the existing work in the open literature considers only state feedback for bifurcation stabilization, compressor control systems employ output feedback because often some of the state variables are not measurable, or too expensive to measure. It is thus necessary to investigate bifurcation stabilization for the case when only output measurements are available, and study the stabilizability property for various bifurcated systems. Our research work on bifurcation stabilization is reported in [16]. Specifically, the nonlinear system under consideration has single-input/single-output, and it involves a single parameter. At the critical value of the parameter, the linearized system possesses either a simple zero eigenvalue, or a pair of imaginary eigenvalues, and the bifurcated solution is unstable. Output feedback stabilization via smooth local controllers is studied for both stationary

and nonstationary bifurcation. Two results are established in [16] for bifurcation stabilization. The first one is stabilizability conditions for the case where the critical mode is not linearly observable through output measurement. It is shown that nonlinear controllers do not offer any advantage over the linear ones for bifurcation stabilization. The second one is stabilizability conditions for the case when the critical mode is linearly observable through output measurement. It is shown that linear controllers are adequate for stabilization of transcritical bifurcation, and quadratic controllers are adequate for stabilization of pitchfork and Hopf bifurcations, respectively. The proofs are constructive. Thus the results in this paper can be used to synthesize stabilizing controllers, if they exist.

- Nonlinear feedback for rotating stall control [17].

A nonlinear feedback control law is proposed for rotating stall control in [17]. This feedback control law is different from that of [25, 37] in that no distributed sensors are required, and output measurement is chosen as pressure rise that is a lumped parameter. This is important as distributed sensors such as hot wire for flow rate measurements are expensive and delicate, while pressure transducers are more durable to volatile flow field. This was the starting point for considering feedback control law of the form

$$u(t) = \frac{K}{\sqrt{\Psi}}$$

where Ψ denotes the pressure rise. The proposed control system employs pressure rise as output measurement and throttle position as actuating signal for which both sensor and actuator exist in the current configuration of axial compressors, and are lumped in nature that is contrast to other control method that employs either distributed actuators, or distributed sensors, or both.

It should be emphasized that the results of the paper of [17] is obtained entirely with classic nonlinear bifurcation theory. This is due to the fact that linear control theory fails to apply to the bifurcated systems such as rotating stall and surge in compression system. Classical bifurcation analysis for nonlinear dynamics is used to derive a nonlinear feedback control law that eliminates the hysteresis loop associated with rotating stall and extends the stable operating range in axial compressors. The stability of the critical operating point for controlled compressor is established using the center manifold theorem. Although the results in [17] are primitive and no advanced bifurcation control developed in [4, 3] is used, it yields similar results as in [25, 37]. The stabilization results are verified via computer simulations with high order compression systems that are surprising. More importantly, the use of pressure rise as output measurement also gives the opportunity for surge control. Recall

that pure surge dynamics is governed by differential equations of flow rate and pressure rise, but not the amplitude of the disturbance flow. Hence the stabilizing control laws of [25, 37] can not work for surge control. We are currently investigating the possibility of surge control with the same feedback control law.

- Linear and nonlinear feedback laws for rotating stall control [9].

The control system proposed in the paper of [9] is similar to that of [17] except that the output measurements can be either pressure rise or averaged flow rate. Both linear and nonlinear feedback control laws are investigated that yield similar results for rotating stall control. The foundation of the paper lies in those results established in [16]. Specifically, the results on nonlinear bifurcation stabilization in [16] are applied to rotating stall control to derive stabilizing feedback controllers in [9]. It should be clear that the challenge to the proposed control system is that the critical mode of the linearized system corresponding to rotating stall is neither controllable nor observable. Both linear and nonlinear feedback control laws are proposed and are shown to be effective in elimination of the hysteresis loop associated with rotating stall and in extension of the stable operating range of the axial flow compressor.

Although the results in this paper are applications of those in [16], it has several interesting points. First, it relates rotating stall control to equivalent bifurcation stabilization, that was studied in [4, 3, 16]. Hence bifurcation stabilization can be used to synthesize stabilizing controllers for rotating stall control. Second, it indicates the stability ranges for different feedback controllers, and these ranges are finite. Moreover it is possible that the stabilizing ranges of the feedback gains can be zero for some of the compressor control systems, and thus stabilizing controllers do not exist in some cases. Fortunately stabilizing controllers do exist for practical compressor control systems such as the one at MIT. Again the results in this paper are validated with computer simulations.

- Further results on rotating stall control [35].

In compressor control with throttle as actuators, an important consideration is that the operating point is different from the critical point of bifurcation, and that the throttle has to be positive due to the physical constraint. This problem is addressed in [35] where sensor signals are averaged flow rate on the circumference of the compressor or the pressure rise. Sufficient conditions are derived for the control law gains to guarantee that the subcritical pitchfork bifurcation responsible for hysteresis is rendered supercritical and that the the bifurcated solution is asymptotically stable. The proposed control laws give practical so-

lution for rotating stall in axial flow compressors. The numerical examples show that the transformation of the bifurcation from subcritical to supercritical and the elimination of the hysteresis region.

- Bifurcation based surge control [21].

  The focus of the paper [21] is surge control for axial flow compressors. Although there exist a family of state feedback laws which stabilize the nonaxisymmetric equilibria near the operating point and eliminate the hypothesis induced by rotating stall, Hopf bifurcation associated with surge still exist under rotating stall control laws. The results in [21] introduce test functions whose zeros are critical to Hopf bifurcation for the closed-loop system where nonlinear feedback control laws are employed. These test functions are given in compact form. A particular test function is also developed to determine stability of the periodic solutions born at Hopf bifurcation. The analysis based on these test functions leads to a new method of feedback design for control of both stationary and Hopf bifurcation in axial flow compressors. Using the techniques proposed in [21], feedback controllers can be designed to meet several bifurcation control requirements, including elimination of the behavior of surge, coupled with rotating stall. This is a result significant because in engineering practice, rotating stall and surge are often couple that is called classic surge.

The success of this research program is inseparable from the control group in Wright-Patterson Air Force Base (WPAFB), led by Dr. Siva Banda. In fact almost all the results summarized in this report are the consequences of collaboration with the control group in WPAFB, including Dr. Andy Sparks, and Dr. Siva Banda, and Mr. Paul Blue. Hence we are extremely grateful to the control group of Dr. Banda, and looking forward for further collaboration in the near future.

4 Conclusion and Future Research

In the past year, our research work has focused on three state Moore-Greitzer model. The results on stabilization of rotating stall and surge control are established for the low order compressor model at MIT. Due to the time constraint, the proposed work for high order compressor model is not investigated, though our results reported in [16, 17, 9, 35, 21] are validated with high order "distributed" model. This will be studied in the future research work. In particular, compressor control systems using air jet as actuators and pressure transducers as measurement sensors will be the emphasis of future research on compressor control. Moreover $\mathcal{H}_\infty$ optimization will be introduced for compressor control to improve compressor performance. We are confident in that with the leadship of Dr. Siva Banda, we will make further contributions to the DoD mission.

References

[1] D. Aeyels, "Stabilization of a class of nonlinear systems by a smooth feedback control," *Systems and Control Letters*, **5** (1985), 467-473.

[2] R.A. Adomatis and E.H. Abed, "Bifurcation analysis of nonuniform flow patterns in axial-flow gas compressors," in *1st World Congress of Nonlinear Analysis*," Aug. 1992.

[3] E.H. Abed and Jyun-Horng Fu, "Local feedback stabilization and bifurcation control, I. Hopf bifurcation," *Systems and Control Letters*, **7** (1986), 11-17.

[4] E.H. Abed and Jyun-Horng Fu, "Local feedback stabilization and bifurcation control, II. stationary bifurcation," *Systems and Control Letters*, **8** (1986), 467-473.

[5] E.H. Abed, P.K. Houpt, and W.M. Hosny, "Bifurcation analysis of surge and rotating stall in axial flow compressors," *J. Turbomachinery*, vol 115, 817-824, Oct. 1993.

[6] O.O. Badmus, S. Chowdhury, E.M. Eveker, C.N. Nett, and C.J. Rivera, "A simplified approach for control of rotating stall – Part 1/2," in *29th Joint Propulsion Conference and Exhibit*, June 1993. AIAA Paper #93-2229/2334.

[7] R.W. Brokett, "Asymptotic stability and feedback stabilization," in *Differential Geometry Control Theory*, Eds. by R. W. Brokett, R.S. Millman, and H.J. Sussmann, (Birkhauser, Boston, 1983), 181-191.

[8] W.W. Copenhaver, private communications, 1995.

[9] X. Chen, G. Gu, P. Martin, and K. Zhou, "Bifurcation control with output feedback and its applications to rotating stall control," submitted to *Automatica*, 1996.

[10] R. D'Andrea, R.L. Behnken and R.M. Murray, "Active control of rotating stall using pulsed air injection: experimental results on a low-speed, axial flow compressor," in *SPIE Conference on Sensing, Actuation and Control in Aeropropulsion*, 1995.

[11] K.M. Eveker, D.L. Gysling, C.N. Nett and O.P. Sharma, "Integrated control of rotating stall and surge in aeroengines," in *SPIE Conference on Sensing, Actuation and Control in Aeropropulsion*, 1995.

[12] K.M. Eveker, D.L. Gysling, C.N. Nett and H.O. Wang, "Rotating stall and surge control," US Patent Application, US Serial Number 08355763, 1994.

[13] M.R. Feulner, G.J. Hendricks, and J.D. Paduano, "Modeling for control of rotating stall in high speed multi-stage axial compressors, in *ASME Gas Turbine Conference*, June 1994.

[14] E.M. Greitzer, "Surge and rotating stall in axial flow compressors – Part I/II," *J. Engineering for Power*, 199-217, April 1976.

[15] G. Gu, S. Banda and A. Sparks, "An overview of rotating stall and surge control for axial flow compressors," accepted by IEEE Conf. on Dec. and Contr., 1996.

[16] G. Gu, X. Chen, A. Sparks, and S. Banda, "Bifurcation stabilization with local output feedback," submitted to *Systems and Control Letters*, 1996.

[17] G. Gu, A. Sparks, and S. Banda, "Bifurcation based nonlinear feedback control for rotating stall in axial flow compressors," submitted to *Int. J. Contr.*, 1996.

[18] G. Iooss and D.D. Joseph, *Elementary Stability and Bifurcation Theory*, Springer-Verlag, New York, 1980.

[19] W. Kang, "Bifurcation and normal form of nonlinear control systems – Part I and II," submitted *SIAM J. Optimiz. and Contr.*, 1995.

[20] W. Kang, "Bifurcation control via static feedback for single input nonlinear systems," submitted *IEEE Trans. Automat. Contr.*, 1996.

[21] W. Kang, G. Gu, A. Sparks, and S. Banda, "Surge control and test functions for axial flow compressors," preprint, 1996.

[22] P. Kokotovic, A.H. Epstein, E.M. Greitzer, A.J. Krener, R.M. Murray, C.N. Nett and J.D. Paduno, "Robust nonlinear control of stall and flutter in aeroengines," pre-print, 1994.

[23] M. Krstic, J.M. Protz, J.D. Paduano, and P.V. Kokotovic, "Back-stepping designs for jet engine stall and surge control," *Proc. of 34th IEEE Conf. Dec. and Contr.*, 3049-3055, 1995.

[24] M. Krstic, H.-H, Wang, "Modeling and control of deep-hysteresis aeroengine compressors," PRET working paper MD96-4-22.

[25] D.-C. Liaw and E.H. Abed, "Active control of compressor stall inception: A bifurcation-theoretical approach," Technical Report, Institute for Systems Research, University of Maryland, 1992.

[26] C.A. Mansoux, J.D. Setiawan, D.L. Gysling, and J.D. Paduano, "Distributed nonlinear modeling and stability analysis of axial compressor stall and surge," in *American Control Conference*, 1994.

[27] F.E. McCaughan, "Bifurcation analysis of axial flow compressor stability," *SIAM J. Applied Mathematics*, vol. 20, 1232-1253, 1990.

[28] F.K. Moore and E.M. Greitzer, "A theory of post-stall transients in axial compressors: Part I – development of the equations," *ASME J. of Engr. for Gas Turbines and Power*, vol. 108, pp. 68-76, 1986.

[29] J.D. Paduano, A.H. Epstein, L. Valavani, J.P. Longley, E.M. Greitzer, and G.R. Guenette, "Active control of rotating stall in a low-speed axial compressor," *J. Turbomachinery*, vol. 115, 48-56.

[30] J.D. Paduano, L. Valavani, A.H. Epstein, E.M. Greitzer, and G.R. Guenette, "Modeling for control of rotating stall," *Automatica*, vol. 30, 1357-1373, 1994.

[31] A. Packard, "Gain scheduling via linear fractional transformations," *Syst. and Contr. Lett.*, vol. 22, pp. 79, 1994.

[32] J. Protz, "A four-state galerkin approximation to the Moore-Greitzer compressor model," PRET working paper M95-7-15.

[33] W. Rugh, "Analytical framework for gain scheduling," *IEEE Contr. Syst. Magz.*, pp. 79, 1991.

[34] J. S. Shamma and M. Athans, "Gain scheduling: potential hazards and possible remedies," *IEEE Contr. Syst. Magz.*, pp. 101, 1992.

[35] A. Sparks and G. Gu, "Control of compressor rotating stall without distributed sensing using bifurcation theory," preprint, 1996.

[36] H.J. Sussmann, "Subanalytic sets and feedback control," *J. Differential Equations*, 31 (1979), 31-52.

[37] H.O. Wang, R.A. Adomatis and E.H. Abed, "Nonlinear analysis and control of rotating stall in axial flow compressors," in *American Control Conference*, 2317-2321, 1994.

[38] S. Wiggins, *Introduction to Applied Nonlinear Dynamical Systems and Chaos*, Springer-Verlag, New York, NY, 1990.

SCALEABLE PARALLEL PROCESSING
FOR REAL-TIME RULE-BASED DECISION AIDS

Chun-Shin Lin
Associate Professor
Department of Electrical Engineering

University of Missouri-Columbia
Columbia, MO 65211
Tel.: (573)882-3520
e-mail address: lin@ece.missouri.edu

Final Report for :
Summer Faculty Research Program
Wright Laboratory

December 1996

9-1

SCALEABLE PARALLEL PROCESSING
FOR REAL-TIME RULE-BASED DECISION AIDS

Chun-Shin Lin
Associate Professor
Department of Electrical Engineering
University of Missouri-Columbia

Abstract

The project was an extension of the study on *parallel processing for decision aids* performed by the principal investigator during the summer of 1995 at the Air Force Wright Laboratory. The rapid technology development in the past two decades has made modern combat a complicated task. A large amount of information can be available in a mission from both on-board and off-board sources. Effectively utilizing the information is necessary to achieve successful and optimal results. This project extended the previous study and investigated three issues relevant to parallel processing for decision aids. The first one was on fault tolerance. The previous study proposed a parallel processing technique for two-state rule-based decision aids. Each subtask was exclusively assigned to a processing node. In this extension study, we examined a modified scheme that assigned each subtask to multiple processing nodes in order to create fault tolerance. The second part of the study was on parallel neurocomputing. Neural networks have become an important part of decision aids/intelligent systems. Basis function networks were considered in this study. Basis function units were grouped into subsets and assigned to different processors. The PARAGON computer has been used for experiments. The speed-up is excellent when the network size is big. This is because the amount of time for inter-processor communication is relatively small compared to that for basis function computation. Results show that the architecture of mesh processors is good for implementation of large basis function networks. In the third part of the report, we discuss automatic task decomposition for scaleability. With the scaleability, a decision aid/intelligent system could fully utilize available processing resources. Automatic task assignment can help efficiently reconfigure the system.

1. INTRODUCTION

Background

The project is an extension of the study on *parallel processing for decision aids* [1] performed by the principal investigator during the summer of 1995 at the Air Force Wright Laboratory. The rapid technology development in the past two decades has made modern combat a complicated task. A large amount of information can be available in a mission from both on-board and off-board sources. Effectively utilizing the information is necessary to achieve successful and optimal results. Decision aids that operate in real-time are an important issue as all DoD components strive to reduce the crew size of their various weapon systems. The decision aids will help reduce the workload of the crew and increase the efficiency and reliability of operations. Since a large number of criteria and rules must be evaluated and checked in a very short time period in combat automation, parallel processing has been suggested to meet the timing requirement [1-3].

An intelligent decision aid that employs a two-state rule-based scheme may consist of four major portions [2,3]: (1) information collection, (2) information processing and criterion evaluation, (3) rule checking, and (4) action execution (see Figure 1). The information is collected by sensors. The information processing may involve conventional computation and algorithms, as well as neurocomputing and fuzzy logic. Rule-checking will take the criteria values (binary) and determine which rules should be fired. Actions that are associated with the fired rules will then be executed.
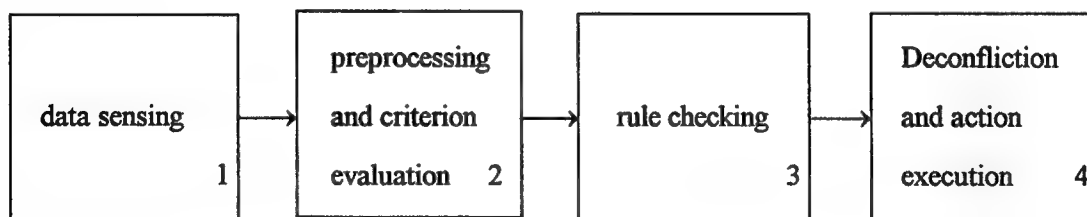
Figure 1. Basic components in a two-state rule-based decision aid

9-3

This extension project investigated three issues. A brief description is given below with details discussed in Sections 3, 4 and 5.

1. *Fault tolerance*

   The previous study [1] proposed a parallel processing technique for two-state rule-based decision aids. Each subtask was exclusively assigned to a processing node. In this extension study, we examined a modified scheme that assigns each subtask to multiple processing nodes in order to create fault tolerance, which is important for reliability.

2. *Parallel neurocomputing*

   Neural networks are becoming an important part of decision aids/intelligent systems. In this study, we considered the implementation of basis function network computation using an architecture of mesh processors. Basis function units were grouped into subsets and assigned to different processors. The PARAGON computer [4] has been used for evaluating the speedup factor.

3. *Automatic task decomposition for scaleability*

   Scaleability is a desired feature. With the scaleability, a decision aid/intelligent system could fully utilize available processing resources. Automatic task decomposition is needed to efficiently reconfigure the system. In Figure 1, each stage can consist of a large amount of small procedures. For instance, evaluating the time derivative of a sensed value or checking whether a rule should be fired can be viewed as basic procedures. In this report, we will discuss some potential techniques for automatically assigning tasks to available processing units.

2. THE INTELLIGENT DECISION AID

The basic block diagram of an intelligent decision-aid has been given in Figure 1. Information is collected by sensors. The information sensed may be preprocessed to generate the derived data for the criterion evaluator. One simple example of derived data is the rate of change of a sensed value. Neural networks may be used in preprocessing too. The outputs of the criterion evaluator are binary values (two-

state). A criterion indicates whether a special condition or a sequence of conditions are satisfied or not. One example is that a specific voltage value has been kept over 5V in the past three time intervals. Criteria are inputs to the rule-checking module.

C_i is used to denote the ith criterion, which has a value of either 0 or 1. $\sim C_i$ denotes the complement of C_i. A rule is represented as a logic minterm (AND of Boolean variables) [2,3]. For instance,

$$R_k : \text{(action list)} \leftarrow C_2 \,\&\, \sim C_5 \,\&\, C_{12}$$

where "&" denotes the logic AND. The above rule is fired when $C_2 = 1$, $C_5 = 0$ and $C_{12} = 1$. When the rule R_k is fired, actions in the action list will be executed. Displaying a piece of information to the pilot, recommending an action or even taking over part of a pilot's tasks are examples of actions.

The Parallel Processing System

This study on parallel processing assumes a 2-dimensional mesh processor architecture. Each processor (a node) can execute its own program and communicate with others through some SEND and RECEIVE commands. The Intel Paragon Computer [4] available in Wright Laboratory for defense research studies belongs to this type. This Paragon consists of 352 general-purpose nodes called GP nodes. Each GP node has a single i860 XP application processor, as well as an additional i860 XP as a message processor for message operations. When an application decides to send a message, the message processor handles the work and frees the application processor to continue with numerical computing. Each GP node has its own 32 Mbytes of memory. The computer system is scaleable and can be easily expanded by adding new nodes. Since the computer is a multi-user system, interference between different processes may exist due to data transmission.

It is noted that the Intel i860 and i960 are used on today's military aircraft. Thus the results from the study using the Paragon are more easily transferable to practical use in operational environments.

With this kind of structure, one can decompose the rule-checking task into p processors and have each processor evaluate the assigned rules. The selection of p should be based on the availability of nodes and the processing load.

Knowledge Representation in Scaleable Two-State Rule-based Systems

As introduced earlier, the rule-based system will have the rules represented in the form

$$R_k : \text{(action list)} \leftarrow C_i \ .. \ \& \sim C_j \ .. \ \& \ C_m$$

The data structure must indicate which criteria are included in each rule. The data structure is illustrated in Figure 2. A list of criteria, called LIST_CRITERIA, used by all rules is constructed. A number i in the list indicates that C_i is included and $-i$ indicates that $\sim C_i$ is included. Another list RULE_POINTER stores the positions of the last criteria of all rules (see Figure 2) [1-2]. For example, RULE_POINTER[j] is the pointer to the last criterion used by the rule R_j. If a = RULE_POINTER[j-1] and b = RULE_POINTER[j], then the rule R_j uses the criteria denoted by LIST_CRITERIA[a+1], LIST_CRITERIA[a+2], ... LIST_CRITERIA[b]. Note that h, p and q in the figure are either positive or negative criteria numbers.
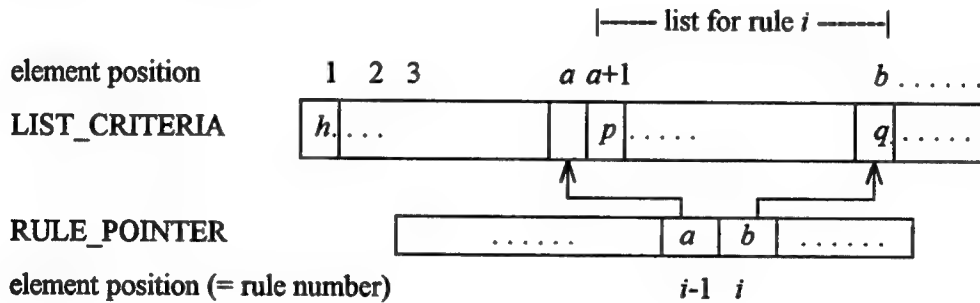
Figure 2. Data structure for rule base.

The system will have a rule fired at the time when all involved criteria become true. The rule will be kept at a fired status until one or more involved criteria become unsatisfied. At any time, only the rules involving the criteria that change values need to be checked. Thus it is more efficient to construct a data structure to make it easier to find the set of rules that need to be checked. This means backward pointers from criteria to rules are needed. This requires the construction of a data structure similar to the one

above. Figure 3 shows such an index structure for backward pointers. CRITERION_POINTER provides information for quickly determining which subset of rules in the list LIST_RULES should be evaluated.
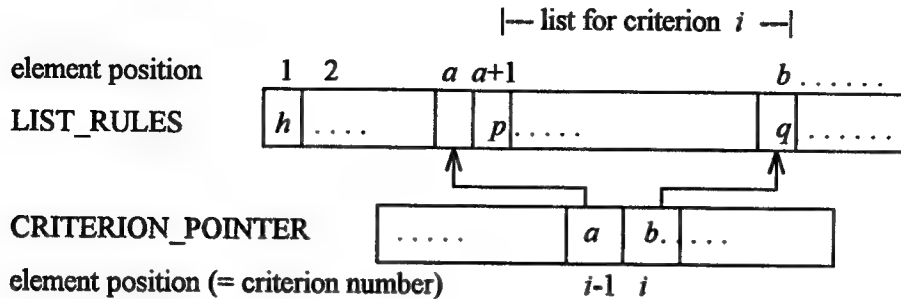
Figure 3. An index structure denoting which rules are used by a criterion

Note that the first data structure consists of complete knowledge and the second one can be derived from it.

Rule-Base Knowledge for Each Processing Node

In the previous study [3], each node checked only a subset of rules. Thus it didn't need the complete rule-base knowledge. The data structure for the subset of rules can be represented in a similar structure as that for the overall knowledge shown in Figures 2 and 3. However, only a sublist from the LIST_CRITERIA and a sublist from RULE_POINTER will be stored for each processor. In the index data structure, the length of CRITERION_POINTER will remain the same but the rules in RULE_LIST not handled by the assigned node will be removed. The subsets of rule bases can be generated from the overall rule base by a computer program.

3. ASSIGNING EACH RULE SUBSET TO MULTIPLE PROCESSORS

The scheme previously investigated decomposed the rule base into subsets and assigned one exclusive node to check a subset of rules. If a processing node fails, all rules assigned to it would not be checked.

To create the fault tolerance, one can divide the rule-checking task into smaller subtasks and have each subtask assigned to at least two processing nodes. Figure 4 illustrates the idea. The rules are divided

into smaller subsets and each processing node covers a larger set of rules (with overlapping). Each subset can now be checked by one of two or more processors. Although a subset is assigned to two or more nodes, it will be checked by only one processor, the one that becomes available first. With the modified arrangement, failure of nodes that are not assigned common subsets will not fail the system.

subsets:

node assignment: ...   n-1   n   n+1 ...
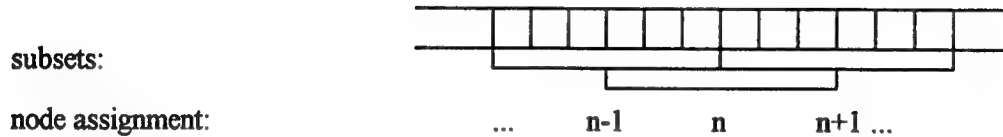
Figure 4. Decomposition of rules and assignment to nodes

We have performed experiments for cases with two processing nodes assigned to each subset of rules. Rules assigned to each processing node were divided into 2 or more subsets. Figure 5 gives examples of different arrangements. Figure 5(a) shows an arrangement for 3 processors which are each assigned 2 subsets. Note that each subset is covered by two processors. Each processing node will start from the middle subset. For example, for the 4 processors/4 subsets case in Figure 5(g), processing node 2 will check subset 4 first, then 5, 3 and 6. Before checking a subset, a processor probes its neighbors that are also assigned the same subset to see if any neighbor has checked it. If not, the processing node will send a message to those neighbors and check the subset. If yes, the processor will skip this subset and try to check others.
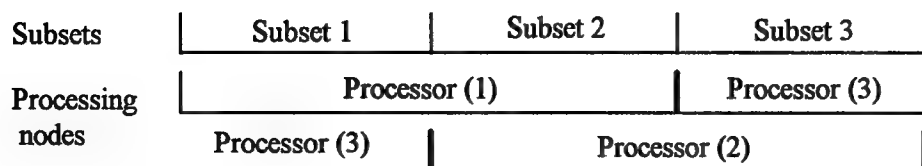
Subsets	Subset 1	Subset 2	Subset 3

Processing nodes	Processor (1)	Processor (3)
	Processor (3)	Processor (2)

(a) 3 nodes, 2 subsets per node.

Subsets				

Processing nodes	(1)	(3)
	(3)	(2)

(b) 3 nodes, 3 subsets per node.

Subsets						

Processing nodes	(1)	(3)
	(3)	(2)

(c) 3 nodes, 4 subsets per node.

Subsets							

Processing nodes	(1)	(3)
	(3)	(2)
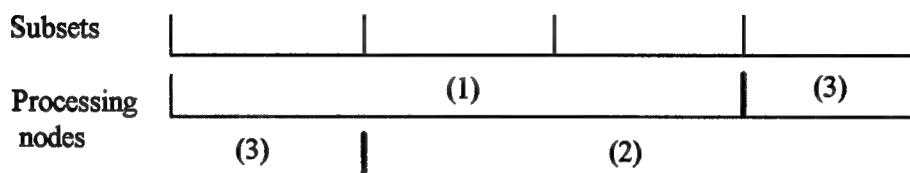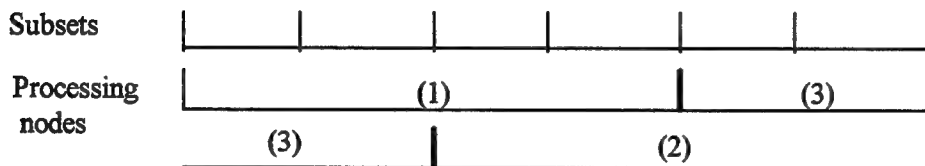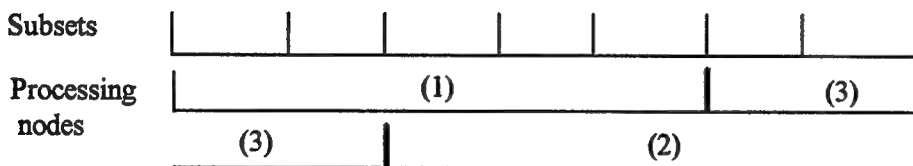
(d) 3 nodes, 5 subsets per node.

Figure 5. (to be continued)
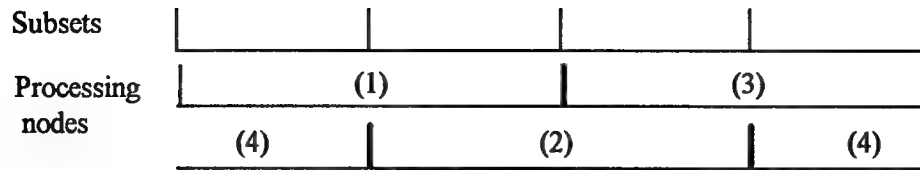
9-9

Subsets

Processing nodes

(1)   (3)

(4)   (2)   (4)

(e) 4 nodes, 2 subsets per node.

Subsets

Processing nodes

(1)   (3)

(4)   (2)   (4)

(f) 4 nodes, 3 subsets per node.

Subsets

| 1 | 2 | 3 | 4 | 5 | 6 | 7 | 8 |

Processing nodes

(1)   (3)

(4)   (2)   (4)

(g) 4 nodes, 4 subsets per node.

Subsets

Processing nodes

(1)   (3)

(4)   (2)   (4)
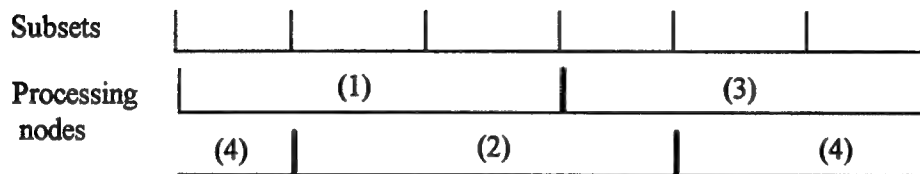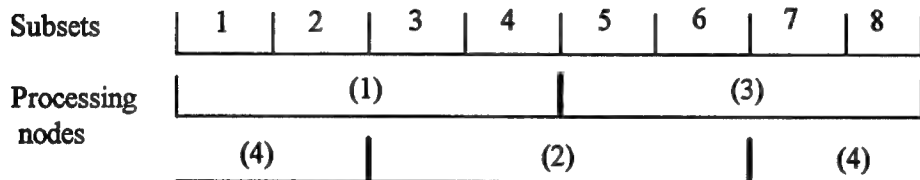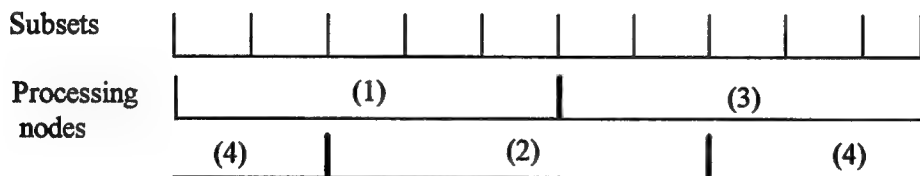
(h) 4 nodes, 5 subsets per node.

Figure 5. Examples of arrangements using different numbers of subsets and processing nodes.

Experiments have been performed to evaluate the performance for the cases with 3 to 9 processors and 2 to 6 subsets per processor. Two different sets of rule bases have been used. These two sets are 31508 and 64010 generated using the following specifications:

31508: 3000 rules, 1500 different criteria, at most 8 criteria in each rule.

64010: 6000 rules, 4000 different criteria, at most 10 criteria in each rule.

The performance for each arrangement is compared to the one using a single processor. *Speed-up* that is defined as

Speed-up = time to execute on one processor / time to execute on *p* processors

is obtained. Curves of *Speed-up* are plotted in Figure 6.

The S*peed-up* factor for the case with three processing nodes is around 1 to 1.6. With the number of nodes doubled, the *Speed-up* can be increased to about 1.4 to 2.3. The improvement in the processing speed is less significant because of the heavy overhead in the necessary inter-processor communication. Unless the rule set is very large such that the communication time is relatively small compared to the time for rule checking, the merit on speed improvement will not be very significant and the main benefit will be fault tolerance.

We have also evaluated the performance assuming that one processor fails. The processing time is plotted in Figure 7. The execution time using a single processor is 0.70528 seconds for the set 31508 and 0.83124 seconds for the set 64010.
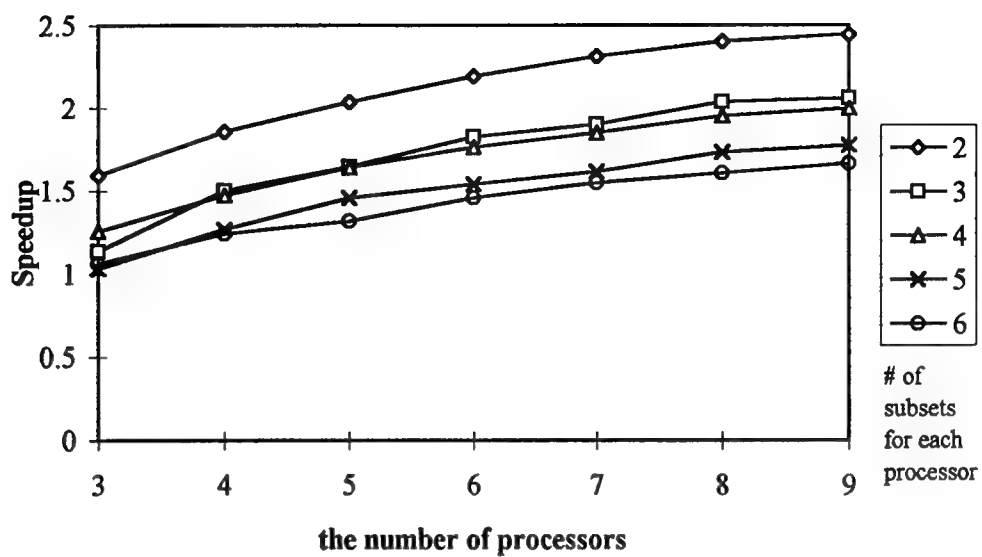
(a) Speedup for the data set 31508.
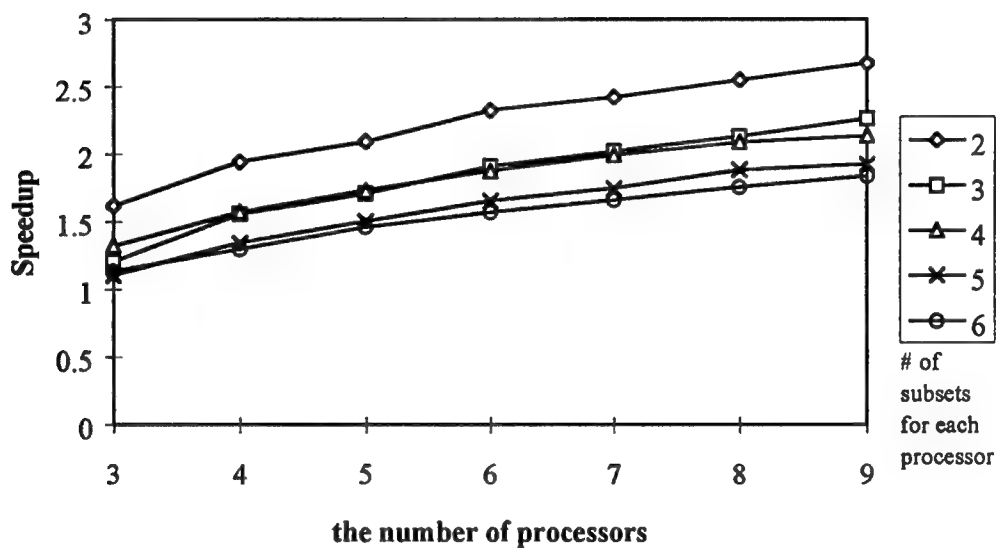
(b) Speedup for the data set 64010.

Figure 6. Speedup for different arrangements.
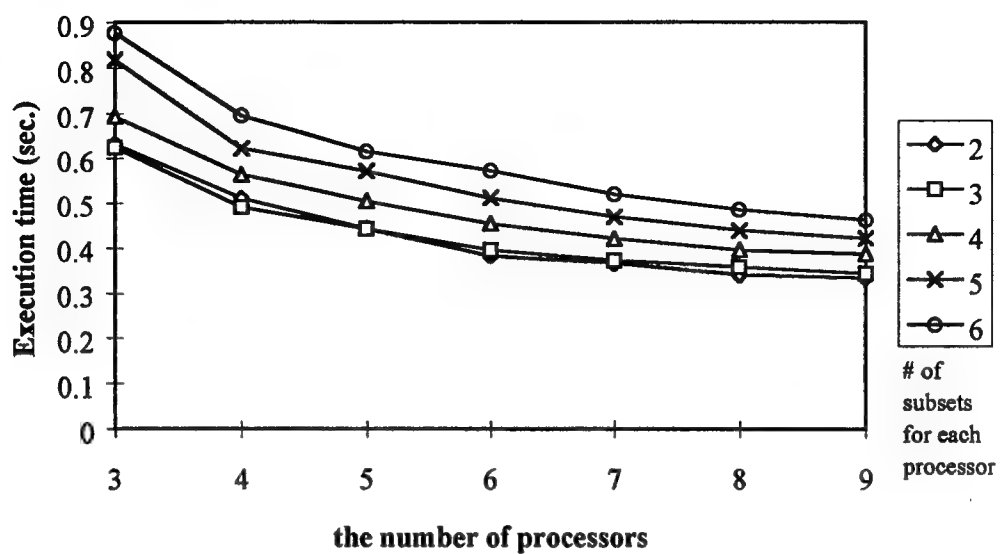
(a) Execution time for the data set 31508.
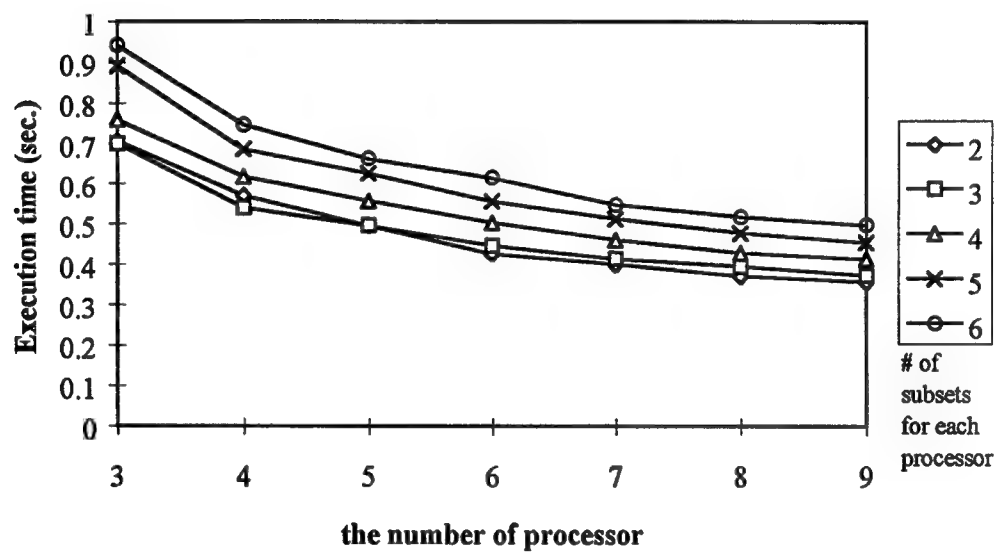
(b) Execution time for the data set 64010.

Figure 7. Execution time for different arrangements.

9-13

4. PARALLEL PROCESSING FOR NEUROCOMPUTING

Efforts have been also devoted to parallel processing of neural nets, which have become important components in decision aids/intelligent systems. The similar idea introduced in Section 2 for rule checking can be applied to parallelizing the neurocomputing. Gaussian function based neural networks are considered. The basis function units are grouped into small subsets. The performance has been evaluated for different sizes of neural networks and the different numbers of processors.

Basis Function Network

Figure 8 shows a basis function network (BFN). Each row is a basis function unit. Notation b denotes the global bias. ψ is the basis function and w_k is the weight. The input vector entering the kth neuron is translated by t_k, rotated by R_k, and then scaled by D_k. D_k is a diagonal matrix, of which each diagonal element s_i is a scaling factor. The transformed vector is used as the input to the basis function ψ.
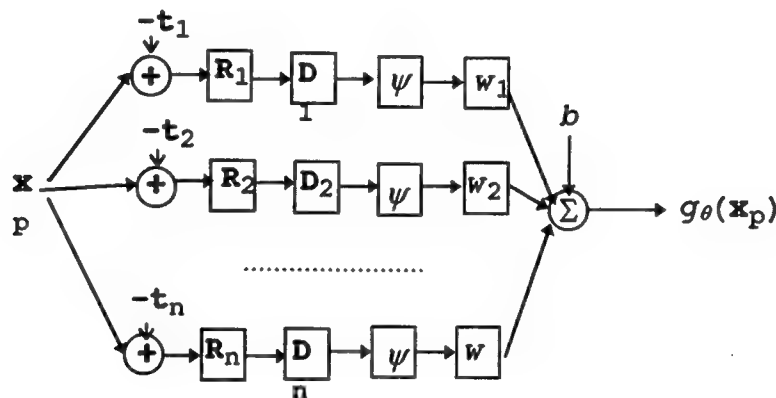
Figure 8. RBFN and its learning parameters.

The network output is computed as

$$g_\theta(\mathbf{x}_p) = \sum_{k=1}^{n} w_k \psi \left[\mathbf{D}_k \mathbf{R}_k (\mathbf{x}_p - \mathbf{t}_k) \right] + b .$$ (1)

Learning tries to minimize the following cost function:

$$c(\theta, \mathbf{x}_p, \mathbf{y}_p) = \frac{1}{2}[\mathbf{g}_\theta(\mathbf{x}_p) - \mathbf{y}_p]^2. \tag{2}$$

The learning rules for development of a desired functional approximation or mapping can be found from [5].

Parallel Processing for BFN Using the PARAGON Architecture

In the parallel processing, processing node 0 is assumed to get the input vector, send it to processing nodes 1 through p, receive the computational results from them, and compute the final output vector. Each of the processing nodes 1 through p is assigned to handle the computation for a subset of basis function units. The structure is shown in Figure 9, in which each row in Figure 8 is denoted by a circle.

Experiments have been performed for Gaussian basis function networks with *four* inputs and *four* outputs, and for those with *eight* inputs and *eight* outputs. The speed-up factor has been evaluated. The results are shown in Figure 10. Curves in the two figures are for different numbers of basis units. The results apparently show that the efficiency increases when the network size becomes large. For big networks, the overhead in inter-processor communication is relatively insignificant.

9-15
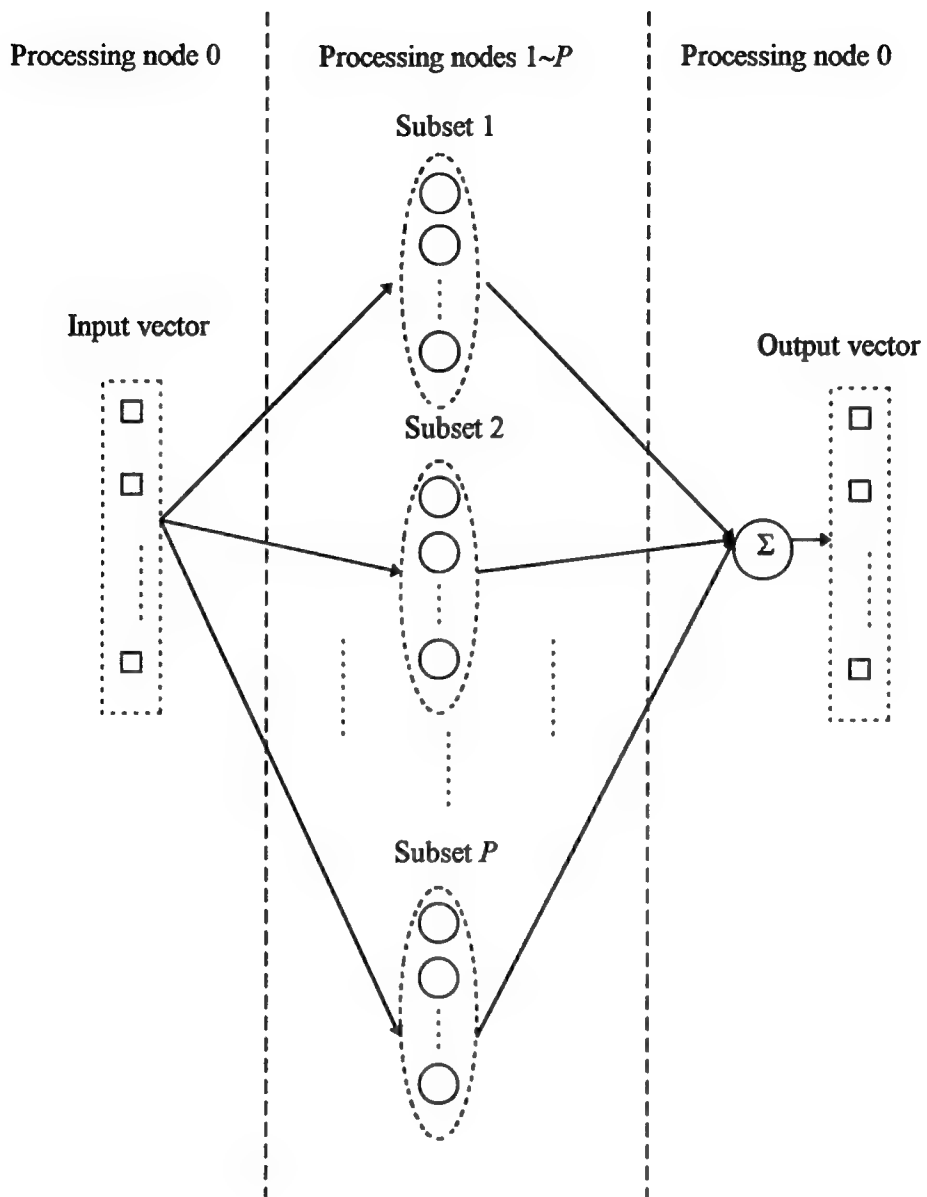
Figure 9. The structure for parallel processing for BFN.
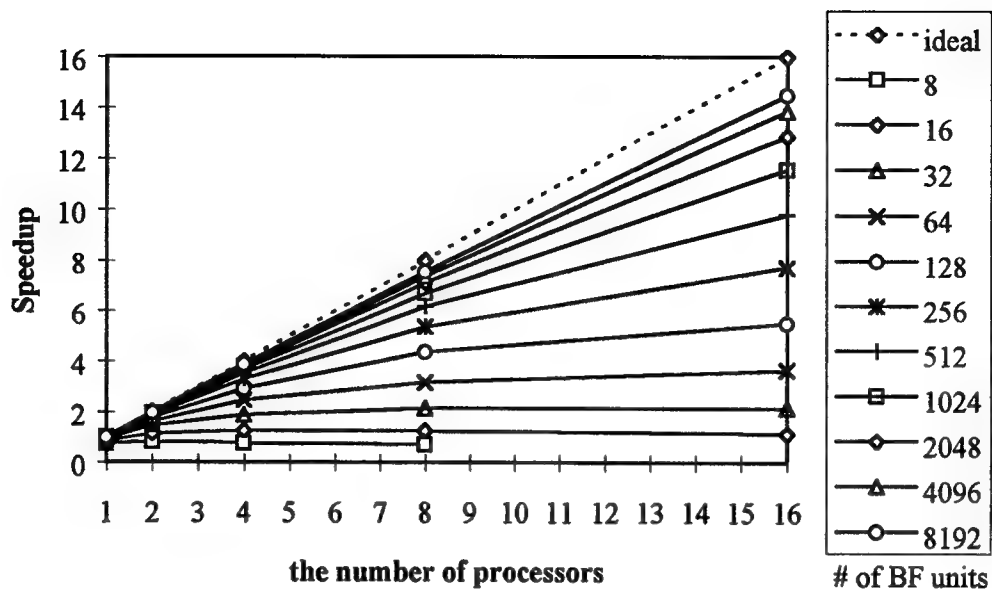
(a) Speedup vs. The number of processors (4 inputs and 4 outputs).
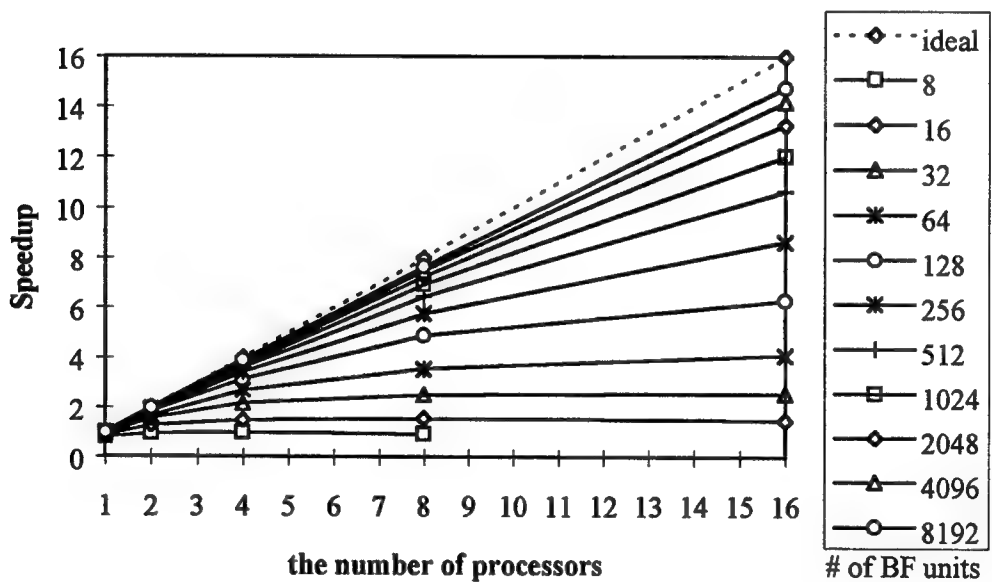
(b) Speedup vs. the number of processors (8 inputs and 8 outputs).

Figure 10. Speedup for different arrangements.

9-17

5. AUTOMATIC TASK DECOMPOSITION FOR SCALEABILITY

Scaleability is a desired feature. It will be necessary to reconfigure the system if there are not enough processing resources or part of the decision aid has been modified. Automatic task decomposition is needed to efficiently reconfigure the system. Each stage in Figure 1 is assumed to include a large amount of small procedures. These procedures should be grouped into subsets and assigned to available nodes. To be able to perform the task decomposition work, information regarding inputs, outputs and the execution time of each procedure (as shown in Figure 11) is required.

stage 1   Stage 2   Stage 3 .

P_{11}: (input list), (output list), (execution time). P_{21}: (input list), (output list), (execution time)   . . .   .

P_{12}: (input list), (output list), (execution time). P_{22}: (input list), (output list), (execution time)   . . .   .

.   .   .

.   .   .

.   .   .

(P_{ij}'s are procedures)

Figure 11. Information for procedures.

When a modification on the decision aid is made (add/delete/modify a procedure), only related parts need to be updated. The information given in Figure 11 implicitly specifies a tree structure of task dependence.

9-18

Task Scheduling

With the information in Figure 11 available, a procedure can be devised to assign tasks to available processing nodes. The goal is to minimize the processing time with available resources. A possible procedure for task scheduling [6,Ch2] uses the following rule:

The number of successors of a subtask is used as its priority. Whenever a processing node becomes available, the unexecuted ready subtask with the highest priority will be assigned.

Figure 12 shows an example of task trees and the results of task assignments. Two numbers in each node in the task trees denote the subtask number and the needed processing time. Subtasks in two trees are to be assigned to two processors. Based on the rule given above, subtask 1 with two successors is assigned to processor 1, and subtask 5 is assigned to processor 2 since it is the only ready task. Subtask 1 is finished earlier. Subtask 3 with one successor will then be assigned to processor 1 (after subtask 1). The assignment will continue until all subtasks are assigned.
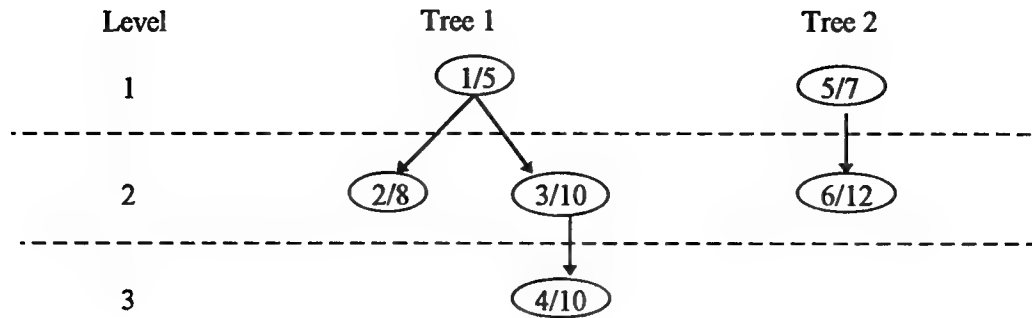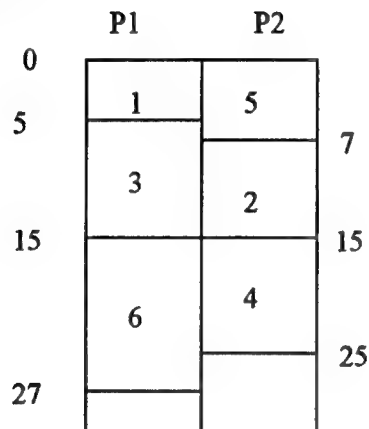
Figure 12. An example of task scheduling.

Clustering Technique

Necessary inter-communication time is not considered in the above scheme. Subtask 6 will need the result from subtask 5 but is assigned to a different processor. Communication time will then be needed. The problem could be solved by applying a clustering algorithm that groups subtasks, and makes them executed on the same processing node. The purpose is to reduce the communication time. The flow chart in Figure 13 shows the procedure [6,Ch6]. The procedure first initializes all links in the task tree to be unmarked and makes each subtask a cluster. It then finds the longest path

composed of unmarked links. The subtask nodes in the path are grouped into a cluster, and the links are marked and link costs are zeroed. The procedure is repeated until all links are marked.

```
                    ┌─────────┐
                    │  Begin  │
                    └────┬────┘
                         │
          ┌──────────────▼──────────────┐
          │ Get the tree structure of the task. │
          └──────────────┬──────────────┘
                         │
          ┌──────────────▼──────────────┐
          │ Initialize all links to be unmarked │
          │ and have each node form a cluster.   │
          └──────────────┬──────────────┘
                         │
          ┌──────────────▼──────────────┐
          │           r = 0.             │
          └──────────────┬──────────────┘
                         │
          ┌──────────────▼──────────────┐
          │ Search for the longest path that │
          │ composed of unmarked links.      │
          └──────────────┬──────────────┘
                         │
          ┌──────────────▼──────────────┐
          │ Put the nodes in the path into   │
          │ cluster r. Mark the links along the │
          │ path. Set the link costs to zero.   │
          └──────────────┬──────────────┘
                         │
          ┌──────────────▼──────────────┐
          │         r = r + 1.           │
          └──────────────┬──────────────┘
                         │
                  ◇ All links are marked ? ◇
                   No │         │ Yes
                      │    ┌────▼────┐
                      │    │   End   │
                      │    └─────────┘
```
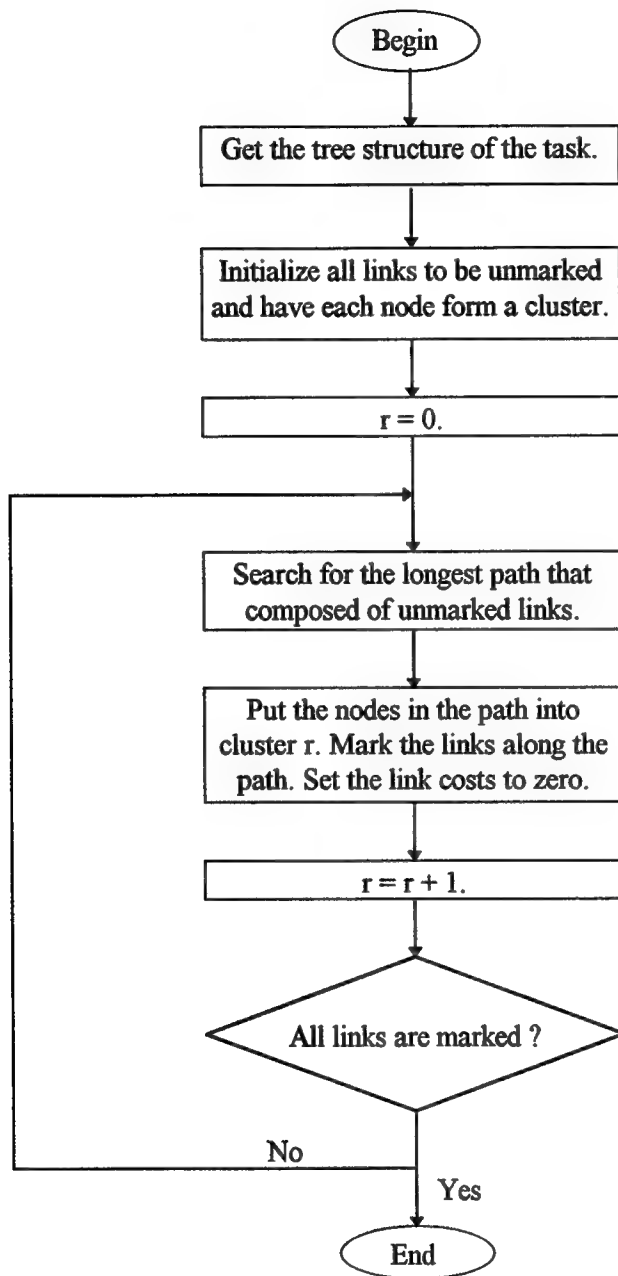
Figure 13. The flow chart for the clustering algorithm

9-21

Figure 14 shows one example applying the clustering algorithm. The time for inter-processor communication will be reduced if a cluster of subtasks is assigned to the same processor. A task scheduling algorithm should assign tasks in the same cluster to the same processing node.
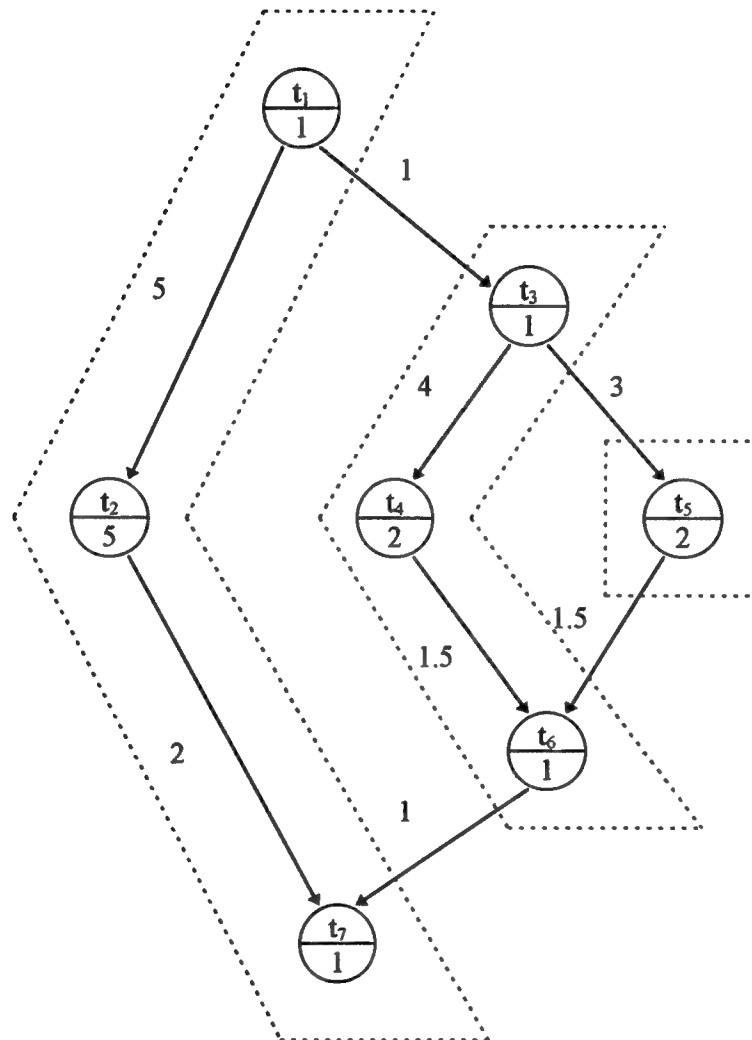
Figure 14. An example after applying the clustering algorithm (after [6]).

6. CONCLUSION

In this project, we investigated parallel processing techniques for possible usage in decision aids. In the first part, we evaluated the performance of parallel processing for two-state rule-based decision aids. Each subset of rules was assigned to multiple processors in order to have fault tolerance. Due to the inter-processor communication time, the improvement in speed was not very significant as expected. Fault tolerance is one merit with such an arrangement. In the second part, we used the PARAGON computer for parallel computation for basis function networks. The speed-up is excellent if the network size is large. This is because the amount of time for inter-processor communication is relatively small compared to that for basis function computation. Results show that the architecture of mesh processors is good for implementation of large basis function networks. In the third part, we discussed techniques for scheduling tasks to multiple processing nodes. The clustering algorithm is a technique that can help reduce the inter-processor communication.

7. REFERENCES

1. Lin, C.S., "Parallel Processing for-Real-time, Rule-based Decision Aids," 1995 Air Force Summer Faculty Research Program Report, Wright Laboratory

2. Raeth, P. G., J L. Noyes and A. J. Montecalvo, "A Scaleable Frame Work for Adding Crisp Knowledge to Pilot/Vehicle Interfaces," 1994 IEEE International Conference on Systems, Man, and Cybernetics, pp. 2091-2096, Oct. 1994.

3. Noyes, J. L., "Expert System Rule-base Evaluation Using Real-time Parallel Processing," WL-TR-93-3098, Fight Dynamics Directorate, Wright Laboratory, Wright Patterson AFB, Ohio.

4. Paragon User's Guide. Intel Corporation, June 1994.

5. Cheng, Y.-H. and C.S. Lin, "Application of Dynamic Radial Basis Function Networks on Image Histogram Clustering," Intelligent Engineering System through Artificial Neural Networks, Vol. 4, Eds. Dagli, C.H. *et al*. ASME Press, 1994.

6. El-Rewini, H., T. G. Lewis and H. H. Ali, "Task Scheduling in Parallel and Distributed System,", NJ: PTR Prentice Hall, 1994.

James Marsh
Report not available at time of publication.

EXPERIMENTAL AND COMPUTATIONAL INVESTIGATIONS OF BROMINE AND IODINE CHEMISTRY IN FLAME SUPPRESSION

Paul Marshall
Associate Professor
Department of Chemistry

University of North Texas
PO Box 5068, Denton, Texas 76203-0068

EXPERIMENTAL AND COMPUTATIONAL INVESTIGATIONS OF BROMINE AND IODINE CHEMISTRY IN FLAME SUPPRESSION

Paul Marshall

Associate Professor

Department of Chemistry

University of North Texas

PO Box 5068, Denton, Texas 76203-0068

Abstract

Rate constants for the reaction of H atoms with the alkyl iodides iodomethane (1), iodoethane (2), 2-iodopropane (3) and 2-iodo-2-methyl propane (4) have been measured using the flash-photolysis resonance fluorescence technique. The resuts are $k_1 = (6.8 \pm 0.3) \times 10^{-11} \exp((-5.4 \pm 0.1)$ kJ mol^{-1}/RT) (T = 297-757 K), $k_2 = (1.1 \pm 0.2) \times 10^{-10} \exp((-5.9 \pm 0.8)$ kJ mol^{-1}/RT) (T = 295-624 K), $k_3 = 1.4 \times 10^{-11}$ (T = 295 K) and $k_4 = 2.0 \times 10^{-11}$ (T = 294 K) cm^3 molecule^{-1} s^{-1}. Estimated accuracies are discussed in the text. The transition state for $H + CH_3I \rightarrow I + CH_4$ was characterized at the Gaussian-2 level of *ab initio* theory, and substitution was shown to be a slow process. H-atom abstraction is also argued to be slow, and the dominant pathway for H + iodomethane reactions is suggested to be I-atom abstraction leading to HI formation.

EXPERIMENTAL AND COMPUTATIONAL INVESTIGATIONS OF BROMINE AND IODINE CHEMISTRY IN FLAME SUPPRESSION

Paul Marshall

Introduction

There is growing interest in the combustion chemistry of iodine compounds, arising from the search for substitutes for the halon fire extinguishing agents CF_3Br and CF_2ClBr.[1] Halon production is banned under the Montreal Protocols on Substances that Deplete the Ozone Layer. CF_3I is a potential candidate for service as a new fire suppressant, but there is a lack of kinetic information for iodine reactions, especially at elevated temperatures. Modeling of the radical inhibition chemistry of CF_3I suggests that significant destruction of H-atom chain carriers occurs via CH_3I formed in flames from $CH_3 + I$ recombination, followed by reaction of CH_3I with H atoms.[2] The reaction

$$CH_3I + H \quad \rightarrow \quad products \tag{1}$$

has been argued to be the dominant process for CH_3I consumption in a stoichiometric CH_4/air flame.[3] To date there have been several studies of reaction 1 at room temperature,[4,5,6,7] but the temperature dependence of the rate constant k_1 has not been measured. Based on the thermochemistry of CH_2I[8] and other species[9] there are three exothermic product channels:

$$CH_3I + H \quad \rightarrow \quad CH_3 + HI \qquad \Delta H_{298} = -61 \text{ kJ mol}^{-1} \tag{1a}$$

$$\rightarrow \quad CH_2I + H_2 \qquad \Delta H_{298} = -3 \text{ kJ mol}^{-1} \tag{1b}$$

$$\rightarrow \quad CH_4 + I \qquad \Delta H_{298} = -201 \text{ kJ mol}^{-1} \tag{1c}$$
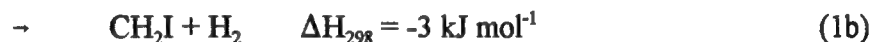
The transition state for 1a has been characterized computationally by Schiesser et al.,[10] while Marshall et al.[3] have analyzed the transition states for channels 1a and 1b using the Gaussian-2 methodology of Pople and coworkers,[11] as extended to iodine compounds by Glukhovtsev et al.,[12] and derived high-temperature *ab initio* rate constants and branching ratios for H vs I abstraction. In the present work the *ab initio* analysis is extended to the dispacement channel 1c.

There has been a single study[13] of

$$C_2H_5I + H \quad \rightarrow \quad products \tag{2}$$

which yielded an experimental room temperature value of k_2 about two orders of magnitude smaller

than literature values for k_1. The present work describes the first measurements of the temperature dependences of k_1 and k_2, and resolves the discrepancy. Structural factors that contribute to the reactivity of iodoalkanes are also considered, and the reactivities of primary, secondary and tertiary C-I bonds are compared through room temperature measurements of

$$CH_3CHICH_3 + H \quad \rightarrow \quad products \tag{3}$$

for which there is one prior determination[13] and

$$(CH_3)_3CI + H \quad \rightarrow \quad products \tag{4}$$

which appears not to have been studied previously. Likely products are discussed, and the results are compared with *ab initio* information about channels 1a-1c.

Experimental method

The experimental apparatus and modifications for H-atom kinetics have been described elsewhere.[14,15,16] Briefly, atomic H was generated by pulsed flash lamp photolysis of NH_3, through MgF_2 optics, in the presence of a large excess of iodoalkane. All experiments were carried in Ar bath gas at a total pressure P. The concentration of H was monitored using time-resolved resonance fluorescence at a wavelength of 121.6 nm. Fluorescence was detected with a solar-blind photomultiplier tube employed with pulse counting and signal averaging. Under the pseudo-first-order conditions and fixed $[NH_3]$,

$$d[H]/dt = -(k_X[X] + k_{diff})[H] = -k_{ps1}[H] \tag{5}$$

where X is an iodoalkane and k_{diff} accounts for loss of H atoms out of the reaction zone other than by reaction with X (mainly by diffusion to the reactor walls). k_{ps1} was obtained by fitting the observed fluorescence intensity I_f versus time profiles to an exponential decay (an example is shown as the inset on Fig. 1), and the second-order H + X rate constant k_X was found from linear plots of k_{ps1} versus typically five values of [X], from 0 to $[X]_{max}$ (see Fig. 1). The temperature T in the reaction zone was monitored with a thermocouple, corrected for radiation errors, before and after each set of k_X measurements. The average residence time of gas mixtures in the heated reactor before photolysis, τ_{res} was varied to check for possible pyrolysis of the iodoalkanes, while the energy disharged through the flash lamp, F, was varied to alter the intial radical concentrations.

The Ar (Air Products, 99.997%) was used directly from the cylinder and NH_3 (MG Industries,

99.99%) was purified by freeze-pump-thaw cycles from 77 K. The iodoalkanes (CH_3I, Aldrich 99% and 99.5%; C_2H_5I, Lancaster, 99%; CH_3CHICH_3, Aldrich, 99%; $(CH_3)_3CI$, Aldrich, 95%)) were purified by distillation, from 273 K for the first two reagents and from room temperature for the latter two, and condensed at 77 K, to remove any iodine contamination.

Results

The experimental conditions and results for k_1, k_2, k_3 and k_4 are summarized in Tables 1-3. The k_1 results were independent of the two different lots of CH_3I employed. The lack of dependence of k_X on F shows that secondary chemistry involving photolysis or reaction products was negligible, and the lack of dependence of k_1 and k_2 on τ_{res} shows that pyrolysis of CH_3I and C_2H_5I was unimportant at the listed temperatures. Data for reactions 1 and 2 at higher temperatures did show consistent variation with τ_{res}, and for reaction 2 showed a decrease in the apparent k_2 above 630 K, and therefore were excluded from further analysis.

The Arrhenius plot for reaction 1 is shown in Fig. 2, and the weighted linear fit yields

$$k_1 = (6.8 \pm 0.3) \times 10^{-11} \exp((-5.4 \pm 0.1) \text{ kJ mol}^{-1}/RT) \text{ cm}^3 \text{ molecule}^{-1} \text{ s}^{-1} \qquad (6)$$

The quoted errors in the Arrhenius parameters are 1σ and are statistical only. Consideration of the covariance leads to a 1σ precision for the fitted k_1 of 1-2 %, and allowance for possible systematic errors leads to 95% confidence intervals of $\pm10\%$. The Arrhenius plot for reaction 2 is shown in Fig. 2, and the weighted linear fit yields

$$k_2 = (1.1 \pm 0.2) \times 10^{-10} \exp((-5.9 \pm 0.8) \text{ kJ mol}^{-1}/RT) \text{ cm}^3 \text{ molecule}^{-1} \text{ s}^{-1} \qquad (7)$$

Consideration of the covariance leads to a 1σ precision for the fitted k_2 of 5-13%, and allowance for possible systematic errors leads to 95% confidence intervals of $\pm28\%$ at the extremes of the experimental T range to $\pm14\%$ at the center. Similar accuracies, about $\pm20\%$, are expected for reactions 3 and 4 which were studied at room temperature only (see Table 1).

Discussion

Our k_1 values are compared with four previous measurements in Fig. 3, and it may be seen that there is particularly good accord with the most recent literature value $k_1(298 \text{ K}) = (7.9 \pm 0.8) \times 10^{-12} \text{ cm}^3 \text{ molecule}^{-1} \text{ s}^{-1}$.[7] There is a single previous determination of k_2, based on a rate measurement

relative to

$$H + HI \quad \rightarrow \quad H_2 + I \tag{7}$$

and which Rebbert et al. reported as $k_2 = 7 \times 10^{-14}$ cm^3 molecule^{-1} s^{-1}.[13] This is a factor of 150 smaller than measured here. Based on Sullivan's measurements of the reverse of reaction 7,[17] Rebbert et al. used $k_7 = 1.7 \times 10^{-13}$ cm^3 molecule^{-1} s^{-1}.[13] However, Baulch et al. used Sullivan's data and the equilibrium constant for reaction 7 to obtain $k_7 \approx 5 \times 10^{-11}$ cm^3 molecule^{-1} s^{-1} for T $\doteq$ 667-800 K,[18] a calculation which we reproduce. The source of the discrepancy appears to be mainly that an incorrect value of k_7 was employed earlier,[13] while the earlier rate constant *ratio* k_2:k_7 was essentially correct. The same explanation accounts for much of the discrepancy between the value of k_3 given by Rebbert et al.,[13] 1.6×10^{-13} cm^3 molecule^{-1} s^{-1}, and our own direct measurement (Table 3) which is 90 times higher. There appear to be no literature values for k_4.

As noted in the introduction, there are three possible reaction pathways for the H plus iodoalkane reactions, I-abstraction, H-abstraction and I-substitution. The most exothermic process is displacement of the I atom. We have characterized the transition state for this process at the HF/6-31G(d) and MP2=full/6-31G(d) levels of theory, and the geometry is shown in Fig. 4. Higher level single-point energy calculations yielded the G2 energy (see Table 4) which approximates a QCISD(T)/6-311+G(3df,2p) result.[11,12] Computations were carried out with the Gaussian 94 program suite.[19] Relative to the G2 energy of H + CH$_3$I,[12] the G2 barrier to substitution at 0 K is predicted to be 45 kJ mol^{-1}. This barrier means that I-atom displacement is kinetically unfavorable. Furthermore, the transition state for this process is found to be tight. The unscaled MP2=full/6-31G(d) frequencies (Table 4) and the geometry, together with entropy data for H and CH$_3$I,[20] lead to the entropy of activation for reaction 1c of $\Delta S^{\ddagger}_{298} = -91$ J K^{-1} mol^{-1} and an implied preexponential factor at 298 K of about 2×10^{-13} cm^3 molecule^{-1} s^{-1}, more than two orders of magnitude below that observed. Substitution will therefore make a negligible contribution to the total k_1.

An approximate idea of the rate constant for channel 1b can be obtained by consideration of the analogous reaction

$$H + CH_4 \quad \rightarrow \quad H_2 + CH_3 \tag{8}$$

for which k_8 is approximately 7.4×10^{-19} cm^3 molecule^{-1} s^{-1} at 298 K.[21] This is about 10^{-7} of k_1 at room temperature, and therefore H abstraction plays a negligible role in reaction 1. This is a reasonable

comparison, bearing in mind the similar C-H bond strengths[8] in CH_4 and CH_3I and, further, is in accord with an earlier G2 *ab initio* analysis.[3] In summary, $k_1 \approx k_{1a}$. A similar assessment of H-abstraction can be made for the heavier iodoalkanes. In these molecules all of the C-H bonds are primary, and the rate constant for H-abstraction from iodoalkanes was estimated as n/6 times the rate constant for $H + C_2H_6$ (4.5×10^{-17} cm^3 $molecule^{-1}$ s^{-1} at 298 K),[21] where n is the number of C-H bonds. The results are shown in Table 5, and in all cases the H-abstraction channel is minor.

k_X at 298 K and the C-I bond dissociation enthalpy DH_{298} are compared in Table 5. DH_{298} values were derived from literature enthalpies of formation for alkyl radicals[22] and iodoalkanes and I atoms,[9] and have uncertainties of about 2-3 kJ mol^{-1}. There is a monatonic trend for k_X along the series CH_3I and primary to tertiary. There is also a rough correlation with DH_{298}, where within the thermochemical uncertainty the species with the weakest C-I bonds are the most reactive.

Finally, we note that there is reasonable accord between the *ab initio* k_1[3] and that measured here: at 298 K the *ab initio* k_1 expression is too high, relative to eq. 6, by a factor of 1.15, which increases to a factor of 2.9 at 760 K. As seen in Fig. 3, the discrepancies at higher temperatures arise from the higher curvature predicted for the Arrhenius plot of k_1. A possible explanation is that variational effects are important, and therefore that the conventional transition state theory analysis overestimates k_1.[23] Such effects are generally more significant for reactions with smaller energy barriers, as is the case here.

Conclusions

The temperature dependences of the rate constants for reactions of H atoms with CH_3I and C_2H_5I have been measured for the first time, and room temperature rate constants for $H + CH_3CHICH_3$ and $H + (CH_3)_3CI$ have also been characterized. The results are consistent with I-abstraction as the main reaction pathway, and any contributions from I-substitution and H-abstraction are small.

ACKNOWLEDGMENTS

References

1. Tsang, W.; Miziolek, A. W. *Halon Replacements: Technology and Science* (ACS Symposium Series 611, 1995).

2. Noto, T.; Babushok, V.; Burgess, D. R. Jr.; Hamins, A.; Tsang, W.; Miziolek, A. *26th Symp. (Int.) Combust.* in press.

3. Marshall, P.; Misra, A.; Berry, R. J. *Chem. Phys. Lett.* in press.

4. Leipunskii, I. O.; Morozov, I. I.; Tal'roze, V. L. *Dokl. Phys. Chem.* **1971**, *198*, 547. Russ. orig. p. 136.

5. Levy, M. R.; Simons, J. P. *J. Chem. Soc. Faraday Trans. 2* **1975**, *71*, 561.

6. Sillesen, A.; Ratajczak, E.; Pagsberg, P. *Chem. Phys. Lett.* **1993**, *201*, 171.

7. Gilles, M. K.; Turnipseed, A. A.; Talukdar, R. K.; Rudich, Y.; Villalta, P. W.; Huey, L. G.; Burkholder, J. B.; Ravishankara, A. R. *J. Phys. Chem.* **1996**, *100*, 14005.

8. McMillen, D. F.; Golden, D. M. *Ann. Rev. Phys. Chem.* **1982**, *33*, 493.

9. Lias, S. G.; Bartmess, J. E.; Liebman, J. F.; Holmes, J. L.; Levin, R. D.; Mallard, W. G. *Gas-Phase Ion and Neutral Thermochemistry, J. Phys. Chem. Ref. Data* **1988**, *17*, Suppl. 1.

10. Schiesser, C. H.; Smart, B. A.; Tran, T.-A. *Tetrahedron* **1995**, *51*, 3327.

11. Curtiss, L. A.; Raghavachari, K.; Trucks, G. W.; Pople, J. A. *J. Chem. Phys.* **1991**, *94*, 7221.

12. Glukhovtsev, M. N.; Pross, A.; McGrath, M. P.; Radom, L. *J. Chem. Phys.* **1995**, *103*, 1878.

13. Rebbert, R. E.; Lias, S. G.; Ausloos, P. *Int. J. Chem. Kinet.* **1973**, *5*, 893.

14. Shi, Y.; Marshall, P. *J. Phys. Chem.* **1991**, *95*, 1654.

15. Ding, L.; Marshall, P. *J. Phys. Chem.* **1992**, *96*, 2197.

16. Goumri, A.; Yuan, W.-J.; Ding, L.; Shi, Y.; Marshall, P. *Chem. Phys.*, **1993**, *177*, 233.

17. Sullivan, J. H. *J. Chem. Phys.* **1962**, *36*, 1925.

18. Baulch, D. L.; Duxbury, J.; Grant, S. J.; Montague, D. C. *Evaluated Kinetic Data for High Temperature Reactions. Vol. 4, J. Phys. Chem. Ref. Data* **1981**, *10*, Suppl. 1.

19. Frisch, M. J.; Trucks, G. W.; Schlegel, H. B.; Gill, P. M. W.; Johnson, B. G.; Robb, M. A.; Cheeseman, J. R.; Keith, T.; Petersson, G. A.; Montgomery, J. A.; Raghavachari, K.; Al-Laham, M. A.; Zakrzewski, V. G.; Ortiz, J. V.; Foresman, J. B.; Peng, C. Y.; Ayala, P. Y.; Chen, W.; Wong, M. W.; Andres, J. L.; Replogle, E. S.; Gomperts, R.; Martin, R. L.; Fox, D. J.; Binkley, J. S.; Defrees, D. J.; Baker, J.; Stewart, J. P.; Head-Gordon, M.; Gonzalez, C.; Pople, J. A. *GAUSSIAN 94*; Gaussian: Pittsburgh, PA, 1995.

20. Gurvich, L.; Veyts, I. V.; Alcock, C. B., Eds. *Thermodynamic Properties of Individual Substances*; Hemisphere Pub. Corp.: New York, 1991.

21. Baulch, D. L.; Cobos, C. J.; Cox, R. A.; Esser, C.; Frank, P.; Just, Th.; Kerr, J. A.; Pilling, M. J.; Troe, J.; Walker, R. W.; Warnatz, J. *Evaluated Kinetic Data for Combustion Modeling, J. Phys. Chem. Ref. Data* **1992**, *21*, 411.

22. Seakins, P. W.; Pilling, M. J.; Niiranen, J. T.; Gutman, D.; Krasnoperov, L. N. *J. Phys. Chem.* **1992**, *96*, 9847.

23. Truhlar, D. G.; Isaacson, A. D.; Garrett, B. C. In *Theory of Chemical Reaction Dynamics. Vol. 4*; Baer, M., Ed.; CRC Press: Boca Raton, 1985; Chapter 2.

TABLE 1: Rate Constant Measurements of the Reaction of $H + CH_3I$

T, K	P, mbar	τ_{res}, s	F, J	$[NH_3]$, 10^{15} molecule cm^{-3}	$[CH_3I]_{max}$, 10^{13} molecule cm^{-3}	$k_1 \pm \sigma_{k1}$, 10^{-11} cm^3 molecule^{-1} s^{-1}
297	101.3	2.1	4.05	1.87	5.39	0.76 ± 0.02
297	69.0	1.4	6.05	1.47	3.67	0.77 ± 0.02
297	69.0	1.4	1.80	1.47	3.67	0.77 ± 0.02
297	53.0	1.1	4.05	0.82	3.58	0.73 ± 0.05
297						0.76 ± 0.01[a]
362	130.5	2.2	4.05	1.19	4.56	1.29 ± 0.03
362	86.7	1.6	6.05	1.08	3.99	1.22 ± 0.06
362	86.7	1.6	1.80	1.08	3.99	1.21 ± 0.07
362	70.1	0.8	4.05	0.72	2.73	1.00 ± 0.03
362						1.16 ± 0.08[a]
427	83.6	1.2	4.05	0.89	1.43	1.42 ± 0.06
427	132.0	1.9	6.05	1.40	3.32	1.60 ± 0.03
427	132.0	1.9	1.80	1.40	3.32	1.59 ± 0.04
427	68.5	0.7	4.05	0.62	1.54	1.38 ± 0.02
427						1.45 ± 0.08[a]
512	70.7	1.2	4.05	1.28	2.42	2.06 ± 0.11
512	110.6	1.9	4.05	1.73	2.57	1.95 ± 0.05
512	52.1	0.6	4.05	0.82	1.59	1.85 ± 0.11
512	50.5	0.9	4.05	0.99	2.43	1.97 ± 0.08
512						1.96 ± 0.03[a]

621	87.2	1.0	4.05	1.13	1.50	2.13 ± 0.09
621	160.8	1.9	4.05	1.41	1.70	2.34 ± 0.05
621	59.4	0.6	4.05	0.67	1.07	2.21 ± 0.10
621	108.6	1.8	4.05	1.13	2.05	2.27 ± 0.09
621						2.28 ± 0.05[a]
757	111.1	1.3	4.05	1.26	1.66	3.00 ± 0.07
757	60.0	0.5	4.05	0.71	0.88	2.61 ± 0.15
757	164.3	1.3	4.05	1.47	1.66	2.86 ± 0.08
757	75.6	0.9	4.05	0.83	1.13	2.63 ± 0.20
757						2.89 ± 0.08[a]

[a]Average value.

TABLE 2: Rate Constant Measurements of the Reaction of H + C_2H_5I.

T, K	P, mbar	τ_{res}, s	F, J	[NH_3], 10^{15} molecule cm^{-3}	[C_2H_5I]$_{max}$, 10^{13} molecule cm^{-3}	$k_2 \pm \sigma_{k2}$, 10^{-11} cm^3 molecule^{-1} s^{-1}
295	76.5	1.6	4.05	1.22	4.62	1.00 ± 0.03
295	55.5	0.9	6.05	0.94	4.18	0.92 ± 0.02
295	55.5	0.9	1.80	0.94	4.18	0.85 ± 0.03
295	109.5	1.7	4.05	0.66	6.62	1.06 ± 0.04
295						0.94 ± 0.04^a
357	131.8	2.3	4.05	1.23	3.92	1.42 ± 0.04
357	88.4	1.5	6.05	1.20	5.08	1.59 ± 0.02
357	88.4	1.5	1.80	1.20	5.08	1.50 ± 0.03
357	67.4	0.8	4.05	0.65	3.48	1.36 ± 0.05
357						1.53 ± 0.05^a
450	132.8	1.8	4.05	0.86	3.05	1.95 ± 0.05
450	91.3	1.2	6.05	1.49	4.15	2.29 ± 0.03
450	91.3	1.2	1.80	1.49	4.15	2.22 ± 0.03
450	68.0	0.7	4.05	0.83	2.89	2.21 ± 0.08
450						2.21 ± 0.06^a
533	129.5	1.8	4.05	0.99	2.71	2.61 ± 0.03
533	85.0	1.0	6.05	0.55	1.99	2.65 ± 0.05
533	85.0	1.0	1.80	0.55	1.99	2.55 ± 0.07
533	69.4	0.6	4.05	0.33	1.79	2.36 ± 0.08
533						2.59 ± 0.04^a

624	155.6	2.0	4.05	1.10	3.02	3.95 ± 0.07
624	96.9	0.9	4.05	0.49	1.79	3.75 ± 0.13
624	153.8	1.8	4.05	0.70	2.75	3.88 ± 0.16
624	76.6	0.6	4.05	0.35	1.30	3.58 ± 0.09
624						3.80 ± 0.09

*Average value.

TABLE 3: Rate Constant Measurements of the Reactions of H + CH$_3$CHICH$_3$ and (CH$_3$)$_3$CHI.

Iodoalkane, X	T, K	P, mbar	τ_{res}, s	F, J	[NH$_3$], 10^{15} molecule cm^{-3}	[X]$_{max}$, 10^{13} molecule cm^{-3}	$k_X \pm \sigma_{kv}$, 10^{-11} cm^3 molecule^{-1} s^{-1}
CH$_3$CHICH$_3$	295	129.0	2.0	4.05	1.19	4.87	1.49 ± 0.02
	295	77.5	1.2	1.80	0.71	3.64	1.39 ± 0.02
	295	77.5	1.2	6.05	0.71	3.64	1.42 ± 0.03
	295	66.0	0.8	4.05	0.44	2.70	1.48 ± 0.04
	295						1.44 ± 0.03[a]
(CH$_3$)$_3$CHI	294	129.6	2.7	4.05	1.47	4.34	1.88 ± 0.05
	294	84.3	1.3	6.05	1.04	3.11	2.05 ± 0.04
	294	84.3	1.3	1.80	1.04	3.11	2.00 ± 0.04
	294	68.9	0.7	4.05	0.53	2.10	1.95 ± 0.07
	294						1.99 ± 0.04[a]

[a]Average value.

11-14

Table 4: Ab initio results for the transition state for H + CH$_3$I $\rightarrow$ CH$_4$ + I.

HF/6-31G(d) frequencies[a]	1199i, 348, 410 (2), 1082 (2), 1187, 1541 (2), 3313, 3495 (2)
MP2=full/6-31G(d) frequencies[a]	1674i, 463, 470 (2), 1160 (2), 1255, 1464 (2), 3193, 3375 (2)
MP2/6-311G(d,p)[b]	-6957.17377
MP4/6-311G(d,p)[b]	-6957.21271
QCISD(T)/6-311G(d,p)[b]	-6957.21898
MP2/6-311+G(d,p)[b]	-6957.17498
MP4/6-311+G(d,p)[b]	-6957.21407
MP2/6-311G(2df,p)[b]	-6957.23020
MP4/6-311G(2df,p)[b]	-6957.27893
MP2/6-311+G(3df,2p)[b]	-6957.25902
G2[all-electron][b]	-6957.31294

[a]Unscaled, in cm^{-1}

[b]Energy in au; 1 au $\approx$ 2625 kJ mol^{-1}.

Table 5: Comparison of iodoalkane properties at room temperature.

Iodoalkane, X	k(298 K) for H abstraction,[a] cm^3 molecule^{-1} s^{-1}	measured k_X(298 K), cm^3 molecule^{-1} s^{-1}	DH_{298}(C-I), kJ mol^{-1}
CH_3I	5.6×10^{-19}	7.7×10^{-12}	237
C_2H_5I	3.8×10^{-17}	1.0×10^{-11}	237
CH_3CHICH_3	5.3×10^{-17}	1.4×10^{-11}	238
$(CH_3)_3CI$	6.8×10^{-17}	2.0×10^{-11}	230

[a]Empirical estimate (see text).

Figure captions

Fig. 1 Plot of pseudo-first-order rate constant k_{ps1} vs $[CH_3I]$ at $P = 70$ mbar and $T = 512$ K. The inset shows the time-resolved fluorescence intensity I_f for the filled point.

Fig. 2 Arrhenius plot of rate constants k_1 for $H + CH_3I$ (●) and k_2 for $H + C_2H_5I$ (○). Each point is the average of four measurements.

Fig. 3 *Ab initio* geometries of the C_{3v} transition state for $H + CH_3I \rightarrow CH_4 + I$. MP2=full/6-31G(d) data shown (HF/6-31G(d) in parentheses). Distances are in 10^{-10} m and the ICH angles are 96.6° (95.8°).

Fig. 4 Comparison of measured k_1 for $H + CH_3I$ (solid line, this work) with *ab initio* results (dashed line, ref. 3) and literature values (●, ref. 4; ■, ref. 5; ▲, ref. 6; ◇, ref. 7).
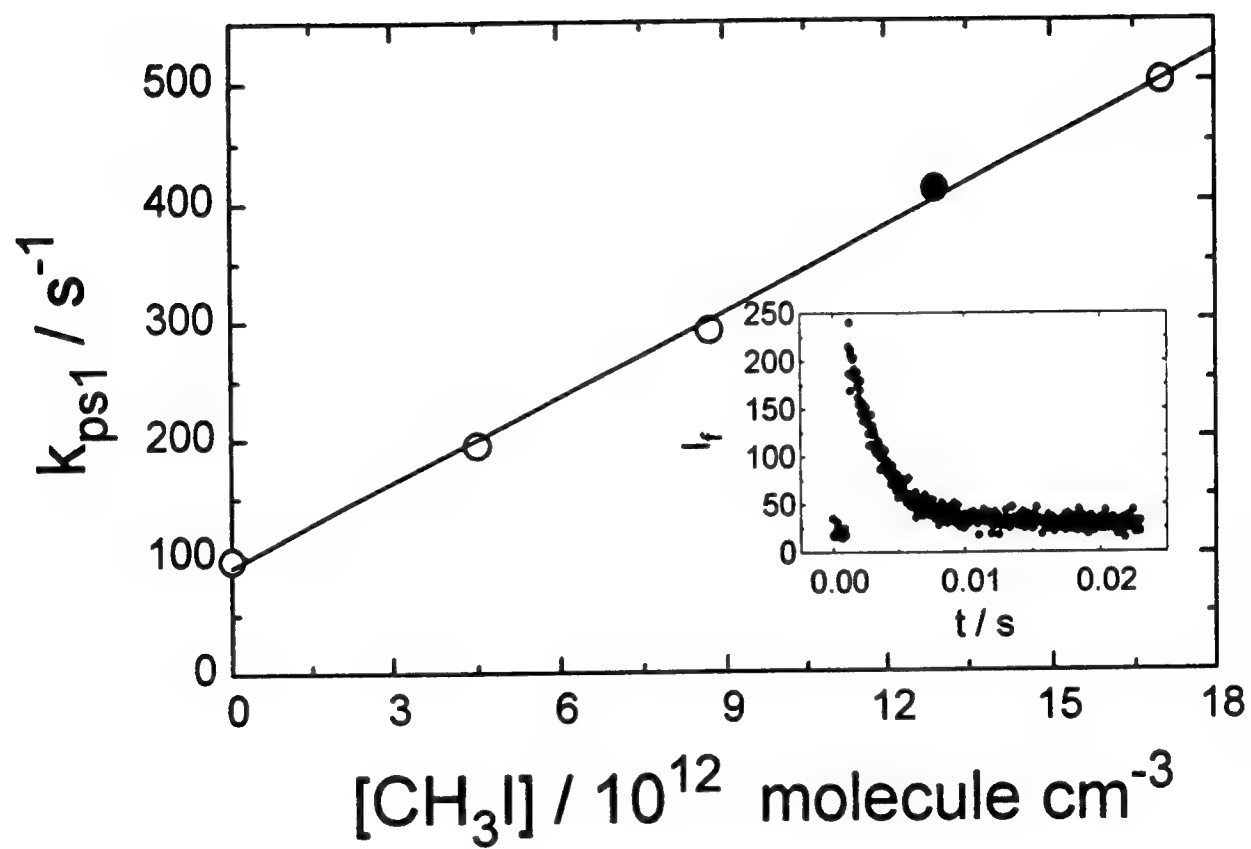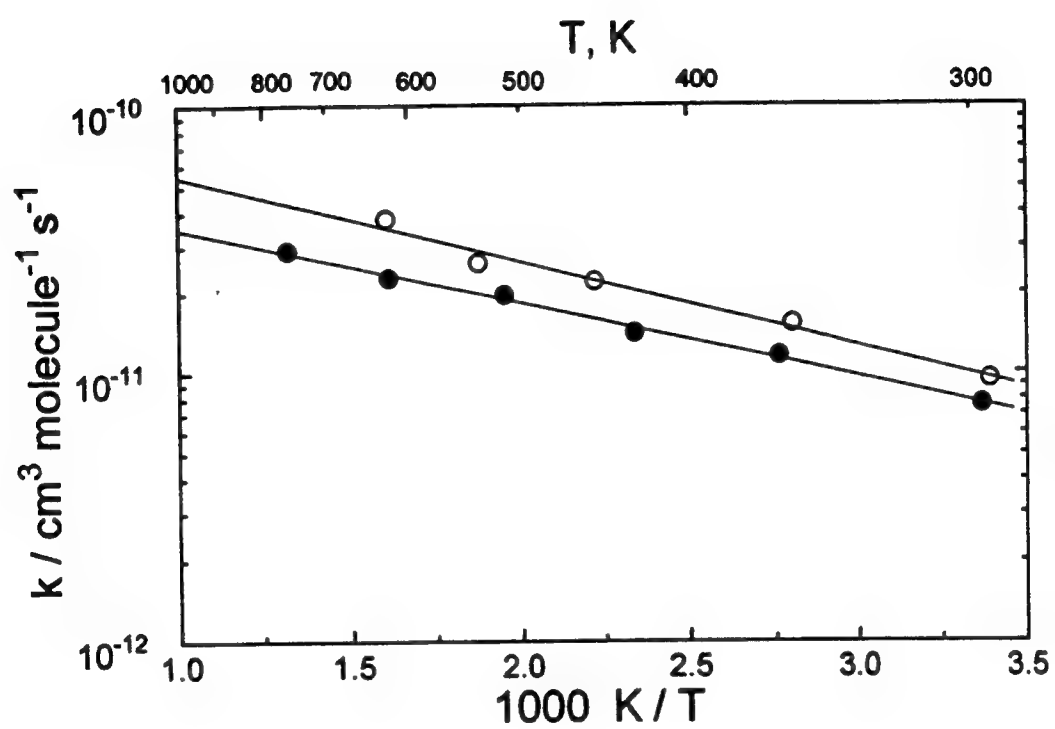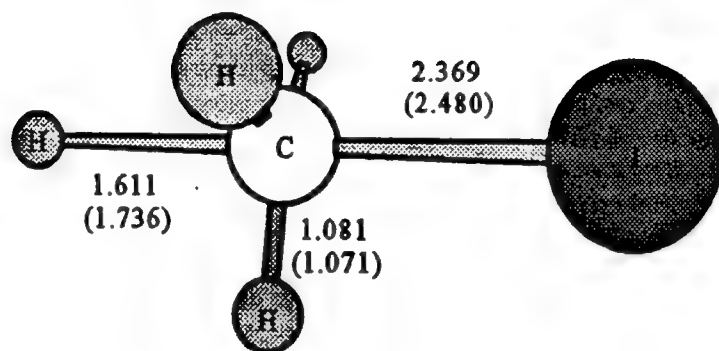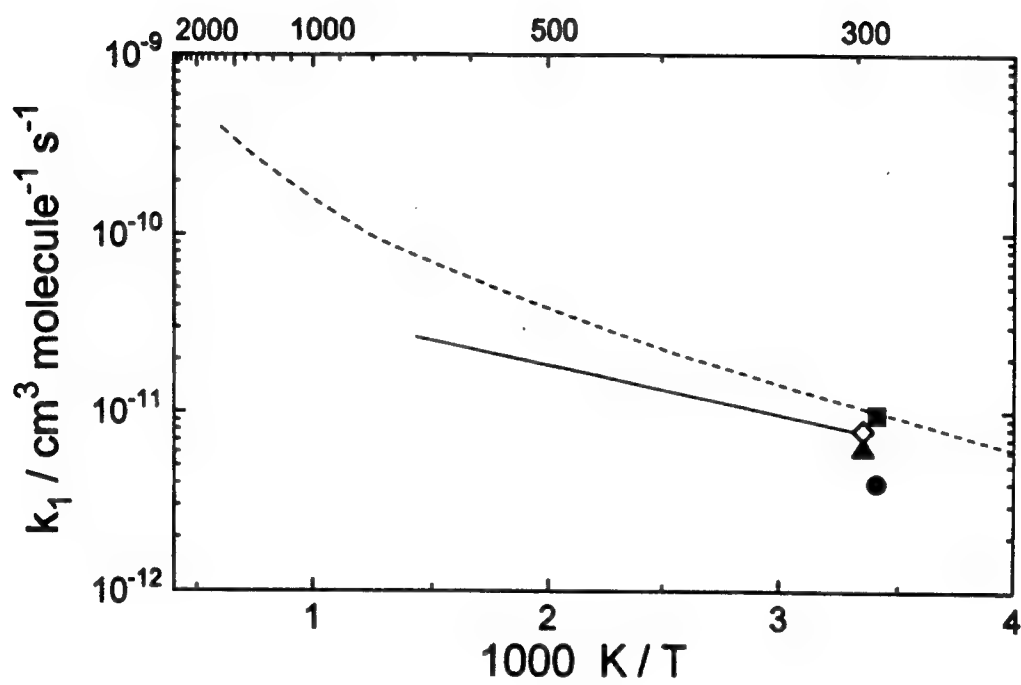
2.369
(2.480)

H

C

1.611
(1.736)

1.081
(1.071)

H

Investigations of Shear Localization in Energetic Materials Systems

James J. Mason
Assistant Professor
Department of Aerospace & Mechanical Engineering

University of Notre Dame
356 Fitzpatrick Hall
Notre Dame, IN 46556

Investigations of Shear Localization in Energetic Materials Systems

James J. Mason
Assistant Professor
Department of Aerospace & Mechanical Engineering
University of Notre Dame

Abstract

An experimental investigation of shear localization at the tip of a U-notch is reported. The initiation and propagation of shear localization from the notch tip in two aging conditions of 300 maraging steel is recorded using ultra-high-speed photography. The shear failure susceptibility of the materials and the transition from shear failure to tensile failure is discussed. These two areas are identified as important because shear localization as a failure mechanism requires, first, that the material be susceptible to such a localization, second, that the localization be dominant over other modes of failure and, last—due to boundary conditions in specific problems—that the shear localization propagate from one point to another. In reference to the first topic, the fundamental issue is whether shear localization susceptibility can be measured at all. In this work it is indicated that peak-aged 300 maraging steel is *qualitatively* more susceptible than under-aged to shear localization. The final failure of the specimen is characterized through ultra-high-speed observation and post-mortem examination. Propagation is generated by impacting side notched plates while observations are made using high speed photography at framing rates of 480,000 fps. Shear failure is seen to propagate at 1000 m/s in peak-aged material and 200 m/s in under-aged material. The peak-aged material fails fully by shear while the shear failure in under-aged material arrests and is followed by tensile failure. Finite element modeling is used to determine the nature of elastic wave propagation in the specimen.

Limitations of the notch geometry used in the first part of the study lead to the investigation of shear localization at the tip of V-notches with interest directed toward the measurement of shear susceptibility. A V-notch of opening angle 90° was chosen to minimize compressive stress on the surface of the shear localization plane while allowing a singular stress field at the notch tip. A lower compressive stress on the shear plane reduces friction on the fracture surfaces thereby allowing the localization to grow independently of the friction parameters. Also, the 90° V-notch allows easy application of dynamic loads to the notch faces making it easier to induce plasticity at the notch tip. Various geometries of dynamic loading are examined for eight different materials; the majority of the materials are high-strength armor materials for which recent investigations have reported the constitutive law parameters. Results indicate the onset of shear localization is much more difficult in most materials than it is in maraging steels.

Investigations of Shear Localization in Energetic Materials Systems

James J. Mason

Preface

Explosive devices for military applications usually involve a reactive material encased in a metal. Often that metal is an ultra-high strength steel having a yield strength well above most other metals. The hardening mechanisms in these steels can be precipitation strengthening as in maraging steels or solution hardening as in the tempered martensite steel. In either case the hardening mechanism often leads to reduced ductility and reduced strain hardening. A consequence of these reductions in ductility and strain hardening is that failure by one of two mechanisms is probable; tensile fracture enhanced by the reduced ductility or adiabatic shear localization nd fracture enhanced by the reduced strain hardening. A competition between these two failure mechanisms is expected and experiments investigating such competition are useful. In what follows a description of an investigation of the failure mechanisms of various ultra-high strength steels and other metals will be described. Focus is on the competition between tensile dominated failure and shear dominated failure. Shear failure is seen as a failure mechanism of importance because it can lead to plug formation in the metal casing of an explosive device followed by loading of the interior explosive by a sharp-edged punch. The temperatures in the metal can be rather high due to shear failure; if the metal in an explosive device fails by this mechanism and the metal subsequently comes into contact with the explosive, the explosive may be subsequently ignited by the hot metal. A full understanding of the shear failure and its competition with tensile failure makes it possible to prevent such ignition.

Note that in a related study, Roessig [1] has investigated punch loading of explosive materials. He concludes that early fragmentation of the explosive prevents the formation of an adiabatic shear band in the explosive itself, but ignition through friction between explosive fragments or between explosive and metal is a probable failure mechanism. Therefore, studies involving friction between the fragmented explosive and a hot, fractured metal may be important in understanding the accidental ignition of military devices by lower velocity impact i.e. impact velocity below the shock threshold of the materials.
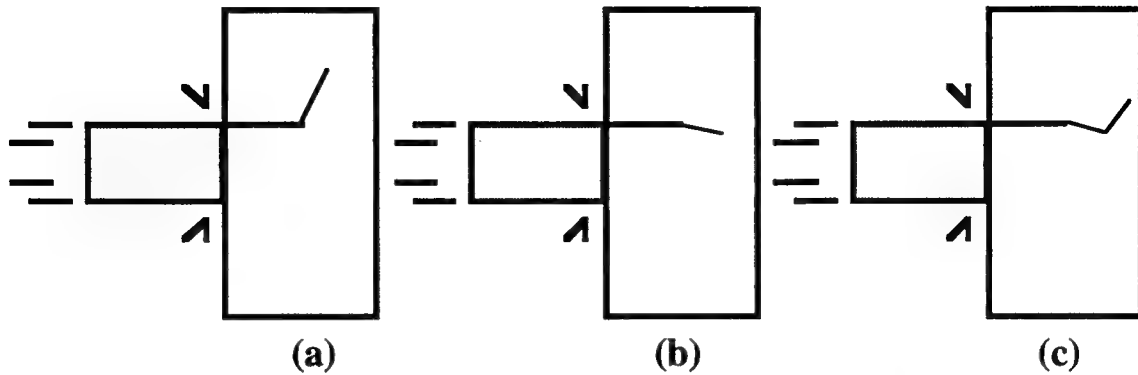
Figure 1: The geometry of the Kalthoff test showing three types of failure; (a) tensile crack propagation due to mostly shear loading, (b) shear crack propagation and (c) shear crack followed by a tensile crack.

1 PART I: Shear Failure at the Tip of a U–Notch

1.1 Introduction

A failure mode transition observed, post mortem, in side impacted, edge-notched plates [2] has received increased attention of late. A review of some recent work in this area can be found in a special issue of the *International Journal of Plasticity* to appear in 1997. Briefly, tests performed on 300 maraging steel in the Kalthoff [3] geometry show a shear localization or shear crack forming at the notch tip at early times after impact followed by a tensile crack being formed at a later, undetermined time. The failure mode transition and specimen geometry are shown schematically in Figure 1(c). This phenomenon is particularly interesting because of the challenges it presents in numerical modeling of such an event—both the material behavior and the geometry determine the crack path in a complex interaction that may be used to test how robustly a numerical code can model dynamic fracture—and because, in one experiment, it invokes a competition between two distinctly different failure mechanisms thus illuminating the important features of each.

It is also important to explore the Kalthoff test because it may serve as a useful test for measuring the shear localization susceptibility of materials. Shear localization is widely understood to occur when thermal softening due to plastic heating occurs at a greater rate than strain and strain-rate hardening [4, 5, 6]. Usually the deformation experiences an initial perturbation due to the existence of a material flaw that leads to a shear localization when thermal softening is dominant. However, this is an initiation criterion and therefore serves as a necessary but, perhaps, not sufficient condition for failure by shear localization. It is known that the shear localization must propagate after initiation before failure occurs [7]; hence it is important to investigate the material resistance to this propagation. In Kalthoff tests shear localization propagates, as shown schematically in Figure 1(b) in a controlled fashion. The notch radius, which can be

12-4

controlled using wire EDM machining, is the determining initiation flaw in the material and the propagation is determined by the material characteristics, specimen geometry and the impact velocity.

Of the work published, several issues remain unresolved in reference to the experimental results regarding failure in the Kalthoff test. First, the nature of the material failure in the shear localization is not known. Two mechanisms may be prevalent; adiabatic shear localization or ductile shear-void nucleation and growth. Most likely, there is a competition between the two. Attempts by Mason et al.[2] to look carefully at the notch tip during the shear failure were thwarted by the formation of an "aperture spot" on high-speed-photography images due to unavoidable vignetting of the collimated laser illumination. Second, the nature and time scale of the failure mode transition has not been reported. It is not known experimentally whether the shear failure arrests before the mode I crack forms or whether the transition from shear failure to tensile failure is a smooth one. Even the time at which the later tensile crack forms is not known. And, lastly, the effects of changes in specimen geometry have not been fully explored. It is reasonable to assume that the transition to a tensile crack occurs due to changes in the crack tip loading resulting from stress wave reflections from the specimen sides, but little experimental verification of that assumption has been made.

In this work some results regarding these three issues will be reported. A high speed photography system has been used to take pictures of the specimen as it deforms shortly after impact; the transition from mostly mode II to mostly mode I crack propagation is also recorded and velocities of the cracks may be measured. Lastly, some simple finite element models are developed to determine the nature of the loading for an edge-notched, but uncracked, plate as the plate geometry is changed with the focus being better determination of the best plate geometry for future tests of less shear-susceptible materials.

1.2 NUMERICAL METHOD

The finite element method was used to numerically examine the nature of the elastic wave propagation in some test geometries as an extension of the work performed by Zimmerman [11], who analyzed the stress intensity factor history in side-notched, 50 mm x 100 mm x 6 mm plates impacted from the side. Her results are shown in Figure 2. It is hoped that the same geometry may be used on other materials that are less susceptible to shear localization, but it is not known for sure if this particular geometry is ideal. Several cases, shown in Figure 3, were examined to determine which changes in the specimen geometry might be beneficial. Case one, Figure 3(a), is that of an infinite plate. This case serves as a basis for comparison to the other cases since no reflections are returned to the notch tip. Case 2, Figure 3(b), represents an infinitely long double cantilever beam (DCB) type specimen. In the figure the beam is infinite to the right but of finite width vertically. Case 3, Figure 3(c), represents and infinitely long bend specimen. The beam is infinite vertically but of finite width in the horizontal direction. Lastly, a square beam, Figure 3(d), is analyzed to
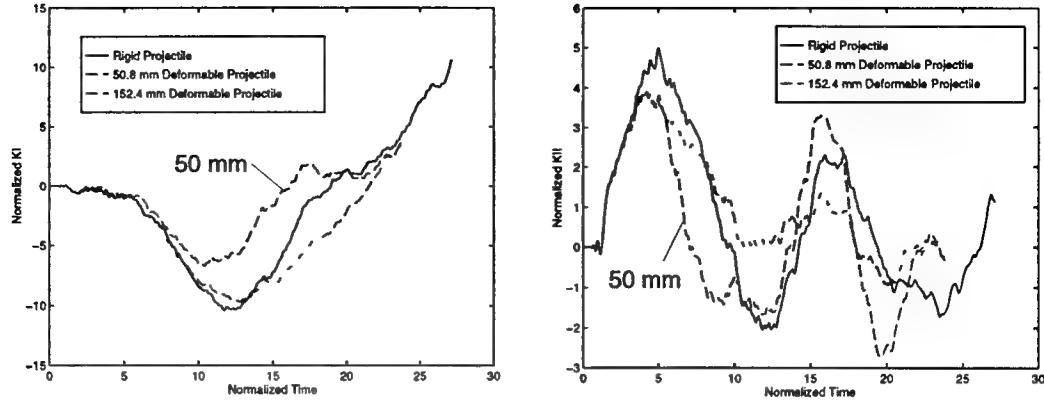
Figure 2: The dynamic mode-I and mode-II stress intensity factors, K_I and K_{II}, respectively, for the current geometry with different projectiles.

demonstrate the effects of multiple reflections.

The finite element package ABAQUS/Standard [8] was used to perform the calculations. A uniform mesh of eight noded, plane stress, square elements, 5mm × 5 mm, was used to model the plate except in the area of the notch tip where eight noded quarter point elements (QPE's) were used to represent the notch tip as a crack tip. The material in the plate is linearly elastic with $\rho = 1190$ kg/m^3, $E = 3.240$ GPa and $\nu = 0.35$. In the three cases that required infinite dimensions, infinite elements were used as per the ABAQUS/Standard User's Manual. The projectile was modeled as a rigid body with an impact velocity of 30 m/s. The contact surface algorithm included in the package was used to model the impact. In some cases, plane strain analyses were performed to examine the effects of dilatational wave speed. This helped determine whether shear waves or dilatational waves were dominating the notch tip behavior. Convergence was established by performing analyses on a coarser mesh. It was seen that both meshes gave the same result.

Quarter point elements were used to model the notch tip and measure the stress intensity factor there. The stress intensity factors were calculated using the William's expansion and the crack tip nodal displacements. This method has been show to be both efficient and simple in its application to transient dynamic analysis [10]. The time step was chosen following the recommendations of Murti and Valliappan [10] to reduce the amount of spurious oscillations in the results.

1.3 EXPERIMENTAL METHOD

Plates of 300 maraging steel were machined to into rectangles, 50 mm x 100 mm x 6mm, and a notch, 25 mm long and 37 mm from the top, as shown schematically in Figure 1, was machined through the thickness using wire EDM resulting in a notch tip radius of 175 μm. Two aging conditions of the 300 maraging steel
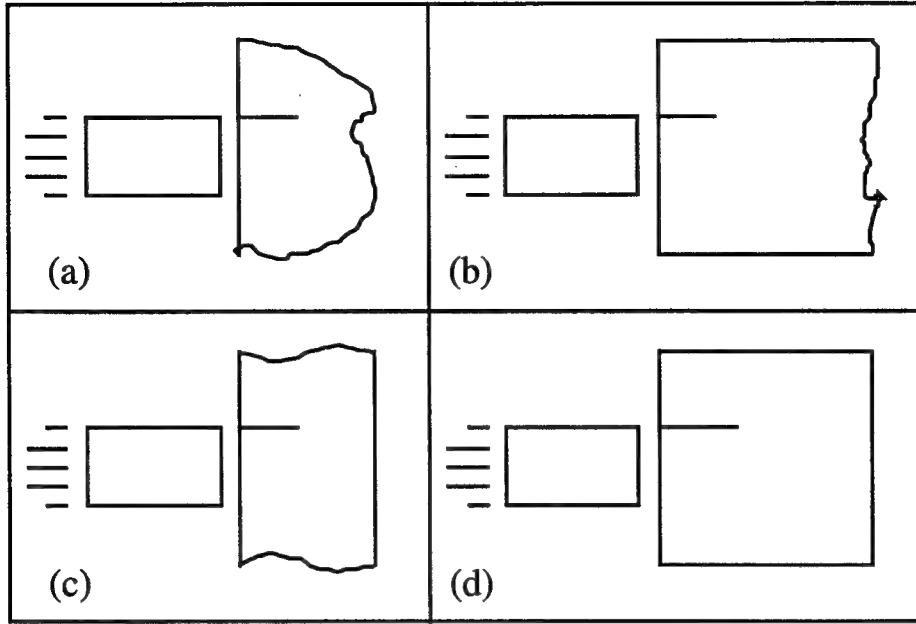
Figure 3: The geometry of numerical cases analyzed; (a) the infinite specimen, (b) bend specimens, (c) DCB and (d) square specimens. The notch length is 25 mm, the horizontal dimension, when applicable, is 75 mm, the vertical dimension, when applicable, is also 75 mm. The projectile is rigid, semi-infinite and 25 mm in width. It impacts perpendicular to the plate with its upper edge on the same line as the crack.

are tested, one under-aged and one peak-aged with aging times of 1/2 hour and 4 hours, respectively [11, 12]. The plates are impacted on the side, as shown in Figure 1, with an air gun and a 25 mm diameter, 50 mm long projectile made of 350 maraging steel. Impact velocity is measured using an infrared detector-emitter pair mounted on the gun barrel. High speed photographs are taken using a Cordin model 330 camera with a Cordin model 607 light source. A strain gage is placed on the side of the plate near the impact area to record the time of impact. A high speed light sensor is used to detect the flash of the light source. Both the strain gage signal and light sensor signal are recorded on a digital oscilloscope to give the timing, with respect to impact, of the recorded photographs.

Some comments should be made on the geometry of the specimens chosen. While Kalthoff used plates with dimensions of 100 mm × 200 mm and a notch machined 50 mm through the width (the lesser dimension), the specimens used here are smaller. As a starting point in this study the specimens were chosen to be of the same geometry as Kalthoff but scaled by one half so that the outside dimensions were reduced to approximately 50 mm × 100 mm and the notch length became 25 mm. This resulted in a considerable cost savings without much change in behavior. Early tests by Zimmerman and Mason [11, 12] showed that this change in size did not affect the salient features of the material behavior, failure mode transition was still observed. It should be noted, however, that the analytical advantage with the Kalthoff geometry, in general, is that the loading of the notch tip is essentially elastic. For all reasonable materials, if the impact

velocity is large enough to cause plastic deformation at the area of impact, the simultaneously generated elastic wave reaches the notch tip before that plasticity. In fact, if the notch length is large compared to the specimen dimensions, as it is in the specimen geometry used here and elsewhere [2, 3], plasticity induced at impact never reaches the notch tip and the notch tip is loaded only by an elastic wave. This simplifies the analysis to elastic loading with small scale plasticity. If the notch length is extremely small, however, plastic deformation generated at impact may be able to reach the notch tip and more complicated analysis may be needed.

1.4 RESULTS AND DISCUSSION

1.4.1 Effects of specimen geometry

First, the solution for the infinite plate, a numerical extension of the solution of Lee and Freund [9] to long times, is shown in Figure 4(a). It can be easily seen or shown that K_I is linearly decreasing in time and K_{II} is increasing logarithmically in time. Contact between the projectile and plate was not lost. The normalization constants are the same as those given by Lee and Freund,

$$K' = \frac{Ev_o}{2c_d^{pl-\sigma}}\sqrt{\frac{l}{\pi}} \qquad \text{and} \qquad t' = \frac{l}{c_d^{pl-\sigma}}, \tag{1}$$

where E is Young's modulus, v_o is the impact velocity, $c_d^{pl-\sigma} = 1761$ m/s is the plane stress dilatational wave speed, and $l = 25\ mm$ is the notch length.

Next, the finite square specimen was examined; see Figure 3(d) for the geometry and Figure 4(d) for the calculated stress intensity factors. In this case it can be seen that the dynamic stress intensity factor K_{II} decreases dramatically after a normalized time of 7. The behavior is quite similar to the results in Figure 2 for the plates in this study. The dashed line represents the solution for the infinite plate. In tests on other specimens [2], it was assumed that this precipitous drop in the shear mode loading at the notch tip was due to a reflected dilatational wave from the opposite side of the finite specimen. For this specimen the dilatational wave first reaches the crack tip at $t/t' = 5$, reflects off the projectile/plate interface and returns at $t/t' = 7$, the approximate time of the drop in K_{II}. Later behavior is due to reflections from the side wall and multiple reflections within the specimen. The negative K_I behaves roughly like the infinite plate until a normalized time of 10 where it begins to increase in value and eventually becomes positive. This is a result of the induced vibration in the finite plate. The projectile lost contact with the plate after 170 μs or a normalized time of 11.7.

Next, the specimen was reconfigured as shown in Figure 3(b) to model a long DCB specimen. In this configuration it was expected that the reflected dilatational wave from the opposite surface would be eliminated thereby eliminating the drop in K_{II}. The calculated stress intensity factors are shown in Figure
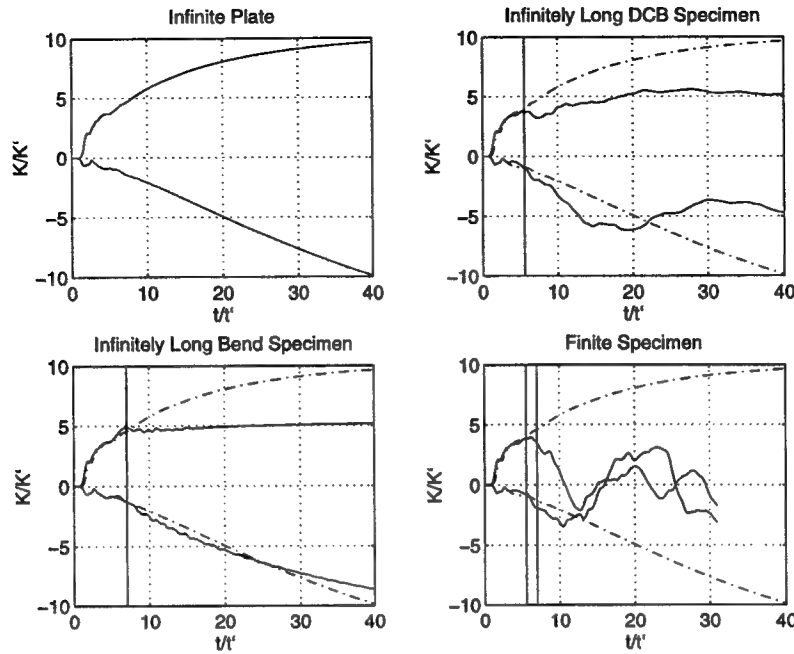
Figure 4: The dynamic mode-I and mode-II stress intensity factors, K_I and K_{II}, respectively, for (a) a notched infinite plate, (b) a notched, infinitely long DCB specimen, (c) a notched, infinitely long bend specimen and (d) a small, square specimen.

4(b). As can be seen the drop in K_{II} seen in Figure 4(d) is eliminated, but the rate of increase in K_{II} is still significantly curbed when compared to the infinite plate. Calculation of the time for shear wave reflected from the side to reach the crack tip is $t/t' = 5.5$. This time is shown as a solid vertical line in the figure, and it corresponds with the divergence of the solution from that of the infinite plate. Dilatational waves reflected from the sides arrive much earlier and have little effect. The K_I factor roughly repeats the behavior of the infinite plate until a normalized time of approximately 20-25, after many multiple reflections have occurred.

Last, the specimen was reconfigured to be an infinite bend specimen as seen if Figure 3(c). In this case it was hoped to eliminate effects of the shear wave and isolate the effects of the dilatational wave reflected from the back surface.. The results of the calculation are shown in Figure 4(c). It is easy to see that the drop in K_{II} seen in Figure 4(d) is eliminated as it was in the DCB specimen, but, once again, the rate of increase in K_{II} is reduced to near zero. A calculation of the time for a dilatational wave to reach the notch tip from the back surface gives $t/t' = 5$, at that time little change to the notch tip, mode-II intensity factor occurs. If, however, the time is increased so that the wave may reflect off the projectile/plate interface and return to the notch tip, then a significant change occurs. The time of arrival of such a wave is $t/t' = 7$ and is shown as a vertical solid line in the figure. At this time the K_{II} diverges from the result for the infinite plate and becomes roughly constant. K_I models the behavior of the infinite plate closely.

It is clear that a larger specimen is desirable because the longer distances give more time before reflected elastic waves reach the notch tip and change the loading there. This can be seen in Figure 4 where the infinite plate shows a monotonically increasing K_{II} but the others do not. The longer it takes for waves to reflect back to the notch tip, the longer the duration of monotonically increasing K_{II} with a negative K_I. The negative K_I is somewhat desirable because it increases the compressive hydrostatic stress directly ahead of the notch tip thereby suppressing brittle failure modes. The monotonically increasing K_{II} is desirable because it leads to shear failure; however, the K_{II} loading can also lead to tensile failure at an angle of approximately 70° as reported by Kalthoff [3], and shown schematically in Figure 1(a). With the objectives of generating an increasing K_{II} and a negative K_I at the notch tip in mind, the question of whether it is better to have a bend type specimen, like Kalthoff's, or a double cantilever beam (DCB) type specimen arises. From this investigation, it appears that the bend specimen is not the best option because the K_{II} reaches a constant level. The DCB is a bit more promising because the K_{II} is still increasing, but it is doing so at a very low rate. In the former case, it is the reflection of the dilatational wave from the opposite surface to the projectile/plate interface and back to the notch tip that determines the duration of the increasing K_{II} loading. In the latter case, it is the reflection of shear waves from the side surface that determines the duration of the increasing K_{II} loading. In the small specimen, Figure 3(d) and Figure 4(d), the combined arrival of, first, the shear wave from the side, shown as the solid vertical line at $t/t' = 5.5$ in the figure, and, next, the dilatational wave from the projectile/plate interface by way of the back surface, shown as the solid vertical line at $t/t' = 7$, lead to the precipitous drop in K_{II}. (This is a simplified view of the process since we have not considered the effects of wave reflected first off the side then off the back and so on.) Consequently, it seems that neither the DCB or the infinite bend specimens offers any significant improvement over the other. The strategies of using momentum traps on the specimen to replicate the behavior of the infinite plate or of using very short notches and higher impact velocities seem to be the next logical step in the evolution of this test.

1.4.2 Observations of shear localization and tensile fracture

The results of impacting two materials at nominally 40 m/s are reported. For the first case, under-aged 300 maraging material, the resulting photographs of the material failure are shown in Figure 5. At approximately 6 μs after impact, normalized time of 1.3, a shear failure began propagating directly ahead of the notch. Examination of the fracture surfaces after the test indicates that this is indeed a shear failure in agreement with Mason et al. [2] and Zimmerman and Mason [12]. This failure continues for approximately 14.5 μs and arrests at a total normalized time of 4.4 when the upward slope in in K_{II} stops as seen in Figure 2. During that growth period the notch is closing due to lateral expansion—this is to be expected as shown in
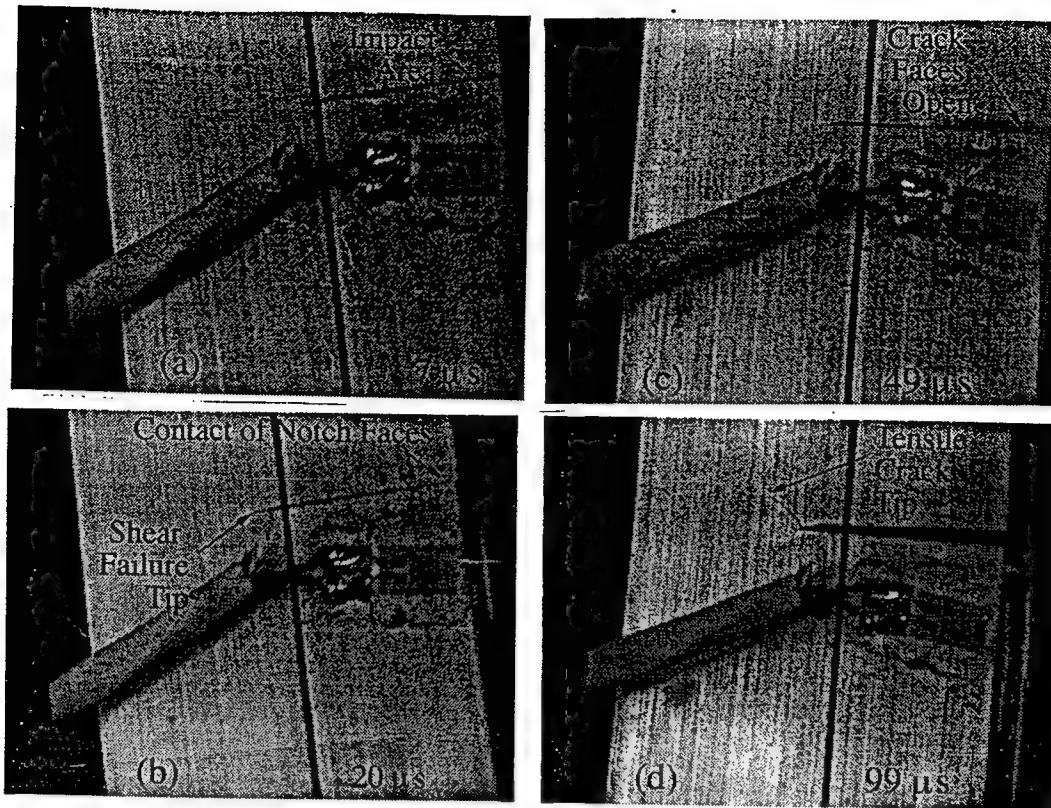
Figure 5: The dynamic fracture of under-aged 300 maraging steel. The vertical black stripe is light removed from the photographs by the Cordin 330 camera for streak photography, if needed.

the analysis of Lee an Freund [9] and Zimmerman and Mason [12]—and the notch faces come into contact at approximately the same time that the shear crack stops growing. It is not clear whether the shear crack arrests because of the peak in K_{II} or the contact of the faces, or both. Contact is held for about 27 μs. After which, the notch begins to open, after a total normalized time of 10.2 corresponding to a minimum K_I in Figure 2, until a total normalized time of 16.4, 29 μs later, when K_I becomes positive and a crack appears growing at an angle upward from the shear crack. The numerical solution is considered no longer valid after the crack opens and effectively changes the geometry of the specimen. This new crack is tensile and growing under mixed-mode, shear and tensile, loading. The transition corresponds to the change in K_I from compressive to tensile. The subsequent arrest of this secondary crack is not recorded. Clearly, this failure is a two step process where each failure mode is distinct from the other. The arrest of the shear crack, well before the appearance of the tensile crack, appears to be caused by either the closing of the notch faces and the loss of a monotonically increasing K_{II} loading or both.

In the second case a peak-aged 300 maraging material was tested and significantly different results were observed. The photographs of the material failure, taken at slightly higher magnification than in the previous case, are shown in Figure 6. As with the under-aged material, at approximately 6 μs after impact, a normalized time of 1.3, a shear failure began propagating directly ahead of the notch. However, this failure propagates more rapidly than in the under-aged material; in the peak-aged material the shear
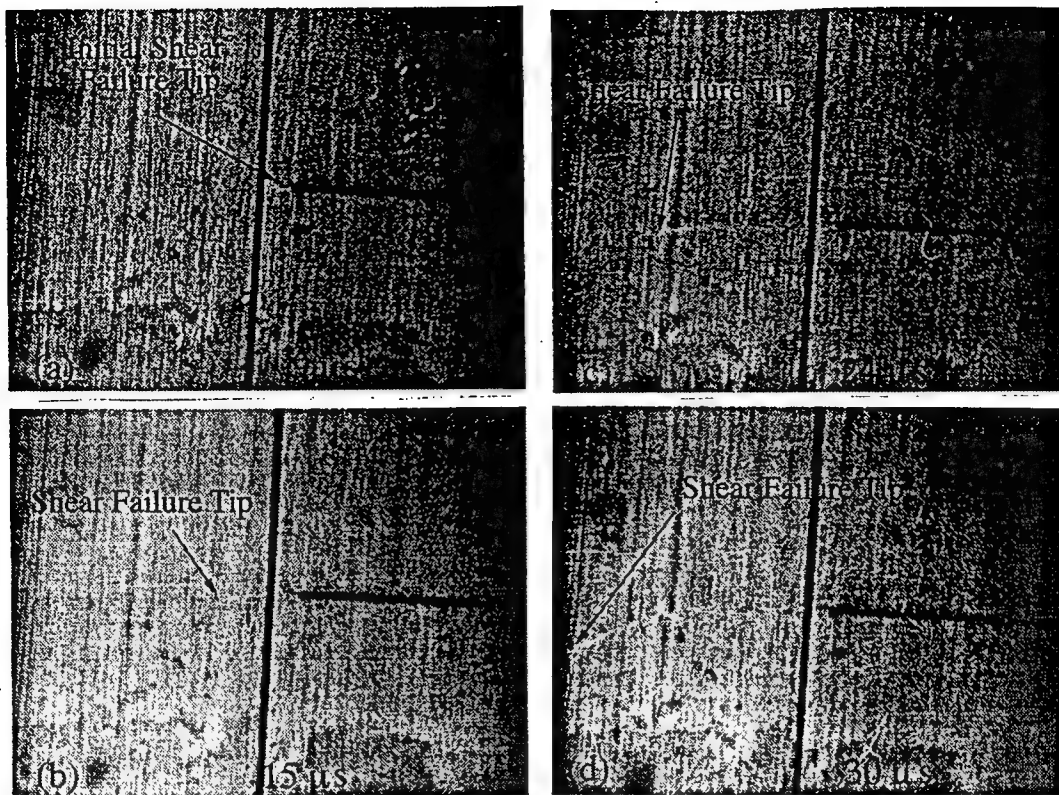
Figure 6: The dynamic fracture of peak-aged 300 maraging steel.

failure propagates at approximately 1000 m/s, a typical speed for dynamic fracture in steel, whereas in the under-aged material the propagation rate was much slower, 200 m/s. Approximately 25 μs after initiation, a normalized time of 6.6, the shear failure has traversed the 25 mm uncracked section of specimen and fully failed the specimen. Failure is complete before a significant drop in K_{II} can occur, although K_{II} has ceased to increase, and contact of the notch faces can occur. Again, during the shear failure the notch is closing due to lateral expansion, but in this case it has no effect upon propagation of the shear failure. Since the entire notch is not visible, it is not clear when contact of the notch faces initially occurs outside the field of view; presumably it occurs at the same time as in the under-aged test. But, as in the under-aged test, evidence of the notch opening is seen after a normalized time of 10.2 when the maximum negative K_I is achieved. After shear failure, the opening mode serves to propel the two separated pieces away from each other. It appears that the material failure and separation occurs in the shear mode since at later times the crack opens in approximately 4 μs which corresponds to an exceedingly high crack speed of 6000 m/s, well beyond the theoretical maximum speed or any experimentally measured speed in steels [13]. The failure is a one-step process dominated by shear failure.

2 Part II: Shear Failure at the Tip of a V-Notch

2.1 INTRODUCTION

The U-notch, a notch with the two notch faces parallel and separated by the notch tip diameter, used by Kalthoff introduces almost pure mode-II loading at the notch tip which leads to a dominant shear mode. However, its disadvantages are great: (i) the notch tip loading is determined by the magnitude of the stress pulse which is, in turn, limited by the elastic limit of the material, therefore it may only be useful for very-high-strength, exotic materials such as maraging steels; (ii) it requires large specimen dimensions or some type of momentum trap to remove the effects of pulse reflections in finite specimens; (iii) contact of the notch faces, as demonstrated in part I, complicate the loading behavior and (iv) loads cannot be easily applied near the notch tip. For these reasons it was decided that specimens of other geometry be investigated.

Specimens with a V-notch, a notch with faces inclined at an angle to each other and intercepting at a sharp corner of predetermined radius, have behavior that is similar to the U-notch; for many V-notch angles there is a singular stress field, but some of the disadvantages of the U-notch are alleviated. The notch faces are further apart preventing contact of those faces. Also, the V-notch angle may be chosen so that impact can occur very near the notch tip, and, consequently, plasticity at the tip may be more easily introduced. For these reasons the V-notch geometry was investigated here for several materials and several loading conditions.

Seweryn and Molski [14] have recently outlined the stress singularity at a V-notch for various static loading and displacement boundary conditions and for different opening angles. A V-notch may be of arbitrary opening angle, 2α, as shown in Figure 7 . Just like a stationary U-notch, or a crack, the stress singularity for the V-notch is expected to be the same for the static and dynamic cases with the stress intensity factor varying in time. Therefore, the work of Seweryn and Molski [14] gives a valid indication of the stress singularity at the tip of the V-notch under dynamic loading conditions. Like Williams [15] assumed for the Airy stress function, these authors assume a solution of the form $r^\lambda f(\theta)$ for the displacements and found a general solution that can be separated into a symmetric (similar to Mode-I for a crack) and anti-symmetric (similar to Mode-II for a crack) part. The application of stress free boundary conditions on the V-notch faces leads to two sets of equations for λ which can be satisfied only if

$$\lambda \sin 2\alpha + \sin 2\lambda\alpha = 0.$$

The solutions for λ may be real or complex, depending upon α. When the exponent is complex, $\lambda = \lambda_1 + i\lambda_2$, the dependence upon r may be written

$$r^\lambda = r^{\lambda_1} \left[\cos(\lambda_2 \ln r) + i\sin(\lambda_2 \ln r)\right]$$
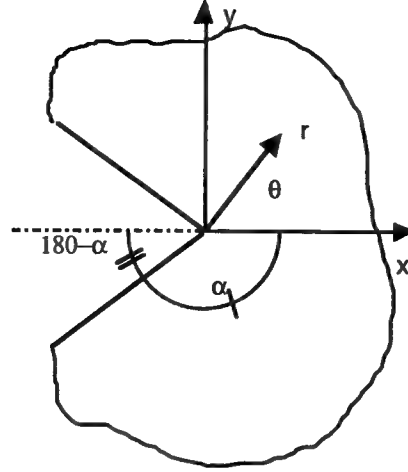
Figure 7: The geometry and coordinates of the V-notch specimen with half-angle, α.

so that only the real part of λ contributes to the singularity in stress. For the antisymmetric case a very similar equation may be found.

$$\lambda \sin 2\alpha - \sin 2\lambda\alpha = 0.$$

The solutions to these equations are reproduced in Figure 8. For stress to be singular and displacements to be bounded it must be that $0 < \lambda < 1$. The only meaningful values of α lie in the range $0 \le \alpha \le 180°$. As can be seen in the figure, a V-notch of opening angle $90°$, corresponding to $\alpha = 135°$, has an exponent very near 0.5 for the symmetric case and very near 1.0 for the antisymmetric case. Both values are real; higher order terms are complex. The U-notch or crack, with $\alpha = 180°$ has an exponent of 0.5 for both the symmetric and antisymmetric cases. Both values are real again; higher order terms, however, are real as well.

For the case when $\alpha = 90°$ it is seen that both the symmetric and anti symmetric parts give values of $\lambda \ge 1$ which indicates that no singularity is present for stress free boundary conditions along the V-notch faces. However, if impact conditions are applicable a singularity may occur. For example, if a rigid punch is statically pressed on a flat surface, $\alpha = 90°$, the pressure distribution under the punch, $p(x)$ is singular at the edges [16]

$$p(x) = \frac{P}{\pi\sqrt{a^2 - x^2}}$$

where $x = a$ at the edge of the punch and P is the punch load. The stresses in the solid are singular with respect to r with $\lambda = 0.5$ Likewise, Fung [17] has shown that for arbitrary half-angle, α, with a static distributed load $p(r) = Pr^m$ on the V-notch face the stress is of order r^m. So that if impact occurs on the V-notch surface, a singular stress field of order $1/r^{1/2}$ might be expected.

In all the cases discussed above only the static solutions are examined. Just like for a stationary crack, the
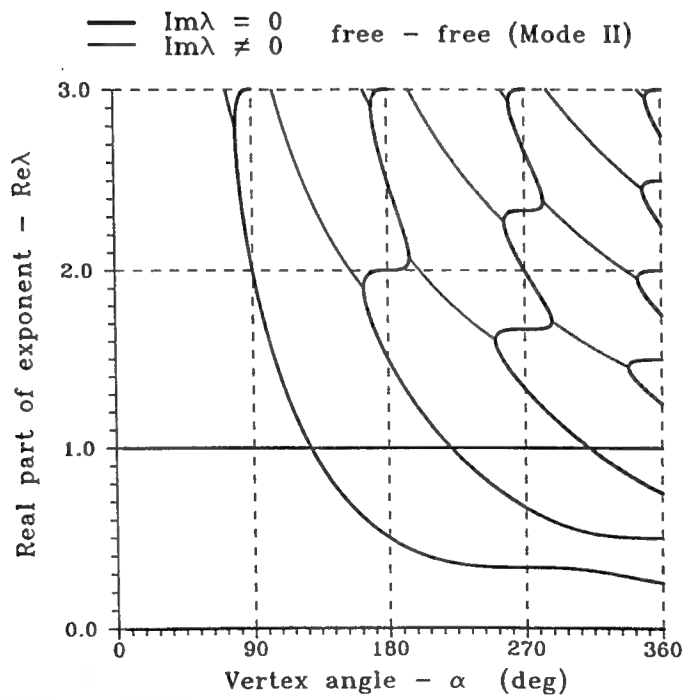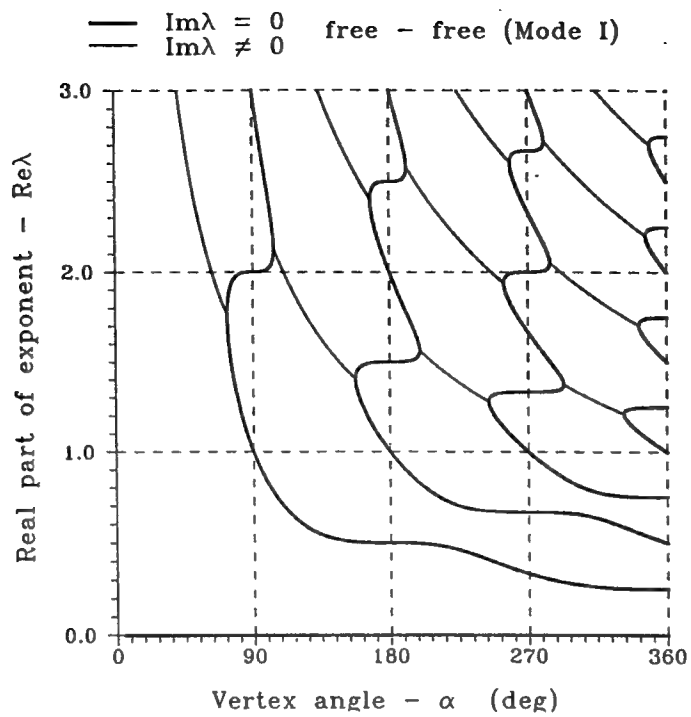
Figure 8: The real part of the exponent λ as a function of the half-angle, α, as per Seweryn and Molski. The half-angle, α, is limited in practice to less than 180°.
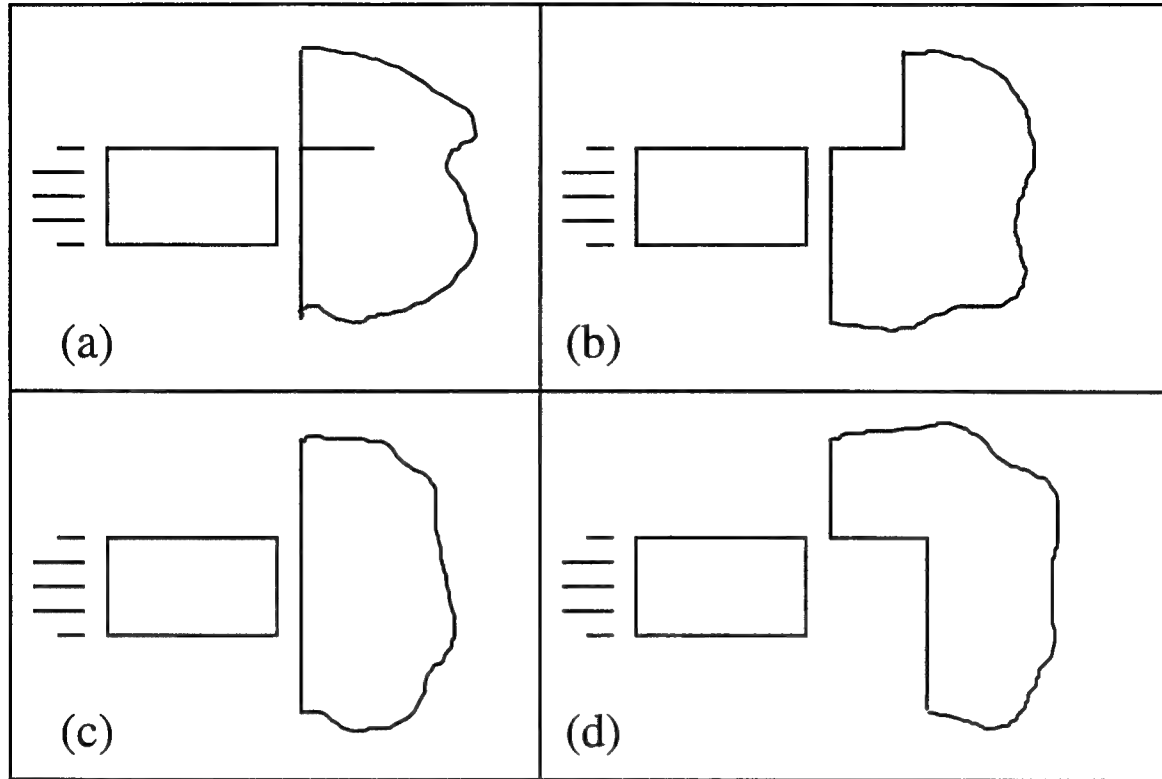
Figure 9: Examples of other geometries that lead to an elastic singularity in stress; (a) Kalthoff geometry, (b) V-notch with stress free faces, (c) impact of a half-space and (d) V-notch with impact on one of its faces.

stress singularity for the V-notch is expected to be the same for the static and dynamic cases with the stress intensity factor varying in time. Consequently, we can list four cases of dynamic loading in which elastostatic analysis indicate there will be a singularity at the tip of a notch; the Kalthoff geometry, any V-notch with stress-free faces and a half-angle, α, greater than 90°, a flat surface under a punch, and any V-notch with a singular distributed load on its faces. Examples of each of these cases is illustrated schematically in Figure 9. The present study set out to examine the dynamic fracture behavior of several metals under the conditions shown in the figure.

2.2   EXPERIMENTAL METHOD

The experimental method is simple in that only postmortem examination of the materials was performed. Since these tests are relatively new, it was not certain what type of shear failure, if any at all, would be observed. The purpose of the experiments was first to determine if shear localization could be induced using dynamic loading of V-notches. Two V-notch geometries were tested along with the Kalthoff geometry and a side impact geometry as shown in Figure 9; the latter cases were tested for comparison. The dimensions of each specimen are shown in Figure 10.
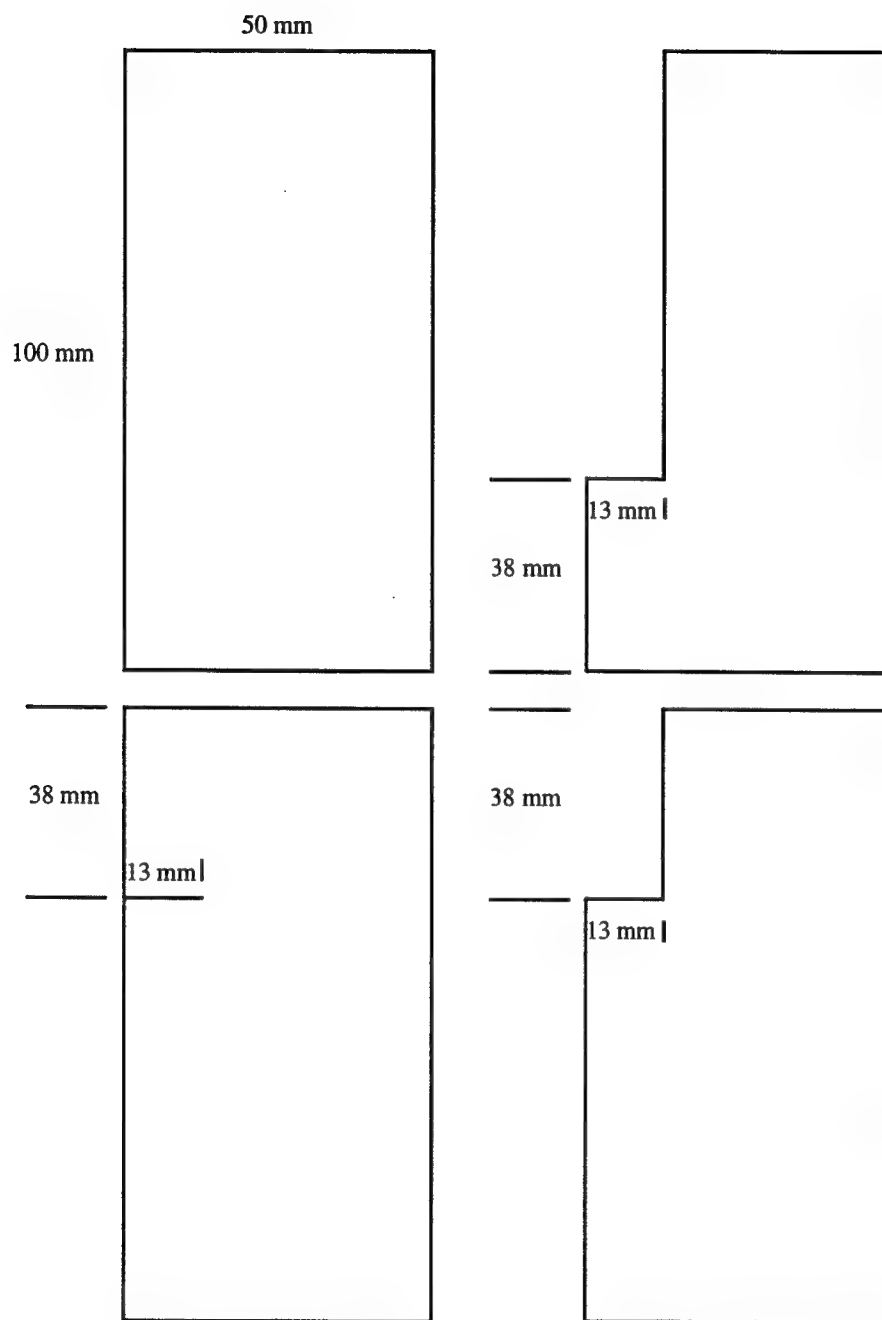
Figure 10: Dimensions of specimens tested.

Plates of metal were machined to into rectangles, 50 mm x 100 mm x 3mm, and an appropriate notch for each case was machined through the thickness using wire EDM resulting in a notch tip radius of 175 μm. The plates were impacted on the side, as shown in Figure 9, with an air gun and a 30 mm diameter, 150 mm long steel projectile. Impact velocity was measured using an infrared detector-emitter pair mounted on the gun barrel.

Eight different metals were tested: titanium 6-4, 1018 steel, aluminum 6061-T6, maraging steel C350, 4340 steel, D6AC steel, HP-9-4-20 steel, 300M steel. Of these, the last five are ultra-high strength steels; the first three were tested for comparison with their properties revealed in punch studies by Roessig and Mason [18]. Some heat treatments of the ultra-high strength steels are taken from the work of Dilmore and Foster [19], for which the Johnson-Cook constitutive law parameters were evaluated. Others were provided by the manufacturer with the materials. Finally, the titanium, 1018 steel and 6061-T6 aluminum were tested in the as received state. All treatments performed at Notre Dame are shown in Figure 11

2.3   RESULTS

Because of delays in procuring the materials and machining the specimens, only an initial set of tests could be performed. All materials and only three of the geometries in Figure 9 were tested at one impact velocity, 42 m/s. The results may be divided by specimen geometry.

The Kalthoff tests, Figure 9(a), gave a wide range of behavior depending upon the materials. For the ultra-strength steels the maraging steel failed completely by shear localization resulting in two pieces. The HP-9-4-20, 4340, D6AC and 300M seem to exhibit behavior more similar to the under-aged 300 maraging steel in Part I of this report. A small crack grows straight ahead of the notch for a less than three millimeters and is followed by a tensile type failure that exhibits shear lips. The specimen is partially fractured and remains intact. For D6AC and 300M the secondary crack was large while for 4340 and HP-9-4-20 the secondary tensile crack was either small or nonexistent. As shown in the first part of this report, the tensile failure most likely occurs at later times after impact when the reflections of the impact pulse from the free surfaces results in mostly mode-I type loading at the notch tip. The titanium alloy exhibited only a very small amount of deformation at the notch tip. No failure could be seen. The 1018 steel and aluminum alloy exhibited large amounts of plasticity at the impact area and the formation of a dimple at the notch tip. The dimple appears to be due to negative mode-I loading since the material in that area has expanded above the original specimen surface. No failure could be seen.

The stress free V-notch tests, Figure 9(b), were carried out at 42 m/s impact velocity. The high strength steels showed various ranges of failure. The 350 maraging steel again fully failed, but this time it did so in a tensile mode. The D6AC specimen failure path was almost identical to that of the maraging steel, but

350 Maraging

1500 F
1 hrs
Oil Quench
900 F
12 hr
Air Cool

4340

1600 F
3 hrs
1575 F
2 hrs
Oil Quench
600 F
1 hrs
Air Cool

300M

1700 F
2 hrs
1600 F
2 hrs
Oil Quench
600 F, 2 hrs
Air Cool
950 F
2 hr
Air Cool

D6AC

1700 F
1 hrs
Oil Quench
400 F, 1 hr
Air Cool
650 F
4 hr
Air Cool

HP-9-4-20

1575 F
1 hrs
Oil Quench
1020 F
2 hr
Air Cool
1020 F
2 hr
Air Cool
Cool 1 hr, -100 F, Air warm
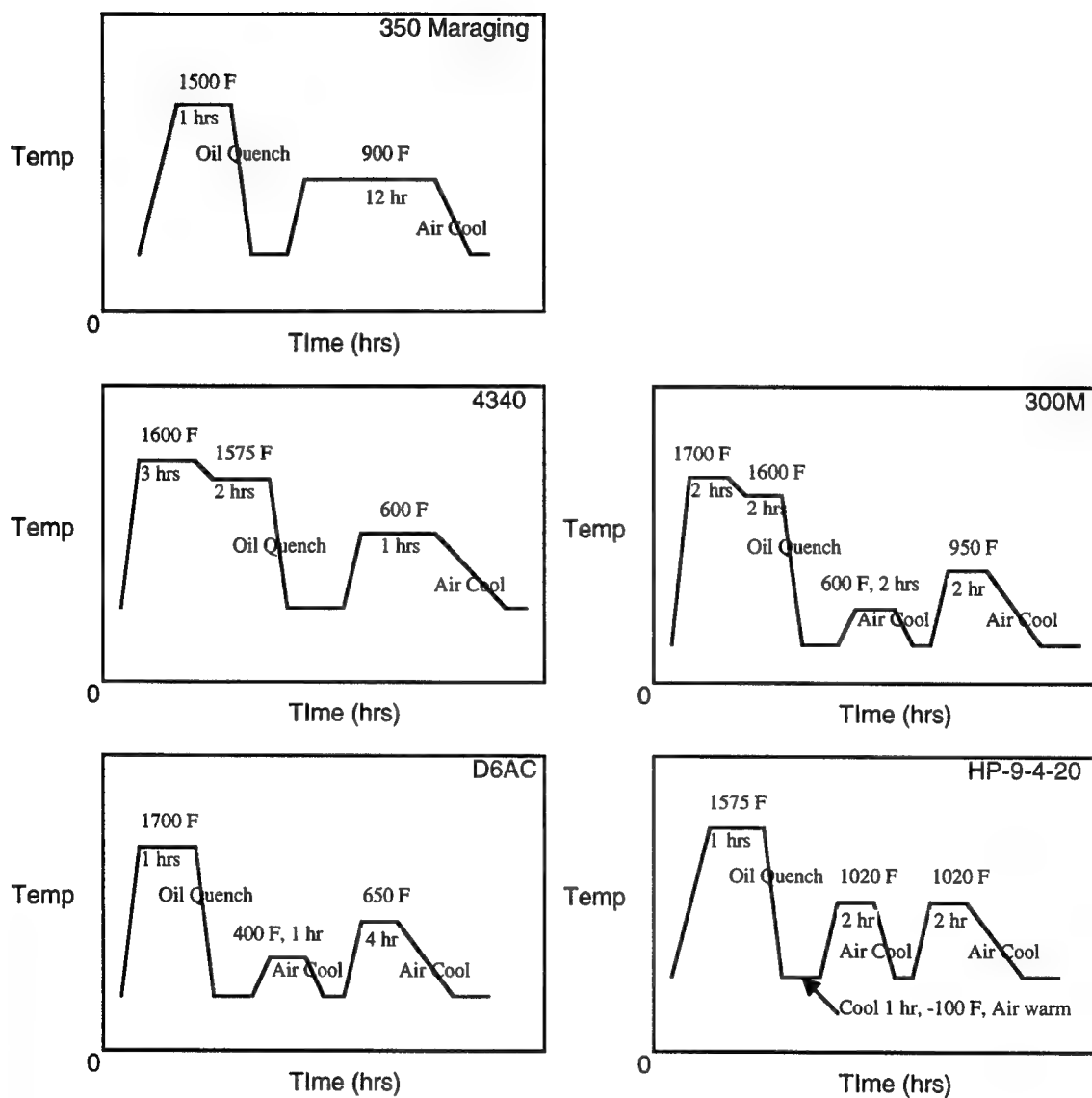
Figure 11: The heat treatments used for the ultra-high strength steels in the study.

the presumably tensile crack arrested before total failure occurred. The remaining ultra high strength steels showed small cracks from one to three millimeters in length; these too are most likely tensile. Again due to the finite size of the specimen and the boundary conditions at the edges, tensile loading at later times results in fracture of the metal. The titanium alloy, aluminum alloy and the 1018 steel showed no signs of failure. Some dimpling due to plastic deformation at the notch tip could be seen in the lower strength aluminum and steel materials.

Impact on the notch faces was achieved as shown in Figure 9 (d) for an impact velocity of 42 m/s. In these tests the aluminum alloy, titanium alloy and 1018 steel, again, showed no signs of failure. Surprisingly, however, neither did any of the ultra-high strength steels.

Tests on flat plates were delayed by errors in the machining of specimens.

2.4 CONCLUSIONS

Punch tests and associated finite element modeling of such tests by Roessig and Mason [18] on the three control materials, the aluminum alloy, the titanium alloy and 1018 steel, have indicated that titanium will fail by shear localization in low clearance punch tests with a punch velocity of about 1 m/s. The 1018 steel will begin to show signs of failure by shear localization at punch velocities of 15 m/s. And, the aluminum alloy does not show signs of shear localization in punch tests up to 15 m/s; it fails by tensile crack growth from the bottom of the plate. Furthermore, Zhou et al. [20] have reported shear band growth in the same titanium alloy in Kalthoff tests with specimens twice as big as the ones used here for the same impact velocity. Clearly, the titanium alloy has a high propensity to fail by shear localization, however, in the tests described in part II of this report it showed no signs of failure at all, not to mention failure by shear localization. The key issue appears to be the duration of the shear loading and the amount of accumulated shear strain. In the punch tests, and other test that show shear localization of many materials such as the torsional Hopkinson bar, the geometry of the loading and support ensures that a region of material will see mostly shear loading for a long period of time. In the tests described in part I and II of this report that is not the case. The reflection of waves from the stress free surfaces results in a change in the loading conditions from mostly shear to mostly bending. This results in tensile failure, if shear failure has not already occurred. Efforts to save costs by using smaller plates only exacerbate the problem. Thus, there is a seemingly insurmountable disadvantage to shear localization tests using this geometry; they only work on maraging steel or extremely large specimens.

The disadvantages of existing tests are that they do not allow easy observation of the shear localization failure. In the punch test the failure occurs on the interior; in the torsional Hopkinson bar the specimen is small and the location of shear failure initiation is not known. So, it is worthwhile to examine a few more

variations on the specimens shown in Figure 10. Namely, changes in the boundary conditions will be made so that the back surface of the plate is supported more like the punch test. This will result in a longer duration of shear loading, and it is easily achieved using the punch-die apparatus of Roessig and Mason [18].

2.5   FURTHER WORK

As was stated in the results section, delays were encountered in the purchasing and machining of the materials for the specimens in part II of this study. Even though the contract will have expired the work will be continued to its completion. Changes in the boundary conditions on the specimens will be made to ensure that a longer duration of shear loading will be experienced at the tip of the notch, whether it be a U-notch or a V-notch. The effects of those changes will be modeled using finite elements. Test will be carried out at higher velocities and numerical solutions for the elastic stress field at the notch tip will be found. Results of that investigation will be relayed directly to the site contact, Dr. J.C. Foster, at Eglin A.F.B.

References

[1] Roessig, K.M., SREP Report, 1996

[2] Mason, J. J., Rosakis, A. J., and Ravichandran, G., *J. Mech. Phys. Solids*, **42**, 11, 1994, pp. 1679-1697.

[3] Kalthoff, J. F., *Int. Conf. Photomechanics and Speckle Metrology*, SPIE, **814**, 1987, pp. 531-538.

[4] Clifton, R. J., Duffy, J., Hartley, K. A., and Shawki, T. G., *Scripta Met.*, **18**, 1984, p. 443.

[5] Anand, L., Kim, K. H., and Shawki, T. G., *J. Mech. Phys. Sol.*, **36,** 4, 1987, pp. 407-429.

[6] Myers, M.A., *Dynamic Behavior of Materials*, Chapter 15, John Wiley & Sons, Inc, New York, NY, 1994

[7] Marchand, A., and Duffy, J., *J. Mech. Phys. Sol.,* **36**, 3, 1988, pp 251-283

[8] ABAQUS/Standard, Hibbitt, Karlsson and Sorenson, Inc., 1080 Main St, Pawtucket, RI, 02860-4847

[9] Lee, Y. J. and Freund, L. B., *J. App. Mech.*, **57**, 1990, pp. 104-111.

[10] Murti, V. and Valliappan, S., ' *Eng. Frac. Mech.*, **23,** 3, 1986, pp. 585-614.

[11] Zimmerman, J.A. and Mason, J.J., *submitted to International Journal of Plasticity*.

[12] Zimmerman, J.A., *M.S. Thesis*, University of Notre Dame, Notre Dame, IN 46556, 1995

[13] Freund, L.B., *Dynamic Fracture Mechanics*, Cambridge University Press, New York, 1990

[14] Seweryn, A. and Molski, K., ' *Eng. Frac. Mech.*, **55**, 4, 1996, pp. 529-556.

[15] Williams, M.L., *J. Appl. Mech.*, **19**, 1952, p. 526-528

[16] Johnson, K.L., *Contact Mechanics*, Cambridge University Press, New York, NY, 1985

[17] Fung, Y.C., *J. Aeronautical Sciences*, **20**, 9, 1953

[18] Roessig, K.M., and Mason, J.J., *work in progress*

[19] Dilmore, M.F., and Foster, J.C., *presented at ADPA conference*, Huntsville, AL 1995

[20] Zhou, M., Rosakis, A.J. and Ravichandran, G., *SM Report 94-01* Graduate Aeronautical Laboratories, California Institute of Technology, Pasadena, CA 91125

A STUDY OF REAL-TIME MESSAGE TRANSMISSION OVER THE SCALABLE COHERENT INTERFACE (SCI)

Sarit Mukherjee

Assistant Professor

Department of Computer Science & Engineering

University of Nebraska-Lincoln

115 Ferguson Hall

Lincoln, NE 68588-0115

A STUDY OF REAL-TIME MESSAGE TRANSMISSION OVER THE SCALABLE COHERENT INTERFACE (SCI)

Sarit Mukherjee

Assistant Professor

Department of Computer Science & Engineering

University of Nebraska-Lincoln

Abstract

The Scalable Coherent Interface (SCI) is a recently developed IEEE standard that defines a scalable high performance multiprocessor network in which bus-like functionality can be provided to a large number of processor nodes. The SCI concept offers enormous potential improvement in both performance and life-cycle-cost with regard to the future of multiprocessor computing. Realizing the potential benefit of a SCI based parallel computer, the Joint Advanced Strike Technology (JAST) program office has selected SCI with real-time extensions (SCI/RT) as their baseline approach for a universal data distribution network for advanced strike aircraft of the next century.

Unfortunately, the high potential offered by SCI, as it is currently specified, cannot be directly exploited for real-time systems. This is because the existing SCI specification is targeted for non real-time (i.e., time shared) applications. Suggestions have been made by various SCI working group members on how to best extend/modify SCI to support real-time applications (SCI/RT). However, because of some limitations of each of the proposed candidate SCI/RT schemes, progress in developing a universal agreed upon SCI/RT standard has been slow.

In this document, we propose a more efficient and lower cost alternative SCI/RT scheme, called the job packing scheme. We believe that the implementation of the job packing scheme will require minimal changes to the existing SCI baseline protocol. The scheme is based upon solid theoretical foundation of generalized rate monotonic scheduling theory and bin-packing methodology in which global information is exchanged through selected bits of the SCI idle symbols. The scheme is flexible and load sensitive, and thus can work efficiently in a dynamic environment like SCI.

In this effort we develop analytical methods to prove different properties of the scheme. A detailed simulation platform is built for its performance evaluation and comparison. We have also built simulators for some of the SCI/RT candidate schemes and have shown the superiority of the job packing scheme over them. We then investigated the applicability of several popular real-time message scheduling schemes in the SCI environment. Their pros and cons are studied and evaluated through simulation, and compared with the job packing scheme.

Contents

A STUDY OF REAL-TIME MESSAGE TRANSMISSION OVER THE SCALABLE COHERENT INTERFACE (SCI)

Sarit Mukherjee

1 Introduction

Large scale distributed memory processor networks or massively parallel processors (MPP) have become the computers of choice for large computationally intensive tasks in recent years. MPP architectures consist of a set of nodes where nodes consist of processors(s), local memory, message router, and other support devices. MPP architectures often connect nodes through direct network in which each node has a connection to a set of other nodes, called neighbors. Since memory is distributed, MPP nodes communicate by sending messages through the network. The Scalable Coherent Interface (SCI) is standardized [6, 4] for very high performance multiprocessor systems that supports a coherent shared memory model scalable to systems with up to 64K nodes. It delivers GBytes/sec transmission rate along unidirectional point-to-point links that are connected into a ring topology. SCI was developed by a working group of leading computer researchers who wished to overcome the fundamental physical limits imposed by bus technology. SCI provides the services of a backplane.

Because of the cost and performance potential offered by the SCI concept, the Joint Advanced Strike Technology (JAST) program has selected SCI and its unspecified derivative SCI Real-Time (SCI/RT) as the baseline architecture to address the needs of military aircraft in the post-2005 time frame. JAST requirements were defined by several system studies, including Air Force PAVE PACE efforts and the Navy's Next Generation Computer Resource Program. SCI/RT is intended to be an enhancement for SCI which improves the real time and fault tolerance capabilities of SCI. Currently, the Air Force and Navy are jointly involved in two separate contracts in which SCI-based hardware is being developed.

SCI is an attractive candidate for real-time communication because of its high performance guarantee. However, the current version of the SCI protocol is not suitable for real-time applications. The purpose of this research is to recommend minimal changes to the current standard to make it amenable to real-time message transmission. Before describing the goals of our research in detail, we elaborate on the main difficulties with SCI that make it inherently complex for real-time traffic support. In the following, we first outline a brief overview of the SCI protocol, and then elaborate on the difficulties.

1.1 Overview of SCI

The SCI is a new high-speed multiprocessor interconnection standard [6, 4] that delivers GBytes/sec transmission rate along unidirectional point-to-point links that is connected into a ring topology. The protocol includes three different layers: the physical layer, the packet transportation layer, and the cache coherence layer. Figure 1 shows the layers in the SCI protocol. Entities on the

Cache Coherence Layer
Packet Transportation Layer
Physical Layer
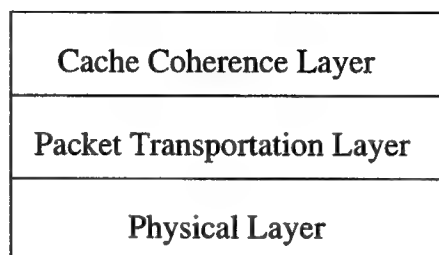
Figure 1: Layers in the SCI Protocol.

cache coherence layer provide services to application entities, like processors and memory chips, offering a shared memory with cache coherency. Entities on the packet transportation layer provide services to entities on the cache coherence layer. Services include transmission of packets across the interconnect. The task of the physical layer is to provide service to the packet transportation layer, including transmission of symbols from one node-interface to the next. The physical layer is implemented in a unidirectional point-to-point link, and various links have been defined.

This section will give an overview of the SCI node structure, and then introduce the layer protocol. We will focus mainly on the packet transportation layer, since the real-time extension will be applied on this layer, keeping the cache coherence and physical layers unchanged.

1.1.1 SCI Node Structure

The SCI interface (also referred to as SCI node) is the unit through which the compute and memory components communicate with other compute and memory components connected to the ring. Its logical queueing structure is identical to that of a buffer-insertion ring interface [1] (see figure 2). The node interface consists of two unidirectional links (input and output) which are used to connect nodes in a ring topology. The bypass FIFO stores packets arriving from upstream neighbor while the node is transmitting packets. This enables a node to concurrently (1) transmit packets, (2) process packets addressed to other nodes, and (3) accept packets addressed to itself.

1.1.2 Cache Coherence Protocol

High-performance processors use local caches to reduce effective memory-access times. In a multi-processor environment, this leads to potential conflicts. The SCI cache-coherence protocol defines
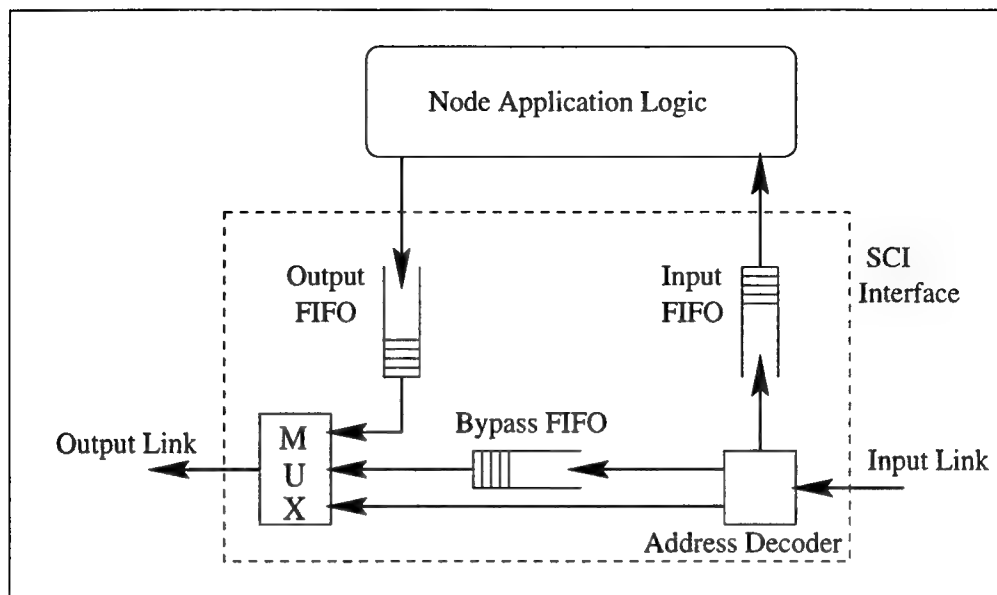
Figure 2: SCI interface (also referred to as SCI node).

mechanisms that guarantee consistent data even when data are locally cached and modified by multiple processors. The SCI cache-coherence protocol can be hardware based, thus reducing both the operating system complexity and the software effort to ensure consistency.

SCI uses a distributed directory-based cache-coherence protocol. Each shared line of memory is associated with a distributed list of processors sharing that line. All nodes with cached copies participate in the update of this list. Every memory line that supports coherent caching has an associated directory entry that includes a pointer to the processor at the head of the list. Each processor cache-line tag includes pointers to the next and previous nodes in the sharing list for that cache line. Thus all nodes with cached copies of the same memory line are linked together by those pointers. Coherence protocols can be selectively enabled, based on bits in the processor's virtual-address-translation table. Depending on processor architecture and application requirements, pages could be coherently cached, non-coherently cached, or not cached at all.

1.1.3 Packet Transportation Protocol

The key idea behind the SCI packet transportation protocol is the use of unidirectional, point-to-point links that can be clocked at a rate independent of the signal latency between nodes. Each node-interface has one input-link and one output-link. The basic logical structure of the interconnect is a ring. By using switches, which is a special node with more than one node-interface, multiple rings can be connected and various topologies can be formed. Since the links

are unidirectional, all information in a ring move in the same direction.

The interfaces communicate by exchanging packets, which are finite sequences of symbols. A *symbol* is 16 bits and the smallest information fragment transmitted between node-interfaces. A link transmits one symbol at a time. Because SCI protocols are synchronous, special idle symbols are transmitted across the links in the absence of packets, and at least one idle symbol is always sent between consecutive packets. Although SCI uses idle symbols for a variety of purposes, they are of key importance in its flow control protocol [13], which prevents node starvation and fairly allocates bandwidth to all nodes on the ring.

There are two main types of packets, *send packets* and *echo packets*. A send packet carries information generated by the higher layer to the destination node. An echo packet is returned to the source by the destination as an acknowledgment. The send packets can be divided into two sub-types, *request send* and *response send* packets, corresponding to the requests and responses generated at a higher layer, respectively. Similar distinctions can be made for echo packets as well.

When a node wants to send a packet, it places the packet in its output FIFO. If the bypass buffer is empty, and the node is not currently transmitting a packet from the address decoder, the send packet may be immediately output onto the ring. If bypass buffer is not empty, or the node is currently busy in transmitting a packet, the send packet must wait in the output FIFO. When the packet is transmitted, a copy of that packet must be saved into an optional active buffer. The copy is either discarded or used for retransmission when the echo packet for the send packet is received.

A packet is transmitted symbol by symbol to the downstream neighbor. When a packet arrives at a node, the destination address field (target ID) in the packet header will be checked. If the address does not match the address of the current node, it will be passed on to the next node. This will go on until the packet reaches the destination node and will there be stripped from the ring.

When a packet is to be passed but the output FIFO (source queue) at that node is currently transmitting a packet, or the bypass FIFO is not empty, the passing packet is routed into the bypass FIFO instead. If a passing packet and an output (source) packet are ready for transmission at the same time, the output queue (source queue) is given priority and the passing packet is routed to the bypass queue. When the output queue (source queue) is done transmitting, if the bypass FIFO has accumulated any symbols, output resumes from the bypass FIFO. This is called recovery stage and lasts until the bypass FIFO is completely emptied. The node is not allowed to transmit any output packet during the recovery stage — the output packets wait in the output FIFO.

When the packet arrives at the target node, if the input FIFO is not full, the receiving packet is striped and placed into the input FIFO. Otherwise the receiving packet is discarded due to buffer overflow. The last four symbols of the send packet are replaced with an echo packet that continues its way around the ring to the packet's source.

When the echo packet reaches the source node, it is matched with the saved copy of the send packet. The saved packet is discarded if the transmission was successful. Otherwise it is retrans-

mitted.

1.1.4 Physical Layer

The task of the physical layer is to provide a unidirectional point-to-point link to transmit symbols from one node to the next. SCI protocol defines various links, including *Parallel electrical link* operating at 1 Gbyte/sec and used over short distances (meters); *Serial optical link* operating at 1 Gbit/sec and used over longer distances (kilometers); *Serial electrical link* operating at 1 Gbit/sec and used over intermediate distances (Tens of meters).

1.2 Difficulties in Real-Time Support

The SCI defines an interconnect system that scales well as the number of attached processors increases, that provides a coherent memory system, and that defines a simple interface. As the SCI was intended for time-shared applications (i.e., non real-time), the SCI designers were concerned with the optimization and efficient implementation to achieve low average response time, high average throughput, and fairness in bandwidth utilization.

However, real-time systems require guarantees on when certain tasks complete. The notion of a deadline is used to measure the timeliness of task completion, that is, if a task completes before its deadline, it is on time. The correctness of the system depends on meeting the deadlines of the tasks [18]. Therefore, guaranteed timing behavior (i.e., guaranteed latency) is the essential metric for real-time systems. If the system activities are schedulable, then all requests will be serviced. For this reason, fairness and guaranteed forward progress are seldom of concern in real-time systems.

Unfortunately, the SCI protocol, as it stands today, cannot be applied to real-time systems. This is because the SCI protocol ensures forward progress but not deterministic latency. Thus, the fundamental problem is to modify the SCI protocol from one which guarantees forward progress to a SCI/RT protocol which guarantees latency.

The problem of obtaining guarantees on latency with a distributed network such as SCI is inherently complex[1]. The complexity arises mainly because of the buffer insertion feature of SCI. This is explained with the help of figure 3. Consider a SCI ringlet with three nodes as shown, one intermediate node in between the source and the target. We are concerned with providing deterministic latency between the source and the target. The latency can be divided into two components: (1) waiting time at the source, which is the local component, and (2) the ring transfer time[2] between the source and the target, which is the distributed component. The most critical component of latency in a distributed environment is the ring transfer time. The ring transfer time in SCI consists of three components, namely the transmission time of the packet by the source, the

---

[1]Real-time solutions exist for similar ring protocols, e.g., slotted ring [12], token ring such as FDDI [14], etc.

[2]It is the time between the transmission of the first bit of a packet from the source to the ring and the reception of the last bit of the packet by the target from the ring.
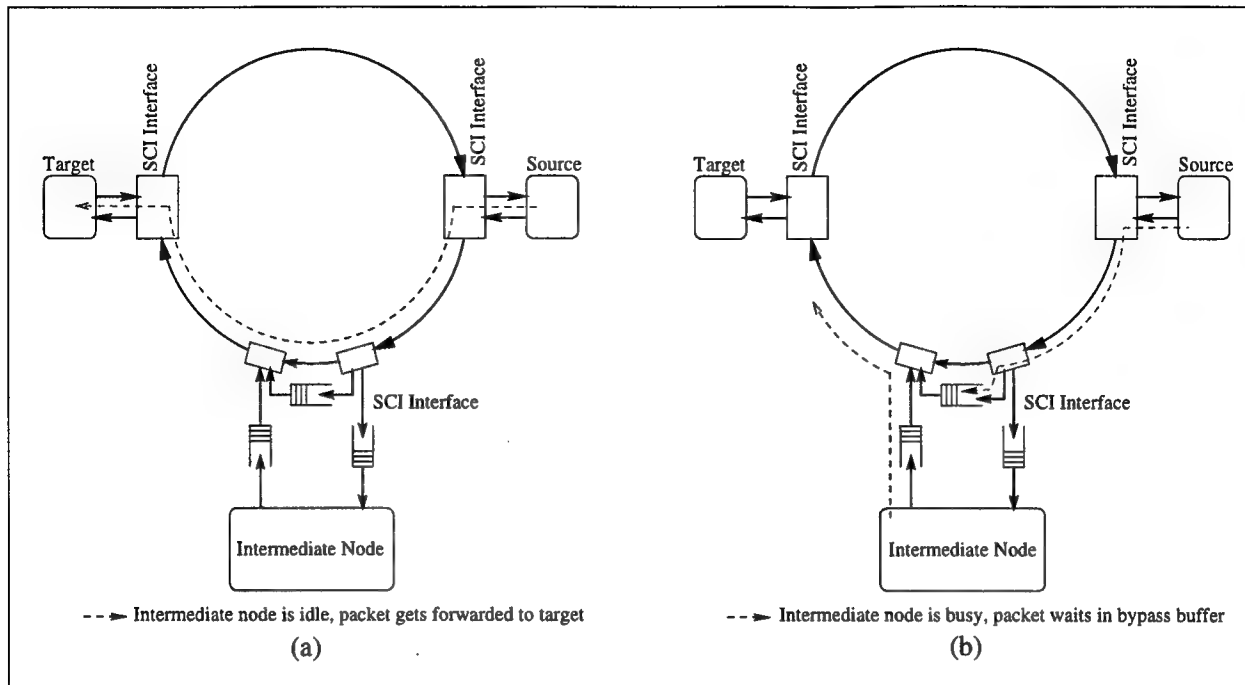
Figure 3: SCI ring with and without a busy intermediate node between source and target.

propagation delay from source to target and buffering delay (in bypass FIFO) in the intermediate nodes. Both transmission time and propagation delay[3] are fixed for a given SCI network. The only variable component is the buffering delay at the intermediate nodes. As this example will elaborate, this component of delay makes the real-time message delivery over SCI ring inherently complex.

Consider figure 3(a). When the intermediate node is idle (i.e., not transmitting), then the source to target transmission traces the path indicated by the dashed line and reaches the target after the transmission time and the propagation delay. This results in deterministic ring transfer time. However, if the intermediate node is busy (i.e., transmitting), the source to target packet is buffered in the bypass FIFO of the intermediate node (see the two part dashed line in figure 3(b)). It is forwarded to the target after the packet transmission from intermediate node is completed. Thus the ring transfer time between the source and the target becomes a function of the load at the intermediate node and moreover, it is a function of the length of the packet that contend for concurrent transmission at the intermediate node. This results in the non-determinism in ring transfer time in SCI.

Protocols similar to SCI, e.g., slotted ring or token ring [1] do not suffer from this problem, i.e., the intermediate nodes do not introduce any additional buffering delay (other than the one for

---

[3]Since the distance between the source and the target is fixed, and address decoding time at an intermediate node is constant, therefore, source to target propagation delay is fixed.

13-9

address decoding which is constant and can be included in the propagation delay). Thus, the ring transfer time in these protocols is fixed. Therefore, in order to guarantee latency in these protocols, determination of start time for transmission of a packet from the source is sufficient. However, as the above example elaborates, the same strategy cannot be applied to SCI/RT.

There are several other difficulties with the SCI protocol regarding real-time traffic support. These difficulties include the FIFO queueing discipline, insufficient number of priority bits, etc, that are independently identified by other researchers as well [5, 7]. We do not elaborate on these in this document, since the solution to the non-deterministic ring transfer time encompasses solutions to them as well.

1.3 Our Contributions

In this report we discuss our studies on the development on and experimentation with real-time protocols for SCI. The objective of the research is to develop a theoretical foundation for the scheduling of real-time messages using the SCI. An underlying goal is to keep the differences between the SCI and SCI/RT protocols to an absolute minimum. This will allow the possibility that the future chip-sets can support both protocols or at least pin-for-pin compatible versions will be available. To this effect, at the time of writing this report, we have achieved the following:

- We have established a theoretical foundation under which various SCI/RT protocol options can be analyzed. We have designed and experimented with workloads which are representative of the tasks that a SCI/RT would be subjected to, and have shown how such a workload can be synthetically generated.

- We have created a simulation platform for the two most popular SCI/RT candidate schemes already proposed (they are briefly described in section 2). Through simulation and analysis of the results we have outlined some of the shortcomings of these schemes.

- We have proposed a novel real-time message scheduling scheme over SCI called the job packing algorithm. The method, based on generalized rate monotonic theory [17], is a distributed implementation of a real-time protocol. The scheme consists of two stages: job admission and job scheduling. The first stage can be computed centrally by the node where the job arrives. The second stage is carried out in a distributed fashion only for the admitted jobs. In this way, the computational overhead is reduced drastically, and at the same time delivery is guaranteed.

- We have built a detailed simulation platform for the job packing algorithm. The centralized and the distributed components of the scheme are simulated and evaluated through the synthetic workload.

- We have adopted and studied several existing popular real-time message scheduling techniques for SCI. This, we believe, constitutes several other options towards the realization of SCI/RT. A generalized simulation platform is developed to examine their performance and feasibility.

- Last but not the least, using the simulators and the synthetic workload, we have done a detailed comparison of the different SCI/RT schemes. They include the candidate SCI/RT schemes, our job packing scheme and the other adopted schemes. The results, described in section 5 show the relative performance of different schemes. It also establishes the superiority of the job packing scheme.

The rest of the report is organized as follows. In section 2 we describe the candidate SCI/RT schemes and point out their shortcomings. In section 3 we describe our job packing algorithm in detail. Several other real-time message scheduling techniques and their adoptions are detailed in section 4. Details of the synthetic workload generation and simulation experimentations and comparisons are presented in section 5. The report is concluded in section 6 and future research directions are pointed out.

2   Real-time Extensions to SCI (SCI/RT)

When the SCI standard was awaiting approval, interest had already grown in using the SCI protocol in real-time environment. This activity branched off into the SCI/RT working group (IEEE P1596.6) and work has progressed since then. The goal of SCI/RT working group is to modify the existing SCI protocol for real-time purposes. Compared to time-shared systems like SCI, real-time systems have additional requirements which affect the design process. The real-time scheduling requires the interconnect to have worst case latency guarantees, worst case bandwidth availability guarantees, and the ability to insure that tasks running in the background using excess bandwidth do not interfere with those that are currently scheduled to receive the available bandwidth. To meet these requirements, several modifications to the SCI protocol have been proposed. In this section we describe three major SCI/RT proposals: Preemptive Priority Queue Protocol [2], Train Protocol [16], and 2-bit/8-bit Protocol [7], .

2.1   Preemptive Priority Queue Protocol

The preemptive priority queue protocol [2] is designed to work at the network (ring-local subaction) protocol level, leaving the inter-network (end-to-end transaction) and cache-coherency protocol levels unchanged, and thus allowing full interoperability with SCI through switches or bridges. It views the SCI/RT system as a queueing network. There are three basic components in the queueing network: host input queue, link input queue, and bypass queue. It proposes to modify them as preemptive priority queues. The echo waiting queue and the response waiting queue

are made content addressable for efficiency. The amount of space in the bypass queue needed to absorb an arriving packet equals the amount of the packet remaining to be transmitted from the host input queue. Therefore, nodes should preempt only the minimum number of lower-priority packets, necessary to ensure completion of transmission of the packet from the host input queue, as determined at the time of packet's arrival.

By allowing preemption it can support rate-monotonically scheduled message transmission efficiently over the network. For details of the protocol refer to [2]. This proposal was not accepted because it is very expensive to implement, and it deviates significantly from the original SCI specifications.

2.2 Train Protocol

The train protocol [16] is a token based scheme. It is an alternative approach to SCI/RT compared to the approaches of modifying the SCI protocol to create a system obeying the priority based scheduling theories, such as the preemptive priority queue protocol [2].

The train protocol uses a special token, the LocalMotive that circulates around the ring, carrying priority information. Train protocol provides 8 bits of priority field, i.e., 256 priority levels, to differentiate the order in which tasks should complete. This guarantees that the lower priority tasks will not interfere with tasks of higher priorities. A train is sent around the interconnect to determine which packets should be sent and which should be saved for later transmission to avoid interference with higher priority traffic. The train guarantees the most efficient use of the interconnect based on the priority level, while at the same time guarantees that no bandwidth is unused on the interconnect. Train protocol also provides a fast transmit mechanism to reduce the latency of transmission during times of low activity in the interconnect.

The train is made up of a LocalMotive followed by tickets. The LocalMotive carries information about the train structure, leads the train circulating around the ring, and provides the nodes with information needed to make a transmission decision. The tickets are placed after the LocalMotive by a node wishing to transmit, and when returned to the node may grant permission to transmit a packet. The packet which had received permission and the other tickets will follow the LocalMotive circulating on the ring. A ticket contains all the information about the packet that the node desires to send. The ticket also provides the negotiation mechanism by which the nodes determine which packets are to be sent.

There is a designated TicketMaster node in the ring that performs the central services for the train protocol. This node is responsible for generating and removing the LocalMotive from the interconnect as well as marking the train that has had the ticket attached.

2.3 2-bit/8-bit Priority Protocol

The 2-bit/8-bit priority protocol [7] is a hybrid protocol scheme. The 2-bit priority protocol is simpler to implement and appears to be sufficient for typical personal-computer and workstation applications. The 8-bit priority protocol implementation is more complex, but provides a relatively complete set of protocols for implementing hardware-based rate-monotonic scheduling [17] between limited priority levels per node. The 8-bit priority protocol is very similar to the train protocol. Therefore, in this section, we describe the 2-bit priority protocol only.

The major goal of 2-bit priority scheme is to define an efficient mechanism for transmitting prioritized packets over SCI, to support real-time personal-computer/workstation applications by providing superior bandwidth and latencies for prioritized transactions. It defines four priority levels defined among two classes as shown in table 1.

Class	Subclass	Level	Usage	Bandwidth Share
Unfair	unfairHi	3	emergency	3/4 of total
	unfairLo	2	normal	ring bandwidth
Fair	fairHi	1	emergency	1/4 of total
	fairLo	0	normal	ring bandwidth

Table 1: Priority and class definitions of 2-bit protocol.

The unfair and fair classes are allocated different portions of the ring bandwidth depending on the load of the unfair traffic. If there is no unfair traffic, the full ring bandwidth can be used by the fair class. In the presence of unfair traffic, most of the bandwidth is allocated to them, the residual being used for the fair class. The high and low subclasses within each class provide finer mechanism to reduce the latency of emergency messages. The 2-bit protocol (re)defines the idle symbol to carry different priority and node-status information to implement the bandwidth allocation. This protocol is too simple (few priority levels) to handle a number of concurrent real-time message transfer sessions.

3 The Job Packing Algorithm

In this section we outline our algorithm to conduct real-time job scheduling in a SCI ring. The algorithm is based on generalized rate-monotonic scheduling theory (GRMS) [17]. However, unlike GRMS, our scheme is a distributed one that is suitable for an environment like SCI. The proposed algorithm performs two essential functions: (1) job admission and (2) job sequencing. The job admission algorithm, running at each node, decides whether a new job can be admitted or not, so that its messages can be delivered within the deadline without violating the deadline of the

previously accepted jobs. Once a job is accepted, the next step is to sequence the job in the nodes' transmission "calendar", i.e., to determine when the job should be transmitted with respect to the existing schedule of jobs.

The intuition behind dividing the scheduling functionalities in two parts is to achieve efficiency. The GRMS, although a powerful technique, is applicable for a centralized environment. An SCI ring is inherently a distributed system and the application of GRMS is not straight forward. In our algorithm, we use this powerful technique in such a way so that it becomes amenable for distributed treatment. To achieve our goal, we perform the job admission locally, i.e., a node need not consult other nodes in order to admit a new job. This is achieved by keeping sufficient information per node about the global scheduling behavior. Note that the easiest and naive way of achieving this would be to replicate the schedule of all the nodes in each node. However, this is a huge information and very expensive to maintain as well. We keep minimal global information to perform this task. In the job sequencing phase the neighboring nodes exchange information and update their job sequences using a derivative of GRMS technique developed by us. This update information makes one complete round through the ring to let every node know and collect the necessary information. Thus, global information is exchanged only when a job is accepted, not otherwise. Moreover, the information kept per node is sufficient to make sure that a local decision about a job admission will always be accepted by all the nodes in the ring, if they were to take part in the job admission decision.

We assume that a job consists of a set of real-time messages. For ease of exposition, in the rest we will assume that the size of the set is unity, and will use the terms job and message interchangeably. A real-time message M is defined as a five tuple, $M = \{P, D, C, S, T\}$, where P, D, C, are, respectively, the period, deadline and transmission time of the message transmitted by source S to target T. The message is periodically generated at source S after every P time units. It is ready for transmission at the beginning of the period and it has to be received within the deadline. We assume that $D = P$ in the rest of the discussion. The message transmission requires C time units. Notice that a job defined this way succinctly models real-time process control messages such as messages generated by a sensor periodically, real-time animation, etc. Messages that do not repeat, in other words, aperiodic messages such as an interrupts can also be modeled in our framework by assuming that the message does not repeat.

In the rest of this section we describe the job admission and sequencing schemes. At the time of writing this report, all the necessary concepts regarding the algorithms were developed. Some of the proofs of the algorithms need some more work and will be reported in a future paper. Below we explain the main concept behind the scheme and elaborate it through instructive and detail examples. We conduct a performance comparison of our scheme with the other proposed SCI/RT schemes in section 5.

3.1 Job Admission

As mentioned before the job admission decision can be carried out locally at the arriving node. The necessary global information is kept in the node's data structures. Once a job is admitted, those data structures are updated.

In order to check if a job can be admitted into the system, the admission controller ensures that the utilization[4] of the node remains below 1 and all the local jobs meet their deadlines. To compute the utilization of node s, we only consider the messages that originate or pass through the node. Let Ψ_s denote such a message set. Then the utilization of node s, denotes as U_s, can be defined as

$$U_s = \sum_{j}^{M_j \in \Psi_s} \frac{C_j}{P_j} \leq 1.$$

If the newly arrived job makes U_s higher than 1, the job is rejected straight away.

Next the deadline of the newly arrived job is considered. The end-to-end deadline (i.e., the time within which the message has to reach its destination) can be broken down into two parts: transmission delay and propagation delay. Transmission delay, in turn, consists of two parts, namely transfer time (C), and waiting time at intermediate nodes, for higher priority job transmission. The computation of the propagation delay and waiting time are explained below:

As mentioned before, each node keeps a job sequence, and the newly admitted job has to fit in the sequence without violating any timing constraints. The job sequence for node s is defined as $\tau_1, \tau_2, \ldots, \tau_i, \ldots, \tau_j, \ldots, \tau_n$, where the priority of job τ_i is higher than τ_j if $i < j$. Note that we have omitted the node subscript since there is no confusion. Node subscript will be used if there is any confusion. The minimum delay between two successive transmissions of τ_i is a function of the job sequence [17], and we denote it by $f_{\tau_i}(\tau_1, \tau_2, \ldots, \tau_n)$. The function can be evaluated as:

$$f_{\tau_i}(\tau_1, \tau_2, \ldots, \tau_n) = \frac{\sum_{j=1}^{i} C_j}{1 - \sum_{j=1}^{i} \frac{C_j}{P_j}}.$$

The waiting time of the message τ_i will be $f_{\tau_i}(\tau_1, \tau_2, \ldots, \tau_{n-1}, \tau_n)$. So we have:

$$\text{Transmission delay} = C_i + f_{\tau_i}(\tau_1, \tau_2, \ldots, \tau_n).$$

The propagation delay is contributed by the link propagation delay and the block time at the bypass buffer of the intermediate node(s). So we define,

$$\text{Propagation delay} = E + B,$$

where E is the total link delay on the network from the source to the destination, B is the summation of the block time at the intermediate node(s). For a given source-destination pair, E is fixed and

---

[4]Utilization of a job is defined as C/P.

can be ignored by subtracting E from P. B can be computed as:

$$B = \sum^{\forall \text{ Intermediate Node}} f_{\tau_i}(\vec{\tau}),$$

where $\vec{\tau}$ is the set of messages that are scheduled before the message τ_i at an intermediate node.

The utilization U_i' of each message can be revised with regard to the block time as:

$$U_i' = \frac{C_i + B_i}{P_i}$$

In the admission control procedure we try to keep $U_s' < 1$ at node s. In the following we elaborate the job admission process through an example.

Example: Consider an SCI ringlet consisting of three nodes (as shown in figure 4). The job arrivals at each node are shown in the following table.

Node	Job	C	D	P
Node 1	τ_{11}	1	9	9
	τ_{12}	1	10	10
Node 2	τ_{21}	1	5	5
	τ_{22}	1	6	6
Node 3	τ_{31}	2	7	7
	τ_{32}	1	9	9
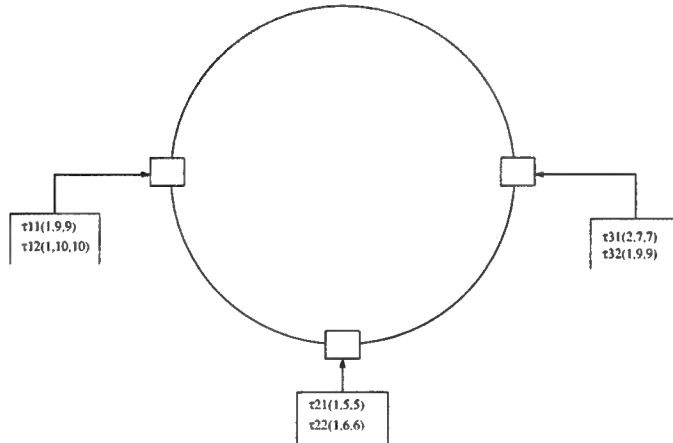
Figure 4: A three node SCI ring.

The utilization of each node is:

$$U_1 = \sum_j^{M_j \in \Psi_1} \frac{C_j}{P_j} = \tfrac{1}{9} + \tfrac{1}{10} + \tfrac{2}{7} + \tfrac{1}{9} = 0.61 \le 1,$$
$$U_2 = \sum_j^{M_j \in \Psi_2} \frac{C_j}{P_j} = \tfrac{1}{5} + \tfrac{1}{6} + \tfrac{1}{9} + \tfrac{1}{10} = 0.58 \le 1,$$
$$U_3 = \sum_j^{M_j \in \Psi_3} \frac{C_j}{P_j} = \tfrac{1}{5} + \tfrac{1}{6} + \tfrac{2}{7} + \tfrac{1}{9} = 0.77 \le 1.$$

13-16

So the first condition is satisfied. If we use the earliest deadline first scheduling, we get

Node 1

$B(\tau_{11}) = 0 + 60/19 = 3.16$

$U(\tau_{11}) = (1 + 3.16)/9 < 1$

$B(\tau_{12}) = 9/8 + 270/47 = 6.87$

$U(\tau_{12}) = (1 + 6.87)/10 < 1$

Node 2

$B(\tau_{21}) = 0 + 0 = 0$

$U(\tau_{21}) = (1 + 0)/5 < 1$

$B(\tau_{22}) = 5/4 + 5/4 = 2.5$

$U(\tau_{22}) = (1 + 2.5)/6 < 1$

Node 3

$B(\tau_{31}) = 0 + 0 = 0$

$U(\tau_{31}) = (2 + 0)/7 < 1$

$B(\tau_{32}) = 14/5 + 189/38 = 4.97$

$U(\tau_{32}) = (1 + 4.97)/9 < 1$

These messages are schedulable under the earliest deadline first scheduling discipline.

3.2 Job Sequencing

When a new job is admitted, all the intermediate nodes (i.e., the nodes that fall between the source and the destination of the message) need to place the job in their already existing job sequence. Job sequencing is performed in a distributed fashion among all the nodes.

Consider a unidirectional ring with n nodes $N_1, N_2, ..., N_n$. If we ignore the link delay (which can be done as described in the previous section), then a message output at N_i, is immediately available at N_{i+1}. This way of modeling the scheduling is helpful because the link delay can be factored out of the schedule construction. When a message becomes available at node N_{i+1}, the message either has to be transmitted immediately, or will wait in the bypass buffer. In other words, the incoming message contends for the outgoing link with the node's own messages. In case of contention, the job sequence determines which message will be transmitted first.

Each node keeps a job sequence which determines the priority of transmission in case of contention. When a new job arrives, either from this node or from an upstream node, the sequence will be recomputed to make room for the new job. Suppose a node has a current job sequence $s_1 s_2 ... s_k$, and a set of newly arrived jobs $\tau_1 \tau_2 ... \tau_n$, as shown in figure 5. Then the newly arrived
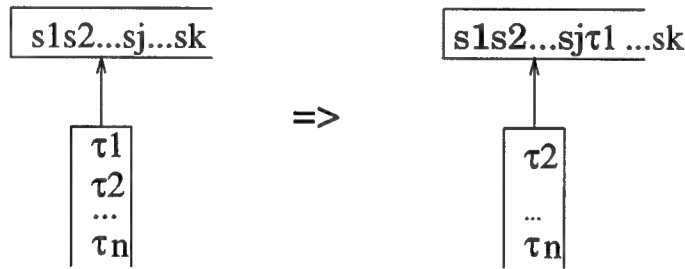
Figure 5: Job sequencing procedure.

jobs will be inserted into the sequence to form the new job sequence. The mechanism by which the new schedule is decided is explained below.

In order to compute and update the sequence we introduce two state variables per node, $L[s, j]$ and $M[s, j]$. $L[s, j]$ is the latest time by which j^{th} job has to be scheduled at node s, so that its

deadline can be met. $M[s, j]$ is the earliest schedulable position of the jth job at node s in a job sequence so that the jobs before this one can meet their deadlines. After the admission of a new job, these two variables are updated in a distributed fashion as described in the following. We use $D[s, j]$ to denote the deadline of the jth job at node s.

$$D[s+1, j] - L[s, j] \geq D[s+1, M[s+1, j]]$$
$$M[s, j] = \min_i \forall_i^{j-1} k \left\{ L[s, k] - f_{\tau_j}(\tau_1, \tau_2, \ldots, \tau_j \tau_{k+1}) > 0 \right\}$$

$$\implies L[s, j] \leq D[s+1, j] - D[s+1, M[s+1, j]] \tag{1}$$

Equation (1) is computed incrementally by all the nodes in turn and the new values of $L[s, j]$ and $M[s, j]$ are computed. This fixes the job sequence. Each job in the sequence keeps the information of $L[s, j]$ and $M[s, j]$. We elaborate the idea through the following example.

Example: Consider the same ringlet as shown in the previous example. Consider the following job arrivals.

Job	S	T	C	D	P
τ_1	1	3	16	80	80
τ_2	2	3	80	420	420
τ_3	2	1	16	95	95
τ_4	3	1	80	510	510
τ_5	1	2	16	90	90
τ_6	3	1	16	72	72
τ_7	1	3	80	390	390
τ_8	2	3	80	440	440
τ_9	3	2	16	77	77
τ_{10}	2	1	16	69	69

The following steps show the computation of the job sequence at each node.

$\tau_1[16,1,3,80]$

Source node: Node1:   **Current Scheduling:**
M[1,1]=0; L[1,1]=64;   NULL;
Intermediate node: Node2:   **Current Scheduling:**
M[2,1]=0; L[2,1]=64;   NULL;

$\tau_2[80,2,3,420]$

Source node: Node2:   **Current Scheduling:**
M[2,2]=1; L[2,2]=340; τ_1: M[2,1]=0; L[2,1]=64; C[2,1]=16; f(τ_1,τ_2)=157.37

13-18

$\tau_3[16,2,1,95]$

Source node: Node2: **Current Scheduling:**
M[2,3]=1; L[2,3]=79; τ_1: M[2,1]=0; L[2,1]=64; C[2,1]=16; f(τ_1,τ_2)=157.37
                         τ_2: M[2,2]=1; L[2,2]=340;C[2,2]=80;f(τ_1,τ_2,τ_3)=253.39
                         $\Rightarrow \tau_1$: M[2,1]=0; L[2,1]=64; C[2,1]=16; f(τ_1,τ_3)=50.63
                         $\Rightarrow \tau_3$: M[2,3]=1; L[2,3]=79; C[2,3]=16; f(τ_1,τ_3,τ_2)=253.39
                         $\Rightarrow \tau_2$: M[2,2]=2; L[2,2]=340;

Intermediate node: Node3: **Current Scheduling:**
M[3,3]=0; L[3,3]=79   NULL;

$\tau_4[80,3,1,510]$

Source node: Node3: **Current Scheduling:**
M[3,4]=1; L[3,4]=430; τ_3: M[3,3]=0; L[3,3]=79; f(τ_3,τ_4)=142

$\tau_5[16,1,2,90]$

Source node: Node1: **Current Scheduling:**
M[1,5]=1; L[1,5]=74; τ_1: M[1,1]=0; L[1,1]=64; C[1,1]=16; f(τ_1,τ_5)=51.44

$\tau_6[16,3,1,72]$

Source node: Node3: **Current Scheduling:**
M[3,6]=1; L[3,6]=56; τ_4: M[3,4]=1; L[3,4]=430; f(τ_3,τ_4,τ_6)=247.3
                         $\Rightarrow \tau_6$ need schedule before τ_4;
M[3,4]=2; L[3,4]=430; τ_3: M[3,3]=0; L[3,3]=79; f(τ_3,τ_6)=53
                         τ_6: M[3,6]=1; L[3,6]=56; f(τ_3,τ_6,τ_4)=247.3

$\tau_7[80,1,3,390]$

Source node: Node1: **Current Scheduling:**
M[1,7]=2; L[1,7]=310; τ_1: M[1,1]=0; L[1,1]=64; C[0,1]=16; f(τ_1,τ_5)=51.44
                         τ_5: M[1,5]=1; L[1,5]=74; C[0,5]=16; f(τ_1,τ_5,τ_7)=268.58;

Intermediate node: Node2: **Current Scheduling:**
M[2,7]=?; L[2,7]=310; τ_1: M[2,1]=0; L[2,1]=64; C[2,1]=16; f(τ_1,τ_3)=50.63
                         τ_3: M[2,3]=1; L[2,3]=79; C[2,3]=16; f(τ_1,τ_3,τ_2)=253.39
                         τ_2: M[2,2]=2; L[2,2]=340; C[2,2]=80; f($\tau_1,\tau_3,\tau_2,\tau_7$)=813.56
                         $\Rightarrow \tau_1$: M[2,1]=0; L[2,1]=64; C[2,1]=16; f(τ_1,τ_3)=50.63
                         τ_3: M[2,3]=1; L[2,3]=79; C[2,3]=16; f(τ_1,τ_3,τ_7)=262.91
                         τ_7: M[2,7]=2; L[2,7]=310; C[2,3]=80; f($\tau_1,\tau_3,\tau_7,\tau_2$)=813.56;

$\Rightarrow \tau_7$ Rejected; Delete τ_7.

$\tau_8[80,2,3,440]$
Source node: Node 2: **Current Scheduling:**

M[2,8]=?; L[2,8]=360;

τ_1: M[2,1]=0; L[2,1]=64; C[2,1]=16; f(τ_1,τ_3)=50.63

τ_3: M[2,3]=1; L[2,3]=79; C[2,3]=16; f(τ_1,τ_3,τ_2)=253.39

τ_2: M[2,2]=2; L[2,2]=340; C[2,2]=80; f($\tau_1,\tau_3,\tau_2,\tau_8$)=738.46

$\Rightarrow \tau_8$ Rejected; Delete τ_8

$\tau_9[16,3,2,77]$
Source node: Node 3: **Current Scheduling:**

M[3,9]=?; L[3,9]=61;

τ_3: M[3,3]=0; L[3,3]=79; f(τ_3,τ_6)=53

τ_6: M[3,6]=1; L[3,6]=56; f(τ_3,τ_6,τ_9)=129.73

$\Rightarrow$ Reject τ_9;

$\tau_{10}[16,2,1,69]$
Source node: Node2: **Current Scheduling:**

M[2,10]=?; L[2,10]=53;

τ_1: M[2,1]=0; L[2,1]=64; C[2,1]=16; f(τ_1,τ_3)=50.63

τ_3: M[2,3]=1; L[2,3]=79; C[2,3]=16; f(τ_1,τ_3,τ_{10})=80

$\Rightarrow$ Reject τ_{10}.

Therefore the accepted job sequences are:

Node 1	**Node 2**	**Node 3**
τ_1: {M=0, L=64; C=16}	τ_1: {M=0, L=64; C=16}	τ_3: {M=0, L=79, C=16}
τ_5: {M=1, L=74; C=16}	τ_3: {M=1, L=79, C=16}	τ_6: {M=1, L=56, C=16}
τ_7: {M=2, L=310; C=80}	τ_2: {M=2, L=340, C=80}	τ_4: {M=2, L=430, C=80}
Utilization = 0.583	Utilization = 0.559	Utilization = 0.548

4 Application of Popular Real-time Schemes

In a distributed real-time system, the problem of routing a set of messages through the network so that each message can be sent on-time is an important issue. There are several real-time scheduling algorithms proposed [3] that deal with this problem. Although rate monotonic scheduling (RMS) [10] is a seminal work in real-time scheduling, it does not scale well in a distributed system. Several heuristic algorithms have been proposed in the literature [8, 9]. In this section, we describe some of the popular ones. Each of them can solve some restricted cases of the problem. These algorithms are studied for alternative SCI/RT schemes and are used as references of comparison with our job packing algorithm.

4.1 Earliest Available First Algorithm

RMS is not the only priority scheduling theory. Depend on how the priority is defined, different scheduling algorithms can be devised. Earliest Available First algorithm (EAF) defines the priority level according to a message's ready time. The earlier the message is ready, the higher the priority it gets. This algorithm is the simplest scheduling algorithm, similar to FCFS. The algorithm works as follows: Whenever a node is ready for transmission, it sends the earliest available message. Ties are broken arbitrarily. A set of messages with identical origin nodes, destination nodes, release times, and deadlines is feasible with respect to non-preemptive transmission if and only if EAF is feasible [8, 9]. If there is no restriction on the origin nodes, destination nodes, or release times, EAF cannot give the guarantee that an accepted message can meet its deadline.

4.2 Earliest Deadline First Algorithm

Earliest Deadline First algorithm (EDF) assigns a job's priority according to its deadline. The intuition behind EDF is to send the message that has earliest deadline first in order to avoid missing its deadline. The algorithm is follows: Whenever a node is ready for transmission, it sends the message with minimum deadline among all the messages present at that time. Ties can be broken arbitrarily. It has also been shown [8, 9] that EDF is the optimal algorithm if the messages have identical origin nodes, destination nodes, and release times.

4.3 Smallest Slack Time First Algorithm

Slack time of a real-time job is defined as the laxity of the job, i.e., in our terminology, $P - C$. Smallest Slack Time First Algorithm (SSF) treats the job with the smallest slack time as the most critical job, and assigns it the highest priority. The underlying assumption is bigger the slack time, more deadline tolerance the job is. The basic algorithm is as follows: Whenever a node is ready for transmission, it sends the message with the smallest slack time, among all the messages present at that time. Ties can be broken arbitrarily. As shown in [9], the SSF algorithm is optimal for a set of messages with identical origin nodes, and is optimal for the set of messages with identical release times.

4.4 Farthest Away First Algorithm

Farthest Away First (FAF) algorithm considers the distance from the source to the destination. A job that is far away from its destination is assigned higher priority since it needs more time to pass through the longer path. The FAF algorithm works as follows: Whenever a node is ready for transmission, it sends the message with the farthest destination. Ties can be broken arbitrarily. In [8] it has been proven that FAF is optimal for a set of messages with identical deadlines.

5 Numerical Results and Comparison

In this section we describe our experimentation model for SCI/RT, present the results obtained and discuss the results. We also compare the relative performance of various SCI/RT schemes.

5.1 Simulation Model

In order to study the feasibility and the performance of different candidate real-time schemes for SCI and our scheme, we have built a detailed simulation model for each of them. We started with a baseline simulation model developed at the University of Wisconsin [15]. It is a time-driven simulator that simulates only the base SCI packet transmission protocol (without the cache coherence protocol) in a single SCI ring with multiple nodes. It uses simplified buffer management, i.e., single transmit and receive queue per SCI node. The simulator was extended by the author during his summer stay at the Wright Laboratory as a participant of the AFOSR Summer Faculty Research Program. The simulator developed in [11] was extended to implement different plausible SCI/RT protocols. In the following we outline only the main features of each of the simulation models. Refer to [11] for a detailed report on the simulator.

Job Packing Scheme: We have designed and developed a simulator for the job packing algorithm. The simulator consists of three essential parts, namely the job admission controller, the job sequencer, and the job scheduler. The job admission controller performs all the tests described in section 3, and keeps the necessary data structures up-to-date. The job sequencer distributes the information regarding the new job to all the nodes and computes the job sequences in a pseudo-distributed (i.e., distributed in a simulated environment) manner. The function of the job scheduler is to schedule the jobs in the simulated SCI ring. It uses part of the idle symbols for distributing scheduling related information to all the nodes.

Candidate SCI/RT Schemes: From the candidate SCI/RT protocol suite, we have selected the train protocol and the 2-bit/8-bit priority protocols. Since the 8-bit protocol is very similar to the train protocol, we simulate only the 2-bit part of the priority protocol. The train protocol requires a significant change on the baseline model in order to simulate the LocalMotive and the TicketMaster. The 2-bit protocol is implemented from its specification.

Popular Real-time Schemes: We have built a simulator to study any priority based scheduling discipline (refer to section 4) on the SCI/RT platform. We use this platform to study the EAF, EDF, SSF and FFA algorithms described in section 4. Note that all the protocols in this suite are different variations of priority based scheduling. They differ in the way the priority per job is computed and assigned. We developed algorithm specific priority computation procedures and plug them in the corresponding scheme.

The simulators are tested rigorously before they were used for the performance study. We conduct the performance study with synthetically generated real-time job workload. The workload generation process is described next.

5.2 Workload Generation

In order to evaluate the performance of different protocols and to compare the performance of the proposed job packing scheme, we created different sets of workloads. The simulators were subjected to each set of workloads. Each workload consists of a set of jobs. A job could be either periodic or aperiodic. The periodic jobs are representative of sensor generated data, while the aperiodic jobs characterize one time operation like interrupt processing. They are both representative of real-time traffic [18].

Periodic Workload: Each job set contains 1000 periodic jobs, with an average job utilization of $\rho = \sum_i C_i/P_i$. The value of ρ is varied over the job sets. Abiding by the standards of SCI packet sizes, we make the computation time of a job (C) equivalent to 16 (command/address), 80 (16 bytes address + 64 byte data), and 272 (16 bytes address + 256 bytes data) time units, where one time unit represents the time needed to transmit one symbol. In our job set, the computation time of each job is selected randomly from 16, 80, and 272. Once the value of C is selected, we go on to choosing the value of P. This value is chosen in such a way so that the value of C/P of each job falls randomly within $[\rho - r, \rho + r]$, where r is a tunable parameter. Each job is assigned a source and a destination node randomly from all the nodes connected in the ring.

Aperiodic Workload: Aperiodic job sets are created from periodic job sets by assuming that a job does not repeat. We use $D = P$ to define the deadline of an aperiodic job. Each job in an aperiodic job set is assigned a randomly selected arrival time.

5.3 Comparative Study of Job Packing with Train and 2-bit Protocols

We conducted several sets of experiments to study and evaluate the performance of the job packing algorithm with train and 2-bit protocols. In a real-time environment since we are more concerned with a job's deadline guarantee rather than fairness and forward progress, we use different sets of performance metrics, namely job reject ratio and average node utilization, and study them as a function of load on the ring. We express the load on the ring in terms of cumulative job utilization of a job set. It is defined as $\sum C_i/P_i$ (i.e., ρ) for all the jobs present in the set. Job reject ratio defines the fraction of jobs that were rejected by a particular protocol since their deadlines cannot be met. The average node utilization is time averaged over the simulation duration. The experiments are classified according to the workload used, and are described below.

Figure 6: Performance of Job Packing, Train, 2-Bit protocols for periodic job set (Part I).

Periodic Workload: Our first set of experimentation used the periodic workload as the input to the real-time SCI protocols, and the results are plotted in figures 6 and 7. Each pair of graphs show the job reject ratio and the average node utilization as a function of cumulative job utilization. Different pairs of graphs show the simulation results with different degree of randomness in the workload job set (i.e., r). The following observations can be made from the figures:

- Job reject ratio is the lowest with job packing algorithm, and the highest for train protocol, with 2-bit protocol in between. This is due to the fact that the job packing algorithm tries to accommodate as many jobs as possible through local (very low overhead) job admission, and global job sequencing (more overhead). It can move jobs around in the sequence so that more new jobs can get in. This results in low job reject ratio. The train protocol, on the other hand, wastes a significant amount of ring resource in maintaining and circulating the train
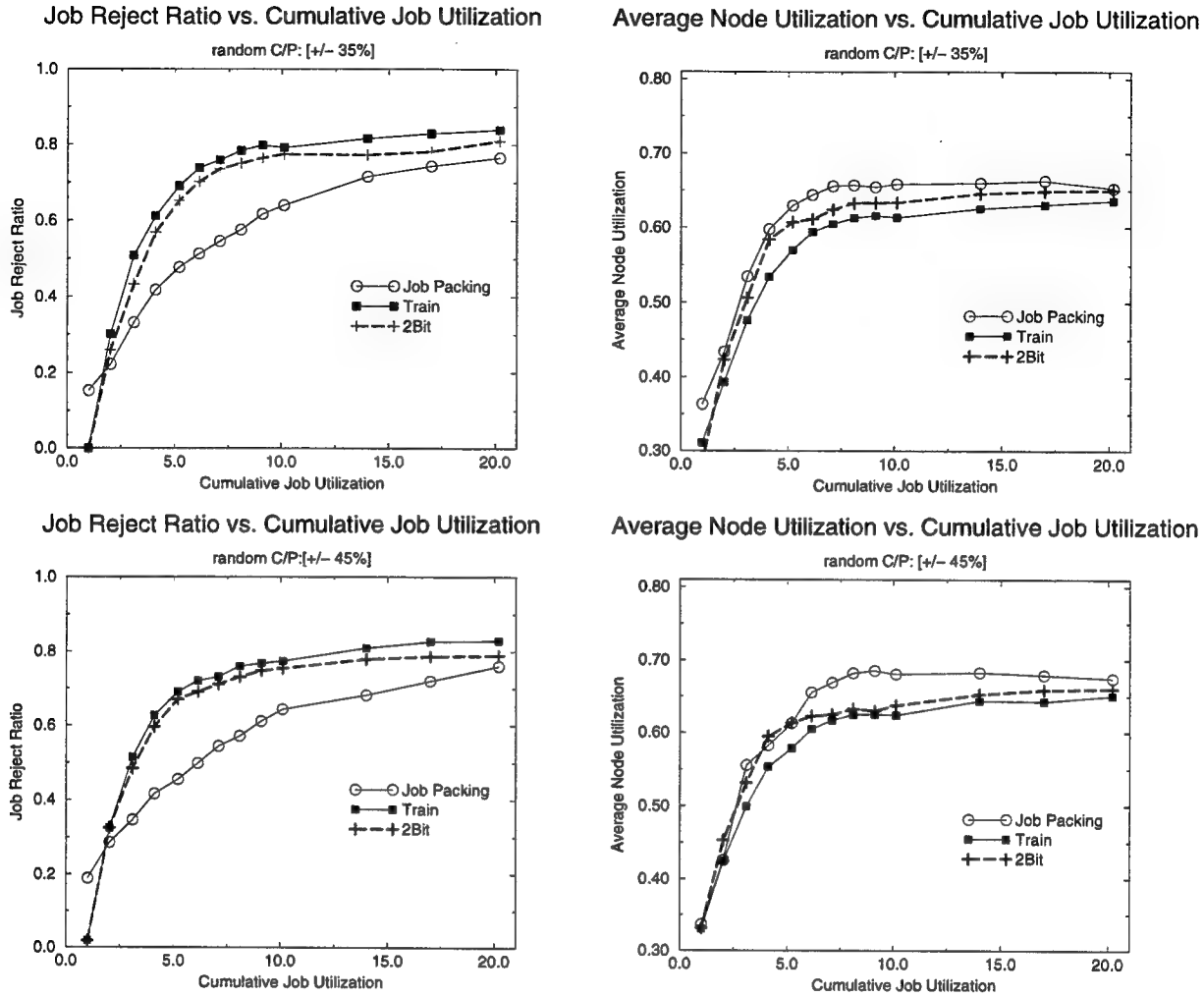
Figure 7: Performance of Job Packing, Train, 2-Bit protocols for periodic job set (Part II).

over the ring. A job has to wait at least one round trip before it gets permission (or rejection). This extra overhead forces the train protocol to reject more jobs. The 2-bit protocol, with its limited priority levels, cannot accept a lot of jobs. Since its overhead is lot lower than train protocol, it performs better.

- Average node utilization is highest for job packing algorithm, and lowest for train protocol, with 2-bit protocol in between. This behavior can be explained from the job reject ratio. More jobs a protocol admits, more utilization a node will achieve for the corresponding protocol.

- As the randomness in the job set increases, job packing algorithm performs even better (i.e. lower job reject ratio and higher node utilization). This is due to the fact that randomness in job parameters allows the job packing algorithm to make the packing tighter. In other

words, during the job sequencing phase, there is more flexibility in moving jobs around and this results in higher job acceptance rate. This flexibility cannot be exploited by train or 2-bit protocols.
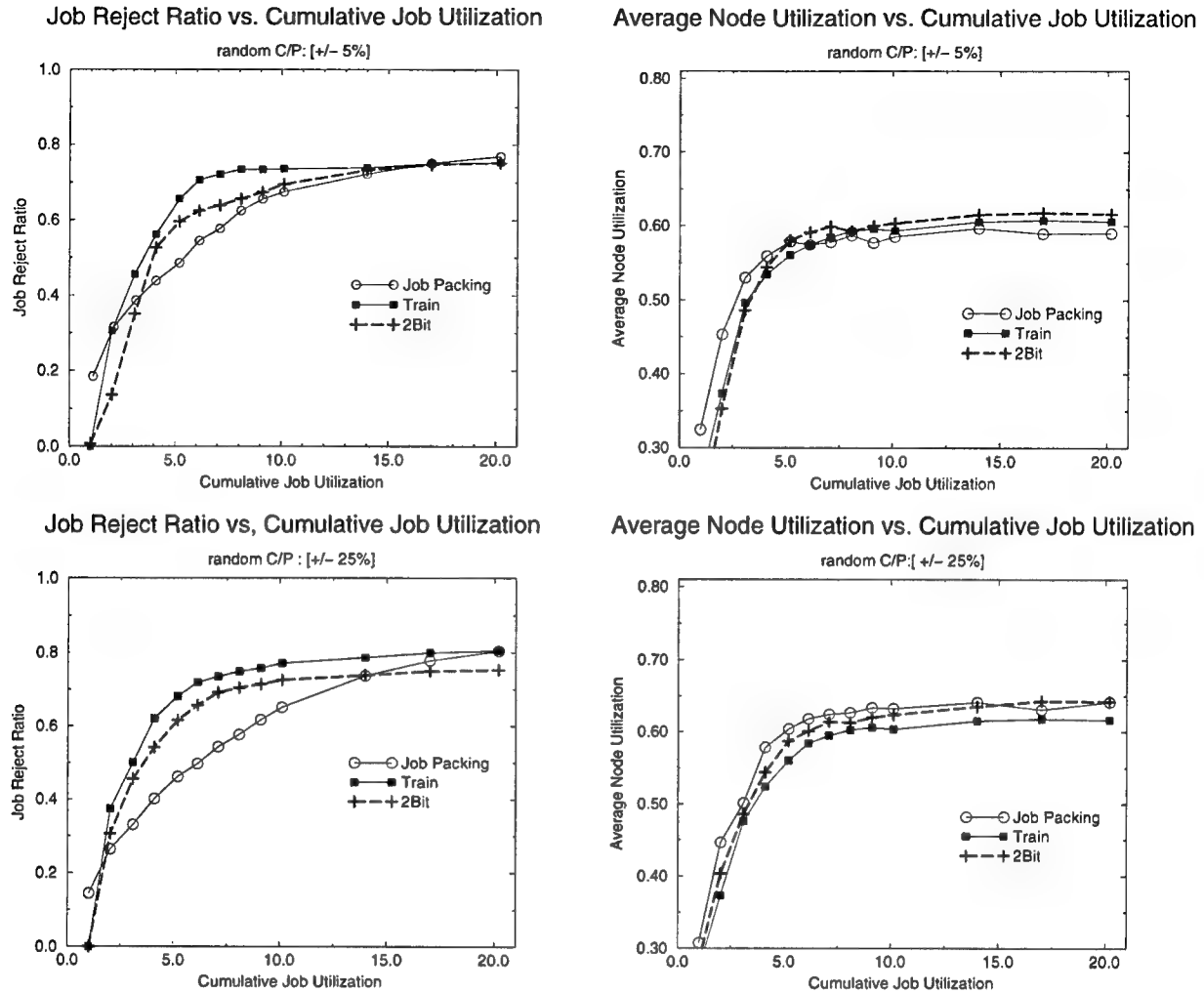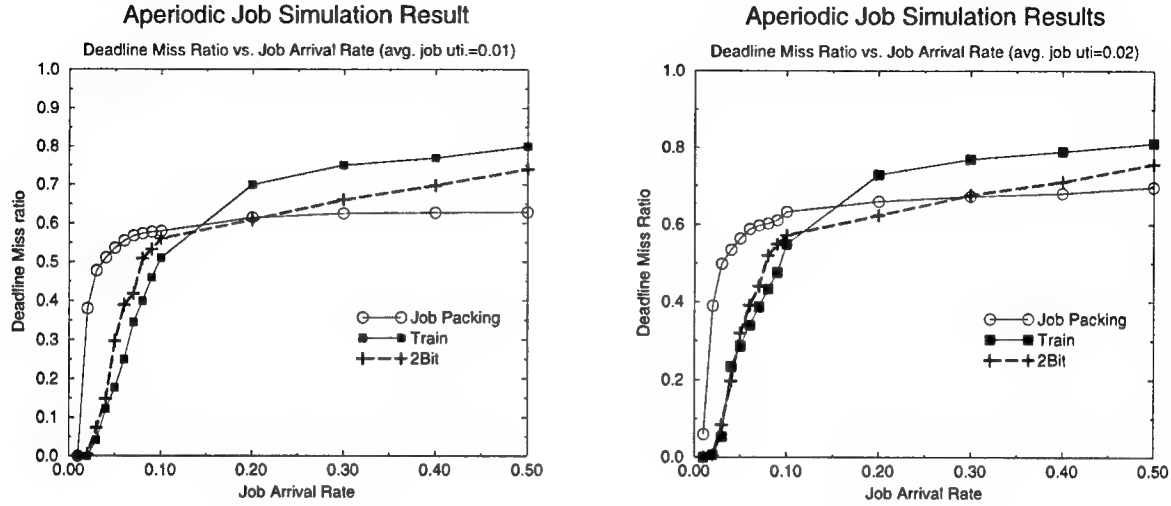

Figure 8: Performance of Job Packing, Train, 2-Bit protocols for aperiodic job set.

Aperiodic Workload: The next set of experiments use the aperiodic job sets as the workload. Note that cumulative job utilization does not make the same sense in this context as it does for periodic jobs. Instead we use job arrival rate to define the intensity of workload. The arrival rate is measured in time units of symbol time[5] to make it independent of link bandwidth. We assume that the jobs arrive according to a Poisson arrival process. The results obtained from the simulation are plotted in figure 8. Deadline miss ratio is defined as the fraction of jobs that miss their deadlines, which is the most important metric in their schedule. Observe from the figure that at low aperiodic job arrival rate (i.e., low load) the train protocol has the lowest miss ratio, job packing algorithm being the highest and 2-bit protocol in between. However, just the reverse sequence can be observed at higher job arrival rate (i.e., high load). The results can be explained again by the philosophy behind the design of each of these protocols. Since job packing algorithm tries to pack jobs as compactly as possible, in lower job arrival rate it does not perform very good since there is nothing much to pack (as the jobs do not repeat). Whereas both train and 2-bit protocols use the lightly loaded ring to send whatever job is coming, as quickly as possible. However, as the load increases, the overhead of train protocol and insufficiency of 2-bit protocol priority levels become more prominent and they fail to guarantee the deadline. In this scenario, job packing algorithm works very well since it is able to construct the sequence more appropriately.

---

[5] One symbol time is defined as the time it takes to transmit one symbol over the ring.

This load sensitivity of the job packing algorithm is a desirable feature for real-time job scheduling over SCI.

5.4 Comparative Study of Job Packing with Popular Real-Time Schemes

In this section we present our experimental results on the performance of popular real-time message scheduling algorithms on a SCI ring. We used similar experimental setup with different classes of workload as we did in the previous section. Below we describe and analyze the results obtained for each of the categories. We also compare the results with the job packing algorithm.
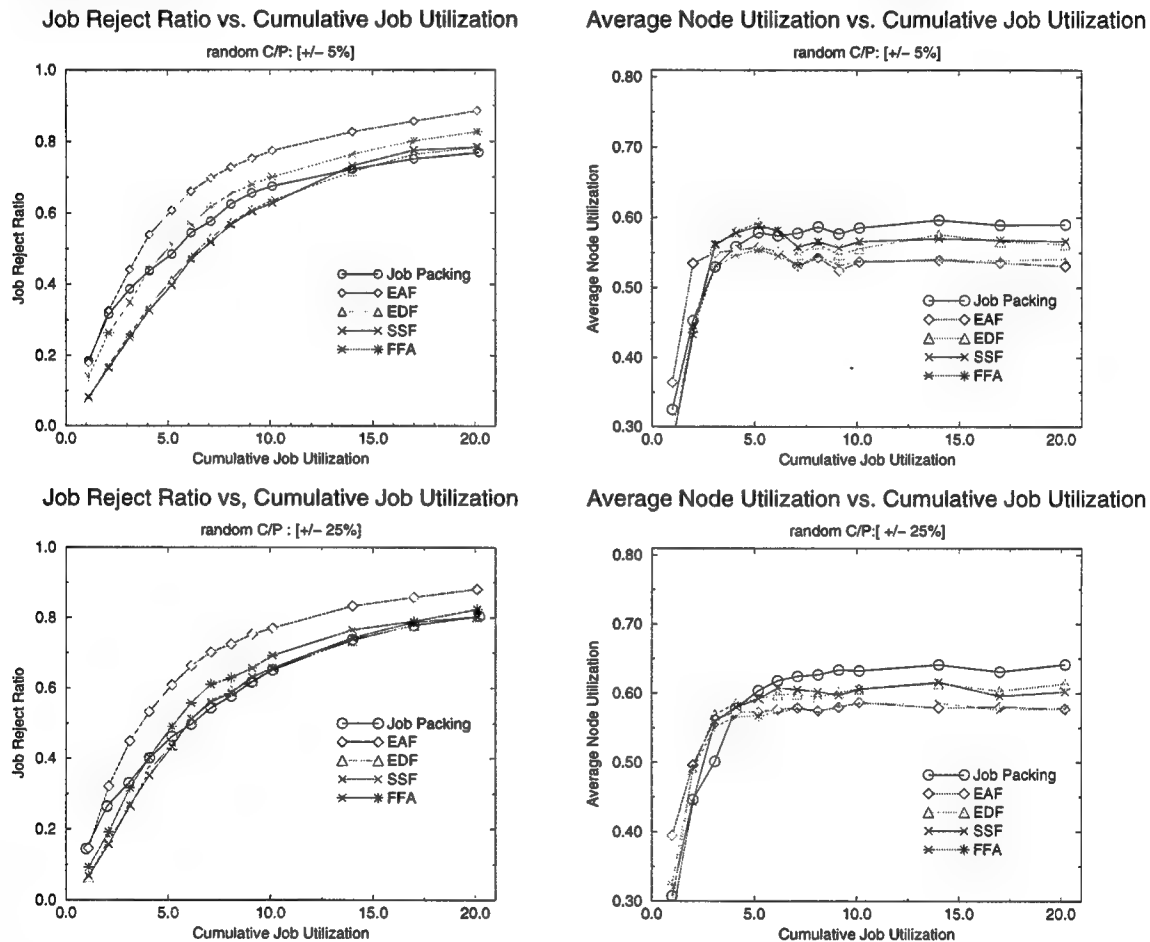
Figure 9: Performance of Job Packing, EAF, EDF, SSF and FFA for periodic job set (Part I).

Periodic Workload: The workloads and the performance metrics used in this set of experiments are the same as what were used before (train and 2-bit protocols). We evaluate and compare the performance of EAF, EDF, SSF and FFA schemes with the job packing algorithm. The results are
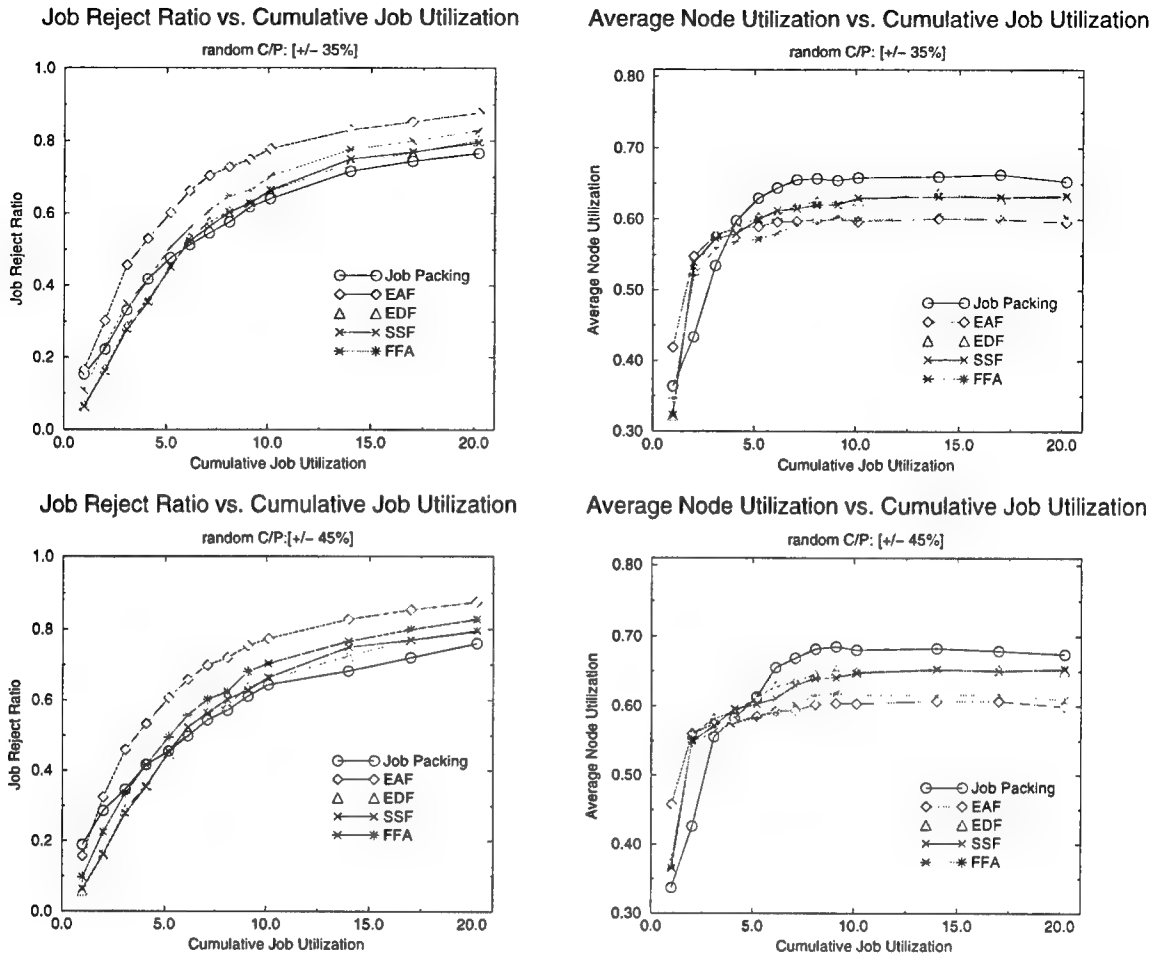
Figure 10: Performance of Job Packing, EAF, EDF, SSF and FFA for periodic job set (Part II).

plotted in figures 9 and 10. General conclusions drawn from these figures are the following:

1. Simple algorithms like EAF, which is a variation of FCFS service discipline, does not work well in a real-time environment.

2. FFA, which depends only on the destination, but ignores the deadlines of the jobs fails to capture the real-time requirements of the jobs.

3. Both EDF and SSF work well in a real-time environment since both of them are sensitive to the deadline (and computation time for SSF). However, the algorithms may fail to guarantee message deadline at high load because they are not able to change the job priorities adaptively with load.

4. The job packing algorithm works well in a real-time environment. Although EDF and SSF work better than job packing at low load, the role reverses with increase in load and degree

of randomness in workload. Job packing algorithm can exploit the flexibility to maneuver the job sequence and change their priorities dynamically by resequencing the jobs.

The average node utilization is a direct manifestation of the effect of job reject ratio, and can be explained in a similar way.
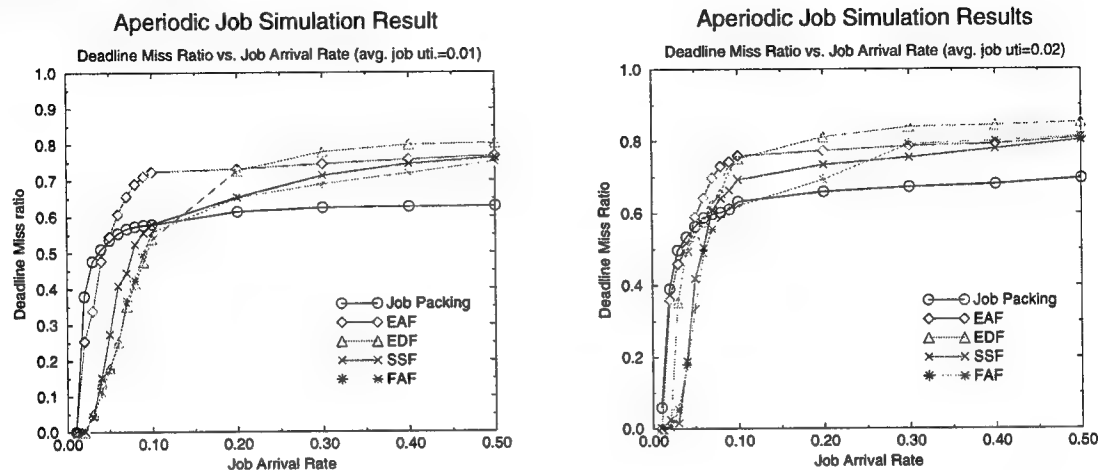
Figure 11: Performance of Job Packing, EAF, EDF, SSF and FFA protocols for periodic job set.

Aperiodic Workload: We use the same aperiodic workload for this set of experiments. The results are plotted in figure 11. A trend similar to the one observed for the previous set of experiments can be observed here as well. At low load job packing performs not as good as others. At high load, due to the load sensitivity feature of job packing scheme, it performs much better than the rest.

5.5   Discussion

The experiments reveal that the train protocol suffers from high maintenance overhead, whereas 2-bit protocol may fall short in providing sufficient priority levels. Simple protocols like EAF and FAF do not work well in a real-time environment. EDF and SSF perform well during low load, but their high load performance is not so good since their job priority scheme is not load sensitive. An algorithm that is load sensitive and is able to dynamically prioritize the real-time jobs is well suited in the SCI/RT environment. The job packing algorithm is an ideal candidate for that. However, we would like to mention here that the current version of the proposed algorithm has moderately high overhead in the job sequencing phase. More work needs to be done to lower the complexity and make it more amenable to run online.

6   Conclusion and Future Research

In this document we have reported the work conducted on real-time message transmission over Scalable Coherent Interface. The main thrust of the work was to study the performance of different SCI/RT candidate schemes and the suitability of some of the popular real-time message delivery techniques applied to the SCI paradigm. The study is made through extensive simulation of all these schemes. We observe that different schemes suffer from different limitations, and conclude that a flexible, load sensitive scheme is well suited for SCI/RT. In this regard we have developed a new real-time message scheduling protocol over SCI, called the job packing algorithm. We have conducted simulation study using real-time workload, and have shown the superiority of the proposed scheme.

The current version of the job packing protocol, although shows great potential, suffers from moderately high overhead in the job sequencing phase and hinders its online implementation. At the time of developing this report, we had several conjectures regarding the job packing algorithm. We have verified them through experimentation, but theoretical proofs are yet to be developed. We plan to revise the algorithm to make it amenable for online use, specify the detail protocol steps and complete the theoretical study. We will carry that as our future work in this direction.

Acknowledgement

References

[1] B. W. Abeysundara and A. E. Kamal. High-Speed Local Area Networks and Their Performance: A Survey. *ACM Computing Surveys*, 23(2):221–264, June 1991.

[2] D. L. Anderson. A Proposal to the P1596.6 (SCI/RT) Working Group for a Preemptive Priority Queue Protocol. Technical report, Edgewater Computer Systems, Inc., 1995.

[3] C. M. Aras, J. F. Kurose, D. S. Reeves, and H. Schulzrinne. Real-Time Communication in Packet-Switched Networks. *Proceedings of the IEEE*, 82(1), January 1994.

[4] D. B. Gustavson and Q. Li. The Scalable Cohorent Interface (SCI). *IEEE Communications*, 34(8), August 1996.

[5] D. B. Gustavson, B. E. Stewart, and D. L. Anderson. *SCI/RT: D0.13*, November 1992.

[6] IEEE Computer Society. *IEEE Standard for Scalable Coherent Interface (SCI)*, August 1993. IEEE Standard 1596-1992.

[7] D. James and D. Gustavson. *Draft Proposals for Real-Time Transactions on SCI*. Apple Computer Inc. and SCIzzL, June 1995. Version 0.279.

[8] J. Y-T. Leung, T. W. Tam, C. S. Wong, and G. H. Young. Routing Messages with Release Time and Deadline Constraints. *Journal of Parallel and Distributed Computing*, 31, 1995.

[9] J. Y-T. Leung, T. W. Tam, and G. H. Young. On-Line Routing of Real-Time Messages. *Journal of Parallel and Distributed Computing*, 34, 1996.

[10] C. L. Liu and J. Layland. Scheduling algorithm for multiprogramming in a hard real-time environment. *Journal of the ACM.*, 20(1):46–61, Jan. 1973.

[11] S. Mukherjee. *A Systems Study of the Scalable Coherent Interface (SCI)*. Department of Computer Science & Engg., University of Nebraska-Lincoln, September 1995. AFOSR Summer Faculty Research Program Report.

[12] S. Mukherjee, D. Saha, M. C. Saksena, and S. K. Tripathi. A Bandwidth Allocation Scheme for Time Constrained Message Transmission on A Slotted Ring LAN. In *Proceedings of the IEEE 14th Real-Time Systems Symposium*, pages 44–53, 1993.

[13] D. Picker, R. D. Fellman, and P. M. Chau. An Extension to the SCI Flow Control Protocol for Increased Network Efficiency. *IEEE/ACM Transactions on Networking*, 4(1), February 1996.

[14] F. E. Ross. An Overview of FDDI: The Fiber Distributed Interface. *IEEE Journal on Selected Areas in Communications*, 7(7):1043–1051, September 1989.

[15] S. L. Scott, J. R. Goodman, and M. K. Vernon. Analysis of the SCI Ring. Technical Report 1055, Computer Science Department, University of Wisconsin-Madison, November 1991.

[16] T. Scott. *Full Performance Train Protocol for SCI/RT*, 1995.

[17] L. Sha, R. Rajkumar, and S. S. Sathaye. Generalized Rate-Monotonic Scheduling Theory: A Framework for Developing Real-Time Systems. *Proceedings of the IEEE*, 82(1):68–82, January 1994.

[18] K. G. Shin and P. Ramanathan. Real-Time Computing: A New Discipline of Computer Science and Engineering. *Proceedings of the IEEE*, 82(1):6–24, January 1994.

Accurate Calibration of High Temperature Superconductor (HTS) Dielectric Resonator Measurements

Krishna Naishadham
Associate Professor
Department of Electrical Engineering
Wright State University
Dayton, OH 45435

Accurate Calibration of High Temperature Superconductor (HTS) Dielectric Resonator Measurements

Krishna Naishadham

Department of Electrical Engineering

Wright State University

Dayton, OH 45435

Abstract

Dielectric resonators (DRs), formed by sandwiching a cylindrical piece of polished dielectric material (sapphire) between two planar HTS thin–films, offer an attractive platform for microwave testing of HTS materials. They also find dual use as components in low–noise microwave receivers. We have measured each DR as a two-port system, by exciting and detecting the modal fields with loop-terminated coaxial cables. The observed Q factor of the resonator is a gauge of the surface resistance of the endplates, an important property for the microwave characterization of HTS thin films. In HTS DR measurements, because of the extremely high Q's (of the order of 10^6) resulting from very low dissipation, the measured parameters are very sensitive to the background "noise" contributed by the coupling mechanism, fixturing case modes, radiation, etc. Therefore, it becomes important to properly calibrate out all the parasitics of the fixture in order to accurately measure the unloaded Q factor of the resonator. In this paper, we report an accurate calibration procedure based on the application of least squares minimization with convergence enhanced by the non-linear Marquardt algorithm. As it is impossible for the loop–coupling mechanism to employ traditional hardware calibration applicable to network analyzer measurements, we have alternatively developed this software calibration approach to effectively filter out the background noise and extract the unloaded Q of the DR. We have developed a computer program in LabWindows C to directly interface with the network analyzer and extract the HTS parameters of interest using the calibration algorithm. We discuss the utilization of this method in the characterization of HTS DRs with small area thin–films, at frequencies in the 20–40 GHz range, and at cryogenic temperatures.

1 Introduction

The discovery of high temperature superconductivity in LaBaCuO at 30K by Bednorz and Müller (1986) [1], and in YBaCuO (YBCO) at temperatures above 90K by Chu and several others (1987) [2], has significant impact on the design of microwave systems. Because of extremely small losses (or high Q-factor), low noise, low power consumption, potential for circuit miniaturization, high critical current densities, and uniform small-signal behavior over a wide temperature range, high temperature superconductor (HTS) materials are becoming increasingly useful in aerospace industry, where size, weight and performance need to be optmized. Several designs of passive HTS microwave circuits, such as ultra low-loss transmission lines, sharp-skirt microwave filters, high-gain antenna arrays, etc., have been reported [3]. In addition, HTS materials exhibit non-linear field effects at the macroscopic level (*e.g.*, Josephson tunneling effect), which made possible a number of active devices, such as field effect transistor (FET) and heterojunction bipolar transistor (HBT), operating with improved performance over their room-temperature normal conductor counterparts [4].

Most of the microwave applications of HTS materials employ thin-film technology in contrast to bulk materials. An important microwave electrical property of the HTS film is the surface resistance, which determines the dissipation in microwave devices, and hence the Q. Dielectric resonators are attractive as characterization tools for the determination of surface resistance of superconducting (particularly HTS) thin films. It is possible to form a resonator using only two planar films and a sapphire cylinder, yet high sensitivity is attainable. High-Q resonators have dual use as characterization tools and as components in microwave systems (*e.g.*, sharp–skirt filters and low–noise oscillators). In the latter application, it becomes very important to minimize the losses in the DR package. In this report, we address the challenges associated with accurate experimental characterization of (miniature) sapphire dielectric resonators of approximately 1cm^2 HTS endplate areas, a criterion which would make the design particularly atractive to aerospace applications. The utility of such characterization in non–destructive testing of HTS material samples is evident. Measurement of surface resistance is very important for material and circuit optimization in microwave applications. Sapphire is an attractive substrate dielectric material for this measurement because of its low loss tangent and moderate dielectric constant.

We measure each DR as a two-port system, by exciting and detecting the modal fields with loop–terminated coaxial cables. The observed Q factor of the resonator is a gauge of the surface resistance of the endplates. Our objective of testing superconducting samples adds the complication of cooling the resonator to cryogenic temperatures. Because the resonant frequency shifts substantially as the temperature is varied, and because the properties of the test cables and coupling loops vary with temperature, maintaining accurate calibration is difficult. The fact that a loop-coupled DR cannot be experimentally calibrated adds to the complexity of parameter extraction. The loop coupling fixture is inherently difficult to compensate, because multiple measurements such as thru–reflect–load

(TRL) cannot be accomplished at cryogenic temperatures within reasonable accuracy. Besides, the aggravation of making these additional measurements at several temperatures precludes their utility. In this paper, we discuss a method for the *software calibration* of two-port resonator data, which is capable of compensating for the background noise resulting from attenuation, multiple reflections and dispersion introduced by cables and discontinuities leading to the resonator. The proposed method of DR measurement and calibration is more accurate than the insertion loss measurements typically reported in previous investigations [5] – [8], because both magnitude and phase of the four two-port S-parameters, measured at several frequencies using a vector network analyzer, are employed to fit Q-circles [9] to the measured data.

The research reported in this paper has been performed collaboratively with WL/MLPO as part of the AFOSR SREP project. The HTS thin films have been grown over sapphire substrates by pulsed laser deposition (PLD). The microwave measurements have been performed on cryogenically cooled HTS DR over several frequency bands in the 20 – 40 GHz range, using a vector network analyzer. The details of microwave measurement procedure are covered in [10] - [12], and are not dealt herein. The reported research met the following two objectives set forth in the pertaining proposal: (a) to develop a robust and accurate curve-fitting procedure (referred henceforth as software calibration) for extracting the surface resistance from inherently noisy measurements of S–parameters of the films, (b) to develop a convenient graphical user interface (GUI) based on LabWindows, which facilitates automatic processing of measured data sets spanning several frequencies and temperatures. The GUI is still being refined to accommodate more fitting functions, and make the software a user–friendly, comprehensive package for calibrating any two–port resonator measurements (not just DR) applicable to the characterization of HTS materials. It is anticipated that this research will result in improved dielectric resonator measurements by providing a better understanding of the minimization of parasitic noise sources in the measurement process.

The report is organized as follows. The next section presents background information on our preliminary research on the analysis of DR measurements. The fundamental technical approach followed in the project is based on electromagnetic analysis of dielectric resonators, and will be detailed in Sec. 3. The first subsection will provide the experimental details, and the second dwells upon the electromagnetic field analysis of the resonator. Sec. 4 presents the equivalent circuit modeling of measured data and introduces the concept of Q-circles. Some earlier approaches to the extraction of parameters from DR measurements, and their limitations, are also discussed. Sec. 5 describes the least squares Marquardt (LSM) curve–fitting procedure, followed by a discussion of sample results derived from implementation of the LSM algorithm, in Sec. 6. Routine programmatic details on the computer implementation are avioded.

2 Background Research

The software calibration algorithm is based on microwave circuit theory for tuned resonators [9], [13], and consists of curve-fitting Q-circles to the measured data. In HTS DR measurements, the measured parameters are very sensitive to the background "noise" contributed by the fixture parasitics such as coupling losses, case modes, radiation, etc. As part of the AFOSR 1996 Summer Research Program [14], we have developed a non-linear curve-fitting procedure, the LSM algorithm, to accurately filter out the noise and extract the unloaded Q of a DR. It has been observed that the noise manifests out of the resonant band as a quasi–sinusoidal envelope. Within the resonant band, ideally, the measured data can be fit to a linear fractional transformation corresponding to mapping of a pure Lorentzian into Q-circles in the complex plane [9]. In order to represent the nearly harmonic noise, we multiply the Lorentzian expression by a sum of complex exponentials pertaining to the standing wave modes of the loop-coupling mechanism. These modes render the fit non-linear. We have implemented this composite non-linear transformation in a computer program developed using LabWindows C (Program *SoftCal*, Version 1), and used it to model raw data from a DR with copper end-plates [13]. The results presented in [13] for the surface resistance of thin copper plates have demonstrated the feasibility of software calibration of noise-corrupted DR measurements. Because measurements were not available for HTS films at that time, the program has not been tested with very high Q's. However, our preliminary analysis shows that the LSM fit is quite satisfactory even in the case of highly corrupted data. We will later present salient features of the LSM algorithm with examples on curve-fitting.

A major drawback of *SoftCal 1* program is that it does not map out measured data into perfect circles in the complex plane, because all the data *and* the noise are fitted to the same model. Therefore, if the data is very noisy and forms open loops instead of closed circles, the LSM method cleans out the noise, but still leaves the loops open. We have resorted to visual interpolation of the fitted curve in order to obtain the closed Q-circles, whose geometrical parameters determine the unloaded Q of the DR. Interpolation of fitted data makes the model dependent on the nature of the noise, and leads to cumbersome changes in the program for different data sets. In order to circumvent this difficulty, we have now begun to implement the LSM algorithm in two steps. In the first, the Lorentzian part of the data is windowed out, and only out-of-the-band "noise" is fitted to a series of decaying complex exponentials. If we assume that the sinusoidal noise is contributed by standing wave modes along the cables terminated in coupling loops, this first step is essentially equivalent to making a "thru" two-port measurement on the network analyzer without the device under test (DR). Second, we model the whole spectrum of measured data, including the Lorentzian, with the LSM algorithm, in the same manner. De-embedding the resonator measurements from the total is accomplished by subtracting the first fit from the second fit, akin to full two–port calibration on a network analyzer. Then, we anticipate to obtain a smooth Lorentzian with nearly constant detuned reflection and transmission coefficients. Such data will form pure Q-circles, and should give very accurate unloaded Q. Because of the similarity of this process to hardware calibration on a network analyzer, we term this two-step

curve-fitting procedure as *software calibration* [13]. We are vaildating this modified LSM algorithm (Program *SoftCal 2*) with measured data on HTS DRs, consisting of 1 cm^2 YBCO films on sapphire pucks. At the time of this reporting, the validation was still in progress.

3 Electromagnetic Approach

3.1 Experimental Details

Cavities containing dielectric resonators are very useful in measuring the surface resistance of HTS thin films. Fig. 1 shows a sapphire dielectric resonator with HTS end caps. Sapphire is an attractive dielectric material for this application because of its low loss tangent and moderate dielectric constant. The resonator can be either free-standing, or enclosed in a metallic package (cavity) as in Fig. 1. Energy is coupled into and out of the cavity through two coupling loops. By proper design and placement of these loops, one can ensure that only the dominant TE_{011} mode is excited within the resonator. Because the fields are well-trapped in the dielectric and within a small cylindrical region outside the sapphire, the losses in the resonator system can be minimized, with the result that extremely large Q's (of the order of a million) can be measured.
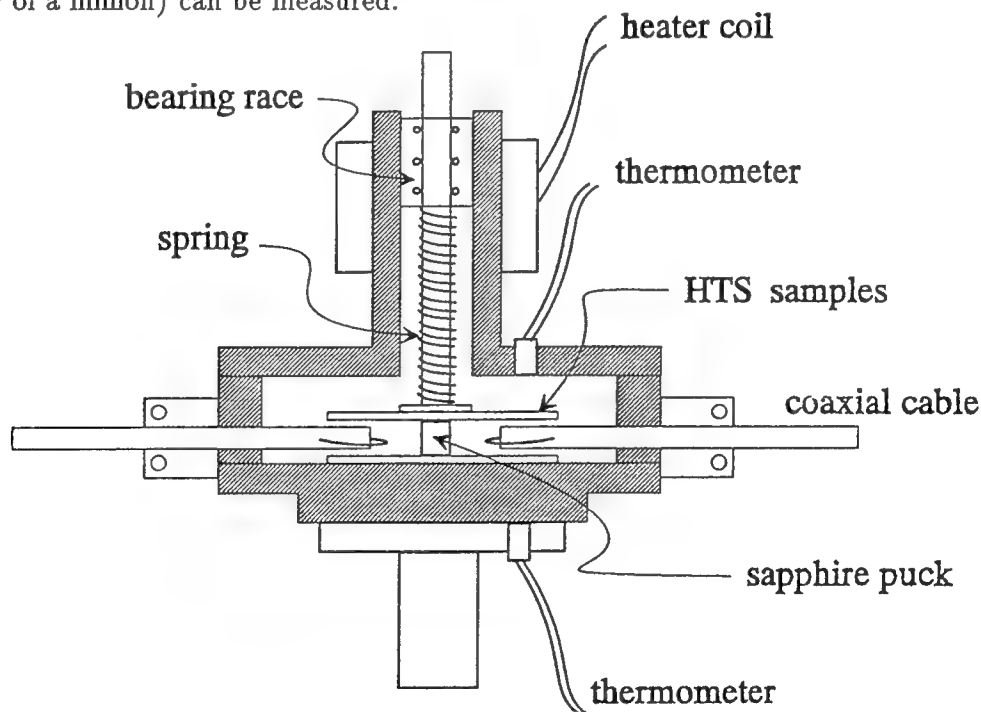
Figure 1: Cross-sectional view of the HTS-sapphire-HTS dielectric resonator fixture.

In order to measure the surface resistance of YBCO HTS films over a wide frequency range, cylindrical sapphire pucks (resonators) of different diameters are employed. The HTS film is placed non-destructively on either end of the sapphire puck, and the resonant frequency and loaded Q of the DR configuration is determined from the measured insertion loss. The coupling coefficients and

unloaded Q are obtained by applying the LSM algorithm to the measured S-parameters. The coupling loops are made using coaxial cables, and are conected to 50 Ω test ports of the network analyzer for automated measurement.

The fields trapped within the dielectric (Fig. 1) are oscillatory and described by Bessel functions of the first kind, $J_n(x)$. The evanescent fields in free space decay exponentially along the radial direction, and are specified by Bessel functions of the second kind, $K_n(x)$. These fields and their behavior are analyzed in [6]. By imposing boundary conditions on the tangential fields at the dielectric interface $\rho = a$, one obtains the transcendental equation

$$\frac{J_1(\xi_1 a)K_0(\xi_2 a)}{\xi_1 a} + \frac{K_1(\xi_2 a)J_0(\xi_1 a)}{\xi_2 a} = 0 \tag{1}$$

where ξ_1 and ξ_2 are radial wavenumbers in the dielectric ($\rho \leq a$) and air ($\rho \geq a$), respectively. In order to solve eq. (1) numerically for the resonant frequency, we provide initial guesses of the frequency and $\xi_1 a$ and calculate

$$\xi_2 a = \pi\sqrt{(a/L)^2 - (2a/\lambda)^2} \tag{2}$$

where λ is the operating wavelength. The resonant frequencies for different pucks were computed from (1) using Mathcad (see Table 1). The dielectric constant of sapphire is assumed as $\epsilon_r = 9.3$. These resonant frequencies are in good agreement with measured values. The DR is immersed in a liquid helium dewar and cooled to cryogenic temperatures.

Table 1. Computed Resonant Frequencies of Sapphire Dielectric Resonators.

Radius a	Length L	Res. Freq. (GHz)
0.09"	0.137"	37.276
0.095"	0.137"	35.888
0.1"	0.137"	34.628
0.12"	0.137"	30.607
0.15"	0.137"	26.587
0.25"	0.137"	20.364

3.2 Field Analysis

The electromagnetic field solutions for the cylindrical dielectric resonator can be determined in terms of cylindrical harmonics, starting from the Helmholtz equation

$$\nabla^2 \vec{E} + k^2 \vec{E} = 0 \tag{3}$$

with the wavenumber given by $k = \omega\sqrt{\mu\epsilon}$. The magnetic field $\vec{H}$ is related to the electric field $\vec{E}$ via Faraday's law. Enforcing the boundary conditions at the cylindrical interface leads to the solutions for the fields of the form [6]

$$\psi = F(\xi, \rho) \begin{bmatrix} \cos(m\phi) \\ \sin(m\phi) \end{bmatrix} e^{-jk_z z} \tag{4}$$

with the wavenumber seperated into radial (ξ) and axial (k_z) components according to $k^2 = \xi^2 + k_z^2$. Inside the radius of the sapphire, F is a Bessel function, J_m, with the radial wavenumber given by $\xi_1^2 = k_0^2\epsilon_r - k_z^2$, where $k_0 = \omega\sqrt{\mu_0\epsilon_0}$, and ϵ_r is relative dielectric constant of sapphire. Outside the sapphire, F is a modified Bessel function K_m, exhibiting an approximately exponential decrease with increasing ρ, with the radial wavenumber given by $\xi_2^2 = -k_0^2 + k_z^2$. Thus, the two radial wavenumbers are related by

$$\xi_2^2 = k_0^2(\epsilon_r - 1) - \xi_1^2. \tag{5}$$

If we visualize the resonator as a cylindrical waveguide terminated at a length equal to an exact multiple of the axial wavelength, then the length is constrained to be $L = p\pi/k_z$ where p is a positive integer. Thus, the condition for ξ_1 becomes

$$\xi_1^2 = k_0^2\epsilon_r - (p\pi/L)^2. \tag{6}$$

Enforcing matching of the fields at $\rho = a$ (the sapphire radius) using these wavenumber constraints leads to the resonant condition (1) for the axisymmetric mode given by $m = 0$. This mode of interest, designated as TE_{011}, has no ϕ dependence, it spans one wavelength in the z direction, with zero axial electric field. The TE_{011} mode is supported by currents moving in a circular pattern in the endplates.

Knowledge of the resonant frequencies allows us to calculate and plot the radial field distribution outside the resonator. We have calculated the fields for $\rho \geq a$ in the DR of Fig. 1 using the expressions for the TE_{011} mode derived in [8]. It was observed that the diameter/length aspect ratio of the DR needs to be large to contain the stray fields. Field containment is a critical issue in our application, because the resonator used at WL/MLPO is an open structure and the films are small in size (about 10 mm^2), thus enhancing the possibility of radiation leakage. In other words, the films are not sufficiently

large to ensure a small field amplitude near their edges, and the presence of coupling loops nearby complicates the analysis. The seperable cylindrical harmonics are not adequate for analyzing such a structure, especially considering that the package also has slots through which the field can radiate. The exact field analysis pertaining to the interaction of the coupling loops with the resonator, which accounts for diffraction at the edges of the film and the package geometry, is formidable. However, numerical methods can be employed for a simplified geometry to facilitate such analysis. It was beyond the scope of the project to implement such numerical methods. However, the analysis based on cylindrical harmonics does provide some insight into the fixture design, and is discussed next.

The key measurables for the resonator are the resonant frequency ω_0 and the quality factor Q. The Q value attributable to losses in the endplate currents is given by $Q_c = \omega_0 W_0 / P_{0c}$, where W_0 is the total energy stored in the resonator and P_{0c} is the power dissipation of the currents in the endplates. The total energy is (see [8])

$$W_0 = \frac{\epsilon_0 \epsilon_r}{2} \int \mid E_{\phi 1} \mid^2 dv + \frac{\epsilon_0}{2} \int \mid E_{\phi 2} \mid^2 dv \tag{7}$$

and the power dissipation due to endplate current losses is

$$P_{0c} = R_s \left[\int \mid H_{\rho 1} \mid^2 dv + \int \mid H_{\rho 2} \mid^2 dv \right]. \tag{8}$$

In the equations above, the integrals with subscripted 1 fields are over the volume internal to the DR ($\rho < a$), while those with subscripted 2 fields are over the volume external to the DR ($\rho > a$). The relationship between Q_c and the average surface resistance R_s of the endplates is

$$Q_c = \frac{240\pi^2 \epsilon_r}{R_s} (2\pi k L)^3 \frac{1 + R}{1 + \epsilon_r R} \tag{9}$$

where R, the ratio of electric energy stored outside the sapphire DR to that inside the sapphire, is given by

$$R = \frac{1}{\epsilon_r} \frac{\int \mid E_{\phi 2} \mid^2 dv}{\int \mid E_{\phi 1} \mid^2 dv}. \tag{10}$$

The factor R indicates the level of field confinement within the sapphire. Lower values of R imply better field trapping inside the DR, and enhance the quality factor Q_c. Another useful quantity in the design of a DR is the ratio of energy stored in the evanescent field outside a given radius (greater than a) to the total stored energy, denoted $ER(\rho)$. It can be evaluated at different radii of interest.

For instance, a resonator designed to test endplates with a radius $\rho = 5mm$ must have a sufficiently low value of $ER(5mm)$. Some implications of endplate size and shape are discussed by Mourachkine [15]. It is interesting to note that the energy ratio does not consider any package losses, such as power dissipated in the lateral cylindrical cavity walls, leakage through slots, interaction with higher–order cavity modes, etc. ER does account for all these parasitic effects. Ideally, one should locate the package lateral wall at a radius where ER is sufficiently small that the loading of these parasitics can be neglected.

In order to test 1cm^2 area films, it is necessary to miniaturize the sapphire cylinder accordingly, to sizes that imply resonant frequencies in the range of 20-40 GHz. The minimum spacing L is limited by the requirement of inserting coupling loops between the endplates, from the sides, with satisfactory clearance. For a given resonator height L, the radius a can be chosen for optimum field confinement as gauged by the radial wavenumbers and the two energy ratios embodied in R and ER. The example of $L = 2.4mm$ is considered in Fig. 2, where the critical parameters of the DR are displayed. The degree of field confinement varies as the cylinder geometry (choice of L and a) is changed. While R decreases with increasing radius (for a given L), it is found that the energy stored in the evanescent tail outside the sapphire has an optimum around $a = 2mm$, and increases with the endplate radius beyond the optimum. The longer the tail, the shorter is the energy ratio, ER, and hence, more desirable. The optimum ER appears to favor miniature squat resonators.
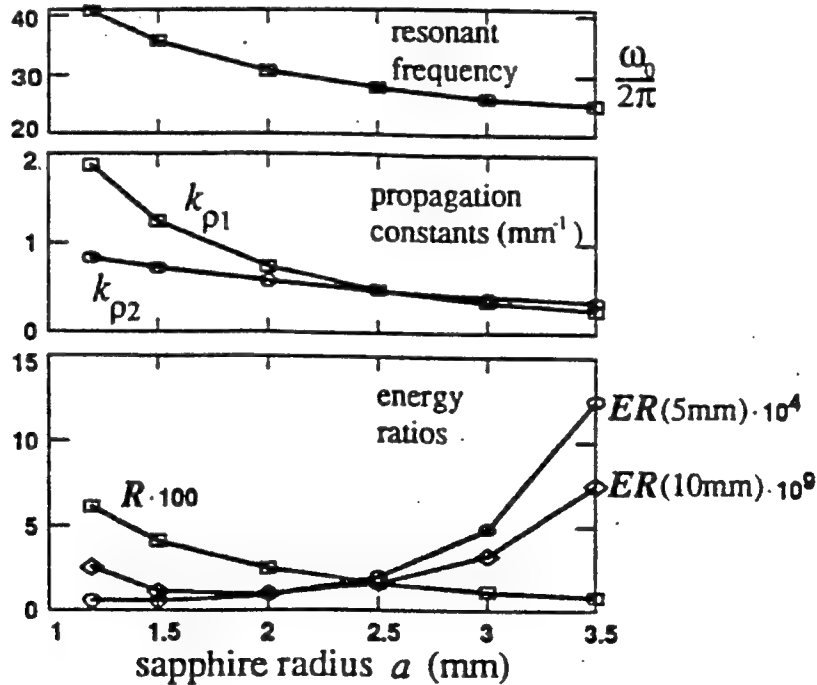

Figure 2: Variation of the resonant frequency (in GHz), radial wavenumbers ξ_1 and ξ_2, ratio of energy outside-to-inside the sapphire, R, and energy ratio, ER, at 5mm and 10mm radii, as functions of cylinder radius a, for cylinder height $L = 2.4mm$.

4   Parameter Extraction

Two methods have been in use to extract the unloaded Q-factor of the dielectric resonator, namely, Ginzton method [5] and Kobayashi's method [7]. Both of these methods are applicable to the processing of S-parameters measured by the microwave network analyzer, and will be briefly discussed next. The limitations of these two methods will also be presented.

4.1   Ginzton Method

For a resonant cavity, the magnitude of the insertion loss (S_{21} expressed in dB) follows the peaked behavior shown in Fig. 3. Ginzton's method [5] entails the observation of the resonant frequency, f_L, and Δf, the spread between half-power (3 dB) points, to determine the loaded Q-factor, Q_L, as

$$Q_L = \frac{f_L}{\Delta f}. \tag{11}$$
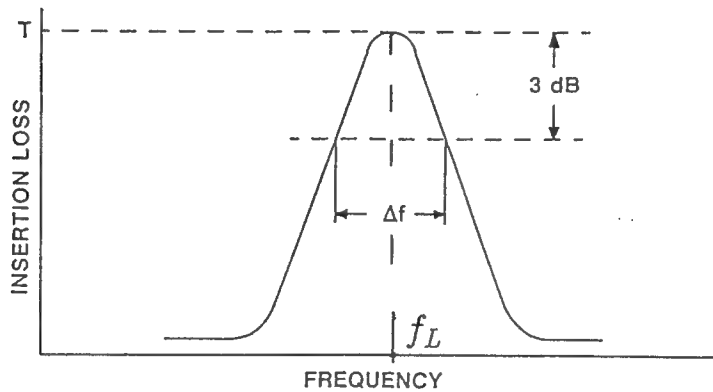
Figure 3: Resonant curve measurement of the loaded Q-factor of a dielectric resonator.

Ginzton's method employs measured data from only two frequencies, and thus, suffers from the following limitations. First, the unloaded Q-factor cannot be calculated because the magnitude response lacks information on the coupling coefficients, which determine the proportion of source power actually coupled into the resonator at each port. Second, if the data is either asymmetric around the peak or corrupted by measurement noise, an extraction procedure based only on magnitudes may yield very unreliable results. The phase of the measured S-parameters becomes important in these situations.

4.2   Kobayashi Method

Kobayashi method [7] also employs an HTS dielectric resonator operating in the TE_{011} mode to determine the surface resistance of HTS films. The extraction procedure in Kobayashi's method

improves upon the Ginzton method by providing the coupling coefficients, from which the unloaded Q-factor may be determined. Essentially, the loaded Q-factor is still computed from the resonant peak and the two 3 dB points, as in Ginzton's method (see (11)). Kobayashi, however, assumes that the input and output coupling coefficients are equal, and determines the unloaded Q-factor from the insertion loss, T, at the resonant frequency f_L (see Fig. 2):

$$Q_0 = \frac{Q_L}{1-T}, \quad T = |S_{21}| = |S_{12}| = \frac{2\kappa_c}{2\kappa_c + 1} \tag{12}$$

where κ_c is the coupling coefficient at either port. We have found that Kobayashi's method requires moderate coupling for accurate prediction of the unloaded Q. It is difficult to ensure that the loops are always correctly positioned for equal coupling, especially with the small resonator fixtures that we employ at higher frequencies. Since Kobayashi's method is also based on magnitude measurements, it suffers from the same limitations as Ginzton's method, namely that the Q can be adversely affected by a few errant or inconsistent points in the sweep.

4.3   Equivalent Circuit Modeling

A resonator, in principle, has many modes with different resonant frequencies. However, if attention is focused on the dominant mode, which is the only one typically excited, the dielectric resonator can be conveniently represented by a parallel tuned circuit [9]. Thus, microwave circuit theory can be employed to formulate a robust extraction alogorithm for the determination of the unloaded Q-factor. Unlike the existing methods of determining unloaded Q from dielectric resonator measurements [8], such an algorithm would utilize both magnitude and phase of the measured S-parameters.

An equivalent circuit of the dielectric resonator configuration of Fig. 1, including the coupling loops, is shown in Fig. 4. The resonator is completely specified by the resonant frequency ω_0, the unloaded quality factor Q_0, and the conductance G_0 (or the resistance R_0). The input and output coupling loops are each modeled by a series resistance R_s and reactance X_s. The series resistance accounts for the power dissipated in the coupling loop. The series reactance includes the reactance of the loop, and encompasses the influence of all higher-order evanescent modes with distant resonant frequencies. This influence is usually negligible. Therefore, the equivalent circuit is valid only near the first (fundamental) resonance. The analyzer is connected to the loops by means of two lossy transmission lines with characteristic impedance R_c. For modeling purposes, these lines are assumed to have lengths ℓ_1 and ℓ_2, respectively, at the input and output ends. In practice, these lengths cannot be determined with any reasonable certainty, and hence, it becomes important to estimate the attenuation and phase shift for a given cable.

The unloaded admittance of the resonator is calculated as
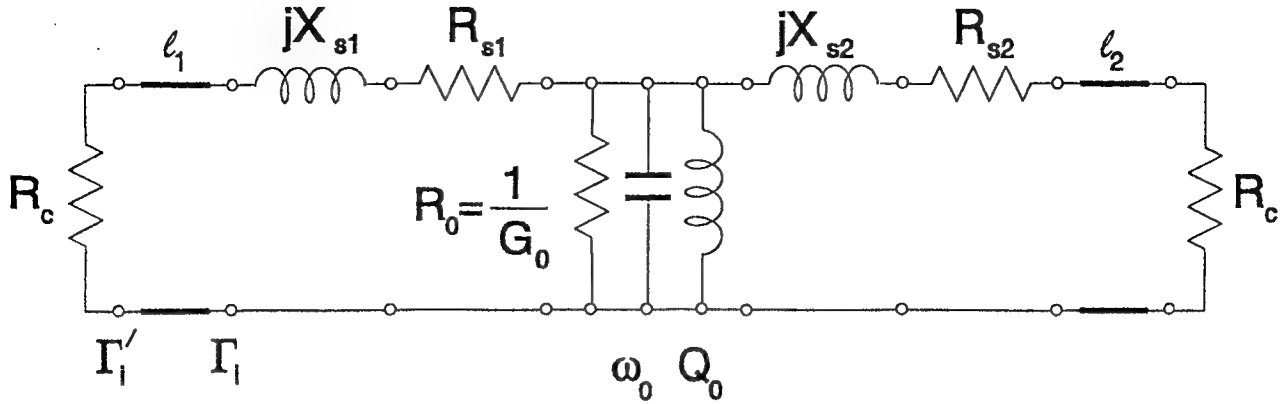
Figure 4: Equivalent circuit of the dielectric resonator with loop coupling.

$$Y_0 = \frac{1}{R_0}\left[1 + jQ_0 2\frac{\omega - \omega_0}{\omega_0}\right] \tag{13}$$

where ω is the operating frequency and ω_0 is the unloaded resonant frequency. This complex admittance does not consider the external loading of the coupling loops and the connecting transmission lines. The complex loaded admittance of the resonator is given by

$$Y_L = \frac{1}{R_0}(1 + \kappa_1 + \kappa_2)\left[1 + jQ_0 2\frac{\omega - \omega_L}{\omega_0}\right] \tag{14}$$

with the coupling coefficients due to external loading calculated as

$$\kappa_1 = \frac{(R_c + R_{s1})R_0}{(R_c + R_{s1})^2 + X_{s1}^2}, \qquad \kappa_2 = \frac{(R_c + R_{s2})R_0}{(R_c + R_{s2})^2 + X_{s2}^2}. \tag{15}$$

Here, ω_L is the loaded resonant frequency. From (15), each coupling coefficient may be written as

$$\kappa_k = \kappa_k^l + \kappa_k^c, \quad k = 1, 2, \tag{16}$$

$$\kappa_k^l = \frac{R_c R_0}{(R_c + R_{sk})^2 + X_{sk}^2}, \qquad \kappa_k^c = \frac{R_{sk} R_0}{(R_c + R_{sk})^2 + X_{sk}^2}. \tag{17}$$

Notice that superscript l denotes coupling associated with the transmission line, whereas superscript c denotes that caused by the loop. Physically, each coupling coefficient equals the ratio of power

14-13

dissipated in the external component (transmission line or loop) to power dissipated in the resonator. Using standard circuit theory [9], the input impedance at each port can be calculated as

$$Z_1 = Z_{e1} + \frac{1}{Y_o + Y_{e2}}, \qquad Z_2 = Z_{e2} + \frac{1}{Y_o + Y_{e1}} \tag{18}$$

$$Z_{ek} = \frac{1}{Y_{ek}} = R_c + R_{sk} + X_{sk}, \quad k = 1, 2. \tag{19}$$

The port reflection coefficients are then given by

$$S_{kk} \equiv \Gamma_k = \Gamma_{dk} + \frac{2\kappa_k^l}{1 + \kappa_1 + \kappa_2} \frac{e^{j\gamma_k}}{1 + jQ_L 2\frac{\omega - \omega_L}{\omega_0}} \tag{20}$$

with the unloaded and loaded Q factors related by

$$Q_0 = Q_L(1 + \kappa_1 + \kappa_2). \tag{21}$$

In the limit as the resonator is detuned to an extremum on either side of ω_L, it is evident from (20) that the reflection coefficient approaches a value Γ_{dk} given by

$$\Gamma_{dk} = \frac{R_{sk} + jX_{sk} - R_c}{R_{sk} + jX_{sk} + R_c}. \tag{22}$$

The transmission coefficient also can be derived by appealing to circuit theory, and is given by

$$S_{21} = S_{12} = \frac{2\sqrt{\kappa_1^l \kappa_2^l}}{1 + \kappa_1 + \kappa_2} \frac{e^{-j\phi}}{1 + jQ_L 2\frac{\omega - \omega_L}{\omega_0}}. \tag{23}$$

The phase angles γ_k and ϕ are functions of loop parameters R_s and X_s, and are given by

$$\gamma_k = 2\arctan\frac{X_{ks}}{R_c + R_{ks}}, \tag{24}$$

$$\phi = \arctan\frac{X_{1s}}{R_c + R_{1s}} + \arctan\frac{X_{2s}}{R_c + R_{2s}}. \tag{25}$$

4.4 Q Circles

As the frequency deviates from ω_0, the reflection and transmission coefficients describe circles in the complex plane, known as *Q circles* [9]. The unloaded Q-factor can be accurately computed from the center and diameter of the Q-circle. As an example, Fig. 5 shows the Q circle for S_{11}, plotted from (20), for the case:

$$\frac{R_o}{R_c} = 2, \quad Q_0 = 1000,$$

$$\frac{R_{s1}}{R_c} = 0.2, \quad \frac{R_{s2}}{R_c} = 0.4, \quad \frac{X_{s1}}{R_c} = 0.5, \quad \frac{X_{s2}}{R_c} = 1.5,$$

$$\beta_0 \ell_1 = 36 \text{ deg.}, \quad \beta_0 \ell_2 = 40 \text{ deg.}, \quad f_0 = 1 \text{ GHz},$$

where β_0 is the free space wavenumber at f_0. The circle is obtained by plotting S_{11} over a frequency band of $\pm f_0(3/Q_0)$ around the unloaded resonant frequency. For lossy coupling loops, the energy coupled into the resonator is reduced by the dissipation in the loops, with the result that the Q-circle is tangential to a circle, known as the *coupling loss circle*, at the detuned point. The loss circle is shown by the dashed curve in Fig. 5. Similar Q-circles and loss circles can be drawn for S_{22} and S_{12}. The reader is referred to Appendix for further details on extraction of the unloaded Q from the geometrical attributes of these circles.
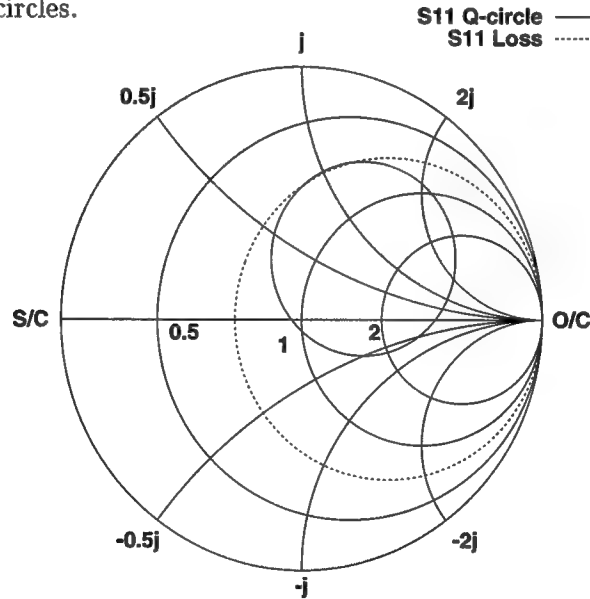

Figure 5: Q-circle for the simulated reflection coefficient data.

In summary, the unloaded Q-factor can be accurately computed from the center and diameter of the Q-circle, which are related to the coupling coefficients, hence, to the circuit element values. These circles can be drawn readily from the assumed element values for simulated resonators. The Q-circles

are usually not smooth for measured data because of extraneous noise and other limitations of the measurement system. These imperfections cannot be calibrated with hardware. However, because of the physical reasoning that the measured S-parameters of loop-coupled resonators must circumscribe Q-circles as a function of frequency [9], a better model than the linear least squares, which takes into account the transmission line loss and phase shift at discontinuities, may be used to filter out the noise. This modified algorithm, discussed next, consists of enhancing the convergence of the least squares iterations using Marquardt method.

5   Least Squares Marquardt Curve Fitting Procedure

The LSM method for parameter extraction of the two-port loop-coupled DR is based on a similar method for the analysis of one-port measurements [9] and multi-mode resonators [16]. Our improved technique involves enhancing the expressions for the reflection and transmission coefficients, given by eqs. (20) and (23), respectively, by considering the complete equivalent circuit including the coupling mechanism, and using least squares minimization to fit the full sweep through the resonance. The fit functions to these coefficients are of the form

$$w_i = \frac{a_1 t_i + a_2}{1 + a_3 t_i} \sum_{j=1}^{p} A_j e^{\gamma_j t_i} \tag{26}$$

with the normalized frequency

$$t_i = 2\frac{f_i - f_L}{f_0}. \tag{27}$$

Eq. (26) may be viewed as a non-linear fractional transformation mapping the normalized frequency variable, t_i, to the space spanned by w_i. The complex transformation constants a_1, a_2, a_3, the amplitudes A_j and the propagation constants γ_j of the p transmission line modes existing on the connecting cables because of impedance discontinuity at the loop interface, are to be determined from the set of i measurements, $f_i, w_i, i = 1, 2, \cdots N$, where w_i denotes theoretical approximation to the measured parameter at the frequency f_i. The functional dependence of these constants on physical parameters of the resonator may be determined by comparing the right hand side of (20) or (23) with that of (26). For example, from (23) we obtain

$$a_1 = 0, \quad a_2 = \frac{2\sqrt{\kappa_1^l \kappa_2^l} e^{-j\phi}}{1 + \kappa_1 + \kappa_2}, \quad a_3 = jQ_L. \tag{28}$$

The terms in the summation in (26) account for cable losses, multiple reflections, and relative phase

14-16

shifts (dispersion) introduced by spurious discontinuities in the cables leading to the resonator. Normally, these factors are calibrated out using multiple sets of independent measurements. One such measurement is the transmission between the two ports without the resonator. However, this measurement is not reliable for a loop-coupled resonator, because the loops are designed to weakly couple to each other. Uncalibrated or poorly calibrated data are better analyzed by using (26) as a fit function. The inclusion of transmission line modes renders the fit non-linear.

Since the measured data is overdetermined, the problem of calculating the transformation constants in the fit function may be cast as minimization of the square error between measurements w_{m_i} and the model w_i, defined by

$$\chi^2(\mathbf{a}) = \sum_{i=1}^{N} \frac{1}{\sigma_i^2} \mid w_{m_i} - w_i \mid^2 . \tag{29}$$

Here, we assume that $N \gg m$, where m is the number of independent parameters of the fit function. For notational convenience, these parameters of (26) are stored in an array $\mathbf{a} = [a_1 \quad a_2 \quad \cdots a_m]^T$, with the superscript T denoting transpose. The factor $1/\sigma_i^2$ denotes the weighting constant for the ith sample, and may be assumed as unity without any loss of generality. When the parameters are allowed to vary from their initial estimates by differential increments, δa_j, the model w_i can be approximated by first-order Taylor's series expansion as

$$w_i \approx w_{i0} + \sum_{j=1}^{m} \frac{\partial w_{i0}}{\partial a_j} \delta a_j \tag{30}$$

where w_{i0} and the derivative are evaluated at the initial guess $\mathbf{a} = \mathbf{a}_0$. Although the model is non-linear with respect to the parameter vector $\mathbf{a}$, the Taylor's series approximation in (30) effectively linearizes the function, so that linear least squares theory can be applied.

Expressing the data, w_{m_i}, and the function, w_i, in complex form as $w_{m_i} = r_{m_i} + jx_{m_i}$ and $w_i = r_i + jx_i$, respectively, the chi-squared error in (29) may be written as

$$\chi^2 = \sum_{i=1}^{N} \frac{1}{\sigma_i^2} \left[(r_{m_i} - r_i)^2 + (x_{m_i} - x_i)^2 \right] . \tag{31}$$

We minimize χ^2 with respect to each of the parameter increments, δa_j, by setting the parametric derivatives equal to zero:

$$\frac{\partial \chi^2}{\partial(\delta a_k)} = -2 \sum_{i=1}^{N} \frac{1}{\sigma_i^2} (r_{m_i} - r_i) \frac{\partial r_i}{\partial(\delta a_k)} - 2 \sum_{i=1}^{N} \frac{1}{\sigma_i^2} (x_{m_i} - x_i) \frac{\partial x_i}{\partial(\delta a_k)} = 0, \quad k = 1, 2, \cdots m. \tag{32}$$

Noting from (30) that

$$\frac{\partial w_i}{\partial(\delta a_k)} = \frac{\partial w_{i0}}{\partial a_k} \tag{33}$$

and replacing w_i with its Taylor's series expansion, we obtain from (32)

$$\sum_{i=1}^{N} \frac{1}{\sigma_i^2} (r_{m_i} - r_{i0}) \frac{\partial r_{i0}}{\partial a_k} + \sum_{i=1}^{N} \frac{1}{\sigma_i^2} (x_{m_i} - x_{i0}) \frac{\partial x_{i0}}{\partial a_k} = \sum_{i=1}^{N} \frac{1}{\sigma_i^2} \sum_{j=1}^{m} \frac{\partial r_{i0}}{\partial a_j} \frac{\partial r_{i0}}{\partial a_k} (\delta a_j)$$

$$+ \sum_{i=1}^{N} \frac{1}{\sigma_i^2} \sum_{j=1}^{m} \frac{\partial x_{i0}}{\partial a_j} \frac{\partial x_{i0}}{\partial a_k} (\delta a_j), \quad k = 1, 2, \cdots m. \tag{34}$$

Eq. (34) can be concisely expressed in matrix form as $[C][\alpha] = [\beta]$ with the elements given by

$$C_{kj} = \sum_{i=1}^{N} \frac{1}{\sigma_i^2} \left[\frac{\partial r_{i0}}{\partial a_j} \frac{\partial r_{i0}}{\partial a_k} + \frac{\partial x_{i0}}{\partial a_j} \frac{\partial x_{i0}}{\partial a_k} \right], \quad \alpha_j = \delta a_j, \quad j, k = 1, 2, \cdots m, \tag{35}$$

$$\beta_k = \sum_{i=1}^{N} \frac{1}{\sigma_i^2} (r_{m_i} - r_{i0}) \frac{\partial r_{i0}}{\partial a_k} + \sum_{i=1}^{N} \frac{1}{\sigma_i^2} (x_{m_i} - x_{i0}) \frac{\partial x_{i0}}{\partial a_k}. \tag{36}$$

The matrix $[C]$ and the vector $[\beta]$ can be completely calculated from the initial guess a_0. The derivatives can be evaluated analytically from the model (26). This procedure can be iterated, with the corrective offset of the parameter vector at each iteration to be computed using $[\alpha] = [C]^{-1}[\beta]$. If the initial guess is close to the solution vector, then, this linearized least squares implementation suffices. However, for the noise-corrupted DR measurements, we found that this procedure does not converge well because of the sensitivity to initial guess, and deviations from an ideal Q circle. Therefore, the correction to vector $[a]$ at each iteration is implemented using the Marquardt algorithm [17], which is formulated to seek a global minimum in the parameter space from a relatively crude initial guess. Marquardt's algorithm employs an interpolating parameter, λ, to influence the direction of search at each iteration. The LSM algorithm is implemented as follows:

1. Compute $\chi^2(a_0)$ given the initial guess.

2. Modify the diagonal elements of $[C]$ as $C'_{kj} = C_{kj}(1 + \lambda)$, with an initial value of $\lambda = 0.001$.

3. Compute the parametric correction, $\delta\mathbf{a}$, from $[\alpha] = [\mathbf{C}]^{-1}[\beta]$.

4. If $\chi^2(\mathbf{a} + \delta\mathbf{a}) > \chi^2(\mathbf{a})$, then, set $\lambda_{new} = 10\lambda_{old}$; else, set $\lambda_{new} = 0.1\lambda_{old}$. Recompute $[\mathbf{C}]$ and the new correction, $\delta\mathbf{a}$.

5. Repeat the previous step until the iterations converge, as indicated by the weighted variance changing by less than 0.01 from one iteration to the next.

5.1 Initial Guess Estimate

Two critical parameters which provide the initial guess to the LSM algorithm are the loaded resonant frequency, f_L, and the loaded quality factor, Q_L. The estimation scheme for f_L is based on the fact that the magnitude of either S_{12} or S_{21}, when plotted against frequency, exhibits maximum slope in the neighborhood of the resonant frequency. For the measured data, it has been found that these two parameters have resonant frequencies which are slightly shifted. Therefore, the arithmetic average of these two parameters is examined for maximum slope of magnitude against frequency. Specifically, the derivative $|\,dw_i/df\,|$ is calculated numerically using the central difference approximation on neighboring frequency points (except at the end points where either forward or backward difference is employed), and the values are arranged in descending order to detect the resonant frequency, f_L. The detected value is confirmed by plotting the derivative against frequency. The unloaded resonant frequency f_0 is approximated as f_L in calculating t_i as per (27). The loaded Q-factor may be estimated from the raw data using [18]

$$Q_L = \frac{\omega_L\,|\,dw_i/d\omega\,|}{2Re(w_i)} \tag{37}$$

where w_i represents the measured parameter. The form in (37) is convenient because the loaded resonant frequency and the derivative estimated in the previous step can be used to evaluate (37) at several frequencies in the resonant band. An average of all these closely spaced values is assumed as the best estimate of Q_L.

As an example of how these estimates of f_L and Q_L can be used in the LSM algorithm, consider the fit function in (26) with only one exponential, whose amplitude is normalized to unity. Then, one needs initial guesses for a_1, a_2, a_3 and γ_1. Clearly, a_2 can be set to the value of the function, w_i, at $f_i = f_L$. From either (20) or (23), it follows that $a_3 = jQ_L$. We have found that the convergence of the algorithm is not sensitive to the estimate of γ_1. Therefore, we start with an estimate of $\gamma_1 = 0$. For the transmission parameters, the model implies $a_1 = 0$ for all iterations (see (28)), while it is set equal to a_3 initially for the reflection parameters.

6   Examples of Curve Fitting

We have determined the unloaded Q of the same resonator as specified in Sec. 4.4, with the raw data for curve-fitting obtained by shifting the reference planes in eqs. (20) and (23) in accordance with a known length of the input and output lines. Curve-fitting of the simulated data provides an intuitive validation of the computer program to implement the LSM algorithm. In order to make the validation over a wide band, simulated data lying within a range of $\pm 10(f_0/Q_0)$, and corrupted by random Gaussian noise, is input to the LSM program. The lines are assumed to be lossless, and one exponential is used for the standing wave mode on each line. Three iterations were used to correct the parameters. From a knowledge of the geometrical attributes of the fitted Q-circle, we have calculated $\kappa_1 = 1.39012$, $\kappa_2 = 0.65508$, and $Q_L = 326.579$, which yield an unloaded Q of 994.5 (within 0.5% of the specified $Q_0 = 1000$). The phase shifts to compensate for the line lengths are estimated to be $\beta_0\ell_1 = 36.012$ deg., $\beta_0\ell_2 = 40.013$ deg., yielding a fitting error of $\chi^2 = 0.001$.
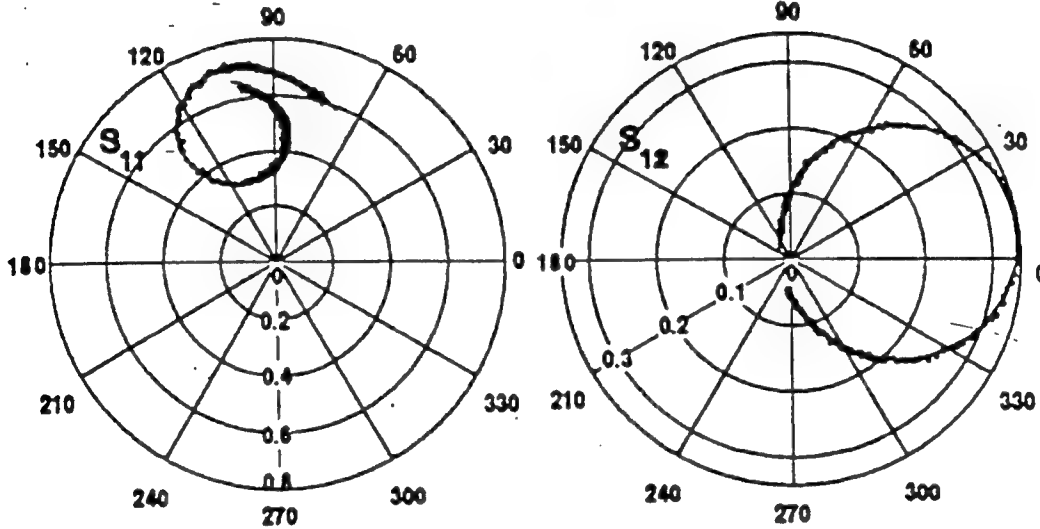

Figure 6: Comparison of the Least Squares Marquardt (LSM) curve-fit result with measured data. The fit functions for S11 and S12 are (16) and (17), respectively.

An example of the improved results obtained by using the LSM method on measured data is shown in Fig. 6, for a dielectric resonator formed using copper endplates with a 12mm radius. The resonant frequency is 26.45 GHz. Using the LSM algorithm, the calculated Q_0 is 3710, with coupling coefficients $\kappa_1 = 0.532$ and $\kappa_2 = 0.219$, and $\chi^2 = 0.02$, as evidenced by the good match in both magnitude and phase (Fig. 6). Kobayashi's method gives $Q_0 = 4336$ for the same dataset, while Shen's method gives $Q_0 = 4206$. The discrepancies are not surprising, given that the raw measurements do not trace out perfect circles in a polar representation.

7 Conclusions

An efficient algorithm, based on least squares minimization of the square error between an assumed fractional non-linear transformation and the measured data, has been developed for the extraction of unloaded Q from dielectric resonator measurements. The convergence of the alogorithm has been enhanced using the Marquardt method. The circuit equivalent of the primary DR mode has been employed to develop idealized expressions for the resonator response, which trace out circles in the complex plane. Starting with the approach of matching Q-circles to the resonator data, we have augmented these expressions to compensate for the undesirable influence of the coupling feed structure. The resulting improved method for analyzing two-port resonators is useful when calibration is difficult. This procedure is more reliable and accurate than previous methods based on three-point resonant curve measurements (*e.g.*, Ginzton's and Kobayashi's methods), because both magnitude and phase of a wide data sweep around the resonant frequency are used to fit the measured data. Poorly calibrated data with a few errant points in the sweep can be analyzed using the LSM method. The extraction program has been applied to compute the unloaded Q of dielectric resonators consisting of copper end plates. A simulated example with additive random noise has been presented to validate the algorithm against a specified DR.

Appendix
Determination of Coupling Coefficients

With reference to Fig. 5, let d_{11} and d_{22} denote diameter of the Q-circle for input and output reflection coefficients, respectively, while that of the corresponding coupling loss circle is denoted by d_{1c} and d_{2c}, respectively. The diameter of the transmission Q-circle is d_{12}. These diameters are obtained from the corresponding transformation vector **a** generated by the fitted curves, following the procedure discussed in [9]. The diameter of the loss circle is computed as

$$d_{kc} = \frac{d_{kk}[1 - |\Gamma_{dk}|^2]}{d_{kk} - (d_{kk}/2)^2 - |\Gamma_{dk}|^2 + |\Gamma_{ck}|^2}, \quad k = 1, 2 \tag{38}$$

where Γ_{ck} denotes the center of the corresponding reflection Q-circle. The various coupling coefficients are calculated as (see eqs. (16) and (17))

$$\kappa_1^l = \frac{d_{11}/2}{1 - d_{11}\left[d_{1c}^{-1} - (d_{12}/d_{11})^2 d_{2c}^{-1}\right]} \tag{39}$$

$$\kappa_2^l = \kappa_1^l \left(\frac{d_{12}}{d_{11}}\right)^2 \tag{40}$$

14-21

$$\kappa_k^c = \kappa_k^l \left(\frac{2}{d_{kc}} - 1 \right), \quad k = 1, 2. \tag{41}$$

The unloaded Q factor follows from these coupling coefficients and the loaded Q, as per (21).

References

[1] J. G. Bednorz and K. A. Müller, "Possible high T_c superconductivity in the Ba-La-Cu-O system," *Z. fur Phys.*, vol. 64, p. 189, 1986.

[2] M. K. Wu, J. R. Ashburn, C. W. Chu et al., "Superconductivity at 93K in a new mixed-phase Y-Ba-Cu-O compound system at ambient pressure," *Phys. Rev. Lett.*, vol. 58, p. 908, 1987.

[3] *IEEE Trans. Microwave Theory Tech.*, Special Issue on Microwave Applications of Superconductivity, vol. 39, no. 9, pp. 1445-1594, Sep. 1991.

[4] T. M. Klapwijk, D. R. Heslinga, and W. M. van Huffelen, "Superconducting field effect devices," in *Superconducting Electronics*, H. Weinstock and M. Nisenoff (eds.), Berlin Heidelberg: Springer-Verlag, pp. 385-408, 1989.

[5] E. L. Ginzton, *Microwave Measurements*, New York, NY: McGraw-Hill, 1957.

[6] D. Kajfez and P. Guillon (eds.) *Dielectric Resonators*, Norwood, MA: Artech House, 1986.

[7] Y. Kobayashi, T. Imai, and H. Kayano, "Microwave measurement of temperature and current dependences of surface impedances for high-T_c superconductors," *IEEE Trans. Microwave Theory Tech.*, vol. MTT-39, no. 9, pp. 1530-1538, Sep. 1991.

[8] Z.-Y. Shen, *High-Temperature Superconducting Microwave Circuits*, Norwood, MA: Artech House, 1994.

[9] D. Kajfez, *Q Factor*, Oxford, MS: Vector Fields, 1994.

[10] Hewlett Packard Product Note No. 8510-3, "The measurement of both permittivity and permeability of solid materials," no. 5954-1535, Aug. 1985.

[11] W. B. Weir, "Automatic measurement of complex dielectric constant and permeability at microwave frequencies," *Proc. IEEE*, vol. 62, no. 1, pp. 33-36, Jan. 1974.

[12] L. P. Ligthart, "A fast computational technique for accurate permittivity determination using transmission line methods," *IEEE Trans. Microwave Theory Tech.*, vol. MTT-31, no. 3, pp. 249-254, March 1983.

[13] E. K. Moser and K. Naishadham, "HTS dielectric resonator as a microwave characterization tool," Applied Superconductivity Conference, Pittsburgh, PA, Paper No. MSD-7, August 1996.

[14] K. Naishadham, "Least Squares Marquardt (LQM) calibration of dielectric resonator measurements," Final Report for Summer Faculty Research Program, Air Force Office of Scientic Research, Bolling Air Force Base, DC, September 1996.

[15] A. P. Mourachkine and A. R. F. Barel, "Microwave measurement of surface resistance by the parallel plate dielectric resonator method," *IEEE Trans. Microwave Theory Tech.*, vol. 43, pp. 544-551, March 1995.

[16] W. P. Wheless and D. Kajfez, "Experimental characterization of multi-moded microwave resonators using automated network analyzer," *IEEE Trans. Microwave Theory Tech.*, vol. MTT-35, no. 12, pp. 1263-1269, Dec. 1987.

[17] D. W. Marquardt, "An algorithm for least-squares estimation of non-linear parameters," *J. Soc. Ind. Appl. Math.*, vol. 2, pp. 431-441, 1963.

[18] D. Kajfez and W. P. Wheless, "Invariant definitions of the unloaded Q factor," *IEEE Trans. Microwave Theory Tech.*, vol. MTT-34, no. 7, pp. 840-841, July 1986.

MODELING OF INITIATION AND PROPAGATION OF DETONATION IN ENERGETIC SOLIDS

Joseph M. Powers
Associate Professor
Department of Aerospace and Mechanical Engineering

University of Notre Dame
Notre Dame, Indiana 46556-5637

MODELING OF INITIATION AND PROPAGATION OF DETONATION IN ENERGETIC SOLIDS

Joseph M. Powers
Associate Professor
Department of Aerospace and Mechanical Engineering
University of Notre Dame

Abstract

Results of a study of the initiation and propagation of detonation in energetic solids are reported on here. The study has focused on two areas:

- shear band formation and reaction initiation in a thin-shelled cylinder rotating under an applied torque

- transition to detonation in granular solid explosives

The shear band analysis employs a simple model to predict conditions under which a global input of mechanical energy localizes in space and time in a manner sufficient to initiate significant chemical reaction. The second portion of the study focuses on characterization of the transition to detonation in granular materials and on conditions necessary for different classes of such detonations.

1. Introduction

This report is concerned with two distinct approaches to studying the initiation of detonation in solid explosives: reactive shear band analysis and multiphase mixture theory. Consequently, the report is divided to treat each approach individually. The reactive shear band study is described in full detail by Caspar, 1996, and Powers, Caspar, and Mason, 1997; the multiphase mixture study is described in full detail by Gonthier, 1996, Gonthier and Powers, 1996, and Gonthier and Powers, 1997. This report will summarize some of the key findings of these works. It is also noted that a third aspect of the work proposed, modeling of reactive Taylor impact with the EPIC code, has been delayed for mainly administrative reasons: the author has initiated within the University the necessary steps to become a member of the proper government-University consortium needed to obtain access to the EPIC code. As such no technical results for the Taylor impact problem are reported here.

2. Reactive shear band formation

2.1 Introduction

Motivated by the long term goal of developing munitions which are insensitive to accidental initiation and the short term goal of understanding shear banding in reactive materials, this paper considers the behavior of energetic and inert solids subjected to simple shear loading. Data from a torsional split-Hopkinson bar (TSHB), built for this study, was reduced to determine shear stress and shear strain characteristics of these materials. These results were then used to calibrate a constitutive law for stress, including the effects of strain and strain rate hardening and thermal softening. A one dimensional finite difference study of shear localization was performed. The effects of thermal conductivity, viscoplastic heating and Arrhenius kinetics were modeled. Results revealed shear localization and reaction initiation in the explosives simulated. Experimental failure of the inert solids, however, occurred at shear strains significantly lower than those predicted by theory. This has been attributed to the presence of failure mechanisms other than macroscale shear localization, which were not included in the theoretical model. While the tested energetic materials did not undergo macroscale shear localization or initiation under the conditions considered, the study has may have intrinsic value for less brittle materials which may undergo macroscale shear localization or even for brittle materials, which could shear localize on a microscale. Some specifics follow; a full literature review and detailed discussion is given by Caspar, 1996

Initiation of reaction in energetic solids due to mechanical insult is an important, yet poorly understood mechanism. In a typical event, a sharp blow will result in an input of mechanical energy into the solid which will initially manifest itself in the form of internally propagating stress waves. These waves will interact with themselves, material interfaces, and boundaries, all the time dissipating mechanical energy into thermal energy. Should the dissipation rate be sufficiently high and geometrically concentrated, it may be possible to initiate a temperature-sensitive exothermic chemical reaction, which can ultimately lead to detonation in the solid.

It is clear that in order to understand this process, it is imperative to have accurate constitutive equations. Additionally, before full scale implementation in large scale design codes, it can be beneficial to test the constitutive equation in a much simpler code. With such a model one can quickly and unambiguously focus on the performance of the constitutive equation in a simple computational environment which contains the key modeling ingredients: non-linear, experimentally verified stress-strain-strain rate relations, finite rate exothermic temperature-sensitive chemical kinetics, and thermal diffusion.

2.2 Experimental Apparatus

In this study the high strain rate constitutive behavior of explosive simulants has been determined through the use of an experimental apparatus known as the torsional split Hopkinson bar (TSHB), constructed specifically for this study, see Figure 1, This apparatus is capable of deforming
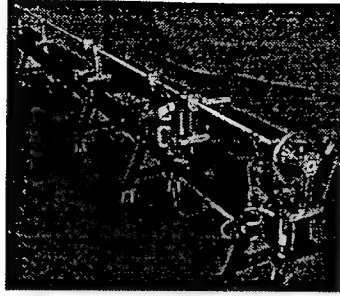
Figure 1: Photograph of the torsional split Hopkinson bar (TSHB) used in this research.

materials in simple shear at shear strain rates of 10^2 to 10^4 s^{-1}. The TSHB has previously been used to determine material characteristics for metals, in which failure often occurs due to a mechanism known as shear localization. Shear localization is one of the least understood initiation mechanisms in solid explosives. If shear localization were to occur, it would be very likely to appear in the TSHB configuration studied here.

Figure 2 describes the mechanism of shear localization. In Figure 2a, a portion of an undeformed material is sketched with thin lines inscribed on its surface. When this material is sheared, the scribe lines begin to slant at a uniform angle, as seen in Figure 2b, reflecting what is known as homogeneous deformation. Increased straining into the plastic range results in material hardening. In addition, if
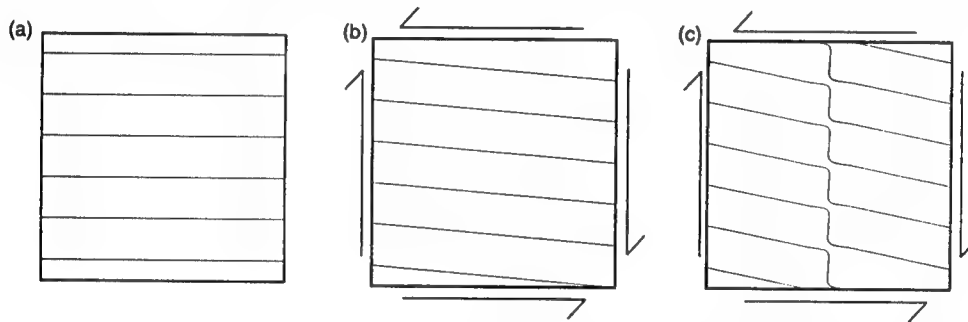

Figure 2: Schematic of the shear localization process. (a) Undeformed grid lines, (b) Homogeneous deformation, (c) Shear localization

there is a geometric discontinuity or other material weakness, straining near that discontinuity will occur at a higher strain rate, which also hardens the material. This increased local deformation, however, also causes plastic heating of the material. If the straining occurs at high strain rates (typically greater than 10^2 s^{-1}), there is not enough time for the generated heat to be conducted away. The local increase in heat results in thermal softening of the material. If this process dominates over the hardening due to strain and strain rate effects, the material strength decreases. As a result of this local softening of the material, deformation is localized into a thin planar region, as depicted by the scribe line deformation of Figure 2c. This final process is known as shear localization or shear banding. Due to the potential concentration of thermal energy in a shear band, it is hypothesized that this could trigger a reaction, which could spread through the material.

2.3 Analytic Model

A simple model for a thin walled cylindrical incompressible reactive material undergoing simple torsional shear was developed. The governing equations utilized are

$$\rho \frac{\partial v_\theta}{\partial t} = \frac{\partial \tau}{\partial z},$$

(1)

$$\rho \frac{\partial e}{\partial t} = \tau \frac{\partial v_\theta}{\partial z} - \frac{\partial q_z}{\partial z} , \tag{2}$$

$$\frac{\partial u_\theta}{\partial z} = \gamma , \tag{3}$$

$$\frac{\partial u_\theta}{\partial t} = v_\theta , \tag{4}$$

$$\frac{\partial \lambda}{\partial t} = Z(1 - \lambda) \exp\left(-\frac{E}{RT}\right) , \tag{5}$$

$$\tau = \alpha \, T^\nu \, \gamma^\eta \left|\frac{\partial \gamma}{\partial t}\right|^{\mu - 1} \frac{\partial \gamma}{\partial t} , \tag{6}$$

$$q_z = -k \frac{\partial T}{\partial z} , \tag{7}$$

$$e = m_A e_A + m_B e_B , \tag{8}$$

$$e_A = c_A T + e_A^o , \tag{9}$$

$$e_B = c_B T + e_B^o , \tag{10}$$

$$m_A = 1 - \lambda , \tag{11}$$

$$m_B = \lambda . \tag{12}$$

Here t is time, z is the axial distance, v_θ is the velocity in the circumferential direction, τ is the shear stress, e is the internal energy, q_z is the heat flux in the axial direction, u_θ is the displacement in the circumferential direction, γ is the shear strain, λ is the reaction progress variable ($0 < \lambda < 1$), and T is the temperature. The parameters Z, E, and R are, respectively, the kinetic rate constant, the reaction activation energy, and the universal gas constant. Also α is a stress constant; subscripts A and B refer to the unreacted and reacted material, respectively; e_A and e_B are the internal energies; m_A and m_B are the mass fractions; c_A and c_B are the specific heats; and e_A^o and e_B^o are the energies of formation. Equation (1) models the conservation of linear momentum in the circumferential direction. Equation (2) models the conservation of energy. Equation (3) is the definition of strain. Equation (4) defines velocity as the time derivative of displacement. Finally, Equation (5) is an Arrhenius kinetics law. Equation (6) is a constitutive law for stress, where ν, η, and μ are the exponents which characterize the thermal softening, the strain and strain rate hardening, respectively. These coefficients were chosen to fit experimental data found as part of this study. Equation (7) is Fourier's law of heat conduction. Equation (8) is a mixture law. Equations (9) and (10) are the caloric state equations. Lastly, Equations (11) and (12) define the mass fractions in terms of the reaction progress.

These equations are supplemented by appropriate initial and boundary conditions and then cast in dimensionless form. It can be shown formally shown that the equations are parabolic and thus suitable for solution via a time-marching technique. They are solved numerically by first replacing all terms involving spatial derivatives with second order accurate finite difference approximations. The resulting system of equations is a set of N non-linear ordinary differential equations in time, where N is related to the user chosen fineness of the finite difference grid. These equations are then integrated implicitly using the standard package, LSODE, to generate time dependent solutions at each grid point. The code has been verified on a number of test problems with known exact solutions; grid refinement studies verify that the numerical approximations converge to the exact solutions at a rate roughly proportional to the square of the spatial grid size.

2.4 Results

Figure 3 compares the experimental and numerical shear stress and shear strain characteristics for an inert simulant of the pressed explosive PBX. From this figure, it is seen that the model predicts the shear stress and shear strain characteristics fairly accurately until just before failure. The code, however, does not predict localization to begin until a nominal shear strain of 4.63 is reached, as compared with the experimentally observed brittle failure at 0.20 shear strain. So, the PBX pressed simulant does not fail due to shear localization.
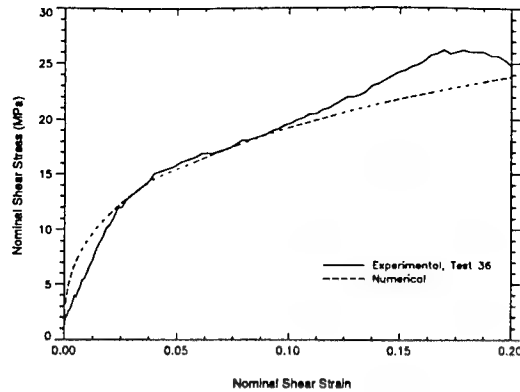
Figure 3: A comparison of the experimental and numerical results for the PBX pressed simulant.

Figure 4, which plots the theoretical predictions of time-evolution of the spatial temperature distribution for a reactive material, PBXN-109. The effects of including reaction proved to have
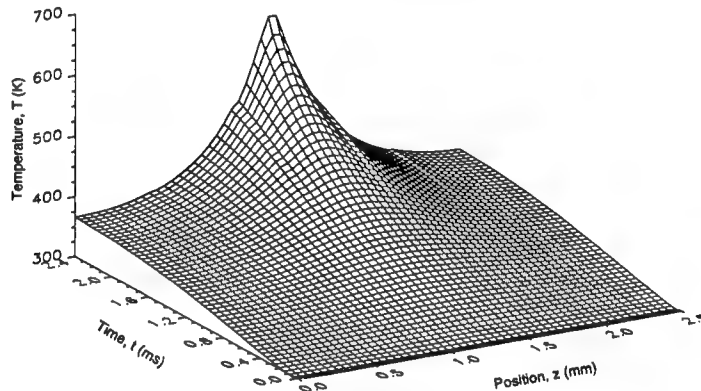

Figure 4: Evolution of the temperature field for PBX 9501 with reaction.

little effect on the results prior to initiation, when compared to a simulation in which reaction was neglected. As was anticipated by the nonreactive case, reaction in the reactive test did occur shortly following the onset of localization. It was predicted that appreciable reaction did not commence until the reaction temperature was reached, at which time reaction quickly initiates in the localized hot spot. It is important, however, to state that the nominal shear strain reached at initiation is approximately 6.4, whereas the simulant failed after a shear strain of 0.2 experimentally. While indeed, this is a weakness of the present model for the system studied, we reiterate that a theory presented here, when applied to brittle materials on a microscale, or to more ductile materials, may through blending simple chemistry and mechanics, may have great promise in gaining understanding of initiation of reaction in complex materials.

3. Transition to detonation in granular solid explosives

3.1 Introduction

Considerable research has been conducted during the past three decades addressing the evolution of detonation in granulated energetic material. This research has largely been motivated by concerns over the accidental detonation of damaged high explosives or propellants in response to weak mechanical shock or thermal insult (Asay and Hantel 1991). Here, damaged material refers to cast solid material which has been inadvertently fractured; thus, local granulated regions exist within the material.

A number of two-phase continuum models have been formulated for analyzing deflagration-to-detonation transition (DDT) in granulated explosives (Butler and Krier 1986; Baer and Nunziato 1986; Powers *et al.* 1990). Numerical simulations based on these two-phase models have been modestly successful in predicting most experimentally observed features of DDT including 1) the formation and propagation of a lead compaction wave, 2) the initiation and subsequent acceleration of a burn front in the compacted material, and 3) the final transition to detonation. However, little emphasis has been given to an analysis of fully-developed detonation structure. Moreover, many DDT simulations are performed using coarse computational grids which are incapable of resolving fine-scale detonation structure. As such, fully-developed detonation structures predicted by two-phase DDT simulations are not well-characterized.

The primary objective of this study is to predict and analyze two-phase detonation structures by numerically simulating DDT whereby combustion is induced by weak, planar mechanical shock due to low velocity piston impact ($\sim 100\ m/s$), and to compare the predicted, fully-resolved structures with results given by a steady-state detonation analysis. A secondary objective of this work is to classify new steady detonation structures. To this end, we use a variant of the model formulated by Powers *et al.* (1990a). The steady analysis is a minor extension of the work performed by Powers *et al.* (1990b). The unsteady analysis is an extension of the work performed by Gonthier and Powers (1996).

3.2 Mathematical model

The model assumes the existence of compressible reactive solid particles and a compressible inert gas. Mass, momentum, and energy exchange between the gas and solid are modeled, as is dynamic compaction of the granular bed due to a mechanical stress imbalance. Diffusive transport mechanisms within each phase are ignored. Also, the effects of lateral boundaries on the two-phase flow are not considered; as such, the flow is assumed one-dimensional (in a macroscopic sense). The dimensional model equations are given by the following:

$$\frac{\partial}{\partial \hat{t}}\left[\hat{\rho}_1\phi_1\right] + \frac{\partial}{\partial \hat{x}}\left[\hat{\rho}_1\phi_1\hat{u}_1\right] = \left(\frac{3}{\hat{r}}\right)\hat{\rho}_2\phi_2\hat{a}\hat{P}_1^m H(I - I_{ig}), \tag{13}$$

$$\frac{\partial}{\partial \hat{t}}\left[\hat{\rho}_1\phi_1\hat{u}_1\right] + \frac{\partial}{\partial \hat{x}}\left[\hat{\rho}_1\phi_1\hat{u}_1^2 + \hat{P}_1\phi_1\right] = \hat{u}_2\left(\frac{3}{\hat{r}}\right)\hat{\rho}_2\phi_2\hat{a}\hat{P}_1^m H(I - I_{ig}) + \hat{\beta}\frac{\phi_1\phi_2}{r}\left(\hat{u}_2 - \hat{u}_1\right), \tag{14}$$

$$\frac{\partial}{\partial \hat{t}}\left[\hat{\rho}_1\phi_1\left(\hat{e}_1 + \frac{\hat{u}_1^2}{2}\right)\right] + \frac{\partial}{\partial \hat{x}}\left[\hat{\rho}_1\phi_1\hat{u}_1\left(\hat{e}_1 + \frac{\hat{u}_1^2}{2} + \frac{\hat{P}_1}{\hat{\rho}_1}\right)\right]$$
$$= \left(\hat{e}_2 + \frac{\hat{u}_2^2}{2}\right)\left(\frac{3}{\hat{r}}\right)\hat{\rho}_2\phi_2\hat{a}\hat{P}_1^m H(I - I_{ig}) + \hat{\beta}\frac{\phi_1\phi_2}{\hat{r}}\hat{u}_2\left(\hat{u}_2 - \hat{u}_1\right) + \hat{h}\frac{\phi_1\phi_2}{\hat{r}^{1/3}}\left(\hat{T}_2 - \hat{T}_1\right) \tag{15}$$

$$\frac{\partial}{\partial \hat{t}}\left[\hat{\rho}_2\phi_2\right] + \frac{\partial}{\partial \hat{x}}\left[\hat{\rho}_2\phi_2\hat{u}_2\right] = -\left(\frac{3}{\hat{r}}\right)\hat{\rho}_2\phi_2\hat{a}\hat{P}_1^m H(I - I_{ig}), \tag{16}$$

$$\frac{\partial}{\partial \hat{t}}\left[\hat{\rho}_2\phi_2\hat{u}_2\right] + \frac{\partial}{\partial \hat{x}}\left[\hat{\rho}_2\phi_2\hat{u}_2^2 + \hat{P}_2\phi_2\right] = -\hat{u}_2\left(\frac{3}{\hat{r}}\right)\hat{\rho}_2\phi_2\hat{a}\hat{P}_1^m H(I - I_{ig}) - \hat{\beta}\frac{\phi_1\phi_2}{\hat{r}}\left(\hat{u}_2 - \hat{u}_1\right), \tag{17}$$

$$\frac{\partial}{\partial \hat{t}}\left[\hat{\rho}_2\phi_2\left(\hat{e}_2 + \frac{\hat{u}_2^2}{2}\right)\right] + \frac{\partial}{\partial \hat{x}}\left[\hat{\rho}_2\phi_2\hat{u}_2\left(\hat{e}_2 + \frac{\hat{u}_2^2}{2} + \frac{\hat{P}_2}{\hat{\rho}_2}\right)\right]$$
$$= -\left(\hat{e}_2 + \frac{\hat{u}_2^2}{2}\right)\left(\frac{3}{\hat{r}}\right)\hat{\rho}_2\phi_2\hat{a}\hat{P}_1^m H(I - I_{ig}) - \hat{\beta}\frac{\phi_1\phi_2}{\hat{r}}\hat{u}_2\left(\hat{u}_2 - \hat{u}_1\right) - \hat{h}\frac{\phi_1\phi_2}{\hat{r}^{1/3}}\left(\hat{T}_2 - \hat{T}_1\right) \tag{18}$$

$$\frac{\partial\phi_2}{\partial \hat{t}} + \hat{u}_2\frac{\partial\phi_2}{\partial \hat{x}} = \frac{\phi_1\phi_2}{\hat{\mu}_c}\left(\hat{P}_2 - \hat{P}_1 - \hat{f}\right) - \left(\frac{3}{\hat{r}}\right)\phi_2\hat{a}\hat{P}_1^m H(I - I_{ig}), \tag{19}$$

$$\frac{\partial \hat{n}}{\partial \hat{t}} + \frac{\partial}{\partial \hat{x}} \left[\hat{u}_2 \hat{n}\right] = 0, \tag{20}$$

$$\frac{\partial I}{\partial \hat{t}} + \hat{u}_2 \frac{\partial I}{\partial \hat{x}} = \hat{k}_I \left(1 - I\right) \left[\frac{\hat{P}_1 \phi_1 + \hat{P}_2 \phi_2 - \hat{P}_{1o} \phi_{1o} - \hat{P}_{2o} \phi_{2o}}{\hat{P}_{1o} \phi_{1o} + \hat{P}_{2o} \phi_{2o}}\right]^2 \exp\left[-\frac{\hat{T}_I}{\hat{T}_1 \phi_1 + \hat{T}_2 \phi_2}\right]. \tag{21}$$

In these equations, the subscripts "1" and "2" denote quantities associated with the gas and solid, respectively. Quantities labeled with overhats "ˆ•" are dimensional, and quantities labeled with subscript "o" are associated with the ambient state. The independent variables are time $\hat{t}$ and position $\hat{x}$. Dependent variables are as follows: the phase density $\hat{\rho}_i$ ($i = 1, 2$), defined as the mass of phase i per unit volume occupied by that phase; the phase pressure $\hat{P}_i$; the phase temperature $\hat{T}_i$; the particle velocity $\hat{u}_i$, measured with respect to a stationary reference frame; the specific internal energy $\hat{e}_i$; the volume fraction ϕ_i, defined as the ratio of the volume occupied by phase i to the total volume ($\phi_1 + \phi_2 = 1$); the radius of the spherical solid particles $\hat{r}$; the number of particles per unit volume $\hat{n}$ ($\equiv 3\phi_2/4\pi\hat{r}^3$); the intragranular stress $\hat{f}$; and an ignition variable I. In Eqs. (13-21), $H(I - I_{ig})$ is the Heaviside unit step function, and I_{ig}, $\hat{a}$, m, $\hat{\beta}$, $\hat{h}$, $\hat{\mu}_c$, $\hat{k}_I$, and $\hat{T}_I$ are constant parameters. Closure is achieved by specifying thermal $[\hat{P}_i = \hat{P}_i(\hat{\rho}_i, \hat{T}_i)]$ and caloric $[\hat{e}_i = \hat{e}_i(\hat{\rho}_i, \hat{T}_i)]$ state relations for each phase, and by specifying the functional form for $\hat{f}$.

Equations (1-3) and (4-6) are the mass, momentum, and energy evolution equations for the gas and solid, respectively. Equation (7) is a dynamic compaction equation, Eq. (8) is a particle number evolution equation, and Eq. (9) is an evolution equation for the ignition variable.

3.3 Numerical method

The non-strictly hyperbolic system of model equations were solved using a new high-resolution upwind numerical method (Gonthier and Powers 1997). The method, which is based on Godunov's approach, does not require the explicit use of artificial viscosity, can accurately capture shocks with minimal smearing, and can accurately resolve disparate time scales associated with rate-dependent processes. Rather than using the exact solution of the two-phase Riemann problem at each computational cell boundary to advance the solution in time, an approximate solution is used for increased computational efficiency. The method is convergent, and the spatial convergence rate was determined based on comparisons of numerical predictions with known theoretical results for several test problems. Global convergence rates of ~ 1.0 were determined for problems having embedded shocks, and rates of ~ 1.7 were determined for problems having continuous solutions.

3.4 Results

The numerical simulations predicted most experimentally observed features characteristic of piston-initiated DDT in granular HMX. Experimentally observed time scales, wave speeds, and pressure magnitudes are correctly predicted. Several classes of steady two-phase detonation wave structures were predicted to evolve: Chapman-Jouguet (CJ) and weak detonation structures having a lead shock in the gas and an unshocked solid, CJ structures having a lead shock in the solid and an unshocked gas, and CJ structures having a shock in both the gas and solid (Gonthier 1996). Which structure evolved was found to depend on the material compaction rate, the interphase drag rate, and the ambient mixture density. The results indicate that the CJ wave speed is not the unique wave speed for a self-propagating two-phase detonation. Numerically predicted structures agree well with results given by the strictly steady-state detonation wave analysis.

Shown in Fig. 1 is the predicted gas velocity history (measured relative to a fixed laboratory frame) for the evolution of a two-phase weak detonation having a lead shock in the gas and an unshocked solid. Here, $\hat{\xi}$ is position measured relative to a coordinate system attached to the piston, and $\hat{\tau} = \hat{t}$. Also shown in this figure is the spatial profile at $\hat{\tau} = 120 \ \mu s$. For this simulation, a virial equation of state was used for the gas and a Tait equation of state was used for the solid. The moving piston (located at $\hat{\xi} = 0 \ cm$) induces the formation of a compaction wave propagating at $402 \ m/s$. Ignition is predicted to occur near the piston surface approximately $135 \ \mu s$ after piston

impact; subsequently, there is predicted a rapid transition to detonation. The resulting detonation is propagating at 6168 m/s. A comparison of the *shocked gas - unshocked solid* weak detonation structure predicted by both the numerical simulation and the steady-state analysis is given in Fig. 2. Good agreement exists between the predicted solutions.

4. Acknowledgments

5. References

Asay B, and Hantel L (1991) Major thrust areas for examination of deflagration-to-detonation transition in granular and damaged explosives. Los Alamos National Laboratory Report M-8-91-61, Los Alamos, New Mexico

Baer MR, and Nunziato JW (1986) A two-phase mixture theory for the deflagration-to-detonation transition (DDT) in reactive granular materials. Int J Multiphase Flow 12:861-889

Butler PB, and Krier H (1986) Analysis of deflagration-to-detonation transition in high-energy solid propel- lants. Combust and Flame 63:31-48

Caspar, RJ (1996) Experimental and numerical study of shear localization as an initiation mechanism in energetic solids. MS thesis, Dept of Aero and Mech Engr, University of Notre Dame

Gonthier KA (1996) A numerical investigation of the evolution of self-propagating detonation in energetic granular solids. PhD dissertation, Dept of Aero and Mech Engr, University of Notre Dame

Gonthier KA, and Powers JM (1996) A numerical investigation of transient detonation in granulated material. Shock Waves 6:183-195

Gonthier KA, and Powers JM (1997) A numerical investigation of self-propagating two-phase detonation. submitted to the 16th International Colloquium on the Dynamics of Explosions and Reactive Systems, Cracow, Poland

Gonthier KA, and Powers JM (1997) A high-resolution upwind scheme for two-phase continuum DDT models. J Comp Phys (in preparation)

Powers JM, Stewart DS, and Krier H (1990a) Theory of two-phase detonation – part I: modeling. Combust and Flame 80:264-279

Powers JM, Stewart DS, and Krier H (1990b) Theory of two-phase detonation – part II: structure. Combust and Flame 80:280-303

Powers JM, Caspar RJ, and Mason, JJ (1997) Modeling and experimental investigation of reactive shear bands in energetic solids loaded in tension. submitted to the 16th International Colloquium on the Dynamics of Explosions and Reactive Systems, Cracow, Poland
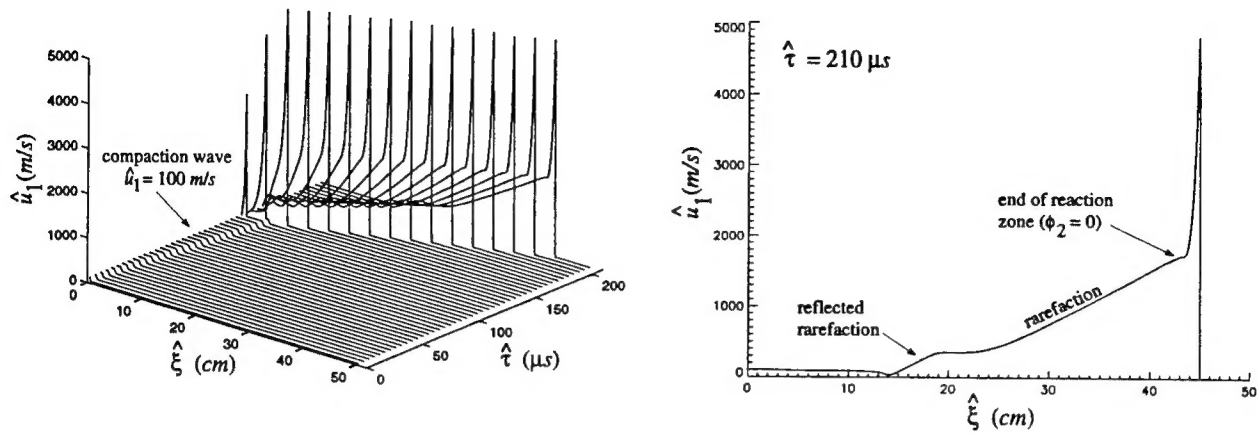
Figure 5: Predicted gas velocity history for the *shocked gas-unshocked solid* weak detonation simulation.
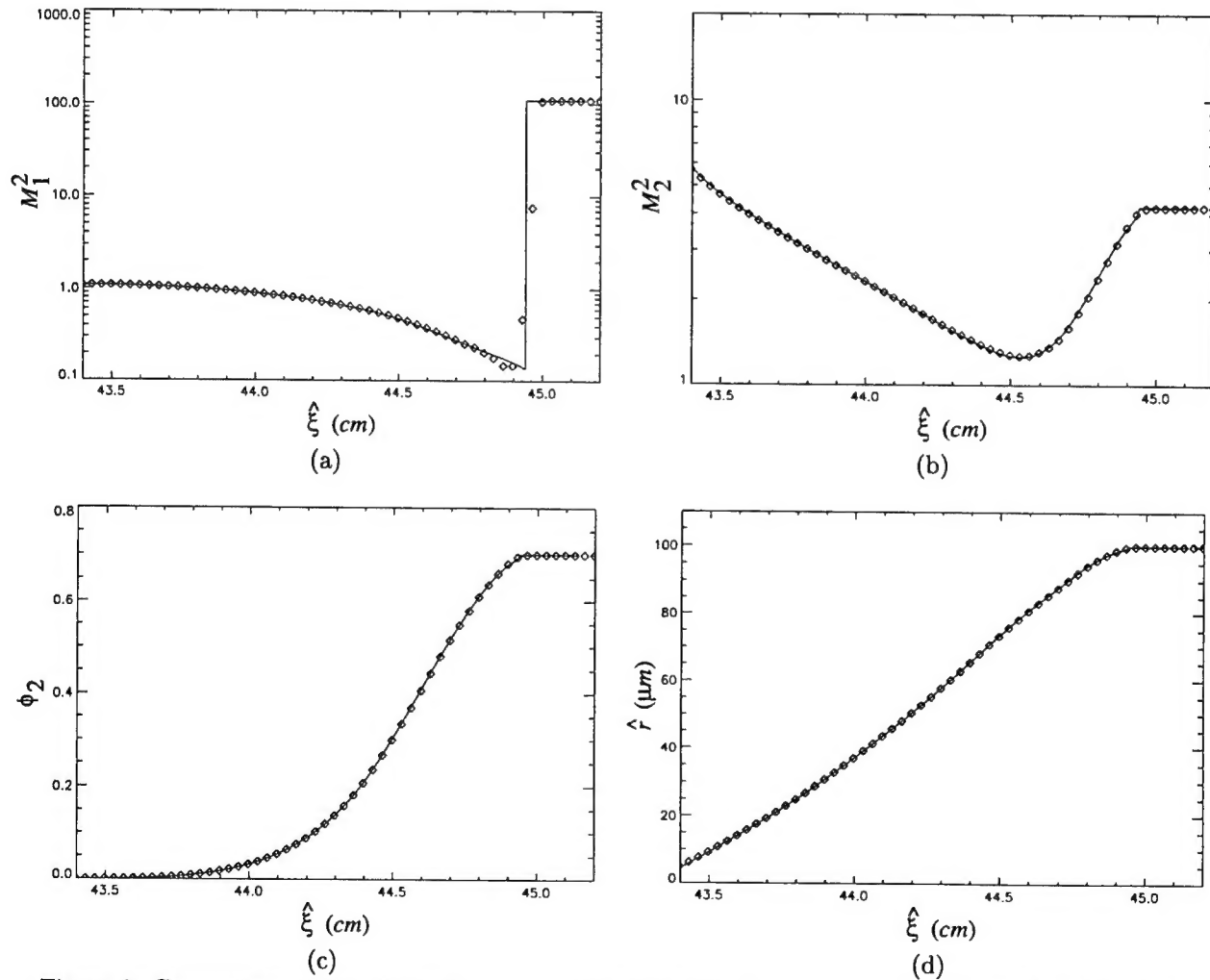

(a)

(b)

(c)

(d)

Figure 2: Comparison of the *shocked gas-unshocked solid* weak detonation structure predicted by the numerical simulation and the steady-state analysis: (a,b) gas and solid Mach number squared (relative to the wave); (c) solid volume fraction; and (d) particle radius.

Zhihua Qu's report not available at time of publication